From a Quantitative Analysis of Wave's Amplitude to Full-Waveform Inversion

Marine Deheuvels

To cite this version:

Marine Deheuvels. From a Quantitative Analysis of Wave's Amplitude to Full-Waveform Inversion. Geophysics [physics.geo-ph]. Pau. Université de Pau et des Pays de l'Adour (UPPA), FRA., 2023. English. NNT : . tel-04479844

HAL Id: tel-04479844
https://hal.science/tel-04479844

Submitted on 27 Feb 2024

THÈSE

UNIVERSITE DE PAU ET DES PAYS DE L’ADOUR
École doctorale Sciences Exactes et leurs Applications (ED 211 SEA)

Présentée et soutenue le 10 octobre 2023
par **Marine DEHEUVELS**

pour obtenir le grade de docteur
de l’Université de Pau et des Pays de l’Adour
Spécialité : Géophysique

DE L’ANALYSE QUANTITATIVE DES AMPLITUDES A L’INVERSION DE FORMES D’ONDES COMPLETES

-

FROM A QUANTITATIVE ANALYSIS OF WAVE'S AMPLITUDE TO FULL-WAVEFORM INVERSION

MEMBRES DU JURY

REVIEWERS	
• Nathalie FAVRETTO-CRISTINI	CNRS Research Director / Université Aix-Marseille
• Holger STEEB	Professor / Universität Stuttgart
EXAMINERS	
• Hélène BARUCQ	INRIA Research Director / INRIA Bordeaux – Sud-Ouest
• Eva CASPARI	Associate Professor / Montanuniversität Leoben
• Alexandre IMPERIALE	Research Associate / CEA – Université Paris Saclay
INVITED	
• Henri CALANDRA	Expert numerical methods and HPC / TotalEnergies
DIRECTORS	
• Daniel BRITO	Professor / Université de Pau et des Pays de l’Adour
• Florian FAUCHER	Research Associate / INRIA Bordeaux – Sud-Ouest

Abstract

In this work we investigate the recovery of heterogeneities of decimeter-scale samples using the measurement of mechanical ultrasonic waves propagating therein. Our studies set a particular emphasis on the attenuation property of the media, which is a frequency-dependent phenomenon.

One of the difficulties in working with laboratory-scale samples is the presence of multiple wave reflections within the medium, which are due to the free-surface boundary conditions surrounding it as it is a finite domain. With the help of viscoelastic numerical simulations in 3-D performed with the software *Hawen*, we develop a method that takes advantage of the reflections to recover an effective attenuation that is close to the actual attenuation of S-waves. For this purpose, we need to record the wave propagation for a sufficiently long time, until the wavefield reaches an equilibration of energy between P- and S- waves, that results from the successive wave reflections and conversions within the medium, this phenomenon is called equipartition. After this equipartition time, we show that the decreasing envelope of amplitude is no longer affected by the geometrical spreading due to wave expansion and that the decay always corresponds to the S-wave attenuation value, regardless of source-receiver location and component. We develop a method to recover the frequency-dependent attenuation values, by working with selected small bandwidths of frequencies applying a Gaussian filter on the frequency content of the signals. Our method further allows us to deduce viscoelastic models and parameters of the samples.

The method is first validated with numerical experiments. Then, we consider experimental measurements on aluminum, Fontainebleau sandstone, Carrara marble, and diorite samples. We use an experimental setup made up of piezoelectric sources and an interferometer laser receivers that measure the wavefield on the boundary of the samples. From these measurements, we are able to reconstruct the elastic parameters of these samples using first-wave arrivals analysis, and then we reconstruct the viscous parameters with the aforementioned method that we introduce. More precisely, we recover a Maxwell viscoelastic model in aluminum samples, and Zener viscoelastic models in rock samples.

The recovery of the effective viscoelastic laws and parameters gives an initial model for full-waveform inversion (FWI) method, which aims at reconstructing finer heterogeneities within the samples. In this work, we investigate how to reconstruct an anomaly in velocity and/or in attenuation in heterogeneous synthetic 2D media. With FWI, we highlight that the presence of reflections due to free-surface boundary conditions results in severe issues in the procedure. To alleviate these issues, we propose to work with complex frequencies, which act as adding artificial damping in the signal and attenuate the boundary effects. Also, we compare the use of several misfit functions as well as several parameter functions for the inversion of the viscous parameters. We found that the misfit functions that take the modulus of the signal, coupled with the inversion of the parameter squared give the best inversion results. Eventually, we notice the presence of cross-talk between parameters during the inversion when inverting a medium with an anomaly in velocity as well as viscosity in the same location. These presented tests pave the way for 3D and real laboratory-scaled cases.

Résumé

Une étude des ondes mécaniques à fréquences ultrasonores est mise en place afin de déterminer des hétérogénéités dans des roches de tailles décimétriques. L'accent est mis en particulier sur les propriétés d'atténuation de ces ondes mécaniques, phénomène qui dépend de la fréquence.

L'une des difficultés rencontrées dans l'étude des roches en condition de laboratoire est la présence de multiples réflexions d'ondes dans le milieu, dues aux conditions aux limites de surface libre. À l'aide de simulations numériques en conditions viscoélastiques réalisées avec le logiciel *Hawen*, une méthode qui tire parti des réflexions a été développée dans le but de déterminer une atténuation effective du milieu. Pour ce faire, le signal doit être enregistré pendant un temps suffisamment long, jusqu'à ce que le champ d'ondes atteigne un équilibre d'énergie entre les ondes P et S, qui résulte des réflexions et conversions successives des ondes dans le milieu. Ce phénomène est appelé équi-répartition. Après ce temps d'équi-répartition, on montre que l'enveloppe décroissante de l'amplitude n'est plus affectée par la divergence géométrique et que la décroissance correspond toujours à la valeur de l'atténuation de l'onde S, quels que soient l'emplacement et la composante de la source et du récepteur. En travaillant avec de petites largeurs de bande de fréquences sélectionnées en appliquant un filtre gaussien au contenu en fréquences des signaux, il est possible de retrouver les variations d'atténuation avec la fréquence, et ainsi d'identifier les modèles viscoélastiques et leurs paramètres associés des échantillons géophysiques.

La méthode est d'abord validée par des simulations numériques, puis utilisée en contexte de laboratoire en mesurant des échantillons d'aluminium, de grès de Fontainebleau, de marbre de Carrare et de diorite. Le dispositif expérimental est composé de sources piézoélectriques et d'un récepteur laser interféromètre qui enregistre le signal à la surface des échantillons. À partir de ces mesures, les paramètres élastiques de ces échantillons ont été reconstruits en analysant les premières arrivées d'ondes, ainsi que les paramètres visqueux grâce à la méthode développée précedemment. Plus précisément, l'aluminium suit un modèle viscoélastique de Maxwell, et les différentes roches suivent des modèles viscoélastiques de Zener de différents paramètres.

La caractérisation des lois et paramètres viscoélastiques effectifs permet de construire un modèle initial pour la méthode d'inversion de formes d'ondes complètes (FWI), qui vise à reconstruire des hétérogénéités plus fines à l'intérieur des échantillons. Dans ce travail, des milieux synthétiques hétérogènes en 2D comprenant une anomalie de vitesse et / ou de viscosité ont été étudiés. Il a été mis en évidence que la présence de réflexions dues aux conditions aux limites de surfaces libres entraîne des problèmes pour la FWI. Pour dépasser ces problèmes, travailler avec les fréquences complexes peut être une solution car la partie imaginaire agit comme un atténuateur artificiel dans le champ d'onde et fait en sorte que l'onde soit presque complètement atténuée avant d'atteindre le bord et de s'y réfléchir. Aussi, plusieurs fonctions coût et fonctions de paramètres ont été testées pour l'inversion des paramètres visqueux, et il a été constaté que les fonctions coût qui utilisent le module du signal, couplées à l'inversion du paramètre au carré, semblent donner les meilleurs résultats. Enfin, la présence d'une anomalie de vitesse et de viscosité au même endroit peut perturber les

résultats d’inversion. Les tests présentés ouvrent la voie à des cas 3D et à des cas réels à l’échelle du laboratoire.

Where there is a will, there is a way.
- William Hazlitt (1822)

Remerciements

Le goût de la recherche - paramètre important pour mener à bien une thèse - m'a été inculqué lors d'une toute première expérience en Licence. Pour cela je remercie tout d'abord Marceau Gresse et Jean Vandemeulebrouck pour m'avoir initiée à la recherche en L3 et m'avoir permis de faire mon premier terrain et mes toutes premières acquisitions de données. J'en garde un souvenir mémorable !

S'en sont suivis un long cheminement et des expériences divergentes avant d'arriver à ladite thèse. Je tiens à remercier mes directeurs de thèse Florian Faucher et Daniel Brito de m'avoir suivie pendant cette aventure. Florian, merci de m'avoir considérée comme une collègue depuis le début. Merci pour ta réactivité, ta rigueur et toutes tes explications sur le numérique. Daniel merci pour ta patience, merci de m'avoir fait confiance, et de m'avoir laissé les rênes du labo expérimental.

Un merci également à mon jury de thèse, Nathalie Favretto-Cristini, Holger Steeb, Hélène Barucq, Eva Caspari, Alexandre Imperiale et Henri Calandra pour les discussions constructives qui ont contribué à améliorer ce travail.

L'expérience aurait été bien différente si je n'avais pas été très bien entourée. Merci aux collègues de l'IPRA et particulièrement à mes co-bureau Salsa, Maria-Eleni et Lionel. Merci également à Hélène et à toute l'équipe MAKUTU de m'avoir très très bien accueillie pendant ma dernière année. Grosse pensée aux co-bureau Arjeta, Lola, Andréa, Manon, Julien, Ibrahima et Nicolas. Un grand merci à Salsa et Marine pour nos goûters et découvertes culinaires en tous genres. Salsa, tu es un exemple de courage et de résilience ! Un merci tout spécial à Charlie, qui a suivi l'avancée de la thèse depuis le début, avec ses hauts et ses bas, et qui a toujours été là ! Merci également aux copains de Montagne, Marthe, Clem (x3), Ben et Greg pour les sorties de folie ! Et un gros bisou et merci à Laura et Faustine, qui ont toujours soutenu mes projets les plus fous depuis la Licence :) !

Enfin un grand merci à ma famille, ma maman, ma mamie, Laurent, Camille et Hugo, de m'avoir soutenue et supportée depuis le début. Merci Laurent d'avoir cru en moi depuis le début. Merci Camille pour ton soutien et ta patience (surtout pendant la rédaction...). Mamie, merci pour ton soutien indéfectible, merci d'avoir été là à ma soutenance de thèse par la pensée. J'ai une grosse pensée pour papi qui aurait été fier aussi. Il l'est sûrement de là-haut. Mes derniers mots vont à ma maman, merci pour ton amour inconditionnel, qui me permet d'avancer et d'être forte dans tous mes projets.

Contents

Chapter I

Introduction

1 Introduction

The propagation of mechanical waves is commonly used in numerous geophysical applications, such as oil and gas exploration [Tatham and McCormack, 1991], mineral prospecting [Malehmir et al., 2012], civil engineering [Grandjean and Leparoux, 2004], geothermal prospecting [Sena-Lozoya et al., 2020], or more recently for prospects for carbon capture and storage [Zhu et al., 2022]. The different physical properties describing the medium influence the propagation of the waves therein, consequently, observing the propagation of waves gives us measurements that can be related to the different wave attributes [Chopra and Marfurt, 2005], allowing us to characterize a medium. In this work, we particularly focus on the attenuation properties of the media.

Mechanical wave attenuation is defined as the intrinsic loss of energy of the wavefield in a medium. Attenuation is of particular interest for porous media (see Dasgupta and Clark [1998] for the determination of the attenuation at a field scale) as it relates to physical properties of rocks such as porosity, density of fractures, and saturation [Pang et al., 2019]. Therefore, being able to characterize the attenuation property of a medium directly relates to its composition. The attenuation property is frequency-dependent [Müller et al., 2010; Gurevich and Pevzner, 2015; Carcione, 2007] and is usually associated with the dimensionless quality factor (Q-factor). Attenuation directly relates to the inverse of the Q-factor, meaning that higher values of Q-factor indicate a medium propagating well the mechanical waves, that is, a medium with low attenuation [Knopoff and MacDonald, 1958]. Conversely, low values of quality factors indicate a strongly attenuating medium.

In this thesis, the frequency-dependent mechanical wave attenuation at ultrasonic frequencies is represented using viscoelastic models of materials. These models are described using two components: an elastic one (represented by the elastic modulus) that does not attenuate, and a damping one (represented by the viscous modulus) that causes attenuation. Multiple viscoelastic models exist to cover the different attenuation behavior of materials [Biot, 1954; Golden and Graham, 1988; Carcione, 2007]. For porous rocks, Biot [1956a,b] developed poroelastic approaches that describe wave propagation in an elastic porous matrix filled with fluids; in this case, the intrinsic attenuation of the medium is defined as the dissipation of the wave due to friction at the fluid/solid interface. Although poroelastic models are more accurate in modeling wave propagation in rocks, they can be approximated by viscoelastic models [Bardet, 1992; Morochnik and Bardet, 1996], which are easier to consider numerically, even though they may lead to inaccuracy near the boundaries, Geertsma and Smit [1961]. This is our choice for this work, although rock materials are usually considered poroelastic.

In our work, we consider the three main viscoelastic models which are the Kelvin-Voigt, Maxwell and Zener models, each providing different behavior of attenuation with frequency, and we refer to [Carcione, 2007] for more details. These models correspond to one mechanism of attenuation for the entire frequency bandwidth, which appears sufficient in our investigation of signals from 60 kHz to 2 MHz. As an alternative, generalized attenuation models can be used to cover wider band, but they include additional physical parameters, hence more unknowns to identify. Another approach is to consider a frequency-independent Q-factor, i.e., constant Q-factor for all frequencies. This can for instance be achieved by fine-tuning the coefficient of the generalized Zener model [Liu et al., 1976] or of Maxwell model [Emmerich and Korn, 1987], which are shown to be equivalent [Moczo and Kristek, 2005]. In our work, we will see that all samples that we investigate have attenuation that varies with frequency hence working in the frequency domain appears more natural for the numerical investigation.

We further refer to Johnston et al. [1979] where a general review of the main aspects of attenuation is given. Different methods have been introduced in the literature to measure the attenuation property of samples, that we describe below. We further refer to Subramaniyan et al. [2014] for more details. Note that in general, the methods described below rely on high-attenuation media. In this thesis, we instead develop a method adapted to low-attenuation media at laboratory scale.

2 Laboratory-scale studies on attenuation

2.1 Reflection-based studies

Mechanical wave attenuation can be studied based upon the decrease in amplitude of wave's reflections in a sample. In the case of contact-source and contact-receiver such as a piezoelectric transmitter, the interface behavior between the source and the sample is unknown. To palliate this, a buffer between the source/receiver and the sample can be used. This buffer technique uses a reference medium with known physical properties, and known contrast of impedance with the measured sample from velocity measurements. The mechanical wave attenuation of the sample of interest is then deduced with the amplitude of the wave arrivals after few reflections. For instance, Roderick and Truell [1952] use a water buffer to analyze the attenuation of several steel samples. In this study the sample is immersed in a water tank and the pulser/receiver transducer records the signal outside of the water tank (Figure I.1).

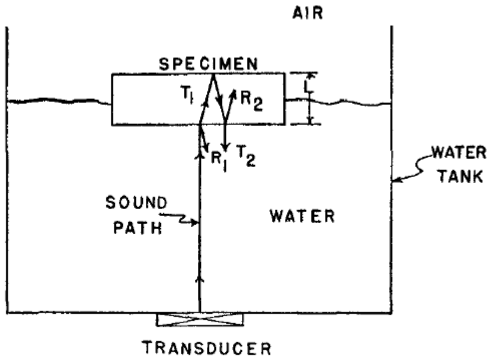

Figure I.1: Experimental set-up figure from Roderick and Truell [1952] for reflection-based studies.

Another buffer technique is presented by Winkler and Plona [1982], which use one of the experimental set-up of Papadakis et al. [1973] and the data processing of Sachse and Pao [1978] to study the mechanical wave attenuation of rocks as a function of frequency. The sample is placed between two known lucite buffers under pressure to prevent a bad coupling between the sample of interest and the lucite. Then, the attenuation information is recovered by the study of the spectral ratio between two reflections.

Another kind of buffer technique is the use of piezoelectric buffers-receivers with piezoelectric transmitters as explained by Yim et al. [2010] for the study of wave attenuation on cements. Their set-up is made as follow: piezoelectric transmitter - buffer-receiver - sample - buffer-receiver - piezoelectric transmitter. The wave is received both by the buffer and by another receiver placed after the buffer so that the wavelet sent by the source is known, as well as the attenuation induced by the buffers.

2.2 Spectral ratio analysis

Other experimental methods to quantify mechanical wave attenuation utilize the spectral ratio of signals between a reference and a sample of interest, or between several locations. It can also be coupled with the reflection-based study, where a spectral ratio between two reflections is analyzed. The interest of using spectral ratio is to have frequency-dependent measurements. The attenuation induced by a change in state of the sample (confining pressure) can also be measured by spectral ratio. Johnston et al. [1979] presented theoretical models for such measurements and Toksöz et al. [1979] defined an experimental method for the attenuation of signals on rocks varying with confining pressure (Figure I.2). This method had been then widely used for laboratory attenuation measurements on synthetic media [Bourbié and Nur, 1984], loose materials [Molyneux and Schmitt, 2000], for geotechnical purposes [Leong et al., 2004], and also for highly heterogeneous materials [Molero et al., 2010].

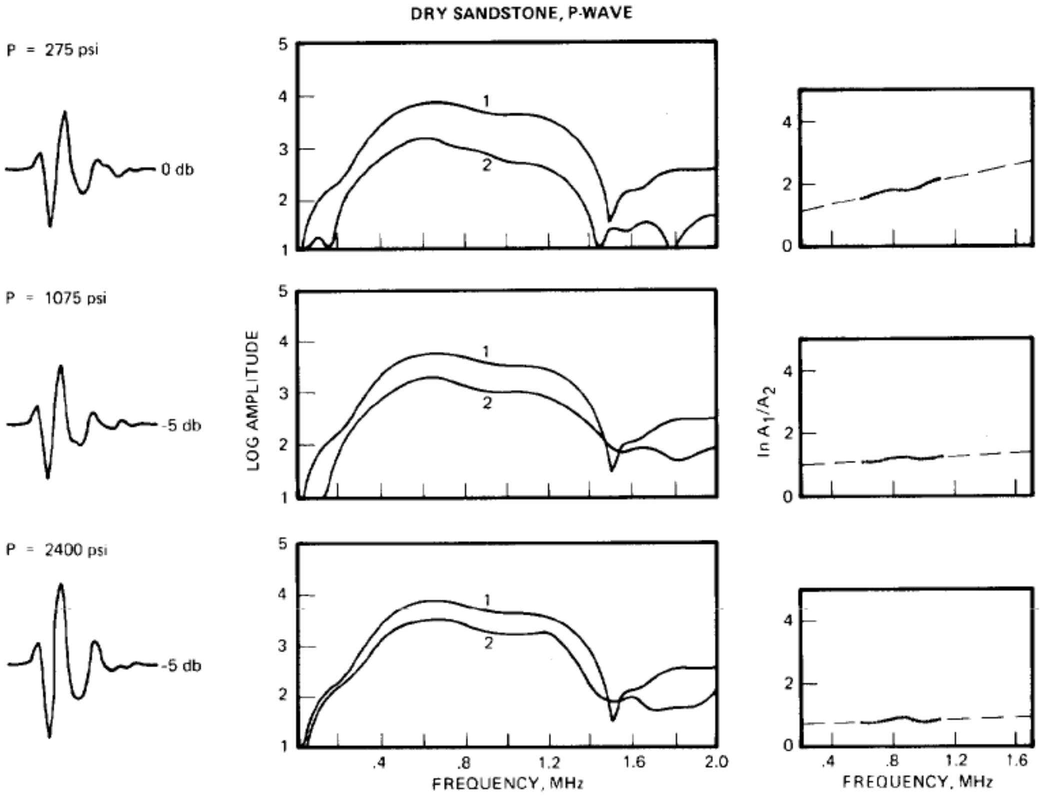

Figure I.2: Spectral ratio analysis figure from Toksöz et al. [1979]. Amplitude spectrum of aluminum reference (1) compared to amplitude spectra of dry Berea sandstone at different pressures (2).

The spectral ratio analysis is also used for Q-factor recovery in field studies. For example, Dasgupta and Clark [1998] estimated a frequency-independent quality factor in reflection data by comparing the amplitude spectrum of time-windowed signal between offsets.

2.3 Oscillation-based studies

The oscillation-based studies can be separated into two methods: the passive resonance method and the forced resonance/oscillations method.

The passive resonance method relies on the natural resonance of a sample due to its geometry, and is based on the analysis of the height of the peaks of resonance in the amplitude spectrum between location of measurements. The resonant bar method developed by Norris and Young [1970] focuses on recovering the complex moduli of viscoelastic materials, followed by experimental research [Madigosky and Lee, 1983; Capps, 1983] mainly for polymer characterization. Ritchie [1973] modified the resonant bar technique by using samples of other shapes such as a rectangular prism and worked on the different modes of vibrations. This technique is used at relatively low frequencies (up to several kHz) to measure the first orders of resonance of higher amplitude. With the aim of covering a large frequency range, from the kHz to several hundreds of kHz, Guillot and Trivett [2011] used simultaneously the resonant bar method and the wave-speed and amplitude analysis. Also, this method allowed to show that attenuation depends on humidity content in air [Pandit and King, 1979], but also fluid saturation [Winkler and Nur, 1979, 1982]. They showed that the attenuation is higher on partially saturated sandstones than on dry or fully saturated ones. In Fontainebleau Sandstone, Bourbie and Zinszner [1985] measured the attenuation depending on the frequency and water saturation until up to 10 kHz; they found for example a Q-factor of 100 in dry conditions around 10 kHz. Therefore, we see that the attenuation properties give information on the composition of the samples.

The forced-oscillations method consists in imposing sinusoidal mechanical stress on a sample and measuring the associated mechanical strain [Spencer Jr., 1981]. The shift between stress and strain relates to Q-factor of the samples (Figure I.3). This technique is used up to 100 kHz for high attenuation values (Q-factor < 300) (see Tisato and Madonna [2012]; Tisato et al. [2014]; Pimienta et al. [2015b, 2017] for measurements on sandstones). Caution should be made when using this technique as shown by [Tisato and Quintal, 2014] because attenuation results might depend on the induced strain on dry mediums. For an example of controlled changes in physical properties in a known rock sample, Pimienta et al. [2019] suggested a method where an artificial heating of the natural sample induces microcracks within the sample. The density of these microfractures are function of heating temperatures, thus it is possible to follow the change in physical properties as the heating temperature increases.

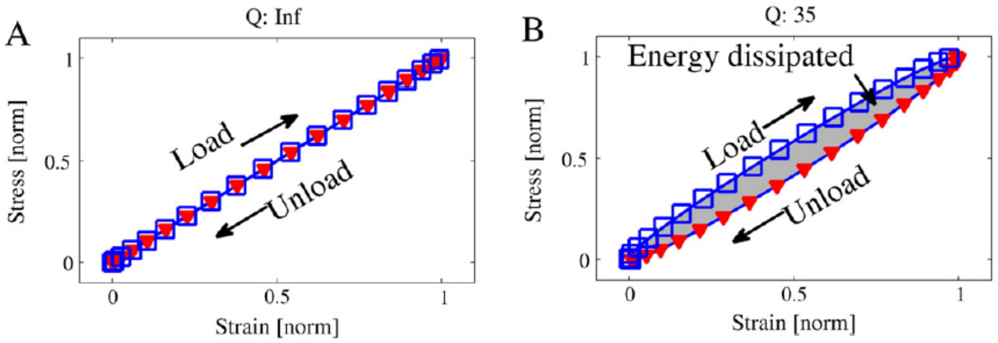

Figure I.3: Stress-strain relationship figure from Tisato and Madonna [2012] without (A) and with (B) attenuation.

3 On the use of full-waveform inversion (FWI) for attenuation recovery

Full-waveform inversion (FWI) is used to estimate quantitatively the subsurface properties / physical parameters of a medium from wavefield measurements. It recasts the problem as an optimization problem measuring the difference between the observed data with synthetic data. It is typically solved following an iterative approach where, at each iteration the physical models are updated and the synthetic data generated, until the difference between the two wavefields (observed and synthetic) is acceptable.

We refer to Bamberger et al. [1979], Tarantola [1984] and Pratt [1999] for the first studies on FWI problems in time and frequency domains, and to Virieux and Operto [2009] for an overview on FWI. In the dedicated chapter on FWI, we propose to study the impact of the presence of attenuation for FWI, where we target the reconstruction of both the elastic and viscous material properties.

In the following subsections, we present some main studies on attenuation characterization for FWI, whether it is to highlight the importance of an accurate consideration of attenuation in the data for FWI, or also for attenuation (Q-factor) imaging.

3.1 FWI on synthetics for quality factor characterization

Synthetic studies were performed in order to highlight the importance of taking into account wave attenuation in a seismic dataset, even to invert velocity. For instance, Groos et al. [2014] invert the S-waves velocity for different Q-factor values, assuming that they know the velocity of P-waves and the density. They highlight the limitation of considering a purely elastic material instead of considering seismic wave attenuation, and obtain artifacts at the source locations when the initial Q-factor selected for inversion is too low or too high compared to the actual one (10 or 40 instead of 20).

Later studies use synthetic field datasets to invert constant Q-factors over frequencies [Pan and Wang, 2020; Yong et al., 2021] and show the importance of the choice of the misfit function. In particular, they show that amplitude-related misfit functions is the best criterion to invert the Q-factor. It is easily understandable as attenuation mostly impact the amplitude of the propagating waves.

3.2 Laboratory scale FWI

At laboratory-scale, Ribodetti et al. [2004] perform numerical and experimental time-domain FWI to recover the velocity and representative attenuation of a lava core sample, relying on the first waves arrivals. Here they consider the known medium to be water, and the anomaly/heterogeneity inside the water is the lava core sample. They found velocity and Q-factor results in good agreement with the literature.

In the frequency domain, Bretaudeau et al. [2013] highlighted some difficulties with working at laboratory scale due to the free-surface boundary conditions that result in multiple reflections within the sample. They used frequency domain 2D FWI to recover P- and S- waves velocity on synthetics as well as on a laboratory-scale sample, with one free-surface border at the top of the model and all other borders with perfectly matched layers (PML). Some artifacts are due to the inaccurate source wavelet inversion, high signal-to-noise ratio at peculiar frequencies, and surface waves behavior. They had to "freeze" the velocity (they did not invert it) at a shallow depth (3 mm) on the free-surface to enhance the results on the experimental data, because the surface waves dominate the wavefield at this location.

To summarize, the difficulties when performing FWI is that having a good attenuation characterization is crucial even when we want to invert the velocities only. Also, the free-surface boundary conditions cause complications because of the reflections and the presence of surface waves. In laboratory context, we have to deal with these boundary conditions even more as all of the surfaces of the samples are free-surfaces.

4 Organization of the manuscript

In our study, we propose an approach to recover the frequency-dependent mechanical wave attenuation of low attenuation materials (Q-factor>200) at a laboratory scale (around decimeter-sized samples). Examples of low attenuation materials in natural rocks are for instance salt [Manthei et al., 2006], volcanic rocks [Rao et al., 2002] or dry pure sedimentary rocks [Bourbie and Zinszner, 1985]. The additional interest of recovering a representative attenuation model and parameters with respect to frequency may be for imaging purposes, such as inversion problems where we need to construct an initial attenuation model as well as guessing the attenuation models with respect to frequency [Faucher and Scherzer, 2023].

We describe in Chapter II the theoretical framework of the study in the frequency-domain for the propagation and attenuation of mechanical waves. This allows us to give frequency-dependent attenuation laws given by viscoelasticity theory and link them to the Q-factor. Then, we perform and analyze 3-D viscoelastic direct numerical simulations of wave propagation in synthetic media in Chapter III, where we build and test methods to recover viscoelastic parameters from the wavefield. This allows us to build numerical simulations close to laboratory conditions and validate a method to recover the known frequency-dependent viscoelastic parameters of the S-waves by taking advantage of the multiple reflections at the boundaries of the domain. After that, in Chapter IV we perform laboratory experiments in aluminum and natural rock samples (Fontainebleau sandstone, Carrara marble and diorite) from which we deduce attenuation properties from the measured wavefield at ultrasound frequencies, between 60 kHz and 2 MHz. In Chapter V we design a 2D medium containing a elastic and/or viscous anomaly, and we aim to recover the viscoelastic laws and properties of this medium with FWI. We also consider complex frequencies to reduce the reflections due to free-surface boundary conditions. Eventually, some conclusions and perspectives are given in Chapter VI.

Chapter II

Theoretical context

In this chapter, we review the different equations for mechanical wave propagation in order to understand their origin. We give the wave equation for elastic media, in time and in frequency domains. We introduce attenuation in the elastic equations by adding viscosity and obtain the underlying viscoelastic wave equation. Then, we mostly work with the frequency domain formulation, choice motivated by the frequency-dependent aspect of attenuation. In the last section, we develop the methodology to recover the viscoelastic parameters from a recorded wavefield.

1 Wave propagation in time domain

1.1 The Hooke's law in elastic context

According to the principle of linear elasticity, an elastic body is defined by its ability to instantly deform under a stress σ (*i.e.* an applied force) and to return to its original state once the stress is removed [Aki and Richards, 2002; Carcione, 2007; Schön, 2015]. The induced strain ϵ is proportional to the stiffness (*i.e.* rigidity) of the media. We can here imagine in 1D a spring being deformed (or shrunk) by a stress. The deformation will be proportional to the rigidity of the spring, *i.e.* the stiffer the spring is, the more difficult it will be to shrink it.

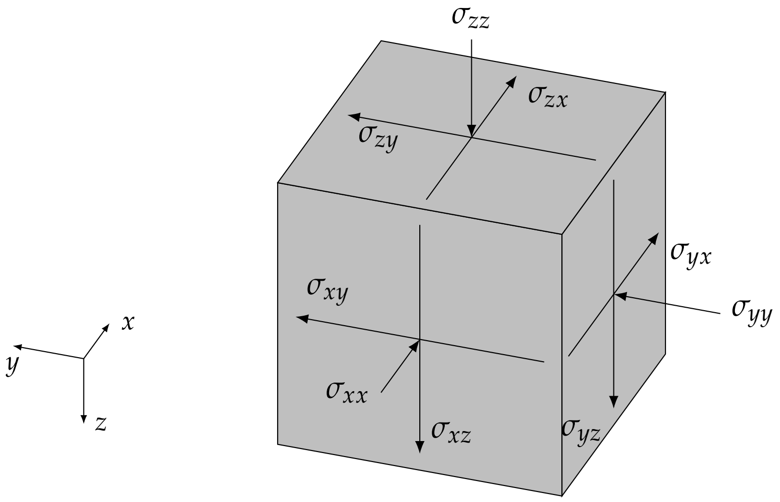

Figure II.1: Representation of the 3D stress tensor $\boldsymbol{\sigma}(\boldsymbol{x}, t)$ components on a cube.

In 3D, the stress tensor $\boldsymbol{\sigma}(\boldsymbol{x}, t)$ can be decomposed into normal and shear stress to the plane (Figure II.1). A normal stress (σ_{xx}, σ_{yy}, σ_{zz}), means for instance that σ_{xx} is the force applied to the plane normal to x in the x direction; and a shear stress (σ_{xy}, σ_{xz}, σ_{yz}, σ_{yx}, σ_{zx}, σ_{zy}) means for instance that σ_{xy} is the force applied to the plane normal to x in the y direction. The stress tensor is then written:

$$\boldsymbol{\sigma}(\boldsymbol{x}, t) = \begin{pmatrix} \sigma_{xx}(\boldsymbol{x}, t) & \sigma_{xy}(\boldsymbol{x}, t) & \sigma_{xz}(\boldsymbol{x}, t) \\ \sigma_{yx}(\boldsymbol{x}, t) & \sigma_{yy}(\boldsymbol{x}, t) & \sigma_{yz}(\boldsymbol{x}, t) \\ \sigma_{zx}(\boldsymbol{x}, t) & \sigma_{zy}(\boldsymbol{x}, t) & \sigma_{zz}(\boldsymbol{x}, t) \end{pmatrix}, \tag{II.1}$$

with $(\boldsymbol{x}, t)$ the space $\boldsymbol{x} = (x, y, z)$ and time dependencies respectively.

We have to ensure a balance of momentum in the body (by Cauchy's law), meaning that an applied force will not result in a rotation of the body. Looking at Figure II.1, this can only be done by symmetrization of stress tensor $\boldsymbol{\sigma}$, that means for instance $\sigma_{xy} = \sigma_{yx}$ and so on for all the shear components. We rewrite:

$$\boldsymbol{\sigma}(\boldsymbol{x},t) = \begin{pmatrix} \sigma_{xx}(\boldsymbol{x},t) & \sigma_{xy}(\boldsymbol{x},t) & \sigma_{xz}(\boldsymbol{x},t) \\ \sigma_{xy}(\boldsymbol{x},t) & \sigma_{yy}(\boldsymbol{x},t) & \sigma_{yz}(\boldsymbol{x},t) \\ \sigma_{xz}(\boldsymbol{x},t) & \sigma_{yz}(\boldsymbol{x},t) & \sigma_{zz}(\boldsymbol{x},t) \end{pmatrix}. \tag{II.2}$$

This stress tensor in 3D induces a strain tensor in 3D linked by the stiffness of the medium, defined by the Hooke's law such that:

$$\sigma_{ij}(\boldsymbol{x},t) = \sum_k \sum_l C_{ijkl}(\boldsymbol{x}) \epsilon_{kl}(\boldsymbol{x},t), \tag{II.3}$$

where i,j,k,l represents the direction x,y,z, $\boldsymbol{C}$ the stiffness tensor, and $\boldsymbol{\epsilon}(\boldsymbol{x},t)$ the strain tensor defined as

$$\boldsymbol{\epsilon}(\boldsymbol{x},t) = \begin{pmatrix} \epsilon_{xx}(\boldsymbol{x},t) & \epsilon_{xy}(\boldsymbol{x},t) & \epsilon_{xz}(\boldsymbol{x},t) \\ \epsilon_{yx}(\boldsymbol{x},t) & \epsilon_{yy}(\boldsymbol{x},t) & \epsilon_{yz}(\boldsymbol{x},t) \\ \epsilon_{zx}(\boldsymbol{x},t) & \epsilon_{zy}(\boldsymbol{x},t) & \epsilon_{zz}(\boldsymbol{x},t) \end{pmatrix}, \tag{II.4}$$

where

$$\epsilon_{ij}(\boldsymbol{x},t) = \frac{1}{2}\left(\frac{\partial u_i(\boldsymbol{x},t)}{\partial j} + \frac{\partial u_j(\boldsymbol{x},t)}{\partial i} \right), \tag{II.5}$$

$\mathbf{u}(\boldsymbol{x},t) = (u_x(\boldsymbol{x},t), u_y(\boldsymbol{x},t), u_z(\boldsymbol{x},t))$ being the displacement field in time domain.

We assume $\boldsymbol{\epsilon}(\boldsymbol{x},t)$ symmetric, *i.e.* $\epsilon_{ij}(\boldsymbol{x},t) = \epsilon_{ji}(\boldsymbol{x},t)$, thus we can rewrite

$$\boldsymbol{\epsilon}(\boldsymbol{x},t) = \begin{pmatrix} \epsilon_{xx}(\boldsymbol{x},t) & \epsilon_{xy}(\boldsymbol{x},t) & \epsilon_{xz}(\boldsymbol{x},t) \\ \epsilon_{xy}(\boldsymbol{x},t) & \epsilon_{yy}(\boldsymbol{x},t) & \epsilon_{yz}(\boldsymbol{x},t) \\ \epsilon_{xz}(\boldsymbol{x},t) & \epsilon_{yz}(\boldsymbol{x},t) & \epsilon_{zz}(\boldsymbol{x},t) \end{pmatrix}. \tag{II.6}$$

$\boldsymbol{C}$ is the elasticity tensor of order four with $3^4 = 81$ coefficients in the three-dimensional case. Knowing that $\boldsymbol{\sigma}(\boldsymbol{x},t)$ and $\boldsymbol{\epsilon}(\boldsymbol{x},t)$ are symmetric, we deduce that the $\boldsymbol{C}$ tensor is symmetric as well and leads to $C_{ijkl} = C_{jikl}$ and $C_{ijkl} = C_{ijlk}$. An other symmetry tells us that $C_{ijkl} = C_{klij}$. The number of coefficients is therefore reduced to 21 [Aki and Richards, 2002]. This allows us to use the Voigt notation to write the relation with matrix-vector product such that,

$$\begin{pmatrix}\sigma_{xx}(\boldsymbol{x},t)\\ \sigma_{yy}(\boldsymbol{x},t)\\ \sigma_{zz}(\boldsymbol{x},t)\\ \sigma_{yz}(\boldsymbol{x},t)\\ \sigma_{xz}(\boldsymbol{x},t)\\ \sigma_{xy}(\boldsymbol{x},t)\end{pmatrix} = \begin{pmatrix} C_{11}(\boldsymbol{x}) & C_{12}(\boldsymbol{x}) & C_{13}(\boldsymbol{x}) & C_{14}(\boldsymbol{x}) & C_{15}(\boldsymbol{x}) & C_{16}(\boldsymbol{x})\\ C_{12}(\boldsymbol{x}) & C_{22}(\boldsymbol{x}) & C_{23}(\boldsymbol{x}) & C_{24}(\boldsymbol{x}) & C_{25}(\boldsymbol{x}) & C_{26}(\boldsymbol{x})\\ C_{13}(\boldsymbol{x}) & C_{23}(\boldsymbol{x}) & C_{33}(\boldsymbol{x}) & C_{34}(\boldsymbol{x}) & C_{35}(\boldsymbol{x}) & C_{36}(\boldsymbol{x})\\ C_{14}(\boldsymbol{x}) & C_{24}(\boldsymbol{x}) & C_{34}(\boldsymbol{x}) & C_{44}(\boldsymbol{x}) & C_{45}(\boldsymbol{x}) & C_{46}(\boldsymbol{x})\\ C_{15}(\boldsymbol{x}) & C_{25}(\boldsymbol{x}) & C_{35}(\boldsymbol{x}) & C_{45}(\boldsymbol{x}) & C_{55}(\boldsymbol{x}) & C_{56}(\boldsymbol{x})\\ C_{16}(\boldsymbol{x}) & C_{26}(\boldsymbol{x}) & C_{36}(\boldsymbol{x}) & C_{46}(\boldsymbol{x}) & C_{56}(\boldsymbol{x}) & C_{66}(\boldsymbol{x})\end{pmatrix} \begin{pmatrix}\epsilon_{xx}(\boldsymbol{x},t)\\ \epsilon_{yy}(\boldsymbol{x},t)\\ \epsilon_{zz}(\boldsymbol{x},t)\\ 2\epsilon_{yz}(\boldsymbol{x},t)\\ 2\epsilon_{xz}(\boldsymbol{x},t)\\ 2\epsilon_{xy}(\boldsymbol{x},t)\end{pmatrix}. \tag{II.7}$$

1.2 Wave propagation in isotropic medium

From now on, the dependencies in space and time $(\boldsymbol{x},t)$ will not be written anymore in order to clarify the equations, unless a new parameter is introduced.

A media is said isotropic when its physical properties do not depend on the direction they apply. It means for instance that if we apply a same force in the normal direction σ_{xx} or σ_{yy} or σ_{zz}, the associated strain will be the same since the stiffness tensor remains the same in every directions (or $C_{11} = C_{22} = C_{33}$ for example). Isotropy allows us to simplify the equations but are only representative of a specific type of medium (for example aluminum) and we have to keep in mind that geological deposits are usually anisotropic. In isotropy, the stiffness tensor is defined from the Lamé parameters, $\lambda(\boldsymbol{x})$ the elastic modulus in [Pa] and $\mu(\boldsymbol{x})$ the shear modulus in [Pa]. Coefficients of $\boldsymbol{C}$ from the Hooke's law with respect to the Voigt's notation as in [Schön, 2015] are:

$$\begin{aligned}\begin{pmatrix}\sigma_{xx}\\ \sigma_{yy}\\ \sigma_{zz}\\ \sigma_{yz}\\ \sigma_{xz}\\ \sigma_{xy}\end{pmatrix} &= \begin{pmatrix}\lambda+2\mu & \lambda & \lambda & 0 & 0 & 0\\ \lambda & \lambda+2\mu & \lambda & 0 & 0 & 0\\ \lambda & \lambda & \lambda+2\mu & 0 & 0 & 0\\ 0 & 0 & 0 & \mu & 0 & 0\\ 0 & 0 & 0 & 0 & \mu & 0\\ 0 & 0 & 0 & 0 & 0 & \mu\end{pmatrix}\begin{pmatrix}\epsilon_{xx}\\ \epsilon_{yy}\\ \epsilon_{zz}\\ 2\epsilon_{yz}\\ 2\epsilon_{xz}\\ 2\epsilon_{xy}\end{pmatrix}\\ &= \begin{pmatrix}\lambda\epsilon_{xx}+2\mu\epsilon_{xx}+\lambda\epsilon_{yy}+\lambda\epsilon_{zz}\\ \lambda\epsilon_{xx}+\lambda\epsilon_{yy}+2\mu\epsilon_{yy}+\lambda\epsilon_{zz}\\ \lambda\epsilon_{xx}+\lambda\epsilon_{yy}+\lambda\epsilon_{zz}+2\mu\epsilon_{zz}\\ 2\mu\epsilon_{yz}\\ 2\mu\epsilon_{xz}\\ 2\mu\epsilon_{xy}\end{pmatrix}\\ &= \begin{pmatrix}\lambda(\epsilon_{xx}+\epsilon_{yy}+\epsilon_{zz})+2\mu\epsilon_{xx}\\ \lambda(\epsilon_{xx}+\epsilon_{yy}+\epsilon_{zz})+2\mu\epsilon_{yy}\\ \lambda(\epsilon_{xx}+\epsilon_{yy}+\epsilon_{zz})+2\mu\epsilon_{zz}\\ 2\mu\epsilon_{yz}\\ 2\mu\epsilon_{xz}\\ 2\mu\epsilon_{xy}\end{pmatrix}\end{aligned}$$

$$\begin{pmatrix}\sigma_{xx}\\ \sigma_{yy}\\ \sigma_{zz}\\ \sigma_{yz}\\ \sigma_{xz}\\ \sigma_{xy}\end{pmatrix} = \begin{pmatrix}\lambda\,\mathrm{Tr}(\boldsymbol{\epsilon}) + 2\mu\epsilon_{xx}\\ \lambda\,\mathrm{Tr}(\boldsymbol{\epsilon}) + 2\mu\epsilon_{yy}\\ \lambda\,\mathrm{Tr}(\boldsymbol{\epsilon}) + 2\mu\epsilon_{zz}\\ 2\mu\epsilon_{yz}\\ 2\mu\epsilon_{xz}\\ 2\mu\epsilon_{xy}\end{pmatrix}. \tag{II.8}$$

We can rewrite in the matrix notation:

$$\begin{pmatrix}\sigma_{xx} & \sigma_{xy} & \sigma_{xz}\\ \sigma_{xy} & \sigma_{yy} & \sigma_{yz}\\ \sigma_{xz} & \sigma_{yz} & \sigma_{zz}\end{pmatrix} = \lambda\,\mathrm{Tr}[\boldsymbol{\epsilon}]I_3 + 2\mu\begin{pmatrix}\epsilon_{xx} & \epsilon_{xy} & \epsilon_{xz}\\ \epsilon_{xy} & \epsilon_{yy} & \epsilon_{yz}\\ \epsilon_{xz} & \epsilon_{yz} & \epsilon_{zz}\end{pmatrix}, \tag{II.9}$$

the operator Tr is the trace of the matrix and I_3 the identity matrix of size 3. The equation (II.9) is compactly written as

$$\boldsymbol{\sigma} = \lambda\,\mathrm{Tr}[\boldsymbol{\epsilon}]I_3 + 2\mu\boldsymbol{\epsilon}. \tag{II.10}$$

1.3 Equations for the displacement field

Now we want to link the stress-strain relationship into wave propagation with respect to Lamé parameters. For that, we use the equation of motion that describes the motion of a particle, $\boldsymbol{u}$, with the Newton's second law, that links the acceleration $\frac{\partial^2 \boldsymbol{u}(\boldsymbol{x},t)}{\partial t^2}$ of this particle to the sum of the stresses applied on it. That means, for each x, y and z components:

$$\begin{aligned}\rho\frac{\partial^2 u_x}{\partial t^2} &= \frac{\partial \sigma_{xx}}{\partial x} + \frac{\partial \sigma_{xy}}{\partial y} + \frac{\partial \sigma_{xz}}{\partial z}\\ \rho\frac{\partial^2 u_y}{\partial t^2} &= \frac{\partial \sigma_{yx}}{\partial x} + \frac{\partial \sigma_{yy}}{\partial y} + \frac{\partial \sigma_{yz}}{\partial z}\\ \rho\frac{\partial^2 u_z}{\partial t^2} &= \frac{\partial \sigma_{xz}}{\partial x} + \frac{\partial \sigma_{yz}}{\partial y} + \frac{\partial \sigma_{zz}}{\partial z},\end{aligned} \tag{II.11}$$

ρ being the density in [$\mathrm{kg\,m^{-3}}$]. Using the divergence operator $\nabla\cdot$, (II.11) becomes:

$$\rho\frac{\partial^2 \boldsymbol{u}}{\partial t^2} = \nabla\cdot\boldsymbol{\sigma}. \tag{II.12}$$

In order to inject the Lamé parameters, we develop and derive the wave equations combining the equation (II.10) and the equation of motion (II.12):

$$\rho\frac{\partial^2 \boldsymbol{u}}{\partial t^2} = \nabla\cdot(\lambda\,\mathrm{Tr}[\boldsymbol{\epsilon}]I_3) + \nabla\cdot(2\mu\boldsymbol{\epsilon}). \tag{II.13}$$

We can further develop the equation (II.5) to have

$$\mathrm{Tr}[\boldsymbol{\epsilon}] = \epsilon_{xx} + \epsilon_{yy} + \epsilon_{zz} = \frac{\partial u_x}{\partial x} + \frac{\partial u_y}{\partial y} + \frac{\partial u_z}{\partial z} = \nabla \cdot \boldsymbol{u}. \tag{II.14}$$

We can replace the strain tensor $\boldsymbol{\epsilon}$ in terms of the displacement field $\boldsymbol{u}$ and further develop the first part of the right-hand side of the equation (II.13) such that

$$\begin{aligned}\nabla \cdot (\lambda\, \mathrm{Tr}([\boldsymbol{\epsilon}] I_3) &= \nabla \cdot \begin{pmatrix} \lambda \nabla \cdot \boldsymbol{u} & 0 & 0 \\ 0 & \lambda \nabla \cdot \boldsymbol{u} & 0 \\ 0 & 0 & \lambda \nabla \cdot \boldsymbol{u} \end{pmatrix} \\ &= \begin{pmatrix} \dfrac{\partial}{\partial x}(\lambda \nabla \cdot \boldsymbol{u}) \\ \dfrac{\partial}{\partial y}(\lambda \nabla \cdot \boldsymbol{u}) \\ \dfrac{\partial}{\partial z}(\lambda \nabla \cdot \boldsymbol{u}) \end{pmatrix} = \nabla(\lambda \nabla \cdot \boldsymbol{u}),\end{aligned} \tag{II.15}$$

then we develop the second part of the right-hand side of the equation (II.13) such that

$$\begin{aligned} 2\mu\boldsymbol{\epsilon} &= \mu \begin{pmatrix} 2\dfrac{\partial u_x}{\partial x} & \dfrac{\partial u_x}{\partial y} + \dfrac{\partial u_y}{\partial x} & \dfrac{\partial u_x}{\partial z} + \dfrac{\partial u_z}{\partial x} \\ \dfrac{\partial u_x}{\partial y} + \dfrac{\partial u_y}{\partial x} & 2\dfrac{\partial u_y}{\partial y} & \dfrac{\partial u_y}{\partial z} + \dfrac{\partial u_z}{\partial y} \\ \dfrac{\partial u_x}{\partial z} + \dfrac{\partial u_z}{\partial x} & \dfrac{\partial u_y}{\partial z} + \dfrac{\partial u_z}{\partial y} & 2\dfrac{\partial u_z}{\partial z} \end{pmatrix} \\ &= \mu \left[\begin{pmatrix} \dfrac{\partial u_x}{\partial x} & \dfrac{\partial u_x}{\partial y} & \dfrac{\partial u_x}{\partial z} \\ \dfrac{\partial u_y}{\partial x} & \dfrac{\partial u_y}{\partial y} & \dfrac{\partial u_y}{\partial z} \\ \dfrac{\partial u_z}{\partial x} & \dfrac{\partial u_z}{\partial y} & \dfrac{\partial u_z}{\partial z} \end{pmatrix} + \begin{pmatrix} \dfrac{\partial u_x}{\partial x} & \dfrac{\partial u_y}{\partial x} & \dfrac{\partial u_z}{\partial x} \\ \dfrac{\partial u_x}{\partial y} & \dfrac{\partial u_y}{\partial y} & \dfrac{\partial u_z}{\partial y} \\ \dfrac{\partial u_x}{\partial z} & \dfrac{\partial u_y}{\partial z} & \dfrac{\partial u_z}{\partial z} \end{pmatrix} \right] \\ &= \mu[\nabla \boldsymbol{u} + (\nabla \boldsymbol{u})^T], \end{aligned} \tag{II.16}$$

with the operator ∇ standing for the gradient.

We can now concatenate the two parts and define the equation in terms of displacement field for an elastic isotropic medium in terms of the Lamé parameters and density:

$$\rho \frac{\partial^2 \boldsymbol{u}}{\partial t^2} = \nabla(\lambda \nabla \cdot \boldsymbol{u}) + \nabla \cdot \left(\mu[\nabla \boldsymbol{u} + (\nabla \boldsymbol{u})^T] \right). \tag{II.17}$$

1.4 P- and S- waves in homogeneous media

Here we consider homogeneous media, where Lamé parameters λ and μ do not depend on $\boldsymbol{x}$. We introduce the two body waves that can propagate in the sample. The P-wave, that is a pressure wave, and the S-wave, that is a shear wave.

We develop equation (II.17) in the aim of rearranging and defining it in terms of P- and S- wave velocities. Thus we have:

$$\begin{aligned}\rho\frac{\partial^2\boldsymbol{u}}{\partial t^2} &= \nabla\lambda\nabla\cdot\boldsymbol{u}+\lambda\nabla\nabla\cdot\boldsymbol{u}+\nabla\cdot\mu[\nabla\boldsymbol{u}+(\nabla\boldsymbol{u})^T]+\mu\nabla\cdot[\nabla\boldsymbol{u}+(\nabla\boldsymbol{u})^T] \\ &= \nabla\lambda\nabla\cdot\boldsymbol{u}+\lambda\nabla\nabla\cdot\boldsymbol{u}+\nabla\cdot\mu[\nabla\boldsymbol{u}+(\nabla\boldsymbol{u})^T]+\mu\nabla\cdot\nabla\boldsymbol{u}+\mu\nabla\cdot(\nabla\boldsymbol{u})^T.\end{aligned} \tag{II.18}$$

Because we consider Lamé parameters λ and μ homogeneous in space, we have $\nabla\lambda = 0$ and $\nabla\cdot\mu = 0$, leading to:

$$\begin{aligned}\rho\frac{\partial^2\boldsymbol{u}}{\partial t^2} &= \lambda\nabla\nabla\cdot\boldsymbol{u}+\mu\nabla\cdot\nabla\boldsymbol{u}+\mu\nabla\cdot(\nabla\boldsymbol{u})^T \\ &= \lambda\nabla\nabla\cdot\boldsymbol{u}+\mu\Delta\boldsymbol{u}+\mu\nabla\cdot(\nabla\boldsymbol{u})^T,\end{aligned} \tag{II.19}$$

with Δ the Laplacian operator.

Because $\nabla\cdot(\nabla\boldsymbol{u})^T = \nabla\nabla\cdot\boldsymbol{u}$, the equation (II.19) can be rewritten

$$\rho\frac{\partial^2\boldsymbol{u}}{\partial t^2} = (\lambda+\mu)\nabla\nabla\cdot\boldsymbol{u}+\mu\Delta\boldsymbol{u}. \tag{II.20}$$

We can also note that $\nabla\cdot(\nabla\boldsymbol{u}) = \nabla\nabla\cdot\boldsymbol{u}-\nabla\times\nabla\times\boldsymbol{u}$, with $(\nabla\times)$ the curl operator, then

$$\begin{aligned}\rho\frac{\partial^2\boldsymbol{u}}{\partial t^2} &= \lambda\nabla\nabla\cdot\boldsymbol{u}+\mu(\nabla\nabla\cdot\boldsymbol{u}-\nabla\times\nabla\times\boldsymbol{u})+\mu\nabla\nabla\cdot\boldsymbol{u} \\ &= \lambda\nabla\nabla\cdot\boldsymbol{u}+2\mu\nabla\nabla\cdot\boldsymbol{u}-\mu\nabla\times\nabla\times\boldsymbol{u} \\ &\boxed{\rho\frac{\partial^2\boldsymbol{u}}{\partial t^2} = (\lambda+2\mu)\nabla\nabla\cdot\boldsymbol{u}-\mu\nabla\times\nabla\times\boldsymbol{u}.}\end{aligned} \tag{II.21}$$

This equation (II.21) is the general equation defined by the displacement field in homogeneous elastic medium in time domain. With this equation we recognize the term $(\lambda+2\mu)$ associated with the divergence part that describes the P-wave, and the term μ associated with the curl part that describes the S-wave, with the P-wave velocity defined as:

$$V_P = \sqrt{\frac{\lambda+2\mu}{\rho}}, \tag{II.22}$$

and the S-wave velocity V_S:

$$V_S = \sqrt{\frac{\mu}{\rho}}. \tag{II.23}$$

We further refer to Subsection 2.3 where the equations for P- and S- waves are obtained from the Helmholtz decomposition.

2 Wave propagation in frequency domain

In this section we define the wave propagation in frequency domain from the equations in time-domain defined above. The use of frequency domain is of interest in the context of attenuation, that is frequency-dependent [Carcione, 2007; Müller et al., 2010; Gurevich and Pevzner, 2015], and allows us to write the attenuation laws and behaviors more conveniently than in time-domain.

2.1 Fourier transform

We note that the Fourier transform is not used formally to write frequency domain, but it gives us hints on how it is constructed. We consider a function $h(t)$ that has to be integrable on $\mathbb{R}$. The Fourier transform of this function is given by:

$$\big(\mathcal{F}(h(t))\big)(\omega) = H(\omega) = \int_{-\infty}^{+\infty} h(t)e^{-\mathrm{i}\omega t}\,dt, \tag{II.24}$$

with $\omega = 2\pi f$ the pulsation in [rad/s] and f the frequency in [Hz].

The inverse Fourier transform from h to H is:

$$\big(\mathcal{F}^{-1}(H(\omega))\big)(t) = h(t) = \int_{-\infty}^{+\infty} H(\omega)e^{\mathrm{i}\omega t}\,d\omega. \tag{II.25}$$

We consider the Fourier transform of the time-derivative of $h(t)$ such that $h(t)' = \dfrac{\partial h(t)}{\partial t}$, and use the integration by part to get the Fourier transform:

$$\begin{aligned}\left(\mathcal{F}\left(\frac{\partial h(t)}{\partial t}\right)\right)(\omega) &= \int_{-\infty}^{+\infty} \frac{\partial h(t)}{\partial t} e^{-\mathrm{i}\omega t}\,dt \\ &= \left[h(t)e^{-\mathrm{i}\omega t}\right]_{-\infty}^{+\infty} - \int_{-\infty}^{+\infty} h(t)(-\mathrm{i}\omega)e^{-i\omega t}\,dt \\ &= \mathrm{i}\omega \int_{-\infty}^{+\infty} h(t)e^{-\mathrm{i}\omega t}\,dt \\ &= \mathrm{i}\omega H(\omega).\end{aligned} \tag{II.26}$$

Based on the same principle, the Fourier transform of $\dfrac{\partial^2 h(t)}{\partial t^2}$ is

$$\begin{aligned}\left(\mathcal{F}\left(\frac{\partial^2 h(t)}{\partial t^2}\right)\right)(\omega) &= \int_{-\infty}^{+\infty} \frac{\partial^2 h(t)}{\partial t^2} e^{-\mathrm{i}\omega t}\,dt \\ &= \left[\frac{\partial h(t)}{\partial t} e^{-\mathrm{i}\omega t}\right]_{-\infty}^{+\infty} - \int_{-\infty}^{+\infty} \frac{\partial h(t)}{\partial t}(-i\omega)e^{-\mathrm{i}\omega t}\,dt \\ &= \mathrm{i}\omega \int_{-\infty}^{+\infty} \frac{\partial h(t)}{\partial t} e^{-\mathrm{i}\omega t}\,dt \\ &= (\mathrm{i}\omega)^2 H(\omega) \\ &= -\omega^2 H(\omega).\end{aligned} \tag{II.27}$$

2.2 Elastic wave equation

The time-harmonic formulation uses the displacement $\boldsymbol{\hat{u}}$ as a function of the pulsation ω [Colton and Kress, 1998]:

$$\boldsymbol{u}(\boldsymbol{x}, t) = \boldsymbol{\hat{u}}(\boldsymbol{x}, \omega) \exp(\mathrm{i}\omega t), \tag{II.28}$$

that is equivalent to

$$\boldsymbol{\hat{u}}(\boldsymbol{x}, \omega) = \boldsymbol{u}(\boldsymbol{x}, t) \exp(-\mathrm{i}\omega t), \tag{II.29}$$

with $\boldsymbol{\hat{u}}$ the displacement field in frequency domain in [m].

The equation in time-domain for homogeneous isotropic medium (II.21) can be rewritten in frequency domain such that

$$\boxed{-\rho\omega^2\boldsymbol{\hat{u}}(\boldsymbol{x}, \omega) = (\lambda + 2\mu)\nabla\nabla \cdot \boldsymbol{\hat{u}}(\boldsymbol{x}, \omega) - \mu\nabla \times \nabla \times \boldsymbol{\hat{u}}(\boldsymbol{x}, \omega).} \tag{II.30}$$

Here we recognize the term ω^2 coming from the second derivative in (II.27). This equation (II.30) is the wave equation defined in frequency domain for homogeneous isotropic elastic medium.

2.3 Helmholtz decomposition

Using the theorem of Helmholtz, the displacement field $\boldsymbol{\hat{u}}$ can be decomposed into a curl-free component and a divergence-free component. It corresponds respectively to the P- and S- waves such that [Kupradze et al., 1976, p. 123]

$$\boldsymbol{\hat{u}} = \nabla\phi + \nabla \times \boldsymbol{\psi} = \boldsymbol{\hat{u}}_P + \boldsymbol{\hat{u}}_S, \tag{II.31}$$

with $\boldsymbol{\hat{u}}_P$ and $\boldsymbol{\hat{u}}_S$ the displacement field associated to the P- and S- waves respectively, ϕ a scalar field potential and $\boldsymbol{\psi}$ a vector field potential.

Given that $\nabla \cdot (\nabla \times \boldsymbol{\psi}) = 0$ and $\nabla \times (\nabla\phi) = 0$, we apply a divergence and a curl on both side of equation (II.31) to distinct the P and the S wave motion such that

$$\nabla \cdot \boldsymbol{\hat{u}} = \nabla \cdot \nabla\phi = \Delta\phi = \nabla \cdot \boldsymbol{\hat{u}}_P, \tag{II.32}$$

because the S-wave is divergence-free, and

$$\nabla \times \boldsymbol{\hat{u}} = \nabla \times \nabla \times \boldsymbol{\psi} = \nabla \times \boldsymbol{\hat{u}}_S, \tag{II.33}$$

because the P-wave is curl-free.

We can now replace $\nabla \cdot \boldsymbol{\hat{u}}$ and $\nabla \times \boldsymbol{\hat{u}}$ in the equation (II.30):

$$\begin{aligned} -\rho\omega^2\boldsymbol{\hat{u}} &= (\lambda + 2\mu)\nabla\nabla \cdot \boldsymbol{\hat{u}} - \mu\nabla \times \nabla \times \boldsymbol{\hat{u}} \\ -\omega^2(\boldsymbol{\hat{u}}_P + \boldsymbol{\hat{u}}_S) &= V_P^2\nabla\nabla \cdot \boldsymbol{\hat{u}}_P - V_S^2\nabla \times \nabla \times \hat{u}_S \\ \{-\omega^2\hat{u}_P - V_P^2\nabla\nabla \cdot \boldsymbol{\hat{u}}_P\} + \{&-\omega^2\boldsymbol{\hat{u}}_S + V_S^2\nabla \times \nabla \times \boldsymbol{\hat{u}}_S\} = 0. \end{aligned} \tag{II.34}$$

From the vector identities, we have:

$$\nabla\nabla\cdot\hat{\boldsymbol{u}}_P = \Delta\hat{\boldsymbol{u}}_P + \nabla\times\nabla\times\hat{\boldsymbol{u}}_P = \Delta\hat{\boldsymbol{u}}_P \tag{II.35a}$$

$$\nabla\times\nabla\times\hat{\boldsymbol{u}}_S = -\Delta\hat{\boldsymbol{u}}_S + \nabla\nabla\cdot\hat{\boldsymbol{u}}_S = \Delta\hat{\boldsymbol{u}}_S, \tag{II.35b}$$

the P and S waves each satisfy a wave equation such that (equation (II.30)):

$$\left(\frac{\omega^2}{V_P^2} + \Delta\right)\hat{\boldsymbol{u}}_P = 0, \tag{II.36}$$

and

$$\left(\frac{\omega^2}{V_S^2} + \Delta\right)\hat{\boldsymbol{u}}_S = 0. \tag{II.37}$$

We define the wavenumber $k = \omega/V$ with V the wave velocity (of P- or S- wave), and we note for an homogeneous 1D equation or a planewave propagation, $\hat{\boldsymbol{u}}(x,\omega)$ can be explicitly written $\hat{\boldsymbol{u}}(x,\omega) = \boldsymbol{u}_0\exp(-\mathrm{i}kx)$, with $\boldsymbol{u}_0$ the amplitude of displacement at source locations and x the offset. Modifying (II.28), we write the displacement field as in Carcione [2007]:

$$\boldsymbol{u}(x,t) = \hat{\boldsymbol{u}}(x,\omega)\exp(\mathrm{i}\omega t) = \boldsymbol{u}_0\cdot\exp[\mathrm{i}(\omega t - kx)], \tag{II.38}$$

and equivalently, from equation (II.29), we write in time-harmonic form:

$$\hat{\boldsymbol{u}}(x,\omega) = \boldsymbol{u}_0\cdot\exp(-\mathrm{i}kx). \tag{II.39}$$

In order to illustrate the P- and S- vector field propagation, let us consider a motion that only varies in the z direction, such that $\boldsymbol{u}(\boldsymbol{x}) := \boldsymbol{u}(z)$. In this case, the potentials $\boldsymbol{\psi}$ and ϕ only vary with z as well, and we have,

$$\frac{\partial\psi_y}{\partial x} = \frac{\partial\psi_z}{\partial x} = \frac{\partial\phi}{\partial x} = \frac{\partial\psi_x}{\partial y} = \frac{\partial\psi_z}{\partial y} = \frac{\partial\phi}{\partial y} = 0. \tag{II.40}$$

From the decomposition of the displacement field $\widehat{\boldsymbol{u}} = \nabla\phi + \nabla\times\boldsymbol{\psi}$, we obtain,

$$\hat{u}_x = \frac{\partial\phi}{\partial x} + \left(\frac{\partial\psi_z}{\partial y} - \frac{\partial\psi_y}{\partial z}\right) = -\frac{\partial\psi_y}{\partial z} \tag{II.41a}$$

$$\hat{u}_y = \frac{\partial\phi}{\partial y} + \left(\frac{\partial\psi_x}{\partial z} - \frac{\partial\psi_z}{\partial x}\right) = \frac{\partial\psi_x}{\partial z} \tag{II.41b}$$

$$\hat{u}_z = \frac{\partial\phi}{\partial z} + \left(\frac{\partial\psi_y}{\partial x} - \frac{\partial\psi_x}{\partial y}\right) = \frac{\partial\phi}{\partial z}. \tag{II.41c}$$

We see that the S-wave (related to $\boldsymbol{\psi}$) shows in the components $\widehat{u}_x$ and $\widehat{u}_y$ of the displacement while the P-wave (related to ϕ) appears in the component $\widehat{u}_z$ only. Therefore, for a motion that is only along the z direction, we have the P-wave propagating in the vertical z direction, and the S-wave propagating in the horizontal x and y directions. The Figure II.2 illustrates this P and S waves propagation when only a vertical motion is generated.

We note that the derived formulations for Helmholtz decomposition are valid in frequency domain as well as in time domain.

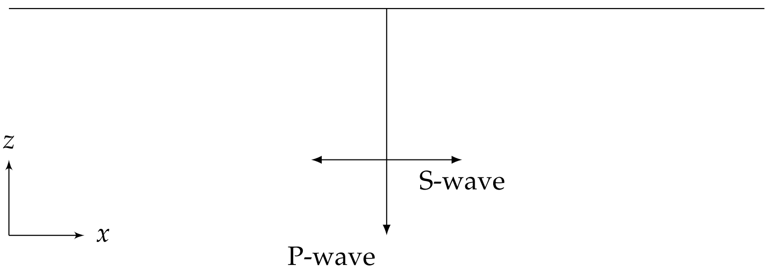

Figure II.2: 2D representation of a wave propagation when the source is only in the vertical z direction. The P wave (pressure wave) propagates in the same direction than the source direction, and the S-wave (shear wave) propagates in the orthogonal direction to the source direction.

3 General attenuation of waves

In this section, we examine the causes of amplitude decay of waves in unbounded media. We consider two main causes of amplitude decay: the beam spreading and the intrinsic attenuation. The beam spreading lies on the wave expansion, where the energy is distributed over the entire surface of the wavefront as it propagates from the source. The amplitude loss due to beam spreading depends only on the geometry of the given wave. As for intrinsic attenuation - the one we will focus on - it depends on the medium properties and/or scattering within the medium. Elastic scattering is commonly linked to poroelastic theories, where there is relative fluid-solid movements, and the energy is not preserved and is converted to heat. Here, we develop the theoretical formalism for mechanical wave attenuation in a viscoelastic medium [Biot, 1954; Golden and Graham, 1988; Carcione, 2007]. A medium is viscoelastic when it has a combined elastic - as in the Hooke's law - and viscous components. The elastic modulus behaves as carrier of wave's energy and the viscous modulus behaves as a weakener of the wave's energy.

For porous rocks, [Biot, 1956a,b] developed poroelastic theories that describe wave propagation in an elastic porous matrix filled by fluids, emphasizing that the intrinsic attenuation is due to friction at the fluid/solid interface. Although poroelastic models are more accurate in modeling wave propagation in rocks, they can be approximated by viscoelastic models [Bardet, 1992; Morochnik and Bardet, 1996], which are easier to consider numerically. This is our choice for this work.

3.1 Amplitude decay due to beam spreading

We consider the propagation of a wave in a 3-D homogeneous medium generated by a point source. The wave expands from the position of source similarly in all direction, *i.e.* as a sphere for the body waves that propagate only in the bulk (P- and S- waves).

The energy of the waves proportional to the square of the amplitude, amplitude that is actually the recorded particle's motion $\hat{\boldsymbol{u}}$. Thus, for the body waves, the amplitude of the waves decreases such that,

$$\hat{\boldsymbol{u}}(r) = \frac{\boldsymbol{u}_0}{r}, \tag{II.42}$$

with $\boldsymbol{u}_0$ being the source amplitude and r the radial distance of the sphere (or the offset from the point source).

For surface waves, the energy decreases differently depending on the direction. It decreases in the planes that are parallel to the surface (*i.e.*, propagation in circle) and decreases exponentially in the orthogonal direction to the surface (with depth). Consequently, the particle's motion amplitude decreases in plane parallel to the surface such that,

$$\hat{\boldsymbol{u}}(r) = \frac{\boldsymbol{u}_0}{\sqrt{r}}, \tag{II.43}$$

with r being the radial distance from the center of the circle [Aki and Richards, 2002].

3.2 Intrinsic attenuation due to the complex modulus

This section focuses on intrinsic attenuation due to viscosity. Depending on the chosen viscoelastic model, the stress-strain relationship differs as a function of a given frequency. That means some viscoelastic models present a higher attenuation for higher frequencies, as other viscoelastic models present a lower attenuation for higher frequencies. The difficulty of following viscoelastic laws - as in following any laws - is the lack of flexibility in the formulations, in particular to cover a large band of frequencies. The simplest models will not usually fit exactly the data, but it is crucial for us to understand where does the attenuation come from with basic formulations before developing more complex models.

The stress-strain relationship is defined as [Carcione, 2007]:

$$\boldsymbol{\sigma}(\boldsymbol{x},t) = \psi(\boldsymbol{x},t) * \frac{\partial \boldsymbol{\epsilon}(\boldsymbol{x},t)}{\partial t}, \tag{II.44}$$

with $\boldsymbol{\sigma}$ and $\boldsymbol{\epsilon}$ previously defined in equations (II.1) and (II.4). ψ is the relaxation function from which the viscoelastic properties can be derived (in the next subsections) and $*$ is a convolution product. It means that equation (II.44) is time-dependent and the stress does not induce an instantaneous strain when viscosity is added, there is a delay instead due to the convolution with the time derivative.

We can illustrate the viscoelastic behavior using usual representations such as a spring for the purely elastic behavior (or modulus), and a dashpot for the purely viscous behavior (or modulus). The purely elastic modulus instantly carries and propagates the energy as in Hooke's law without loss (II.3), that means the spring will infinitely vibrate with the same energy when a force is induced on it. The purely viscous modulus will restrain the propagation of energy, that means a force applied to the dashpot will be dissipated with a time-delay represented by the derivative. The standard viscoelastic rheological models are commonly defined by the combination of these springs and dashpots.

We can write (II.44) in frequency-domain and define the complex modulus $M(\boldsymbol{x},\omega)$ composed of a real part $M_R(\boldsymbol{x},\omega)$ and an imaginary part $M_I(\boldsymbol{x},\omega)$ defined in frequency-domain such that,

$$M(\boldsymbol{x},\omega) = M_R(\boldsymbol{x},\omega) + \mathrm{i}M_I(\boldsymbol{x},\omega), \tag{II.45}$$

that comes from [Carcione [2007], subsection (2.2)]

$$\mathcal{F}[\sigma(\boldsymbol{x},\omega)] = M(\boldsymbol{x},\omega)\mathcal{F}[\varepsilon(\boldsymbol{x},\omega)], \tag{II.46}$$

with $\mathcal{F}$ the Fourier transform, where

$$M(\boldsymbol{x},\omega) = \int_{-\infty}^{+\infty} \frac{\delta\psi(\boldsymbol{x},t)}{\delta t} e^{-\mathrm{i}\omega t} dt. \tag{II.47}$$

$M_R(\omega)$ is the storage modulus (where the energy is kept) and $M_I(\omega)$ is the loss modulus (where the energy is dissipated) [Golden and Graham, 1988]. The real and imaginary parts of the complex modulus will depend on the chosen rheologic models where some are described in the next subsections.

3.3 Quality factor and the complex modulus

The quality factor is commonly used to describe the ability of a wave to propagate throughout a given medium. It is usually frequency-dependent like in the case of viscoelastic media. For one wavelength, the higher the quality factor is, the better the wave propagates. The quality factor $Q(\boldsymbol{x}, \omega)$ can be defined by a ratio between moduli, for instance, in a one-dimensional case, we have, [Carcione, 2007]:

$$Q(\boldsymbol{x}, \omega) = \frac{\mathrm{Re}(M(\boldsymbol{x}, \omega))}{\mathrm{Im}(M(\boldsymbol{x}, \omega))} = \frac{M_R(\boldsymbol{x}, \omega)}{M_I(\boldsymbol{x}, \omega)}. \tag{II.48}$$

The quality factor is developed in the viscoelastic context in the following subsections. Note that the inverse of the quality factor is usually referred to as the dissipation factor [O'connell and Budiansky, 1978].

3.4 Purely elastic modulus

Let us illustrate the purely elastic modulus as a spring (Figure II.3).

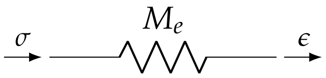

Figure II.3: Illustration of a spring representing the purely elastic behavior.

This spring represents the purely elastic modulus and is real valued, that means an harmonic stress will induce an instantaneous strain and it corresponds to the Hooke's law (Equation (II.3)):

$$\boldsymbol{\sigma} = M_R \boldsymbol{\epsilon} = M_e \boldsymbol{\epsilon} = C \boldsymbol{\epsilon}, \tag{II.49}$$

with M_e being the elastic modulus equivalent to C the stiffness tensor as defined in (II.3). Here, $M_R = M_e = C$ do not depend on frequency, and the equation is valid in time and frequency domains.

It can be deduced from this equation that the spring, being real-valued ($\mathrm{Im}(M_e) = 0$), has a quality-factor (II.48) that tends to infinity. It means that the energy is totally restored and propagates without attenuation in the purely elastic medium.

3.5 Purely viscous modulus

The purely viscous modulus is commonly represented by a dashpot (Figure II.4).

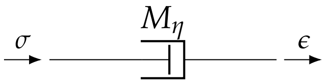

Figure II.4: Illustration of a dashpot representing the purely viscous behavior.

In that case, the time-dependent stress-strain relationship is written from (II.44) such that,

$$\boldsymbol{\sigma}(\boldsymbol{x},t) = M_\eta(\boldsymbol{x})\frac{\partial \boldsymbol{\epsilon}(\boldsymbol{x},t)}{\partial t}, \tag{II.50}$$

and is rewritten in frequency-domain:

$$\boldsymbol{\sigma}(\boldsymbol{x},\omega) = \mathrm{i}M_I(\boldsymbol{x},\omega)\boldsymbol{\epsilon}(\boldsymbol{x},\omega) = \mathrm{i}\omega M_\eta(\boldsymbol{x})\boldsymbol{\epsilon}(\boldsymbol{x},\omega). \tag{II.51}$$

We notice here the difference between the frequency-dependent imaginary part of complex modulus $M_I(\boldsymbol{x},\omega)$ and the frequency-independent viscous modulus $M_\eta(\boldsymbol{x})$ due to the formulation $i\omega M_\eta$ from the harmonic notation, that is, we separate the contribution of the frequency from the viscous parameter.

A dashpot $\mathrm{Re}(M_\eta) = 0$ induces a quality factor (II.48) that is zero in a purely viscous medium. It means that the dashpot will completely absorb the energy given by the stress $\boldsymbol{\sigma}$ and result in no strain $\boldsymbol{\epsilon}$ in return.

3.6 Kelvin-Voigt viscoelastic rheologic model

In the Kelvin-Voigt viscoelastic model, the spring and the dashpot are placed in parallel as we can see in the Figure II.5 [Carcione, 2007].

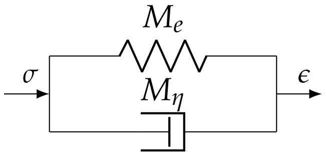

Figure II.5: Illustration of the Kelvin-Voigt viscoelastic rheologic model.

In this configuration, the medium will return to its initial state after the motion. The stress applied to the model is the sum of the stresses applied to each part of the model (*i.e.* the spring and the dashpot respectively). Thus the stress-strain relationship can be written in frequency-domain:

$$\boldsymbol{\sigma} = M_e\boldsymbol{\epsilon} + \mathrm{i}\omega M_\eta\boldsymbol{\epsilon}. \tag{II.52}$$

We can derive the quality factor for the Kelvin-Voigt viscoelastic rheologic model as below. Note that in practice, in the following chapters, we are going to work with Q_P and Q_S associated to P- and S- waves, replacing $M_e = \lambda + 2\mu$ and $M_\eta = \eta_\lambda + 2\eta_\mu$ for the P-waves, and $M_e = \mu$ and $M_\eta = \eta_\mu$ for the S-waves. Here we give the definitions of Q for each chosen viscoelastic model.

$$Q_{KV} = M_e(\omega M_\eta)^{-1}. \tag{II.53}$$

We notice that the quality factor is inversely proportional to the frequency, *i.e.* the higher the frequency is, the lower the quality factor will be for the Kelvin-Voigt viscoelastic model (Figure II.8). It means that high frequencies are more attenuating than low frequencies with the Kelvin-Voigt model of attenuation.

3.7 Maxwell viscoelastic rheologic model

For the Maxwell viscoelastic model, the spring and the dashpot are placed in series (Figure II.6) [Carcione, 2007].

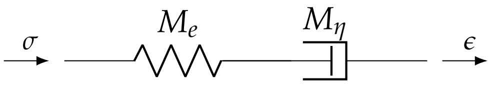

Figure II.6: Illustration of the Maxwell viscoelastic rheologic model.

In this case, the stress-strain relationship of the Maxwell model is:

$$(M_\eta^{-1} + \mathrm{i}\omega M_e^{-1})\boldsymbol{\sigma} = \mathrm{i}\omega\boldsymbol{\epsilon}. \tag{II.54}$$

We rearrange to isolate the complex modulus and we calculate the quality-factor for the Maxwell model:

$$Q_{Max} = \omega M_\eta M_e^{-1}. \tag{II.55}$$

We notice here the linear frequency-dependence of the quality factor of a Maxwell model with ω. It means that an increasing frequency leads to an increasing quality-factor (Figure II.8).

3.8 Zener viscoelastic rheologic model

The Zener viscoelastic model is represented as a combination of a Kelvin-Voigt and a Maxwell models. In this case, we place a spring in series with a Kelvin-Voigt model (Figure II.7) [Carcione, 2007].

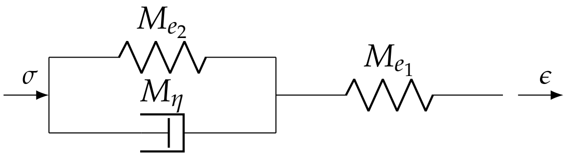

Figure II.7: Illustration of the Zener viscoelastic rheologic model.

The stress-strain relationship of the Zener model is:

$$(1 + \mathrm{i}\omega\tau_\sigma)\boldsymbol{\sigma} = M_E(1 + \mathrm{i}\omega\tau_\epsilon)\boldsymbol{\epsilon}, \tag{II.56}$$

with $(M_{e_1} + M_{e_2})M_E = M_{e_1}M_{e_2}$, $M_{e_2}\tau_\epsilon = M_\eta$ and $(M_{e_1} + M_{e_2})\tau_\sigma = M_\eta$.

We rearrange the complex modulus to be able to separate the real and imaginary parts and we give the definition of the quality factor for a Zener model :

$$\omega(\tau_\epsilon - \tau_\sigma) Q_{Zen} = 1 + \omega^2 \tau_\epsilon \tau_\sigma. \tag{II.57}$$

We illustrate the quality factors for the three models in Figure II.8, where we choose the parameters such that all models coincide at frequency 200kHz. In this figure, we see that the quality factor of the viscoelastic Maxwell and Kelvin-Voigt models respectively linearly increase and decrease over frequency, while the Zener viscoelastic model follows the behavior of the Maxwell model at high frequencies, and it follows the behavior of the Kelvin-Voigt model at low frequencies. This is due to the viscous component in the Zener model (Figure II.7) that will have low resistance in low frequencies (the piston will glide slowly in the cylinder) and behave as a Kelvin-Voigt model; as for high frequencies, the dashpot will have a high resistance and we will need more force to move all the system, as is Maxwell model. Moreover, we notice in Figure II.8 that around the frequency of 200 kHz, the Zener model can be used in the case of a locally constant quality factor [Imperiale et al., 2020] that can be extended to generalized viscoelastic models for a broader bandwidth of constant quality factor [Blanc et al., 2016].

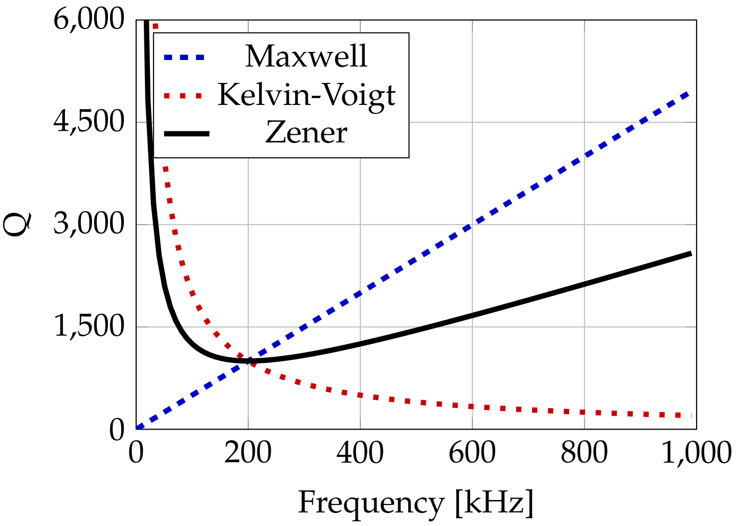

Figure II.8: S-waves quality-factor behavior as a function of frequency for [- - - -] Maxwell viscoelastic model with η_μ = 20.65 MPa s, [· · ·] Kelvin-Voigt viscoelastic model with η_μ = 20.65 Pa s and [——] Zener viscoelastic model with τ_ϵ = 796.57 ns and τ_σ = 794.98 ns, with an elastic parameter of μ = 25.95 GPa. The parameters are chosen such that all attenuation models coincide at frequency 200 kHz.

4 Recovery of viscoelastic parameters

4.1 Displacement field and complex wavenumber

In the following, we introduce the term of complex wavenumber for the time-harmonic displacement field for plane waves, so the wave amplitude decrease is only as a function of intrinsic attenuation.

The time-harmonic definition of elastic plane waves (or after correcting the beam spreading using the equations (II.42) or (II.43)) can be written from equation (II.39):

$$\hat{u}(x, \omega) = u_0 \cdot \exp(-ikx), \tag{II.58}$$

with $\hat{u}$ the displacement field in one direction, u_0 the source amplitude, x the offset, and k the complex wavenumber such that

$$k = \frac{\omega}{V_c} = k_{real} + \mathrm{i}k_{imag} = k_{real} - \mathrm{i}\alpha, \tag{II.59}$$

with $V_c = V_{real} + \mathrm{i}V_{imag}$ the complex velocity and $\alpha > 0$ the attenuation coefficient.

The equation (II.58) can thus be rewritten

$$\hat{u}(x,\omega) = u_0 \cdot \exp(-\alpha x) \cdot \exp(-\mathrm{i}k_{real}x), \tag{II.60}$$

the term $\exp[\mathrm{i}(\omega t - k_{real}x)]$ describing the harmonic oscillations and $\exp(-\alpha x)$ the amplitude decay with respect to distance of propagation as in Figure II.9. This separation will be used to find the real and imaginary parts of the complex wavenumber such that,

$$\mathrm{Im}[\ln(\hat{u})] = -k_{real}x, \tag{II.61}$$

and

$$\mathrm{Re}[\ln(\hat{u})] = -\alpha x + \ln(u_0). \tag{II.62}$$

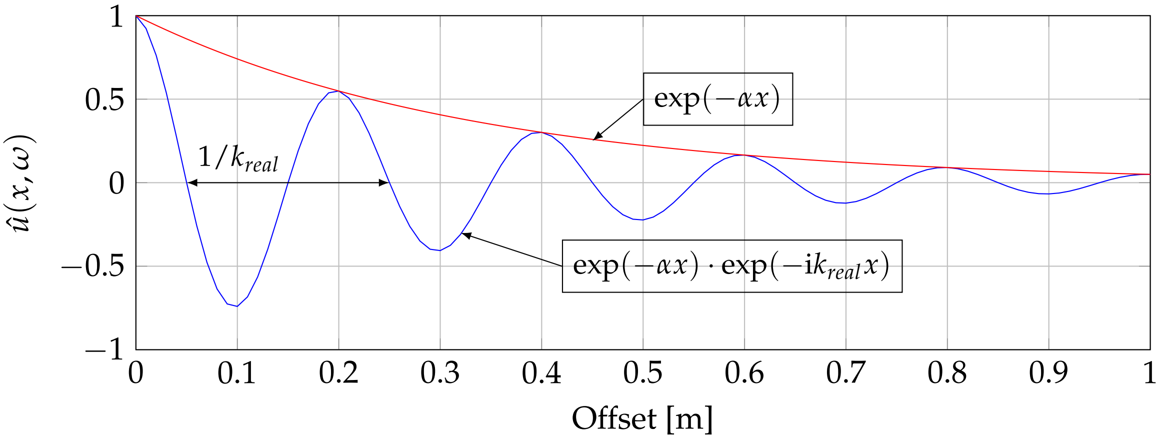

Figure II.9: Illustration of the particle's displacement induced by a wave of initial amplitude $u_0 = 1$, $\omega = 5$, $Real(V_c) = 1$ (leads $k_{real} = 5$), and $\alpha = 3\,\mathrm{Np\,m^{-1}}$.

When we work in time-domain with seismograms, we deal with wave propagation as a function of time. We can take the equation of planewave propagation from Carcione [2007] (written in equation (II.38)) and add attenuation term α from the complex wavenumber such that [Carcione, 2007],

$$u(x,t) = u_0 \cdot \exp(-\alpha x) \cdot \exp[\mathrm{i}(\omega t - k_{real}x)]. \tag{II.63}$$

We can rewrite the equation (II.63) such that the amplitude decays with respect to time by defining the variable $\beta = \alpha V_{real}$, β being the amplitude decay/attenuation in $[\mathrm{Np\,s^{-1}}]$. This is used in Chapter III Section 3 where we recover the attenuation of a wavefield with mixed body, surface and reflection waves, because the velocity term is included in β and we do not need to know it:

$$u(x,t) = u_0 \cdot \exp(-\beta t) \cdot \exp[\mathrm{i}(\omega t - k_{real} x)]. \tag{II.64}$$

Also, we note that in practice, when we measure a displacement field u, there exist the three components (u_x, u_y, u_z) that we later need to link to V_P and V_S. We will see in the next Chapter III how to handle the different components.

4.2 Viscoelastic parameters from the complex wavenumber

In this section, we present how we can recover the complex modulus of a medium with the complex wavenumber. The method is then explained in more details in Subsection 2.3.3 where we use it directly with simulated data.

Let us consider a case of 1D propagation. We start from the complex velocity with the complex modulus $M = M_R + \mathrm{i}M_I$, see (II.45).

$$V_c = \left(\frac{M}{\rho}\right)^{1/2}. \tag{II.65}$$

Using the equation (II.59) in 1D, we have $k = k_{real} + \mathrm{i}k_{imag} = \dfrac{\omega}{V_c}$ and we develop

$$\begin{aligned}
&M = \rho V_c^2 \\
\Leftrightarrow &M = \rho \frac{\omega^2}{(k_{real} + \mathrm{i}k_{imag})^2} \\
\Leftrightarrow &M = \rho\omega^2 \frac{(k_{real} - \mathrm{i}k_{imag})^2}{(k_{real} + \mathrm{i}k_{imag})^2 (k_{real} - \mathrm{i}k_{imag})^2} \\
\Leftrightarrow &M = \rho\omega^2 \frac{(k_{real} - \mathrm{i}k_{imag})^2}{(k_{real}^2 + k_{imag}^2)^2} \\
\Leftrightarrow &M = \rho\omega^2 \frac{k_{real}^2 - 2\mathrm{i}k_{real}k_{imag} - k_{imag}^2}{(k_{real}^2 + k_{imag}^2)^2}.
\end{aligned} \tag{II.66}$$

Then we separate the real and imaginary part of the equation to have

$$M_R = \rho\omega^2 \frac{k_{real}^2 - k_{imag}^2}{(k_{real}^2 + k_{imag}^2)^2} \tag{II.67a}$$

$$M_I = -2\rho\omega^2 \frac{k_{real}k_{imag}}{(k_{real}^2 + k_{imag}^2)^2}. \tag{II.67b}$$

We can notice that in the condition of purely elastic medium, there is no attenuation so $k_{imag} = 0$. The equations (II.67) are then reduced to the real part of the complex modulus only - M_I being equal to zero - and we write

$$M_R = \rho \frac{\omega^2}{k_{real}^2}. \tag{II.68}$$

The strength of the decomposition in terms of complex modulus is that it is independent of attenuation models. We recover a frequency dependent function, and then we can identify any attenuation models. In this thesis, we focus on three viscoelastic rheologic models, but one can extend the method to its chosen attenuation model. All along the manuscript, we link the equation (II.67) with equations (II.52), (II.54), and (II.56) to link the complex modulus with respectively the Kelvin-Voigt, Maxwell and Zener viscoelastic modulus.

4.3 Quality factor and the complex wavenumber

Since we introduced the quality factor as a function of complex modulus in Equation (II.48), and complex modulus as a function of complex wavenumber in equations (II.67), we can derive the quality factor as a function of the complex wavenumber taking a few precautions beforehand.

Linking (II.48) to (II.67), we write:

$$Q = \frac{M_R}{M_I} = \frac{k_{real}^2 - k_{imag}^2}{-2k_{real}k_{imag}}, \tag{II.69}$$

with $k_{imag} = -\alpha$. We rearrange to write

$$Q = \frac{k_{real}}{2\alpha} - \frac{\alpha}{2k_{real}}. \tag{II.70}$$

In the context of weak attenuation, it is assumed that $k_{real} \gg \alpha$ such that we can neglect the term $\alpha/2k_{real}$. Taking

$$k_{real} = \frac{\omega}{V_{real}}, \tag{II.71}$$

we can rewrite the Q-factor definition equivalent to (II.48) such that [O'connell and Budiansky, 1978],

$$Q \approx \frac{\omega}{2\alpha V_{real}} \approx \frac{\omega}{2\beta}. \tag{II.72}$$

This formulation of quality factor will be of particular use when we analyze the wavefield in experimental conditions to identify the attenuation laws from the frequency-dependent attenuation recovered data. This is because we have a direct relation between the quality factor Q, the frequency ω, and the attenuation β.

We want to emphasize that the attenuation α (or β) is the decrease in amplitude over a certain distance (or time), and the quality factor Q is the decrease in amplitude over one wave cycle. We give an illustration in Figure II.10 where we vary only β or Q, and the frequency. We see in Figure II.10 a and c that for the same attenuation β, when the frequency is doubled, the quality factor is doubled as well. Similarly, when we compare Figure II.10 b and d, we need to double the attenuation β to keep the Q constant when we double the frequency. We need to keep these effects in mind when we deal with attenuation parameters as a constant quality factor does not mean a constant attenuation.

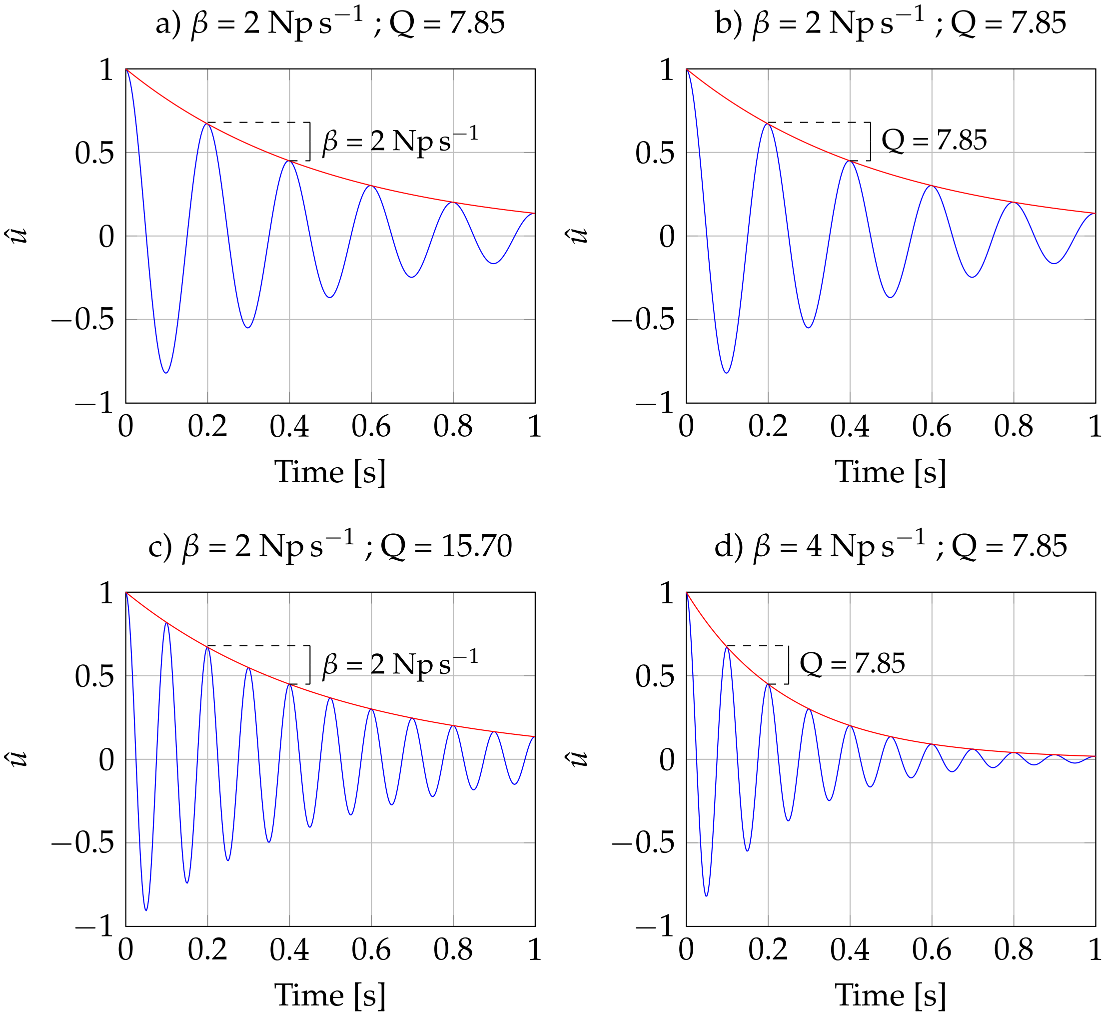

Figure II.10: Illustration of an attenuating plane wave: [——] particle's displacement u, [——] envelope. a) $\alpha = 2\,\mathrm{Np\,s^{-1}}$, f = 5 Hz. b) $\alpha = 2\,\mathrm{Np\,s^{-1}}$, f = 5 Hz. c) $\alpha = 2\,\mathrm{Np\,s^{-1}}$, f = 10 Hz. d) $\alpha = 2\,\mathrm{Np\,s^{-1}}$, f = 10 Hz. The wave's velocity is 1 m/s and the location x=0.

Chapter III

Numerical simulations

We carry out a numerical investigation to understand wave propagation in viscoelastic media. Then we derive a method to reconstruct the attenuation models and viscous parameters from wave measurements. To do so, we need to recover the purely elastic modulus, that is common in homogeneous media [Aki and Richards, 2002], and also the frequency-dependent attenuation of the media.

The objective is to find a method that recovers the viscoelastic parameters of a medium at experimental conditions (source and receivers on the surface of the sample, free-surface boundary conditions allowing wave reflections and conversion, body and surface waves can possibly be mixed altogether). The strength of numerical simulations is that since we impose the viscoelastic law and parameters, we can verify our results and evaluate the robustness of our approach in various configurations, including with noise. It will give us tools to recover the attenuation laws and viscoelastic parameters of actual samples in the next Chapter IV. The numerical simulations are performed in frequency-domain with *Hawen* open-source software [Faucher, 2021].

1 Numerical simulations in a homogeneous cube - an overview

We consider a 3-D homogeneous cube of size 7 cm x 7 cm x 7 cm with Lamé parameters $\lambda = 55.95$ GPa and $\mu = 25.95$ GPa, and a density of 2700 $\mathrm{kg\,m^{-3}}$. Considering an elastic medium and using the equations (II.22) and (II.23), we have here a P-wave velocity of 6320 $\mathrm{m\,s^{-1}}$ and a S-wave velocity of 3100 $\mathrm{m\,s^{-1}}$. These values roughly correspond to the physical parameters of aluminum.

In experimental context, the boundaries of the medium follow free-surface boundary conditions, that is, it imposes the traction (normal stress) to be zero $\boldsymbol{\sigma} \cdot n = 0$ on the boundary [Faucher, 2017], with n the normal direction. As an alternative to work in a simplified medium and get rid of reflections within the sample and work on the direct wave only, we can impose absorbing boundary conditions given in Givoli and Keller [1990]; Faucher [2017]. In this case, the waves are assumed to freely escape the medium, i.e., no waves are expected to be reflected from the boundary (although it is numerically imperfect).

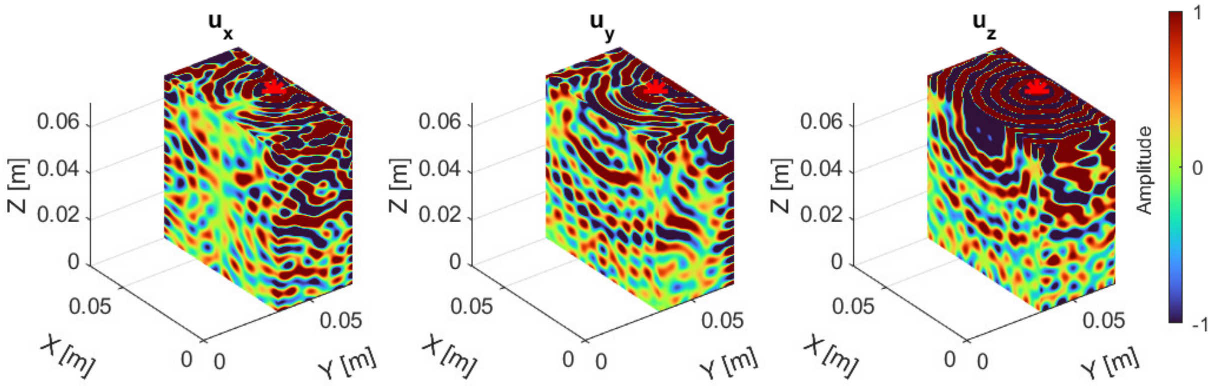

Figure III.1: Visualization of the real part of a seismic numerical viscoelastic wavefield for a Kelvin-Voigt rheologic model ($\lambda = 55.95$ GPa and $\mu = 25.95$ GPa; η_λ = 250 Pa s and η_μ = 500 Pa s) generated in a cube at 400 kHz on a cross-section, lateral and upper boundaries, with free-surface boundary condition on boundaries. Amplitude of the displacement for x, y and z components. Red asterisk: source location.

We see in Figure III.1 the wavefield in viscoelastic context for a Kelvin-Voigt rheologic model (η_λ = 250 Pa s and η_μ = 500 Pa s) in frequency domain and shows the x, y and z components of the particle displacement $\boldsymbol{u}$, respectively denoted u_x, u_y and u_z for the 400 kHz frequency, with the source located at the upper surface of the cube, and with free-surface boundary conditions. In these wavefields, there is a mix of body and surface waves as well as the results of the reflected or converted waves. For instance, there is reflected P-waves (PP-wave in that case), reflected S-waves (SS-wave) and converted waves (the PS-wave is an initially P-wave that has been converted as a S-wave at a boundary), and so on.

1.1 From frequency to time domain

The numerical simulations are in frequency domain to conveniently handle viscoelasticity. In order to generate seismograms allowing us to analyze the wavefield in time domain, we have to calculate the correct amount of frequencies.

A general rule for a time discretization is that the frequency sampling f_s (or the inverse of the step in time dt) has to be higher than two-times the Nyquist frequency f_n (equation (III.1)) because of the symmetry of the frequency spectrum. The Nyquist frequency is the maximum frequency value or the minimum time step a signal has to reach in order to be correctly sampled. Thus, this Nyquist frequency allows us to know the maximum frequency we have to reach for the numerical simulations

$$f_s = \frac{1}{dt} > 2 f_n, \tag{III.1}$$

with f_s the frequency sampling, dt the step in time and f_n the Nyquist frequency.

An other value of importance is the frequency step df, directly deduced by the duration of the signal L given by,

$$df = \frac{1}{L} = \frac{1}{N \cdot dt}, \tag{III.2}$$

with df the step in frequency, N the number of samples in time and L the total duration in time of the signal.

After performing simulations with the appropriate values in frequency, we can move from frequency to time domain with an Inverse Fourier Transform (equation (II.25)). The frequency-domain source considered in the simulations is a "point-source" in space - *i.e.* a Dirac - with constant amplitude on all the frequencies generated on the point-source. Because we cannot simulate an infinite number of frequency solutions, we can only approximate a Dirac signal in time domain performing an inverse Fourier transform. This is why we choose to work on a Ricker wavelet, defined in time domain as [Ryan, 1994]:

$$Ricker(t) = a\left(1 - 2\pi^2 f_P^2 (t_0 + t - t_P)^2\right) e^{-\pi^2 f_P^2 (t_0 + t - t_P)^2}, \tag{III.3}$$

with a the amplitude, f_P the frequency peak of the Ricker, t_0 the starting time of the function and t_P the time peak of the Ricker.

Before performing the inverse Fourier transform on the constant-source simulated frequency solution, the real and imaginary parts calculated by the numerical simulation

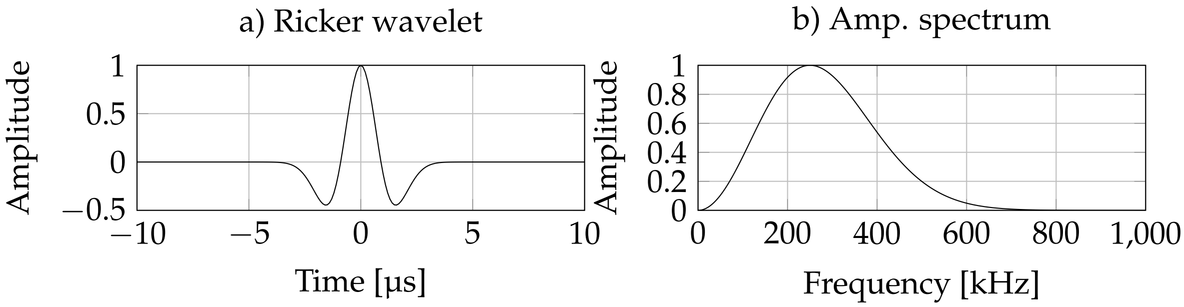

Figure III.2: Representation of a 250 kHz peak frequency Ricker function. Normalized amplitudes.

will be multiplied by the amplitude spectrum of the Ricker wavelet (Figure III.2b). An example can be seen in Figure III.4.

We also note from the Figure III.2 that to recover as precisely as possible a 250 kHz Ricker wavelet, we need to perform simulations in frequency domain until $f_{max} = 700$ kHz at least, where the normalized amplitude actually goes below 0.009. If we do not cover the whole amplitude spectrum of the wavelet of interest, it will result in a lack of information and an ill-shaped wavelet in time domain. An example of a seismogram before and after scaling the frequency solution by a 250 kHz Ricker wavelet's amplitude spectrum can be seen in Figure III.6.

1.2 Steps from performing numerical simulation to generate a seismogram

Let us give an example of the design of a numerical simulation, and the post-processing steps for the creation of a time-domain seismogram from the frequency simulations. The steps are concatenated in a block-diagram in Figure III.3. To design correctly the simulations in frequency domain in *Hawen* software with the aim of generating a seismogram in time domain, it is crucial to know the time where the signal will be entirely dissipated, and the physical (elastic and attenuation) parameters allowing the signal to be completely attenuated at the end of the seismogram. If there is still remaining signal after 0.5 ms and we choose a frequency step of 2 kHz, the signal will be inadequately sampled in frequency and artifacts from simulations will appear in time. When we know the duration of the signal, we can specify the frequency step of the numerical simulation df (equation (III.2)). The number of frequency simulations will be known from the frequency range of the chosen Ricker wavelet (see for example Figure III.2).

The next step after the numerical simulation is to weight our simulation results by the amplitude spectrum of the Ricker of interest (Figure III.4), and to define the sampling frequency f_s of our seismogram that will determine the total length of the data in frequency. Indeed, we need to slightly adapt the frequency-domain data. To do so, we will need to know the frequency range given by the resolution in time (f_s) - with respect to the Nyquist condition - by adding zeros , but also to add the second half of the Fourier transform which is the reverse complex conjugate of the calculated solution (Figure III.5). This is to enforce causality as if we do not add the symmetric conjugate half in the frequency spectrum, the inverse Fourier transformation gives a complex result in time domain where we expect a real-valued result.

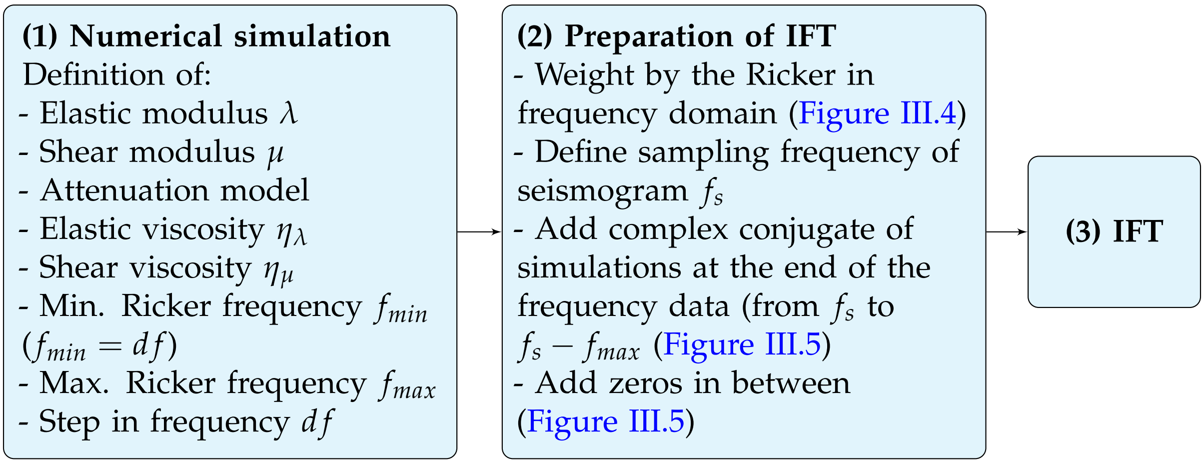

Figure III.3: Block-diagram describing the steps needed to generate a seismogram from the frequency domain numerical simulations.

In the following examples, the viscous parameters has been chosen (η_μ = 1000 Pa·s and η_λ = 500 Pa·s with a Kelvin-Voigt viscoelastic model) to get a total extinction of the wave at 0.5 ms. For this signal of a total length of 0.5 ms with a 250 kHz Ricker wavelet, we perform simulations from 1/0.5ms or f_{min} = 2 kHz to f_{max} = 750 kHz with a step of f_s = 2 kHz.

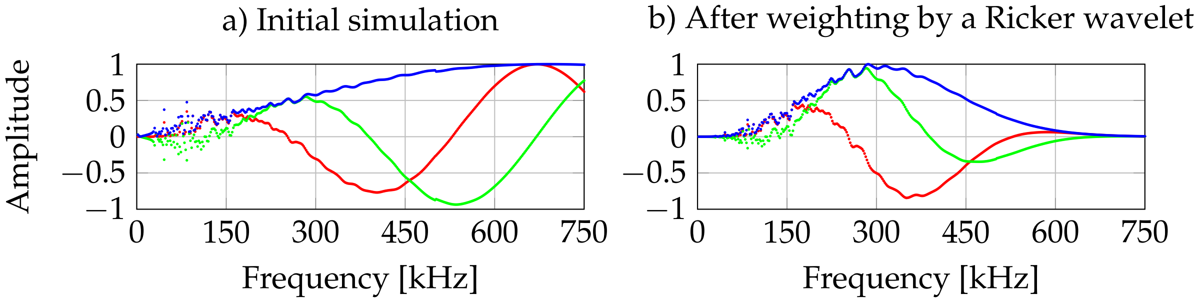

Figure III.4: Example of numerical simulation in frequency domain at 5 mm offset from the source. [—] Real part. [—] Imaginary part. [—] Amplitude spectrum. a) Before weighting by a 250 kHz Ricker. b) After weighting by a 250 kHz Ricker.

The Figure III.4 is an example for illustration of a numerical simulation's solution at 5 millimeters offset from the source for a 2 kHz-step frequency until 750 kHz before and after weighting by a 250 kHz Ricker. To perform the weighting, we multiply each terms of the amplitude spectrum of the Fourier transform of the chosen Ricker function with each terms of the numerical simulations (Figure III.4a times Figure III.2b) and we normalize the amplitudes.

On the Figure III.6 showing the seismograms corresponding to the Figure III.5 numerical simulations, we choose a frequency sampling fs = 20 MHz (following the equation (III.1)) to display the wavelets. It can be seen from the first arrivals that before weighting by a 250 kHz Ricker the wavelets seem to be unstable (see the tremor after the first wave arrival). This is due to the brutal zero-padding (adding zeros) in the frequency solution (Figure III.5a) from 750 kHz and 19.25 MHz, which is equivalent to doing an IFT of a square signal [Donnelle and Rust, 2005]. After Ricker weighting, the zero-padding is smoother so the solution in time is better constrained.

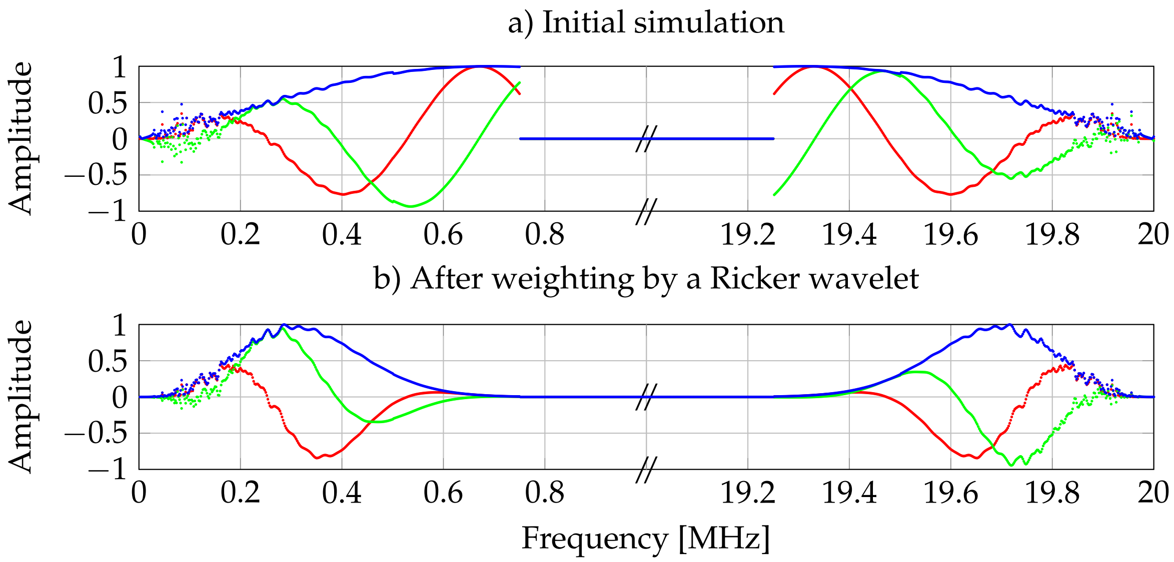

Figure III.5: Example of numerical simulation in frequency domain at 5 mm offset from the source after implementing zero-padding and adding the second half of the calculated frequency solution from Figure III.4. [——] Real part. [——] Imaginary part. [——] Amplitude spectrum. a) Before weighting by a 250 kHz Ricker. b) After weighting by a 250 kHz Ricker. The amplitudes are normalized.

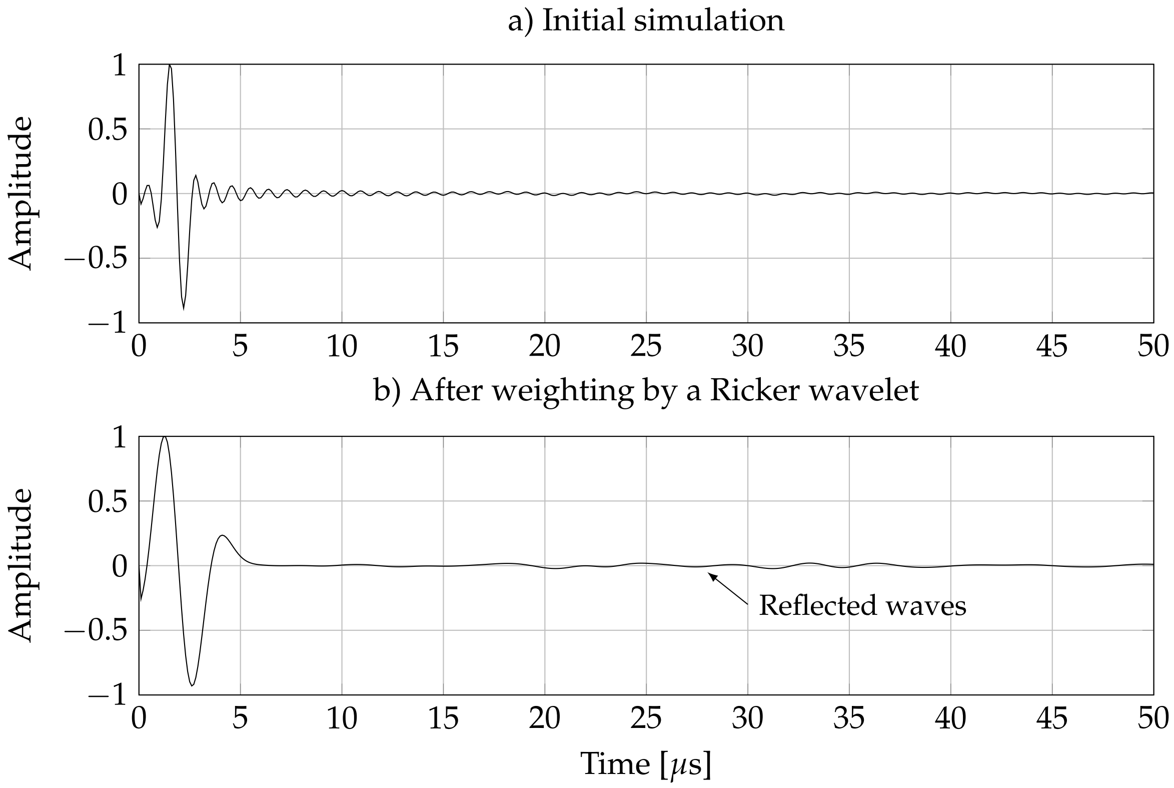

Figure III.6: Example of seismogram in time domain at 5 mm offset from the source (zoom between 0 and 50 μs). a) before weighting by a 250 kHz Ricker. b) after weighting by a 250 kHz Ricker in frequency domain. The amplitudes are normalized.

1.3 Computational cost

When we want to design a numerical simulation, we have to discretize the domain with a mesh (in our 3D case the elements composing the mesh are tetrahedrons) and we need to discretize the wave equation. The software we employ, *Hawen* [Faucher, 2021], uses the Hybridized Discontinuous Galerkin (HDG) method for space discretization. The reader can refer for instance to Bonnasse-Gahot et al. [2018] and references therein for a deeper insight of HDG methods.

It is important to have in mind the different wavelengths when we design the mesh: the bigger the wavelength is, the bigger the cell can be. In addition to adapting the mesh, we can choose which order of polynomials is used for the approximation. For instance, for a given cell size, the longer the wavelength is, the lower the order of polynomial can be. In short, we need to know the minimum number degrees of freedom per wavelength to have a sufficiently accurate solution. For example, in our 7 cm x 7 cm x 7 cm cube, for a wavelength of 1 cm (310 kHz for S-wave of velocity of 3100 m/s), we can use a mesh of about 60000 tetrahedrons with order 3 polynomials (11 degrees of freedom per wavelength) or a mesh of about 40000 tetrahedrons with polynomials of order 4 (12 degrees of freedom per wavelength) to get sufficiently accurate approximated solutions. Selecting more cells or a higher order will impact computational cost and/or time.

When we perform elastic numerical simulations in 3D (especially for high frequency with small wavelength), we need to work with High-Performance Computers (HPC) because of the computational cost. In this thesis, we use the clusters *Plafrim* (University of Bordeaux - Inria) and *Pangea 2* (TotalEnergies) to perform the simulations. In Figure III.7 we give the needed memory for the factorization of the discretized linear system with respect to the number of cells in the domain and the order of each cells, as well as the number of cells we used for our frequencies. Note that in our simulations, we use a mesh of 20000 elements with order 4 polynomials until 200 kHz (50 seconds of calculation for one frequency on *Pangea 2* with 15 nodes), and a mesh of 300000 elements with order 4 polynomials for frequencies between 600 kHz and 800 kHz (30 minutes of calculation for one frequency on *Pangea 2* with 120 nodes). Note that here we use the direct solver MUMPS to solve the linear system (e.g., Amestoy et al. [2019]) which leads to relatively high memory consumption but allows us to solve for many sources at low-cost, which is important for inversion. As an alternative to reduce memory, one could use an iterative solver instead.

Typically, when we wish to design a time-domain seismogram of a duration of 50 ms with a Ricker-wavelet source of 100 kHz of peak frequency, we need to perform frequency-domain simulation each 20 Hz until 300 kHz. That means a calculation of 15000 frequencies. On *Plafrim*, it would take 17-18 days to run this simulation sequentially from 20 Hz to 300 kHz with a maximum of 4 nodes of 182 GiB memory per node (25-40 days on *Pangea 2* with a maximum of 6 nodes of 122 GiB memory per node). In order to save time, we parallelize the simulation and send batches of calculations of low frequencies in parallel to batches of calculations of high frequencies.

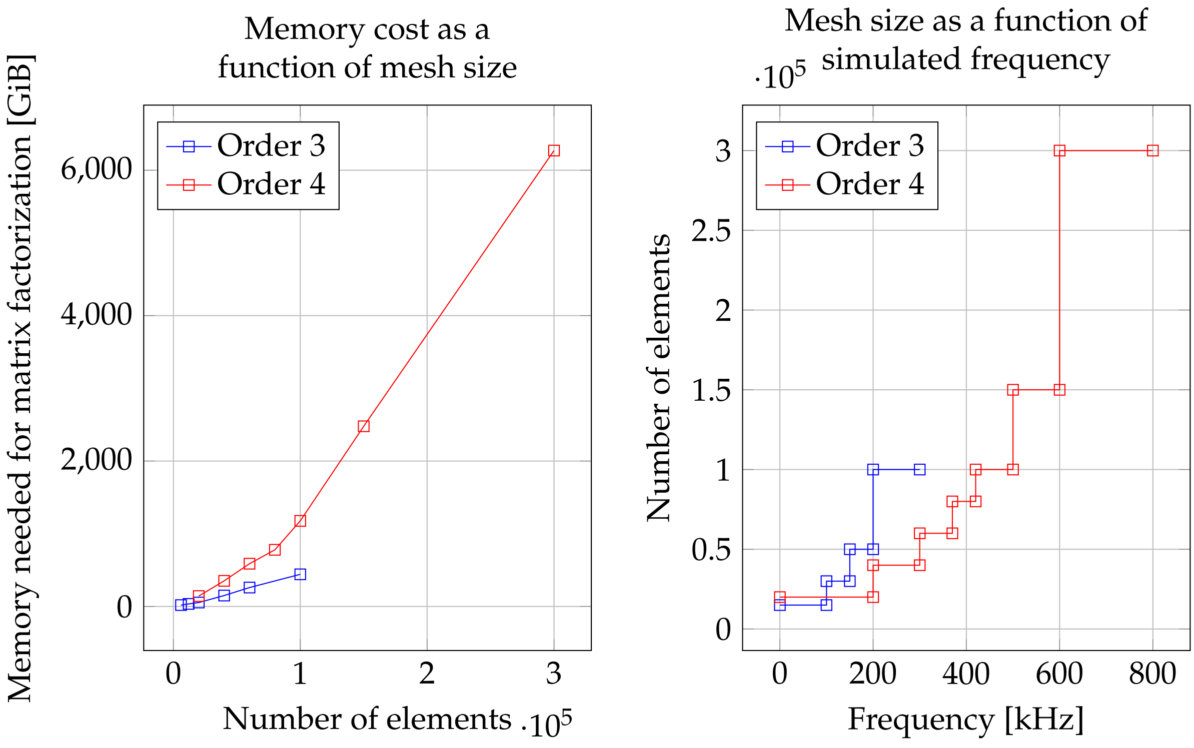

Figure III.7: [left] Computational cost with respect to the number of elements in the mesh for HDG simulation, with cells of order 3 or 4. [right] Used number of elements of order 3 or 4 for a simulation in a 7 cm x 7 cm x 7 cm cube with respect to simulated frequency. The wavelength of the S-waves is 1 cm at 310 kHz.

2 Wavefield analysis inside the sample

In this section, we investigate the wavefield in time and in frequency domains by varying the attenuation values and boundary conditions. By doing so, we aim to understand the wavefield's behavior and to validate our work with simple configurations before entering into more complex conditions such as experimental condition.

2.1 Elastic wave propagation in time-domain - on the effect of absorbing boundary conditions and P- and S- waves separation

The following study in time domain aims to illustrate the waves behavior when we separate the wavefield in P- and S- waves using curl and divergent operators (Subsection 2.3). The source is located in the center of the cube, with a vertical z component only (source function $f = (0, 0, \delta)$ with δ a Dirac in space during the simulation, scaled by a Ricker amplitude spectrum after post-processing). The simulation is performed with absorbing boundary conditions (Robin type) and without viscoelastic attenuation in order to examine the accuracy of the boundary conditions and their effects on the wavefield.

2.1.1 Time domain results

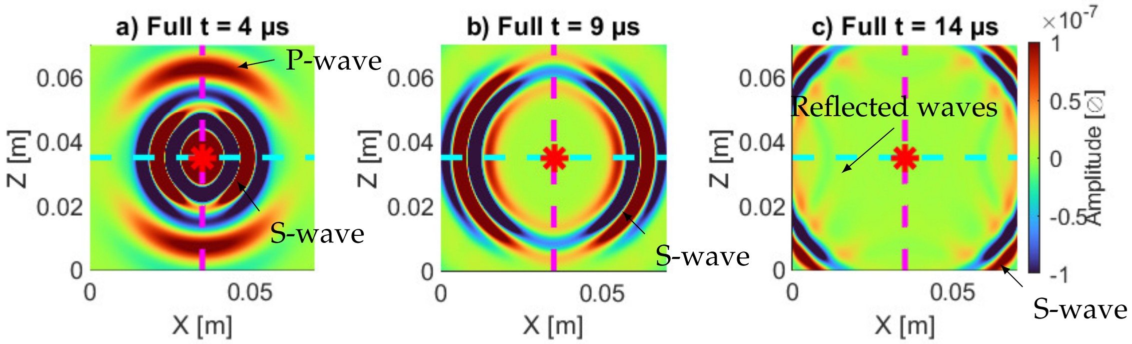

Figure III.8: Cross-section of the 250 kHz Ricker-wavelet propagation (z component) in the center of the cube in time domain (full wavefield with P- and S- waves). The red asterisk represents the source position, the cyan dashed line [- - -] represents the horizontal line virtual receivers' position, the magenta dashed line [- - -] represents the vertical line virtual receivers' position for the seismogram Figure III.10. a) After 4 µs of propagation. b) After 9 µs of propagation. c) After 14 µs of propagation.

This Figure III.8 illustrates the wave propagation of the wavefield in the u_z component in time domain at different times. At a time t = 4 µs, we can differentiate the P-wave propagating in the vertical direction and the S-wave propagating mainly in the horizontal direction. This seems consistent because the source component is in the vertical direction, so the compressive P-wave follows the vertical direction, and the shear S-wave follows the horizontal direction (see Figure II.2). Only the S-wave is visible at a time t = 9 µs. At a time t = 14 µs, we notice the presence of the S-waves in the corners of the cross-section. We notice as well a few reflections of low amplitude, more detailed in Figure III.10. Figure III.8 allows to comment about the absorbing boundary conditions. The P-wave seems totally absorbed by the boundary conditions as the S-wave still has some low-amplitude reflections (see Figure III.8c).

The fact that we still observe reflections at the boundaries with absorbing boundary conditions is explained by Clayton and Engquist [1977]. Indeed, the different P- and S-waves are going to be reduced but not completely canceled depending on their incident angle. Also, they show that the S-wave is more likely to reflect than the P-wave, and with a strong reflection coefficient. After Clayton and Engquist [1977], this phenomenon is increased when the ratio $V_P/V_S > \sqrt{3}$, that is our case. Concerning the P-wave, it is shown by Clayton and Engquist [1977] that it is completely absorbed for incident P-waves of less than 45° of incident angles on the boundary, that is also our case in our chosen configurations with the source located at the center of the cube.

2.1.2 P- and S- waves separation

We separate the wavefield in time using the curl and divergent operations according to the Helmholtz decomposition in Subsection 2.3. We can see from the Figure III.9 that there is only the S-wave in the curl part of the wavefield. However, we notice the presence of S-wave in the divergence, that is not expected in the Helmholtz decomposition, if we have unbounded propagation (i.e., propagation without reflections). It is of very weak amplitude, but still present and can cause interpretation biases when we work in frequency domain. This unexpected S-wave can be due to either the disturbed source that can induce small "reflections" in the mesh cells (that may be reduced by refining the mesh), or also to the boundary conditions. Indeed, we see in Figure III.10 that there is S-wave reflection despite absorbing boundary conditions. This disturbance might be expanded into the frequency-domain (that we simulate) and eventually come to the first S-wave arrival when performing an inverse Fourier transform.

Figure III.9b and d show the S-wave propagation at 4 µs and 9 µs. When this S-wave reaches the boundary of the cube at 14 µs (Figure III.9f), this S-wave is reflected in another S-wave (SS-wave). The divergence of the wavefield displays the presence of the S-wave in the Figure III.9c at 9 µs. Also, we can see that there is no reflections from P- to P-wave. However, at 14 µs we can point out the presence of a converted P-wave from the S-wave (SP-wave) that propagates in the direction normal to the former S-wave, due to the direction of the particle motion (z-direction according to the source).

We also notice in Figure III.9 a numerical artifact at the source location. This is due to the Dirac point-source that can only be reduced by refining the mesh at this location.

2.1.3 Seismogram representations

The seismogram in Figure III.10 highlights on some wave arrivals shows different details about the boundary conditions and wave separations. Only the top-half of the wave arrivals have been highlighted on this figure in order to let the reader have a sense of the amplitude of different waves in this simulation. Figure III.10a and b show the full wavefield propagation as a function of time and offset. They correspond to the cross-section of Figure III.8 along the vertical magenta receivers' line and the horizontal cyan receivers' line respectively. The seismogram on the vertical line (Figure III.10a) displays the presence of the first P-wave and S-wave as well as the reflected SS-waves, and the converted SP-wave, despite the boundary conditions [Clayton and Engquist, 1977]. There is no visible evidence of any P-wave reflection or PS-wave conversion on this seismogram. This observation is confirmed by the divergence of the wavefield

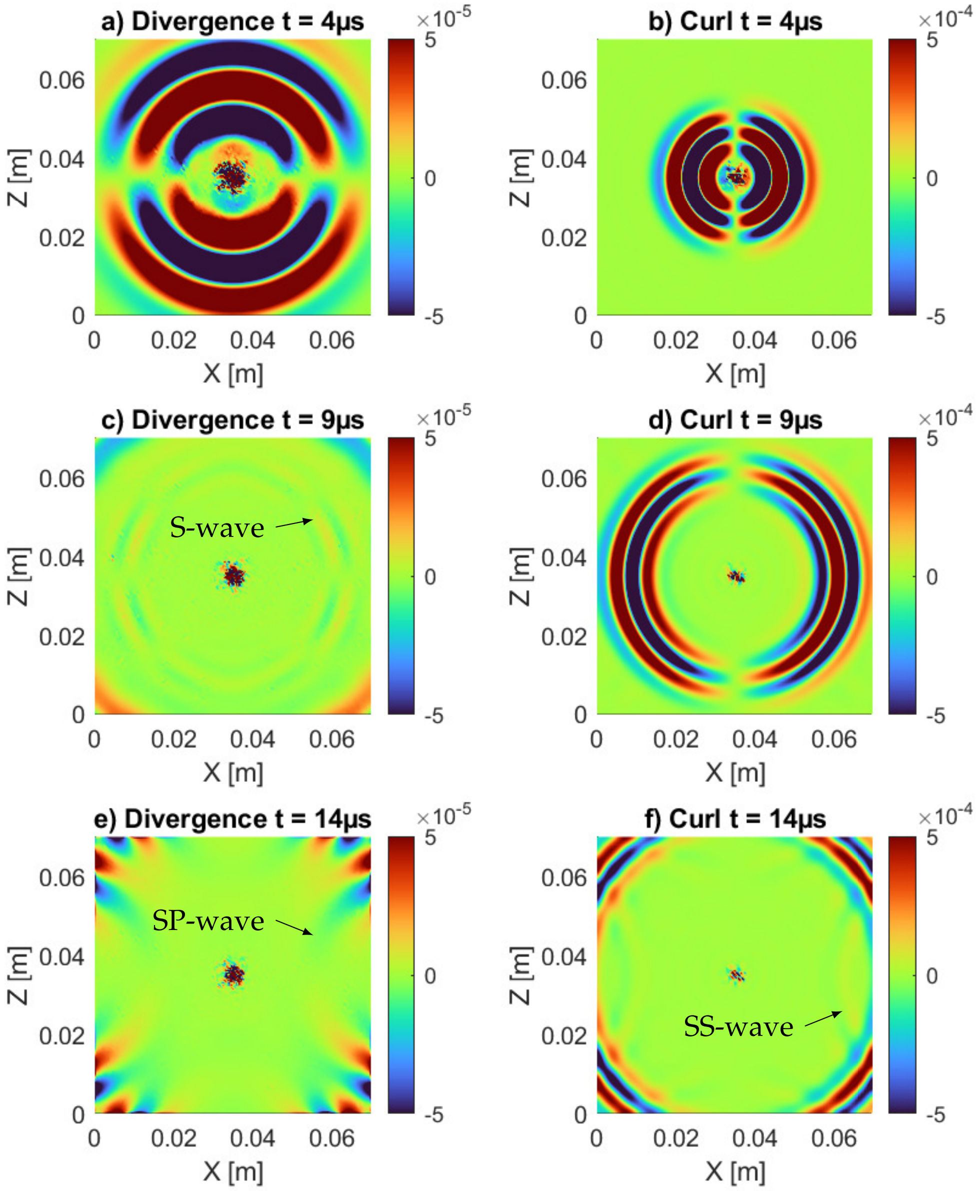

Figure III.9: Cross-section of the 250 kHz Ricker-wave propagation in the center of the cube in time domain after divergence and curl separation. a) Divergence after 4 µs of propagation (P-wave). b) Curl (y component) after 4 µs of propagation (S-wave). c) Divergence after 9 µs of propagation. d) Curl (y component) after 9 µs of propagation. e) Divergence after 14 µs of propagation. f) Curl (y component) after 14 µs of propagation.

(Figure III.10c). The first P-wave arrival to the boundaries is absorbed by the boundary conditions.

The seismogram of Figure III.10b and d displays the S-wave propagation and reflections of small amplitude on the boundaries despite the absorbing boundary conditions. We notice that there is no P-wave on the horizontal receivers' line on the full wavefield (Figure III.10b).

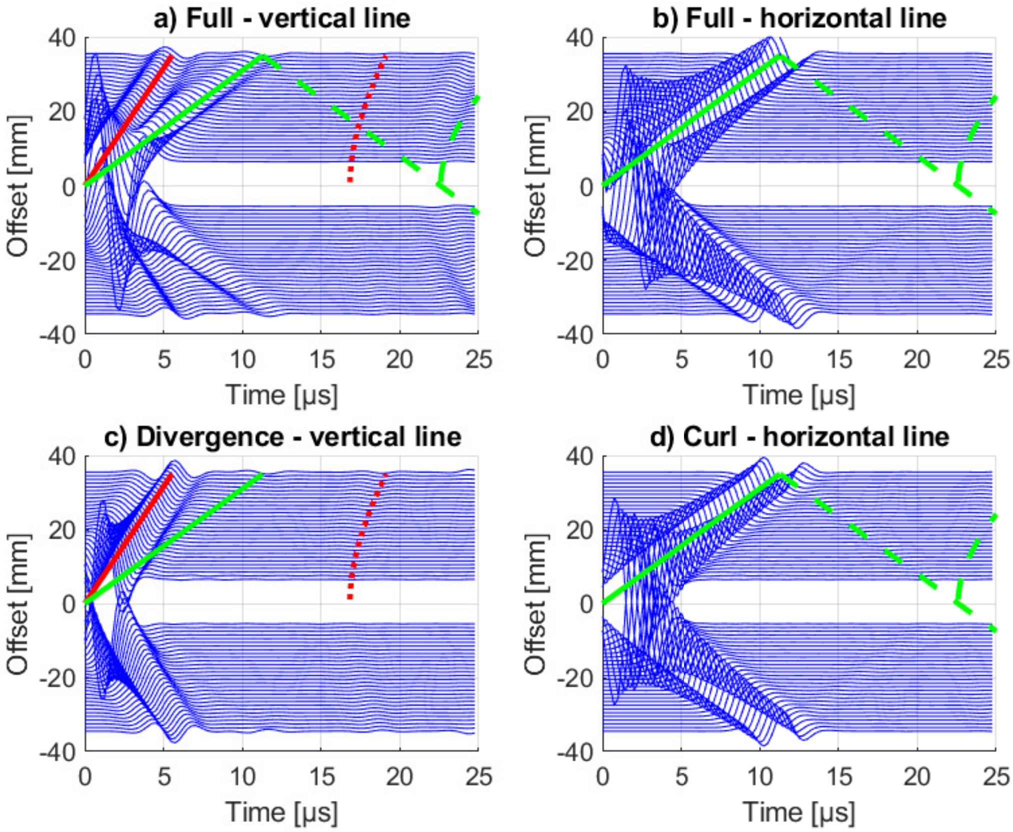

Figure III.10: Seismograms along the virtual receivers' lines of Figure III.8 with highlights of various first-wave arrivals. [—— P-wave. [——] S-wave. [- - -] SS-wave. [·······] SP-wave. a) Full wavefield along the vertical virtual receivers' line. b) Full wavefield along the horizontal virtual receivers' line. c) Divergence of the wavefield along the vertical virtual receivers' line (Figure III.9 left). d) Curl (y component) of the wavefield along the horizontal virtual receivers' line (Figure III.9 right).

The seismogram of Figure III.10c shows that even though the divergence operator is applied to the wavefield, there is the presence of S-wave discussed before as an artifact due to the absorbing boundary conditions, and supported by the fact that there is no P-wave reflection and no P-wave in the curl. Another highlighted wave is the converted SP-wave, well visible on this seismogram. It is not a surprise to detect this wave in the divergence because it is a former S-wave that have been converted into a P-wave.

All of this demonstrates that there is still remaining reflections and conversions on the boundaries of the cube in the simulations after applying the numerical absorbing boundary conditions [Clayton and Engquist, 1977]. A way to try to enhance the absorbing boundary conditions would have been the use of perfectly matched layers (PML) that consists on adding an absorbing layer of a certain thickness all around the boundaries. In that case the wave is allowed to propagate and is attenuated inside the new layer before it reaches a boundary. These PML were not used in this thesis but information can be found in Berenger [1994]; Turkel and Yefet [1998]; Wang et al. [2011].

We will have to keep in mind the presence of remaining reflections and conversions and also the presence of S-wave in the divergence of the wavefield when we are going to process quantitatively the computational data-sets in frequency domain. These tests are important to validate the simulation software and the boundary conditions. This is why we use the results from the software and not the analytical solutions. However, the final goal is to work with experimental conditions, that are free-surface boundary conditions and study the whole wavefield.

2.2 Wavefield analysis in frequency-domain - without attenuation

2.2.1 Wavefield data-set

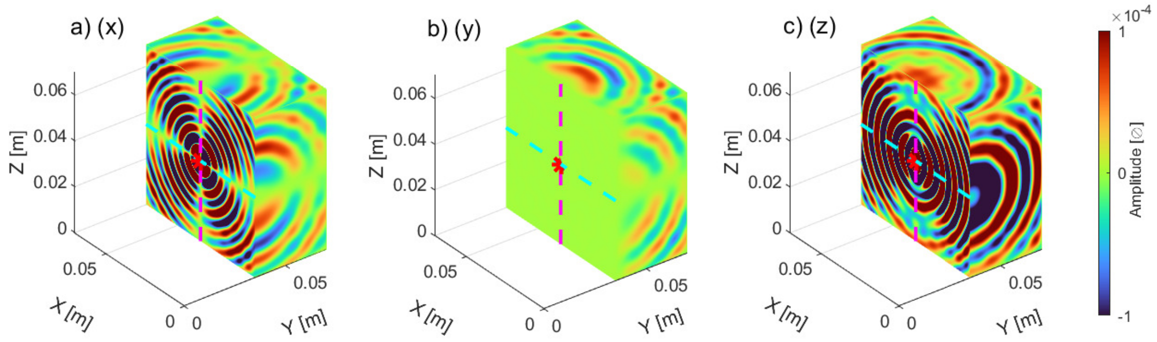

Figure III.11: Cross-section in the center of the cube (y = 35 mm) of the real part of the 400 kHz solution for the homogeneous 7x7x7 cm cube with the source in the middle of the cube without attenuation, absorbing boundary condition on the 6 faces. The red asterisk represents the source position, the cyan line [- - -] represents the horizontal line virtual receivers' position, the magenta line [- - -] represents the vertical line virtual receivers' position, with one receiver every 0.5 mm. a) x component. b) y component. c) z component.

The following simulation reflects a purely elastic wave propagation, without intrinsic attenuation. The elastic parameters are the same as before, *i.e.* λ = 55.95 GPa and μ = 25.95 GPa. The only amplitude decrease as a function of the offset is due to the beam spreading. Figure III.11 represents the real part of the 400 kHz solution for the 3D simulation with absorbing boundary condition on the six faces. As before, the source is located in the center of the cube, and has a vertical component. The presence of remaining reflections can be seen on the edges of the cube, which comes from the imperfect absorbing conditions discussed above [Clayton and Engquist, 1977].

Figure III.11c focuses on vertical component z of the particles, that is, displacement field u_z. We notice that the wave expanding on the vertical direction has a greater wavelength than the one expanding on the horizontal line. As seen previously, it can be interpreted with the help of the source's vertical direction that generates compressive P-waves in vertical direction and shear S-waves in horizontal direction.
Concerning the Figure III.11a, the horizontal x-direction particle's movement expresses itself mostly on the diagonals. It is because there is a mix of P and S waves in the diagonals for the horizontal movement's direction.
There is no wave's amplitude on the y-direction particle's movement (Figure III.11b) for geometrical reasons, because the view is a cross-section of the center of the cube. Indeed, the particles follow the $+y$ and $-y$ direction simultaneously, resulting in total destructive interference at this plane.

As we work in frequency domain, the results in Figure III.11 and Figure III.12 are a mix of direct, converted and reflected waves. The body waves have a spherical propagation in the medium, and have an amplitude decrease as a function of distance to the source (*i.e.* the offset) as the beam expands. Attenuation analysis can thus be made

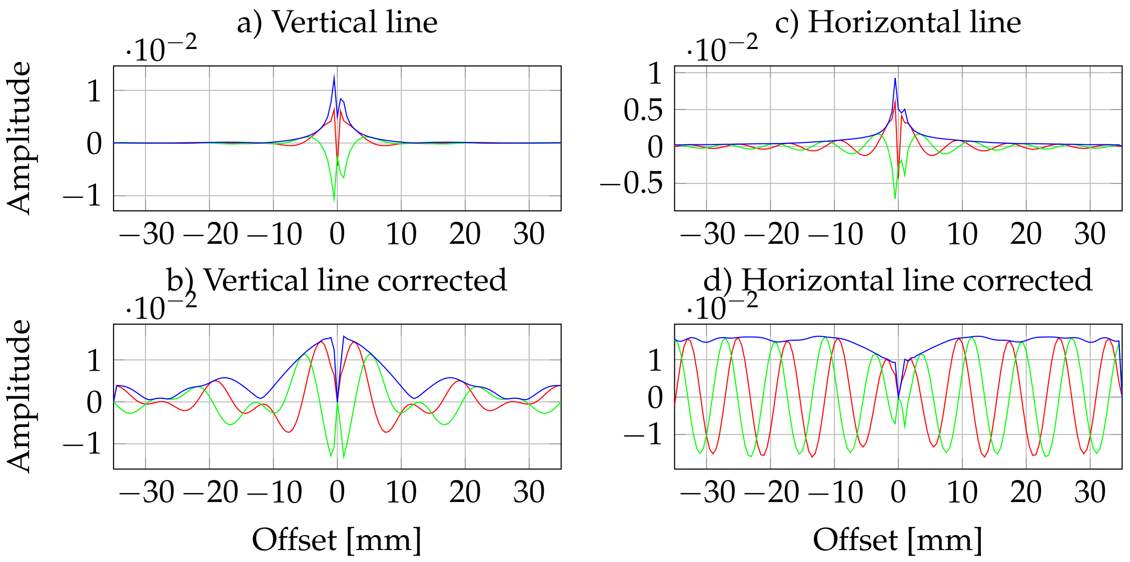

Figure III.12: 400 kHz frequency solution from the z-component receivers of the cross section (Figure III.11c) as a function of offset. [——] Real part. [——] Imaginary part. [——] Amplitude spectrum. a) Magenta vertical receiver's line without beam spreading correction. b) Magenta receiver's vertical line with beam spreading correction. c) Cyan receiver's horizontal line without beam spreading correction. d) Cyan receiver's horizontal line with beam spreading correction.

after performing a beam spreading correction, multiplying the solution by the the offset with equation (II.42). In case of non-attenuating medium, we expect to have a constant amplitude as a function of the offset after the geometrical beam spreading correction.

The Figure III.12c shows the wave propagating in the x direction before geometrical correction. The amplitude is stronger near the source and decrease as the beam expands. We notice in Figure III.12d that after one wavelength farther from the source, the amplitude is almost constant after geometrical spreading correction. It is what we expect since we work in purely elastic context with no viscosity, that means no attenuation.

The correction is less obvious from the Figure III.12a to the Figure III.12b showing the wave propagating in the z direction. It is because there is more reflections and conversions in this location. Also, we point-out on the Figure III.12b that the oscillations seem to have two distinct wavelengths. This is explained by the presence of both P- and S- waves of respectively velocities of $V_P = 6320$ m/s and $V_S = 3100$ m/s on this location (see Figure III.10a).

2.2.2 P- and S- wave decomposition

We refer to Chapter II Subsection 2.3 to remind that P-waves correspond to the divergence or compressional-part of the solution and S-waves to the curl or shear-part of the solution. We separate the P- and the S- waves in order to analyze them independently. Only the curl's y component is displayed because the x and z components are equal to zero in the cross-section of the center of the cube.

The compressional wave propagates in the vertical direction and the shear wave propagates in the horizontal direction according to the Figure III.13. It is still explained because the source's component is vertical. In the next parts, we look for the recovery of elastic parameters along a virtual receivers' line. We are going to study the wavefield

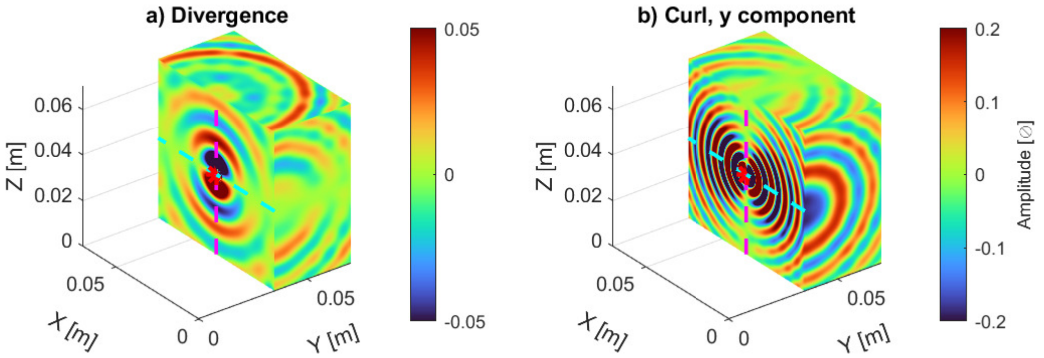

Figure III.13: a) Divergence and b) curl (y component) of the 3D simulation in Figure III.11.

on the vertical (magenta) line to recover the P-wave Lamé parameters, and on the horizontal (cyan) line to recover the S-wave Lamé parameters.

2.2.3 Recovery of μ from the S-wave

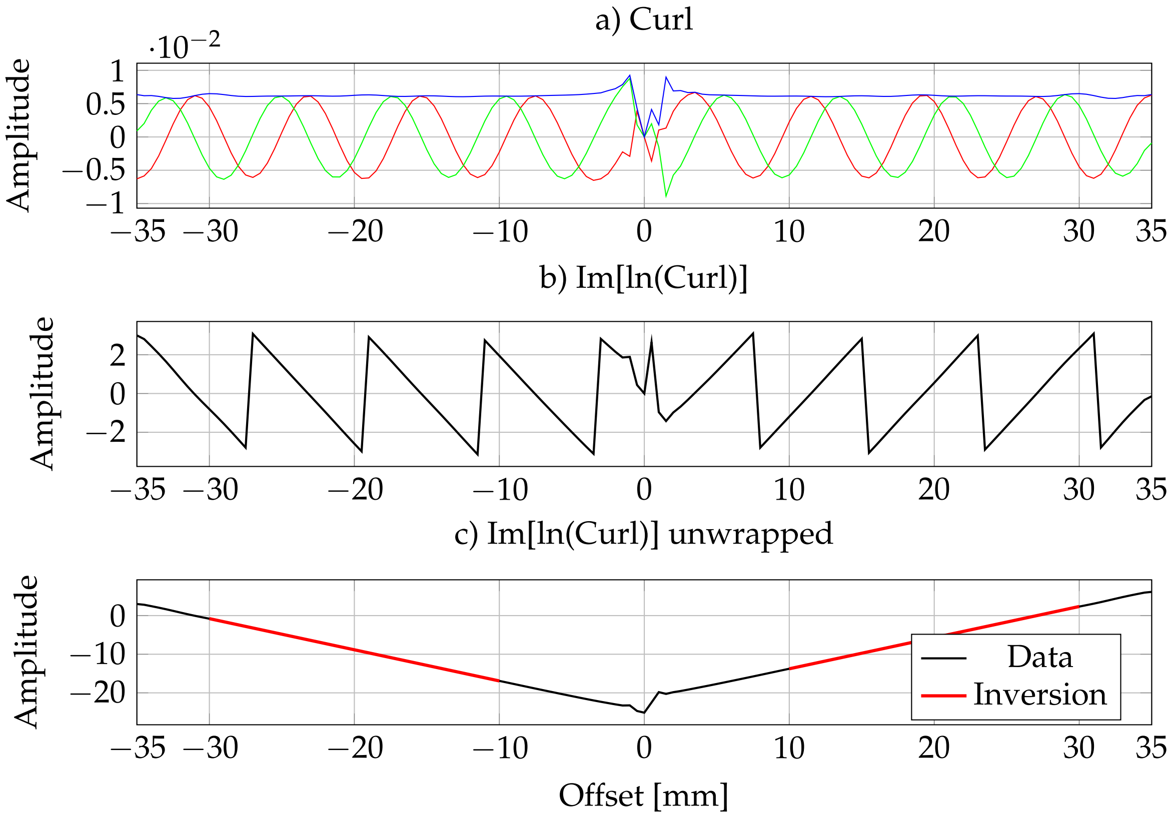

Figure III.14: Data processing for the μ recovery using a) the curl's y component ([——] real part - [——] imaginary part - [——] amplitude spectrum) and calculating b) its natural logarithm's imaginary part. The k_{real_S} is found with c) the unwrapped slope as a function of the offset. μ_r = 26.23 GPa for a 400 kHz frequency.

The objective of this part is to understand how we can recover the elastic parameters from the wavefield in frequency domain. Indeed, they are usually calculated with the time of direct wave arrivals [Aki and Richards, 2002] with equations (II.22) and (II.23). In our case, we want to work with frequency-domain solutions, which are more appropriate as we consider viscoelasticity, hence frequency-dependent physical parameters. To do so, we work with the complex wavenumber and the formulations of complex modulus. Since there is - so far - no viscosity in the media, we recover the Lamé parameters according to the equation (II.68), first for μ working with the S-wave:

$$\mu = \rho \frac{\omega^2}{k_{real_S}^2}. \tag{III.4}$$

We find the S-wave wavenumber k_{real_S} from the curl of the displacement field according to equation (II.61), using the horizontal receivers' line on the center of the cube (Figure III.13b, cyan line). We remind that only the y component is not null at this location. A step-by-step illustration is given in Figure III.14, where the beam spreading has previously been corrected multiplying the amplitude by the offset. The recovered parameter is denoted μ_r while the real/actual one is denoted μ.

The imaginary part of the natural logarithm of the curl is bounded between $-\pi$ and π (Figure III.14b). In order to find the most accurate k_{real} in accordance with the equation (II.61), we have to "unwrap" this data, *i.e.* put together every piece of the linear function to remove the jumps at $-\pi$ and π. By doing so, we can calculate the shear modulus μ over a large offset (Figure III.14c) using the equation (III.4). Also, we will compare the recovered moduli with the actual moduli λ = 55.95 GPa and μ = 25.95 GPa to quantify the accuracy of the method. For instance, the relative error on the shear modulus μ_r is given by:

$$E\% = \frac{|\mu_r - \mu|}{\mu} \times 100, \tag{III.5}$$

with $E\%$ the percentage of error between the actual μ and the recovered μ_r with the data. In the presented example, μ_r = 26.23 GPa with a 400 kHz frequency. That is 1.1% of error between the actual and recovered μ, which displays a good accuracy of the method for this frequency. We tested the method for several frequencies (Table III.1).

2.2.4 Recovery of λ from the P-wave

The λ elastic parameter will be recovered from the divergent displacement field on the vertical receiver's line on the center of the cube (Figure III.13a, magenta line). The method is similar to μ retrieval as we want to invert the slope of the linear function in Figure III.15c to know what the k_{real_P} is, and then deduce λ with the equation (III.6), that is,

$$\lambda = \rho \frac{\omega^2}{k_{real_P}^2} - 2\mu. \tag{III.6}$$

In the 400 kHz simulation using the divergent displacement field, we calculate the recovered λ_r = 62.37 GPa that we compare with the actual elastic parameter λ = 55.95 GPa and find an error of 11.5%.

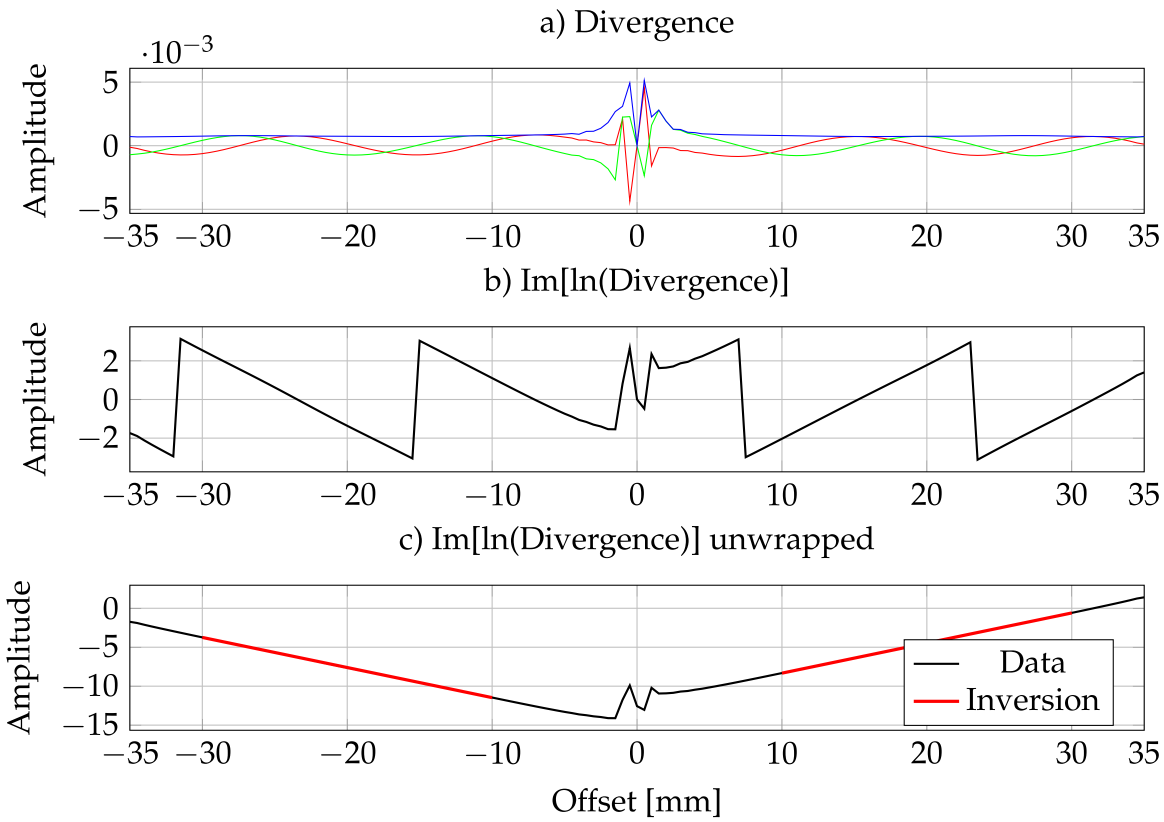

Figure III.15: Data processing for the λ retrieval using a) the divergence ([—] real part - [—] imaginary part - [—] amplitude spectrum) and calculating b) its natural logarithm's imaginary part. The k_{real_p} is found with c) the slope as a function of the offset. λ_r = 62.37 GPa for a 400 kHz frequency.

Frequency [kHz]	λ_r [GPa]	$E\%_\lambda$	μ_r [GPa]	$E\%_\mu$
400	62.37	11.5%	26.23	1.1%
600	58.17	4.0%	26.08	0.5%
800	55.23	1.3%	26.00	0.2%

Table III.1: Different frequencies simulations and elastic parameters retrieval. Each error is calculated using the actual λ = 55.95 GPa and the actual μ = 25.95 GPa.

2.2.5 Concluding remarks

The method to recover the elastic parameters λ and μ within the cube in the case of a simulation without attenuation and with absorbing boundary conditions has been tested for three frequencies - 400, 600 and 800 kHz - and are displayed in the Table III.1. We note that the error is roughly the same between the μ recovered from the S-waves at 400 kHz and the λ recovered from the P-waves at 800 kHz, that have respectively a wavelength of 7.75 mm for the S-wave and 7.9 mm for the P-wave. The method might be more accurate for the higher frequencies because the absorbing boundary conditions are more efficient [Kosloff and Kosloff, 1986] and the unwanted reflections could actually come from the SP-wave conversion in the lateral boundaries propagating where our receivers are located. Indeed, wave propagating with a certain angle displays a large apparent wavelength, or a smaller apparent wavenumber leading to a larger elastic parameter λ calculated with equation (III.6).

2.3 Wavefield analysis in frequency-domain - with Kelvin-Voigt attenuation law

In the following simulation, we aim to recover the viscoelastic parameters (Lamé and attenuation) by adding viscosity into the model. The simulation calculated a viscoelastic wave propagation with respect to the Kelvin-Voigt viscoelastic rheological model. The input viscoelastic parameters are λ = 55.95 GPa, μ = 25.95 GPa, η_λ = 2500 Pa s and η_μ = 5000 Pa s, and we use absorbing boundary conditions.

2.3.1 Wavefield data-set

In this simulation, the amplitude decreases because of the beam spreading and the intrinsic attenuation due to the viscosity. The results of the 400 kHz frequency simulation can be seen in Figure III.16 for the 3 components.

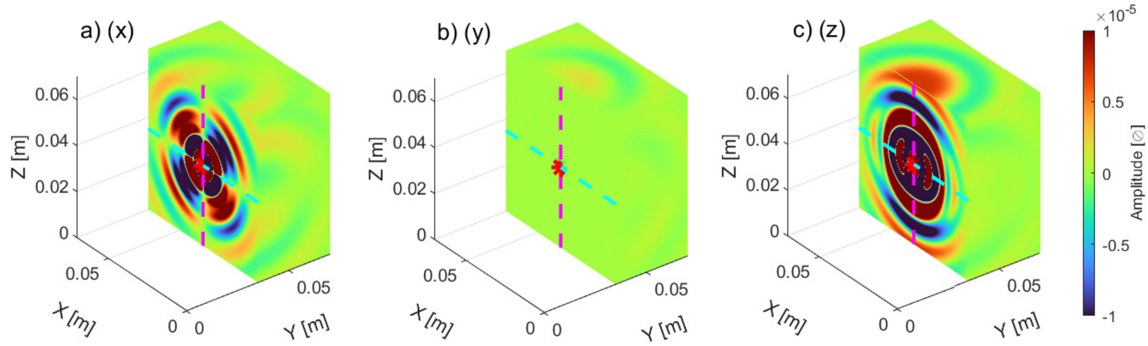

Figure III.16: Cross-section in the center of the cube (y = 35 mm) of the real part of the 400 kHz solution for the homogeneous 7x7x7 cm cube with the source in the middle of the cube with attenuation, absorbing boundary condition on the 6 faces. The red asterisk represents the source position, the cyan line [- - -] represents the horizontal line receivers' position, the magenta line [- - -] represents the vertical line receivers' position. a) x component. b) y component. c) z component.

Figure III.16c showing the z-component of displacement field. Similar to the previous subsection, the source being vertical, the vertical propagation following the magenta line represents mainly the P-wave with a slight presence of S-wave (see seismogram Figure III.10a), and the horizontal propagation following the cyan line represents mainly the S-wave. Concerning the x-component of displacement field, the Figure III.16a displays a mix of P and S waves on the diagonals. The null y-component of the Figure III.16b is due to the geometry of the experiment because the displacement field propagates on the $-y$ and $+y$ directions simultaneously because we are on a plane of symmetry as seen on Figure III.11.

A beam spreading correction has been made on Figure III.17 to be able to visualize the viscoelastic attenuation effect by multiplying the amplitude by the offset as in equation (II.42). There is a strong amplitude decrease as a function of the distance to the source seen on Figure III.17b and Figure III.17d because we chose carefully the viscous parameters so that the wave propagates as much as possible before it reaches a boundary. By doing so, we expect that an eventual reflection has a few impact on the processed data.

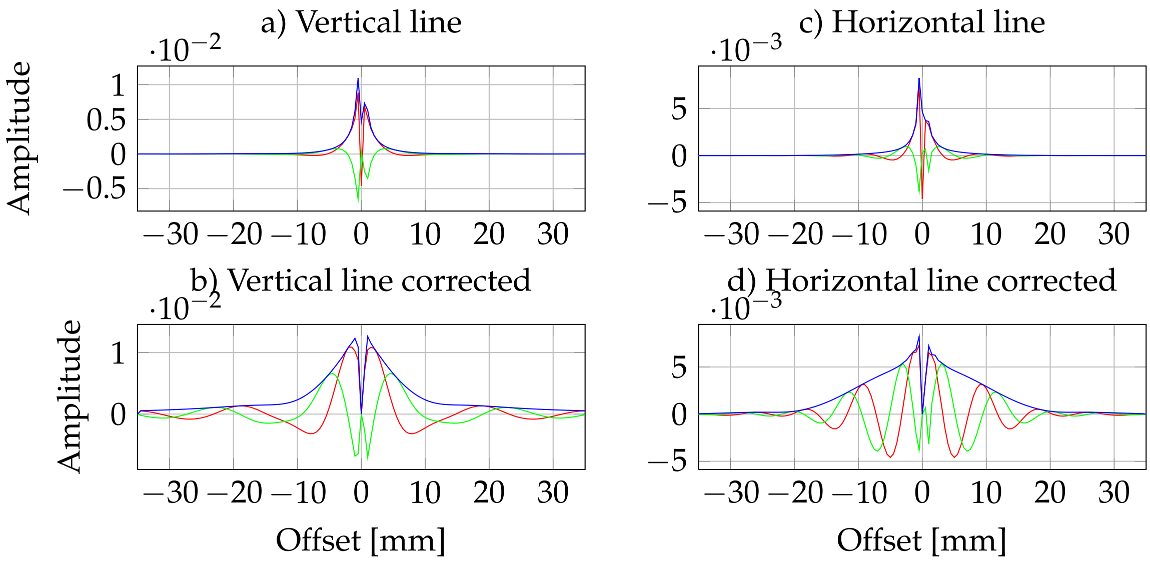

Figure III.17: 400 kHz frequency solution from the z-component receivers of the cross section (Figure III.16c) as a function of offset. [—] real part. [—] imaginary part. [—] Amplitude spectrum. a) Magenta vertical receiver's line without beam spreading correction. b) Magenta receiver's vertical line with beam spreading correction. c) Cyan receiver's horizontal line without beam spreading correction. d) Cyan receiver's horizontal line with beam spreading correction.

2.3.2 P- and S- wave decomposition

In order to increase the accuracy of the viscoelastic parameter's retrieval, we firstly separate the 3-D simulation into its curl (for the S-wave) and divergence (for the P-wave) as in the Figure III.18. By doing so, we recover the shear viscoelastic parameters μ and η_μ from the S-waves and λ and η_λ from the P-waves.

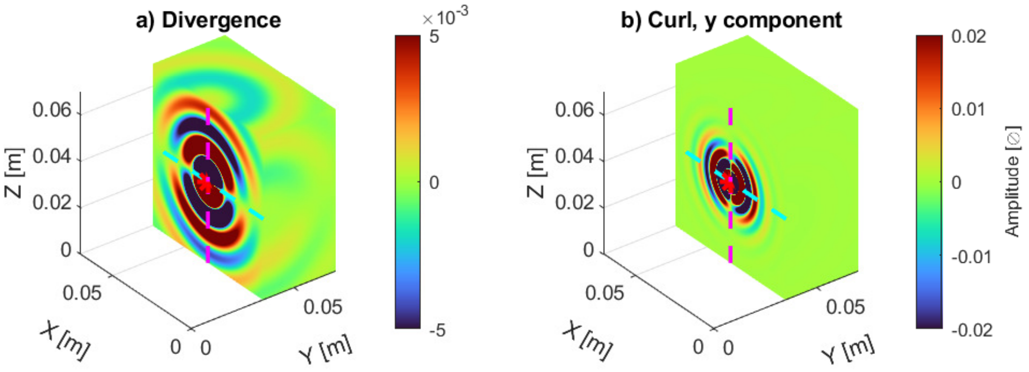

Figure III.18: a) Divergence and b) curl (y component) of the 3D simulation in Figure III.16.

The complex velocities are dependent of the complex modulus M that include elastic λ and μ and viscous η_λ and η_μ parameters. We refer to Chapter II Section 4 for further details.

2.3.3 Recovery of Lamé parameters λ, μ and attenuation factors η_λ, η_μ

We start with reminding the displacement field equation as

$$\hat{u}(x,\omega) = u_0 \cdot \exp(-\alpha x) \cdot \exp(-ik_{real}x), \tag{III.7}$$

and we are going to recover the attenuation α and the wavenumber k_{real} isolating the real part from the imaginary part of $\hat{u}$ for P- and S- waves.

We rearrange to isolate α and k_{real} such that

$$\mathrm{Im}[\ln(\hat{u})] = -k_{real}x, \tag{III.8}$$

and

$$\mathrm{Re}[\ln(\hat{u})] = -\alpha x + \ln(u_0). \tag{III.9}$$

That means that the real and imaginary parts of the complex wavenumber k_{real} and $k_{imag} = -\alpha$ will be found from the real and imaginary parts of the displacement field respectively. We calculate the complex modulus and the viscoelastic parameters in accordance with the equations (II.67) for the Kelvin-Voigt rheological model (equations (II.52)). For the S-wave, we have then:

$$\mu = \rho\omega^2 \frac{k_{real_S}^2 - k_{imag_S}^2}{(k_{real_S}^2 + k_{imag_S}^2)^2}, \tag{III.10a}$$

$$\eta_\mu = -2\rho\omega \frac{k_{real_S} k_{imag_S}}{(k_{real_S}^2 + k_{imag_S}^2)^2}, \tag{III.10b}$$

with k_{real_S} and k_{imag_S} found from the data's curl.

Concerning the viscoelastic parameters for the P-wave, we will use μ and η_μ from (III.10) to write

$$\lambda = \rho\omega^2 \frac{k_{real_P}^2 - k_{imag_P}^2}{(k_{real_P}^2 + k_{imag_P}^2)^2} - 2\mu, \tag{III.11a}$$

$$\eta_\lambda = -2\rho\omega \frac{k_{real_P} k_{imag_P}}{(k_{real_P}^2 + k_{imag_P}^2)^2} - 2\eta_\mu, \tag{III.11b}$$

with k_{real_P} and k_{imag_P} found from the data's divergence.

2.3.4 Recovery of viscoelastic parameters from P- and S- wave - Results

As we have seen in equations (III.8) and (III.9), the complex wavenumber is found from the slope of the different data sets. An illustration of this method is displayed on Figure III.19. The data for the P-wave viscoelastic parameters recovery comes from the magenta vertical receivers' line of the divergent wavefield (Figure III.18a). For the recovery of the S-wave viscoelastic parameters recovery, we use the cyan horizontal receivers' line of the curl part of the wavefield (Figure III.18b).

We first analyze the S-wave (Figure III.19c,d) and invert the complex wavenumber k_{S_r} = 1102-416i to recover the shear viscoelastic parameters μ_r = 26.09 GPa and η_{μ_r} = 5096 Pa·s following the equations (III.10). The actual complex wavenumber is here k_S = 1274-516i. Then, we inject those parameters within the equations (III.11) to calculate λ_r = 59.13 GPa and η_{λ_r} = 3681 Pa·s.

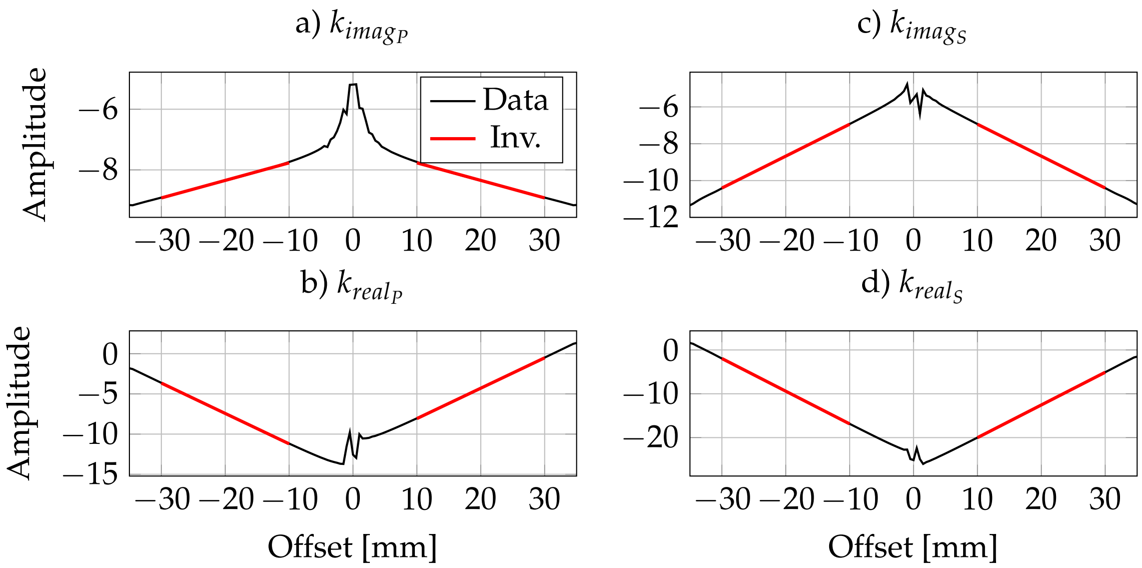

Figure III.19: Recovery of viscoelastic parameters with the inversion of the slope of the different data sets as a function of distance to the source for a 400 kHz numerical simulation. Inv. stands for Inversion. a) Real part of the natural logarithm of the P-wavefield: Re[ln(Divergence)]. b) Imaginary part of the natural logarithm of the P-wavefield: Im[ln(Divergence)]. c) Real part of the natural logarithm of the S-wavefield: Re[ln(Curl)]. d) Imaginary part of the natural logarithm of the S-wavefield: Im[ln(Curl)]. Here, λ_r = 59.13 GPa, μ_r = 26.09 GPa, η_{λ_r} = 3681 Pa·s and η_{μ_r} = 5096 Pa·s.

It is again useful to compare quantitatively the recovered parameters λ_r, μ_r, η_{λ_r} and η_{μ_r} to their actual values λ, μ, η_λ and η_μ respectively with an error calculation as in the equation (III.5). The results of the presented simulation and others as well as the percentage of error for each viscoelastic parameter recovery are compiled on Table III.2.

2.3.5 Concluding remarks

A numerical investigation for various frequencies and viscous parameters were performed in order to confront and compare the used method. The results can be seen on Table III.2 where we can see three trends. The parameters μ and η_μ are better recovered than λ and η_λ, the viscous parameters have a significantly higher error than their elastic parameters, and the reconstructed η_λ have a relatively high error but are still acceptable.

We can discuss these trends by analyzing our reconstruction steps. μ and η_μ are the first parameters calculated and are injected in the equations (III.11) to recover λ and η_λ. Thus, in addition to the internal error of the P-wave wavenumber inversion, we inject and add an error from the S-wave wavenumber. Also, we saw in the Subsection 2.1 that there is a residual presence of S-wave in the divergent wavefield. This can induce significant errors in the calculation of viscoelastic parameters in frequency domain since all the wave are mixed.

Regardless this error analysis aiming to discuss the results in detail, we can still say that the method gives a relatively good recovery of viscoelastic parameters in the presented data sets. The next step in Section 3 is to analyze the wavefield in experimental conditions, with the source and the receivers located at the boundaries of the sample.

Fq [kHz]	λ_r [GPa]	$E\%_\lambda$	μ_r [GPa]	$E\%_\mu$	η_{λ_r} [Pa·s]	$E\%_{\eta_\lambda}$	η_{μ_r} [Pa·s]	$E\%_{\eta_\mu}$
400*	59.13	5.7%	26.09	0.5%	3681	47.2%	5096	1.9%
600*	57.04	1.9%	26.04	0.3%	3117	24.6%	4937	1.3%
800*	56.75	1.4%	25.92	0.1%	3108	24.3%	5146	2.3%
400**	59.95	7.1%	26.14	0.7%	2043	63.4%	2553	2.1%
600**	57.47	2.7%	26.03	0.3%	1425	14.0%	2531	1.2%
800**	56.31	0.6%	26.13	0.6%	1410	12.8%	2489	0.4%
400***	61.25	9.5%	26.16	0.8%	379	51.3%	508	1.6%
600***	57.60	2.9%	26.04	0.3%	203	-18.8%	507	1.4%
800***	56.44	0.9%	25.98	0.1%	316	26.4%	504	0.8%

Table III.2: Different frequency simulations and recovery of viscoelastic parameters. Each error is calculated using the actual λ = 55.95 GPa, μ = 25.95 GPa. The viscous parameters vary such that (*) η_λ = 2500 Pa·s and η_μ = 5000 Pa·s. (**) η_λ = 1250 Pa·s and η_μ = 2500 Pa·s. (***) η_λ = 250 Pa·s and η_μ = 500 Pa·s.

3 Wavefield analysis in experimental conditions

In the previous section, we recover the elastic and viscous parameters of a medium with a wavefield in frequency domain inside the sample, where only body waves propagate. When we work in experimental conditions, with the source and the receivers on the boundaries and free-surface boundary conditions, we have to deal with body and surface waves, as well as wave reflections, wave conversions, and noise.

One difficulty with working at the boundaries of the domain is that we need to know the wavefield information below the receivers (information that we do not have) in order to calculate the derivatives in the three directions, x, y and z and thus deduce the divergence and the curl. Another difficulty is the presence of surface waves, for example Rayleigh wave that propagates with an elliptic retrograde motion following the ray direction [Aki and Richards, 2002], meaning that they have a shear motion as well as a longitudinal motion and are present in both the divergence and the curl of the wavefield. Also, the Rayleigh wave velocity is very close to the S-wave velocity [Aki and Richards, 2002], meaning that the wavenumber is very close to the S-wave one, adding one more difficulty onto wave separation. We need to find a solution for a wave attenuation recovery without separating the waves into curl and divergence.

Solution to get the unknown derivative is proposed by Robertsson and Curtis [2002] that took advantage of free-surface boundary conditions formulations to compute the unknown z derivative from the known x and y derivatives. Also, Sun et al. [2011] use reverse and upward time extrapolation techniques to be able to calculate the wavefield in the z layers just below and above the receivers location. These techniques have not been tested in the frame of this thesis because they do not take into account the surface waves.

In this section, after the contextualization of the experimental laboratory conditions with a view on the first wave arrivals, we develop a method that aims to recover the attenuation of the S-waves in a low-attenuation sample.

3.1 Viscoelastic wave propagation in time domain with Free-Surface boundary conditions - first arrivals

In this section, we aim to be as close as possible of experimental conditions in time domain. We remind that we perform an inverse Fourier transformation to switch from the frequency simulations to time domain seismic wavefield (Subsection 1.2). The source is located at the top-center of the cube with a vertical u_z component only, and the chosen boundary conditions are free-surface on every boundary of the cube.

The viscous parameters are $\eta_\mu = 1000$ Pa·s and $\eta_\lambda = 500$ Pa·s for a Kelvin-Voigt viscoelastic model so that the wave amplitude is totally vanished after 0.5 ms. It allows a frequency step calculation of 2 kHz for the recovery of the time-domain signal (see equation (III.2)). The chosen wavelet is a Ricker of 250 kHz central frequency. It means the numerical simulations are calculated from 2 kHz to 750 kHz with a step of 2 kHz before performing an inverse Fourier transform to display the results in time domain.

3.1.1 3-D results

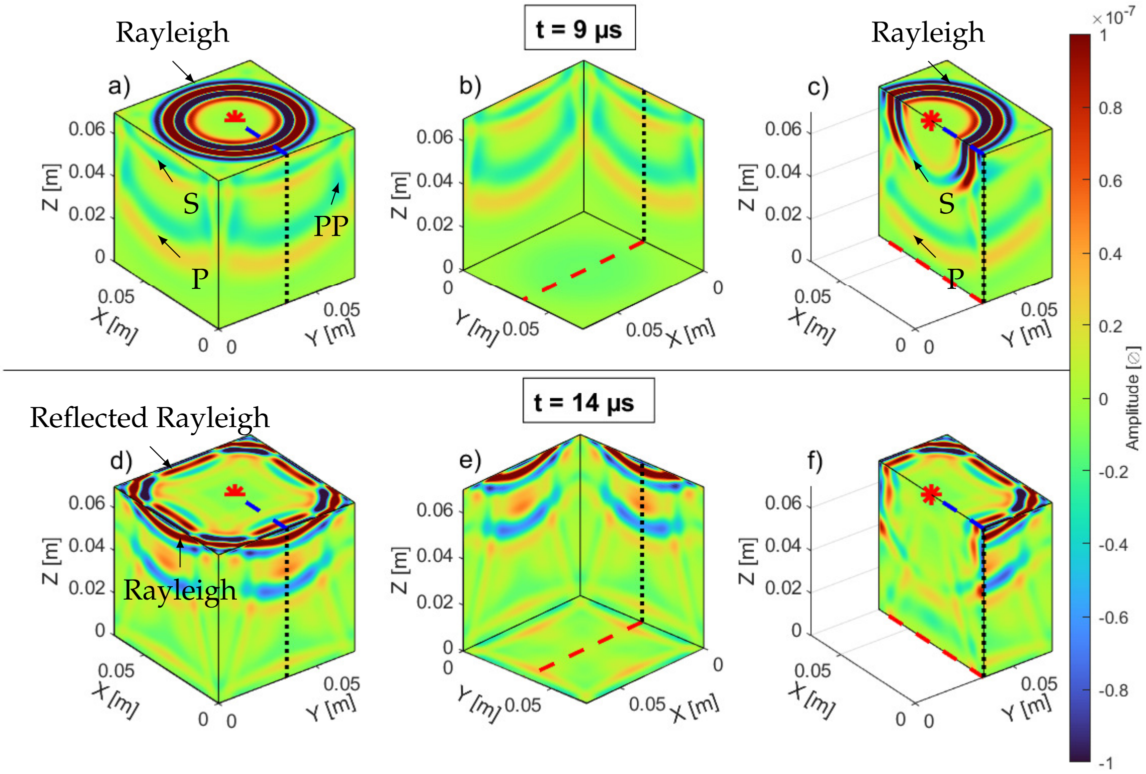

Figure III.20: 3-D view of a simulation calculated in time domain for the homogeneous 7x7x7 cm cube with attenuation and free-surface boundary condition after performing an inverse Fourier Transform. The source (red asterisk) is placed on the top-center of the cube. The blue dashed line, black dotted line and red dashed line represent the receivers' location for the Figure III.21 (blue dashed line [----] receivers 1 to 351, black dotted line [⋯⋯] receivers 351 to 1051, red dashed line [- - -] receivers 1051 to 1751). a) Top view at 9 μs. b) Bottom view at 9 μs. c) Cross-section view at 9 μs. d) Top view at 14 μs. e) Bottom view at 14 μs. f) Cross-section view at 14 μs. The displayed components are these normal to each surface, except for the cross-section (z component).

The wavefield solutions for 9 μs and 14 μs are displayed in Figure III.20. In the top part of the figure (9 μs), we can see the beginning of the wave propagation. The P-wave in the bottom-half has already been reflected (PP-wave) and the reflection can be seen at the top-half of the cube. It is followed by the S-wave well visible in the cross-section (Figure III.20c). The wave of high amplitude visible on the top-surface of the cube is a mix of S- and surface waves, with too similar velocities to be separated so far.

The bottom part of the figure (14 µs), highlights the first reflections and conversions of propagating waves. The surface wave has been transmitted and reflected back around the top-edges of the cube. We can also see in the cross-section view that the reflected and converted waves are mixed together and it is difficult to point and name rigorously a propagating wave.

3.1.2 Seismogram representations

The seismogram of the numerical simulation with receivers around the cube presented in Figure III.20 is displayed in Figure III.21. The virtual receivers are placed every millimeters and the recorded component is normal to each face. The red, green and yellow lines corresponding to P-, S- and surface waves are placed after a calculation of the expected arrival time of each wave. The PP-wave is the P-wave generated at the source, reflected on the bottom of the cube and recorded back to the top-face of the cube.

We can point out from the Figure III.20 and Figure III.21 that because of the large wavelength, it is impossible to distinguish clearly the boundaries of each wavelet propagation (*i.e.* the exact P-wavelet). It is a limitation for attenuation recovery if we want to use the classical methods. Indeed, spectral ratio methods or reflection methods [Johnston et al., 1979; Toksöz et al., 1979; Winkler and Nur, 1982; Adam et al., 2009], to be accurate, rely on an exact wavelet separation and assume the selected wavelet is not mixed with other ones that will interfere and add biases in the data processing. One solution can be to reduce the wavelength by working at higher frequency. Yet, it might reduce the accuracy of lower frequencies and we need them for a frequency-dependent recovery of attenuation. We have to use a totally different approach to recover the frequency-dependent attenuation from mixed waves in the data, presented in the next Subsection 3.2.

3.2 Wavefield analysis and attenuation recovery of a low attenuation medium

In this section, we detail our method to recover the representative viscoelastic properties based on wave measurements at experimental context. Here, we take advantage of the reflections to reach a state of equilibrium of energy and recover the frequency-dependent attenuation of wave. This is why we need to work on low attenuation medium. Subsequently, we carry out numerical simulations to verify the performance of our approach. The numerical calculations are performed in samples whose dimensions are identical to the dimensions of some samples used in the laboratory experiments of Chapter IV.

This Subsection 3.2 is a part of a submitted article on *Geophysical Prospecting* journal, and has been slightly modified to fit the thesis manuscript.

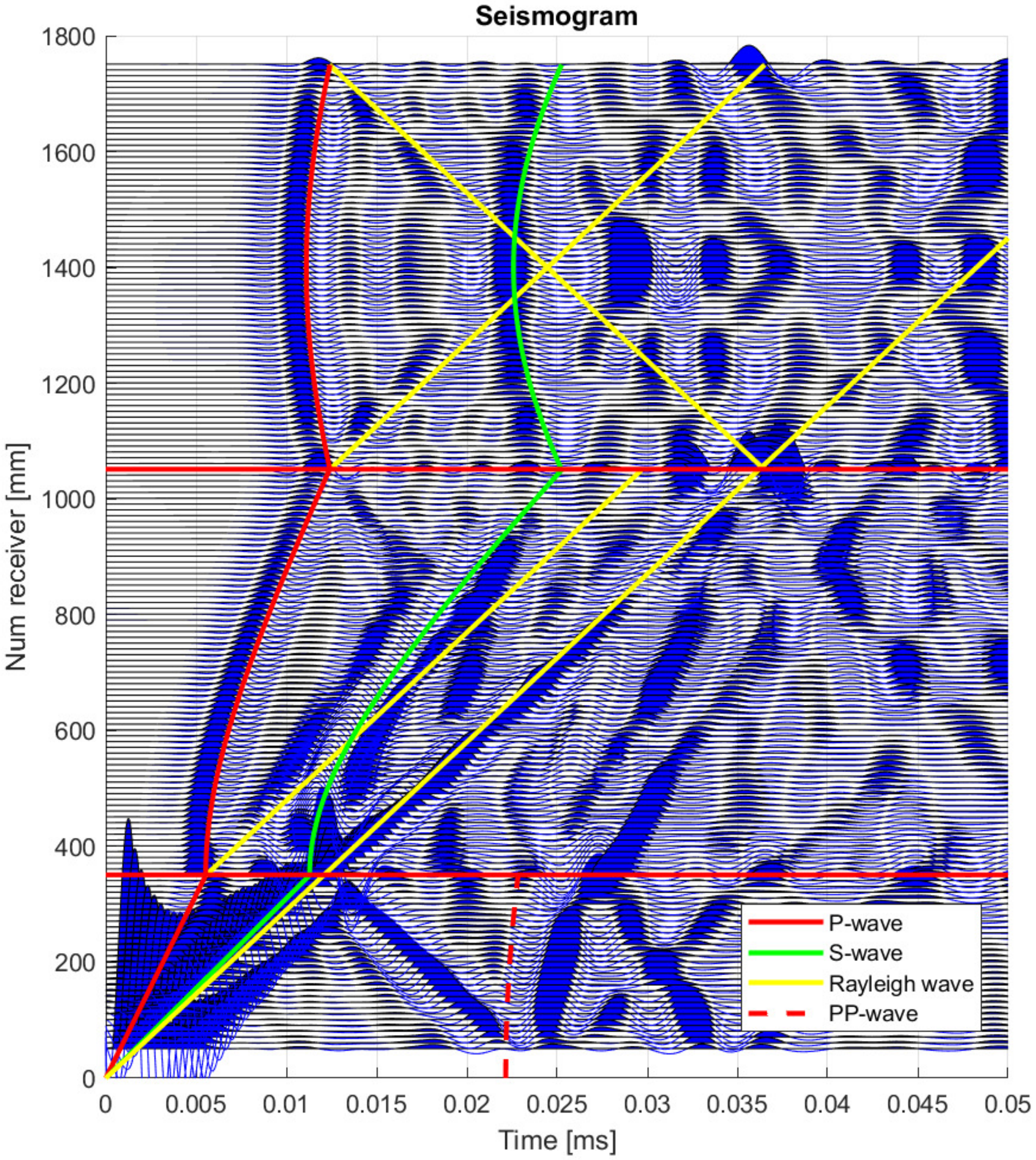

Figure III.21: Seismogram around the simulated cube of the Figure III.20 between 0 and 50 µs with highlights of various first-wave arrivals.

3.2.1 Methodology

Because of weak attenuation, waves reverberate multiple times within the sample over a short time period. The distinctive aspect of our method is that it makes use of all types of seismic waves (P, S, and surface waves) in a single global signal envelope at any seismic receiver location. In our method, we take advantage of the reflections from the free-surface boundary conditions such that the wave energy is conserved within the medium, and the beam spreading effect is no more visible in the data. In this case, the interference between the different reflected / converted waves create an equilibrium of energy that is called equipartition, a phenomenon also used for coda waves [Ryzhik et al., 1996; Margerin et al., 2000]. After several reflections [Snieder, 2002], the wavefield is governed by the S-waves, that is, the observed signals is overwhelmed by the S-wave and, consequently, the attenuation property we recover will be representative of that of the S-waves attenuation.

We present our approach for recovering the representative attenuation coefficients as a function of frequency in flowchart of Figure III.22 for a specific example. The data shown in Figure III.22 corresponds to a 100 kHz Ricker seismic source emitted at time $t = 0$ in a medium following the viscoelastic model of case d (Table III.3). Figure III.22a and b show the seismic signal recorded by receiver R3 using the u_z component, respectively in time and frequency domains: in time, the seismogram displays an exponential characteristic decay of amplitude (equation (II.64)):

$$u(x,t) = \exp(-\beta t) \cdot \exp[\mathrm{i}(\omega t - k_{real} x)]. \tag{III.12}$$

The method proceeds as follows. (i) We need to select a small bandwidth of frequency that we move from low to high frequencies. The use of a square filter on the frequency data would lead to artifacts in time-domain, this is why a Gaussian filter is used on the frequency domain data (Figure III.22b) to select a relatively small bandwidth. In our case, we select a Gaussian filter of ± 10 kHz span around the central chosen frequency ω_c (Figure III.22c). (ii) After filtering, we apply an inverse Fourier transform in order to build the amplitude decrease as a function of time for the small frequency bandwidth selected (Figure III.22d). (iii) The next step consists in using the Hilbert envelope of the signal [Taner et al., 1979]: the attenuation coefficient value β in $[\mathrm{Np\,s^{-1}}]$ is given by the decrease of the envelope as a function of time, and is computed through the natural logarithm of the signal (Equation (II.64), Figure III.22e). (iv) Finally, the Q-factor is deduced from β using equation (II.72). Then, we can move on to the next frequency of interest and repeat these steps in order to cover the entire frequency content of the recorded data.

Selecting an appropriate Gaussian filter width in frequency is a crucial aspect of determining the Q-factor and should be customized based on the dataset being analyzed: insufficient frequencies within the chosen data window can cause instability in the inverse Fourier transform and prevent the method from accurately determining the attenuation value (Figure III.23a). On the other hand, if the Gaussian filter width is excessively large, the decrease in amplitude observed in Figure III.23c will not follow a linear trend due to the mixing of too many frequencies. Indeed, in this case of a large selection bandwidth, we are less sensitive to attenuation variations with respect to frequency. Considering that attenuation is frequency-dependent, the waves of high-attenuation frequencies decrease faster in the beginning of the seismogram, while the waves of low-attenuation frequencies remain energetic until the end of the recorded data. Currently, the optimal filter width is determined empirically in order to obtain a precise recovery of the attenuation model (Figure III.23b). Further analysis would be required to analyze quantitatively how the size of the window depends on, e.g., the wavelength and signal-to-noise ratio.

3.2.2 Numerical set-up configurations

We perform isotropic viscoelastic 3-D numerical simulations of wave propagation for the Maxwell and Kelvin–Voigt models of attenuation, and we consider free surface boundary conditions. The simulations performed in the frequency domain are carried

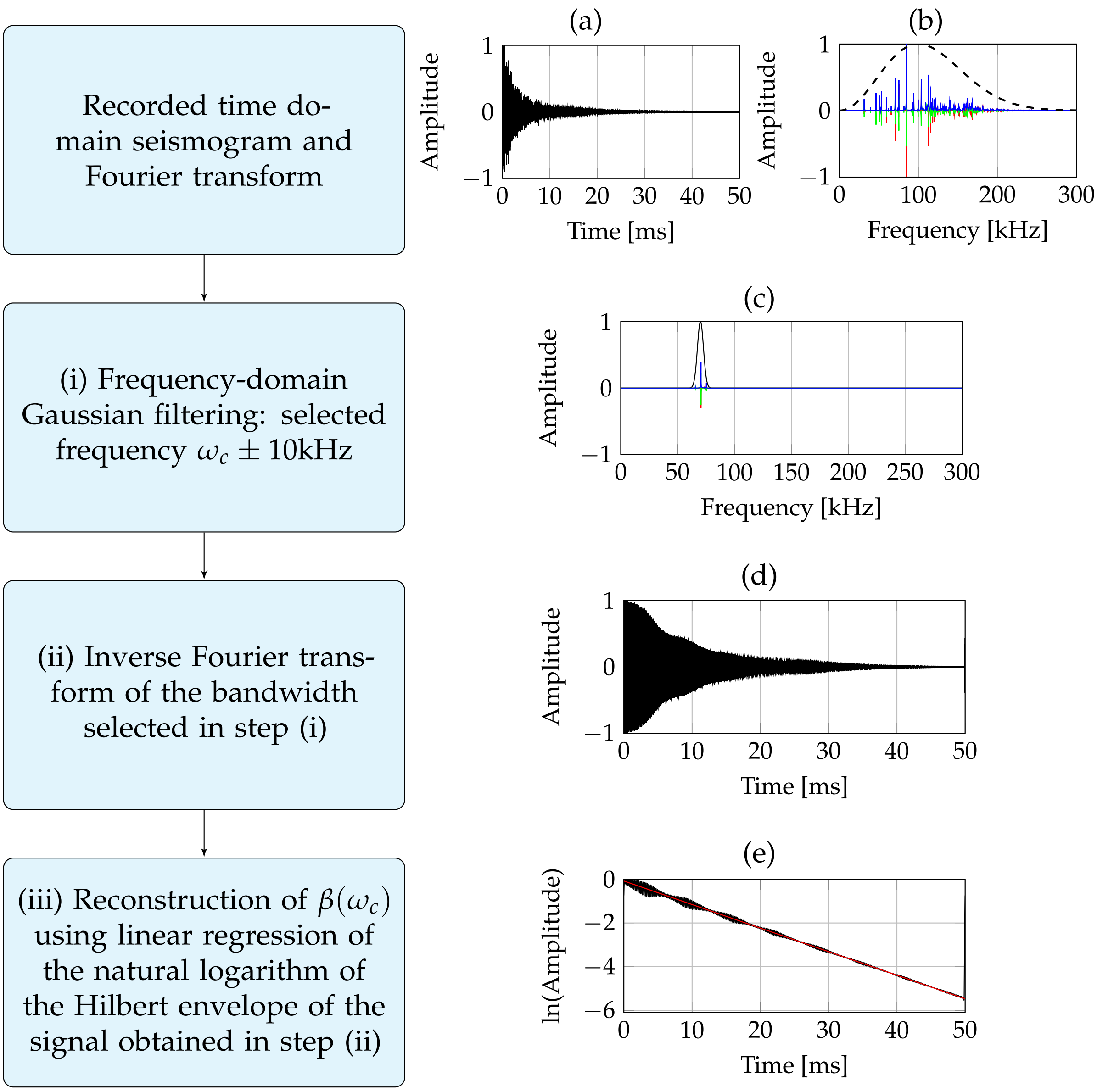

Figure III.22: Flowchart of the signal processing for the recovery of the frequency-dependent attenuation. The numerical illustrations correspond to the configuration described in Table III.3 case d, using a central frequency of 70 kHz. a) Normalized time domain seismogram. b) Normalized frequency-domain Fourier transform: [——] real part, [——] imaginary part, [——] amplitude spectrum, [- - -] amplitude spectrum of the Ricker seismic source. c) Gaussian filtering. d) Normalized inverse Fourier transform of c). e) Hilbert envelope of d) and $\beta(\omega_c)$ recovery.

out in two types of geometries: a cube of size 7 cm × 7 cm × 7 cm and a cylinder of height 9 cm and diameter 5 cm (see Figure III.24a and b respectively). The seismic point-source is positioned in both configurations on the upper surface of the sample and the source motion u_z is directed towards the vertical direction (u standing for the displacement of a particle and $\square_z$ indicating the $z-$direction).

We carry out simulations for frequencies between 20 Hz to 300 kHz with a step of 20 Hz. By doing so, we apply an inverse Fourier transform to obtain the time-domain seismogram for a duration of 50 ms, where we consider a Ricker wavelet source of 100 kHz peak-frequency. The synthetic signals are extracted for three positions of receiver (see Figure III.24), located either inside the volume (R1) or at the boundary of the sample

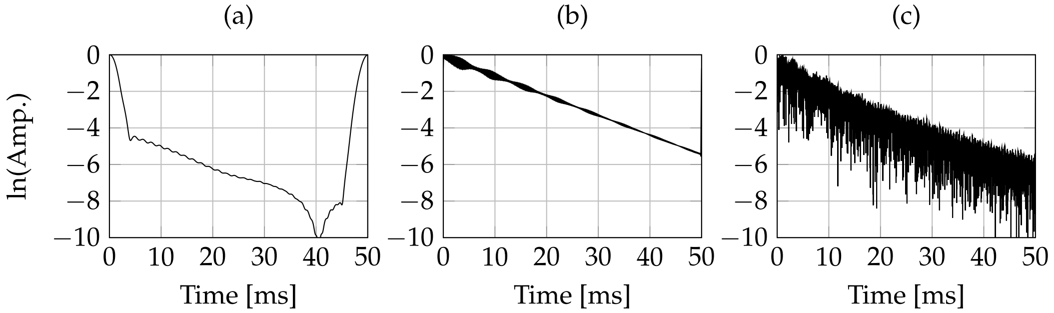

Figure III.23: Comparison of Hilbert envelopes after 3 gaussian filtering of distinct window widths. The viscoelastic simulations parameters correspond to the Table III.3 case d, using the central frequency of 70 kHz. (a) ±0.5 kHz, (b) ±10 kHz, (c) ±50 kHz.

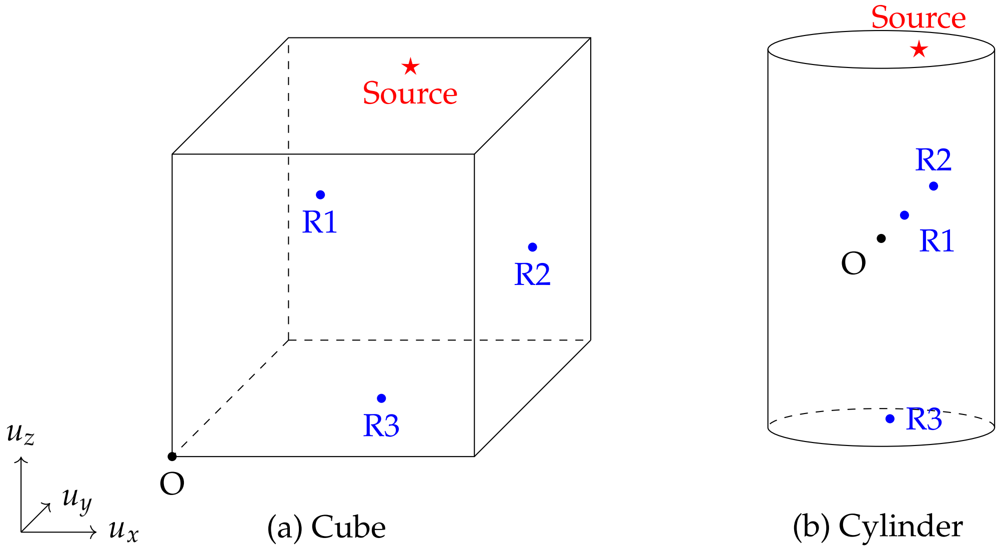

Figure III.24: Numerical set-up used for the numerical simulations. (a) 7x7x7 cm^3 cube with the origin O located at the lower-left corner of the cube. The source is located at [3.5 6 7] cm on the top surface of the cube. The receiver R1 is located in the bulk of the cube at the position [2 2.5 4] cm, whereas R2 at [7 3.5 3.5] cm and R3 at [3.5 3.5 0] cm are on the surface. (b) 9 cm height and 5 cm diameter cylinder with origin O located at the center of the cylinder. The seismic source is located at [1 0.0 4.5] cm on the surface, the receiver R1 is at [1 1 1] cm inside the cylinder, R2 at [0 2.5 1] cm and R3 at [0 1 -4.5] cm on the surface.

(R2 on a lateral face and R3 on the opposite face with respect to the source).

Five different simulations (cases a to e) are analyzed using fixed elastic parameters $\lambda_e = 55.95$ GPa, $\mu_e = 25.95$ GPa, $\rho = 2700$ kg m^{-3} and varying viscous parameters (η_λ, η_ν) as detailed in Table III.3: the choice of viscous parameters may differ significantly between cases, while maintaining a comparable Q-factor, due to the specific constitutive models used for each case (equations (II.52), (II.54), and (II.56)).

As an illustration of the variability of the attenuation induced by the Maxwell - Kelvin-Voigt - Zener viscoelastic models, Figure III.25 shows the behavior of α_s and of the S-quality factor Q_s as a function of frequencies discussed in Chapter II.

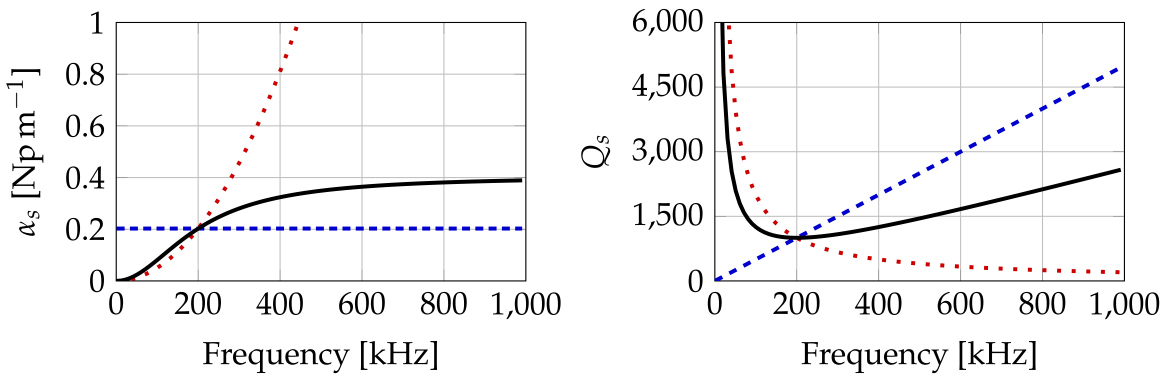

Figure III.25: S-waves attenuation coefficient (left) and quality-factor (right) behavior as a function of frequency for [- - - -] Maxwell viscoelastic model with η_μ = 20.65 MPa s, [· · · ·] Kelvin-Voigt viscoelastic model with η_μ = 20.65 Pa s and [——] Zener viscoelastic model with τ_ϵ = 796.57 ns and τ_σ = 794.98 ns. The parameters are chosen such that all attenuation models coincide at frequency 200 kHz.

Table III.3: Viscoelastic models and viscous parameters used for the numerical simulations. The elastic parameters λ_e = 55.95 GPa and μ_e = 25.95 GPa are kept constant. K-V stands for Kelvin-Voigt.

Case	Geometry	Model	η_λ	η_μ	Q_p(100kHz)	Q_s(100kHz)
a	Cube	Maxwell	100 MPa s	2.5 MPa s	612	60
b	Cube	Maxwell	10 MPa s	20 MPa s	291	484
c	Cube	K-V	100 Pa s	10 Pa s	1430	4130
d	Cube	K-V	20 Pa s	40 Pa s	1717	1033
e	Cylinder	Maxwell	50 MPa s	5 MPa s	350	121

3.2.3 Analysis of the numerical experiments

We present in the following the result of the various numerical simulations described in Table III.3 to validate our methodology and test its robustness. Figure III.26 is an illustration of such a computation in a cubic domain: the propagating seismic wavefield at frequency 400 kHz is represented in a cross-section and on surface boundaries. We follow the wave propagating from the source through the sample with the three components u_x, u_y, and u_z. In this specific numerical simulation, receiver R3 is located exactly in a plane of symmetry of the domain aligned with the seismic source. This configuration results in destructive interference for the u_x wavefield component at this receiver since waves arrive from opposite directions simultaneously and cancel each other out, which means that there is no seismic energy in the u_x component for receiver R3 in Figure III.26. This configuration is highly improbable in practice, but with numerical simulations, singular point measurements such as this one can occur. Thus, we discard the u_x component of receiver R3 from our analysis and consider the other components for R1, R2, and R3 (Figure III.24) in our signal processing.

In the first simulation presented in Figure III.27 case a, waves are propagating in a medium where the attenuation of the S-waves β_S is 10 times higher than the attenuation of the P-waves β_P. Although we expect the P-waves to be of stronger amplitude than the S-waves, we recover numerically with our method - by far - a global attenuation of the medium very close to the attenuation of the S-waves (see Figure III.27 case a). For the sake of clarity in Figure III.27, we have distinguished only the signal recorded by R1 in the bulk from the receivers R2 and R3 at the surface, with no distinctions between components x,y or z for all the receivers. The important information from

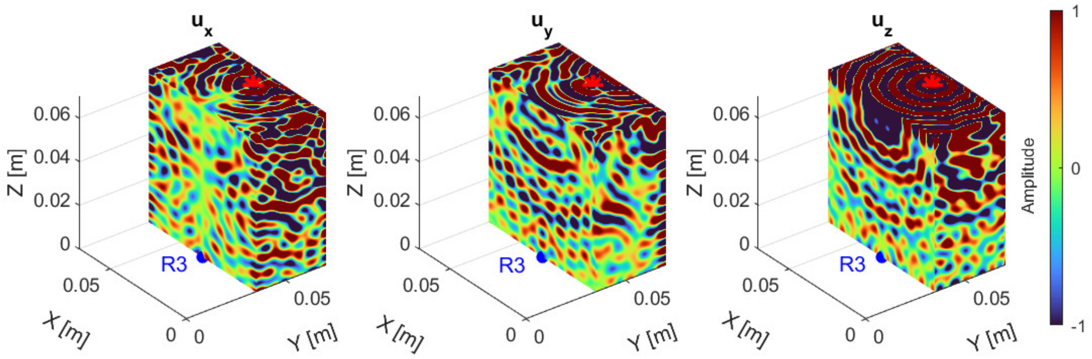

Figure III.26: Visualization of the real part of a seismic numerical wavefield generated in a cube at 400 kHz on a cross-section, lateral and upper boundaries. Amplitude of the displacement for u_x, u_y and u_z components. Red asterisk: source location. Blue dot: receiver R3 location.

Figure III.27a is that we recover approximately the same attenuation value whatever the location of the receivers and whatever components of the wavefield are used for the computation. A qualitative computation of the penetration depth of the surface waves following Vinh and Malischewsky [2007] shows that the receiver R1 located at 2 cm depth is only recording P- and S- body seismic waves as opposed to receivers R2 and R3 on the boundaries which are experiencing all seismic waves (body and surface). We conclude that we recover with our method a representative attenuation of a sample from measuring one seismic component of the wavefield at the boundary of the sample.

We have observed that the attenuation values recovered using our method consistently match the attenuation values of S-waves in the numerical simulations. This phenomenon can be explained by the equipartition effect, which occurs when the energy of a seismic wavefield reaches a state of equilibrium between propagating P- and S-waves due to the numerous wave reflections and conversions that take place in the domain. In this context, Ryzhik et al. [1996]; Sánchez-Sesma et al. [2008] analytically proved that the S-wave is more energetic than the P-wave, a property also observed numerically by Margerin et al. [2000]; Sánchez-Sesma et al. [2018] and experimentally by [Shapiro et al., 2000; Hennino et al., 2001; Margerin et al., 2009]. Snieder [2002] derived an analytical formula to calculate the time τ_{PS} needed to reach the equipartition state (neglecting seismic attenuation):

$$\tau_{PS} = \frac{a(V_S^3 + 2V_P^3)}{2V_P V_S^3}. \tag{III.13}$$

Using values for $V_P = 6320\,\mathrm{m\,s^{-1}}$, $V_S = 3100\,\mathrm{m\,s^{-1}}$ and a characteristic length of $a = 7$ cm, a being the distance between two scatterers, we expect to reach the state of equilibrium between P- and S- waves around $\tau_{PS} = 100\,\mu\mathrm{s}$, a time small compared to the total duration of our numerical simulations, confirming that we reach an equipartition state very fast in the numerical experiments.

Following case a in Figure III.27 where we recovered numerically the S-waves attenuation from a Kelvin-Voigt viscoelastic simulation in a cube, cases b to e (Table III.3) in Figure III.27 show that we systematically retrieve numerically the S-waves attenuation for Kelvin-Voigt and Maxwell viscoelastic models simulations (that have different Q-factor behavior with respect to frequency) in a cube or a cylinder, regardless of which

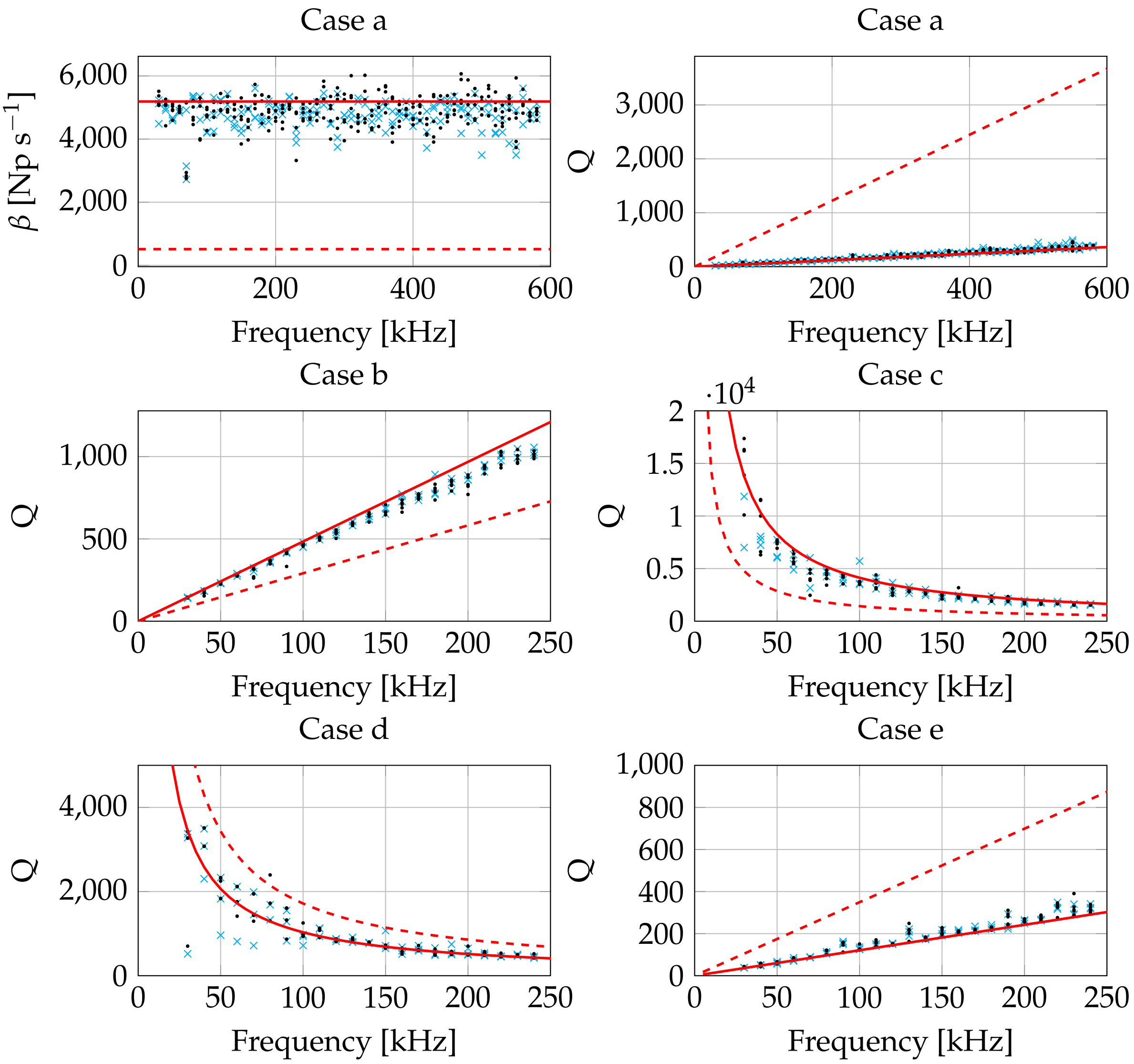

Figure III.27: Attenuation β (case a) and Q-factor recovery from a numerical signal generated in a 7 cm × 7 cm × 7 cm cube (cases a to d) using Maxwell viscoelastic attenuation (cases a and b) or Kelvin-Voigt viscoelastic attenuation (cases c and d) models in the media. Case e: Q recovery in a 9 cm height and 5 cm diameter cylinder with Maxwell attenuation. See Figure III.24 for the geometries and Table III.3 for the viscoelastic parameters. [- - -] Analytical β_p or Q_p, [——] Analytical β_s or Q_s, [·] recovered from the signal at the surface of the medium (receiver 2: u_x, u_y and u_z components; receiver 3: u_y and u_z components), [×] recovered from the signal inside the medium (receiver 1: u_x, u_y and u_z components).

receiver location or which wavefield component is used for the determination of the attenuation.

In summary, our numerical results indicate that we can successfully recover the representative viscoelastic attenuation parameters of a low attenuation media, regardless of the sample geometry, by processing the seismic signal recorded either within the volume or at the boundaries. Due to the equipartition phenomenon, the energy of S-waves is consistently higher in seismic records than that of P-waves. Therefore, we systematically recover the attenuating properties of S-waves in the medium.

3.3 Impact of noise in signal processing

In this part we want to take a step closer to the reality by adding noise in our data, and process it as usual to recover the S-waves attenuation. Investigating how to deal with noise - or at least recognize its pattern in the processed data - is of importance because working in experimental conditions means working with noise.

3.3.1 Before / after noise addition

Signal-to-noise ratio (SNR) takes many definitions depending on authors and objectives. Dash and Obaidullah [1970] and Rietsch [1980] for instance use correlation techniques to separate the coherent signal to incoherent noise, [Zhao et al., 2014] defines a more complex method to calculate the signal-to-noise ratio over time and frequency, or [Shen et al., 2012] consider the noise as the standard deviation of the data at the end of the trace and the signal as the maximum amplitude of that trace.

In our case, we just look for a simple way to add noise in the data and as we analyze the amplitude decrease of a mixed-waves signal after many reflections. For noise addition, we define the signal-to-noise ratio as the maximum of amplitude of the seismic trace divided by the maximum of amplitude taken at the end of the seismogram, where the signal amplitude is vanished:

$$SNR = \frac{signal}{noise}. \tag{III.14}$$

We consider in this example adding a uniform white noise level of 10%, or a signal to noise ratio of 10 in the seismogram. To do so numerically we add a random number comprised between 0 and 10% of the maximum amplitude of the time-domain signal to each point of the data. By doing so, the added noise impacts evenly all frequencies. We can see in Figure III.28 the time- and frequency- domains data before and after noise generation for the case b at receiver R3 and u_z component (see Table III.3 and Figure III.24). In this Figure III.28 we clearly notice the noise level at the end of the seismogram, and at low and high frequencies - actually where there is signal of low amplitude. As a first order interpretation, we can guess that the noise is going to reduce the operative bandwidth as well as the inversion time for attenuation recovery. Indeed, the noise seems predominant in the seismogram from about 5 ms onwards.

This is confirmed in the Hilbert envelopes of the 100 ± 10 kHz frequency of interest with and without noise (Figure III.29). In the initial Hilbert envelope - without noise - the noise level is numerical and is reached at about 15-17 ms. We can recover the attenuation value in the signal between 0 and 15 ms. In the case of the Hilbert envelope of the noisy data, the noise level is reached sooner, and the decrease in amplitude recovery can only be performed between 0 and roughly 4 ms.

3.3.2 Attenuation recovery and discussions

We compare in Figure III.30 the recovered frequency-dependent attenuation β and Q-factor with the method described in Figure III.22 before and after noise addition. We highlight two main consequences of noise due to the reduction in bandwidth (Figure III.28b) and time before reaching the noise level (Figure III.29).

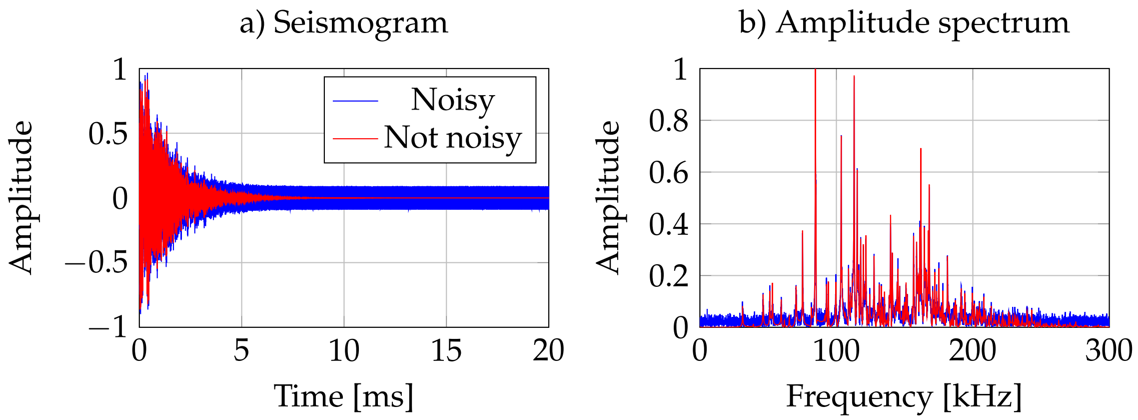

Figure III.28: a) Seismogram and b) amplitude spectrum of the data of R3 for u_z component before and after adding a 10% noise.

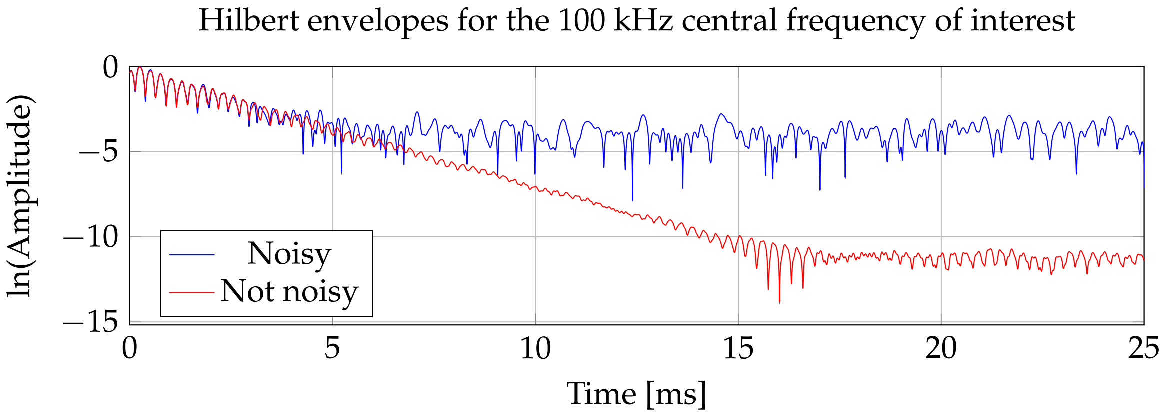

Figure III.29: Hilbert envelopes of the selected frequencies of 100 ± 10 kHz from the data of Figure III.28 before and after adding a 10% noise.

First, the reduction in time means that we recover the amplitude decay on less workable data in time. It leads to a less accurate attenuation recovery and a larger spread of values between the receiver's location and component (see for instance Figure III.30a for 70 kHz, 110 kHz or 180 kHz).

Second, the reduction in bandwidth in frequency between the noisy and not noisy data shows an interesting pattern. In the bandwidth with sufficient signal-to-noise ratio - between 60 and 200 kHz - the recovered attenuation follows the S-waves analytical attenuation as expected. When we shift slowly out of the workable bandwidth towards the low and high frequencies, the recovered apparent attenuation is lower and lower. This is due to the process of taking the natural logarithm of the amplitude envelope. Where the noise level is constant regarding the envelope decreasing exponentially, the natural logarithm calculation is going to underestimate that noise or the higher amplitudes (at the beginning of the seismogram) and overestimate it at the lower amplitudes, leading to an underestimated decaying slope when we deal with noisy data (see the illustration at Figure III.31).

Hence, the two main consequences of noise in the data are a larger dispersion of the recovered attenuation, and a parabolic shape where the signal to noise ratio is low with respect to frequency. These consequences can lead to difficulties in interpretation concerning the best model to fit the data. For the noisy attenuation recovery for instance,

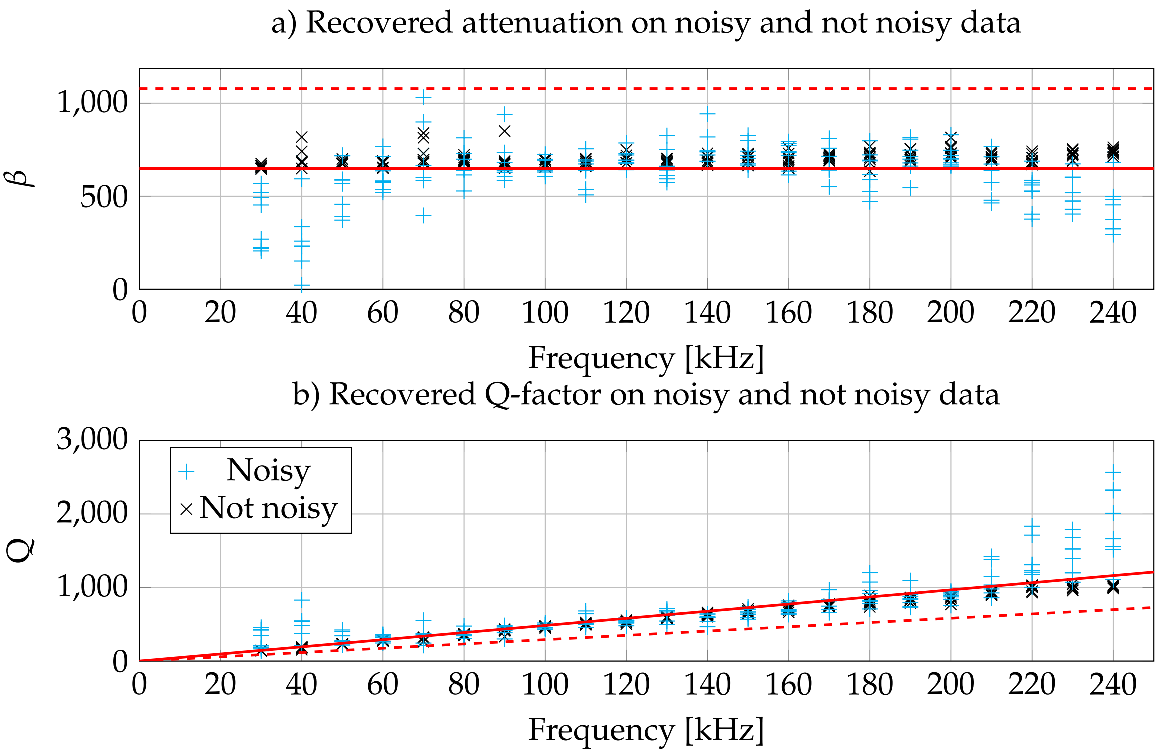

Figure III.30: a) Attenuation and b) Q-factor recovery on noisy and not noisy data of case b (Table III.3) for the 3 receivers R1, R2 and R3 at each components. [- - -] Analytical β_p or Q_p. [——] Analytical β_s or Q_s.

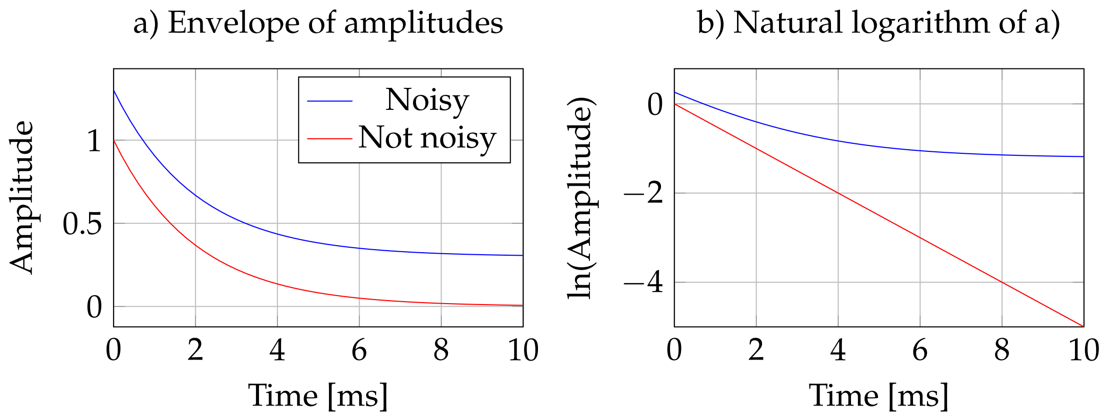

Figure III.31: Illustration of a not noisy and noisy exponential decaying envelope of amplitudes with a 30% noise level. a) Exponential decaying envelope of amplitudes. b) Natural logarithm of the envelopes in a), that we would normally use for attenuation recovery.

instead of fitting a Maxwell model, we could have found that the attenuation reaches a peak at 140 kHz and then decrease, which is false and only due to noise addition.

3.4 Conclusions of numerical simulations in experimental context

Using numerical experiments, we have shown that we can recover the frequency-dependent attenuation parameter of S-waves for each receiver position, each component of the displacement measured, and for different geometries of samples. This is explained by the equipartition phenomenon, that is, a state of balance of energy between propagating waves after multiple reflections and conversions within the medium. This results in the S-waves being more energetic than the P-waves, hence dominating the signals. We demonstrate that the method for the recovery of the attenuation parameter is efficient and works well with numerical simulations, and when we reproduce experimental conditions such that source and receivers at the boundaries of the sample, and with noise addition. Moreover, we explain how the noise impacts the data processing.

4 Summary of numerical simulations

In this chapter, we first analyzed the wavefield inside the homogeneous medium by applying a curl and a divergence to the wavefield. It was an interesting study for a good understanding of wave propagation and viscoelastic behavior inside a domain and to take the numerical tool at hand. We also highlighted some unexpected results such as the presence of reflection waves athough the use of absorbing condtions and the presence of S-waves when applying the operator divergence to the wavefield.

In the next part, we consider "real" experimental conditions, that is with free-surface boundary conditions allowing wave reflections and conversions everywhere and the source and receivers at the surface of the domain. We saw that the S-waves dominate the signal as long as there is enough reflections and conversions, and that the equilibrium of energy *equipartition* due to these reflections and conversions leads us to measure the same S-wave attenuation value at any point of the sample. It is important for actual experimental measurements since it eases the accuracy of location of source and receivers. However, we have to keep in mind that only the S-waves attenuation is recovered, and our method does not allow a P-waves attenuation recovery.

In the next Chapter IV, we investigate the case of experimental measurements with different rock samples.

Chapter IV

Experiments

In this chapter we are willing to use the method described in Chapter III to recover the frequency-dependent attenuation and viscoelastic laws of actual samples of aluminum (a cube of 7 cm x 7 cm x 7 cm to be able to compare the wave propagation with numerical simulations of the chapter above, and a 7 cm x 10 cm x 12 cm block), Fontainebleau sandstone cylinder, Carrara marble cylinder and diorite cylinder using the laboratory data.

The available experimental devices do not allow us to meet the numerical free-surfaces boundary conditions for attenuation recovery because of the receiver in contact with the sample. We have to qualify and understand potential biases in the experiments before interpreting the results. Only then we can choose the best conditions to measure the attenuation in a large frequency bandwidth (between 60 kHz and 2 MHz) to find the viscoelastic laws and parameters of our measured media.

1 Experimental set-up

The physical measurements are performed through an experimental set-up designed and automated as a part of this PhD project. Piezoelectric transmitters are used as a seismic source and non-contact laser Doppler interferometer as seismic receiver. The acquisition can be executed with the use of LabView interface-programming which helps the management and automation of the used devices. The set-up is built to measure wave propagation in decimeter-sized samples.

In this section we explain how the set-up works, we give details about the seismic sources and then we test different configuration (stack number, presence of reflecting tape) that enhances the signal-to-noise ratio while saving acquisition time. Indeed, it is of importance to have good signals and to make as much experiments as possible in a limited time.

1.1 Installation and use of the devices

To build the experimental set-up, we used the existing set-up of Shen [2020] and completely redesign and rebuilt it for the measurements. The receiver, the interferometer laser Polytec VFX-I-120 were new in the laboratory. We had to set-up the installation of this laser from scratch, and included it into the automated set-up via a Python programming routine. Interferometer laser uses Doppler effect to detect movements on the surface of the sample. It means that it sends a light beam of a known wavelength on the sample, and the beam is reflected back from the sample to the laser. The vibrations at the surface of the sample due to wave propagation induce a change in the reflected wavelength (Doppler effect) and are detected by the laser.

The acquisition is made as follows (Table IV.1). The sample (aluminum or rock in this thesis) is laid on a platform operated by motors for horizontal and vertical movement as in Figure IV.1. Once the sample in place, (1) the laser Doppler interferometer Polytec VFX-I-120 is focused on the recording point. (2) Then, a wave is designed by a waveform generator Tabor 8024, (3) is amplified by an amplifier Falco Systems WMA-300, and (4) is generated though the sample with a ©Panametrics piezoelectric transmitter. (5) The displacement of the sample's surface due to the vibration can then be recorded by the laser Doppler interferometer Polytec VFX-I-120 and (6) saved after a given number of

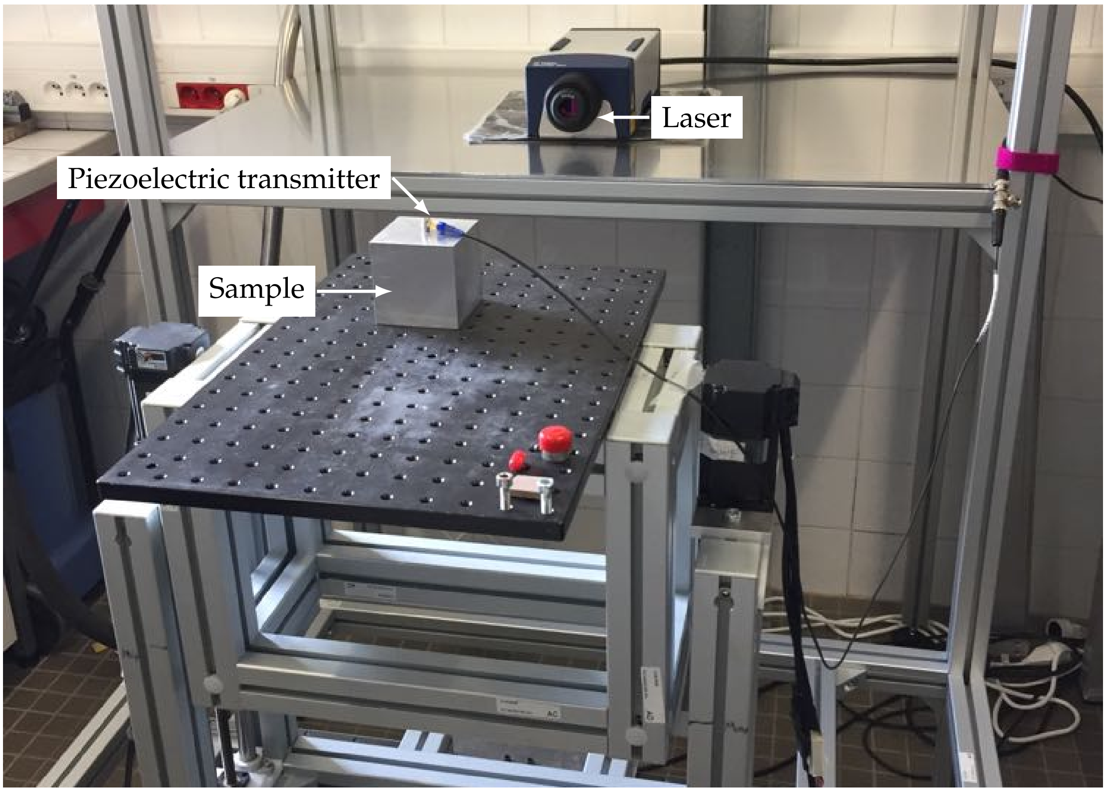

Figure IV.1: Picture of the used experimental set-up. The sample is placed on a platform allowing a vertical and horizontal displacement. The source is a piezoelectric transmitter and the receiver is a laser interferometer.

stack (average of seismic traces) by an oscilloscope Keysight DSO-S 054A. After that, (7) we can move the sample laid on the platform vertically and/or horizontally in order to record on a line or on several parallel lines via motors allowing millimeter-accurate displacement. Eventually, we can restart at the step (1) for a new recording.

Table IV.1: Steps for wave recording on a sample

SOURCE	RECEIVER
	(1) Focus laser on the sample
(2) Waveform generation	
(3) Waveform amplification	
(4) Waveform transmission from the PZT to the sample	
	(5) Sample's vibration recording
	(6) Recording saved in oscilloscope < if stack, go back to step (2) >
(7) Vertical and/or horizontal displacement of the platform; back to step (1)	

1.2 Piezoelectric transmitters (PZT)

We worked with six different ©Panametrics piezoelectric transmitter sources of different central frequency in order to work with a large bandwidth in frequency. The piezoelectric transmitters are of different size and different central frequency. As we have shown numerically in Chapter III Section 3 that the source location has no impact on attenuation recovery, the impact of the surface of contact between the PZT and the sample will actually be discussed in Subsection 3.2 of this Chapter IV.

Table IV.2: Contact diameters of the piezoelectric transmitters.

PZT name Central frequency	V1011 100 kHz	V150 250 kHz	V151 500 kHz	V102 1 MHz	A197S 2.25 MHz	V1091 5 MHz
Diameter [cm]	3.8	2.5	2.5	2.5	2.9	0.3

We detail in Table IV.3 the name of each PZT as well as their central frequencies; followed by a picture of the PZT placed on the 7 cm x 7 cm x 7 cm aluminum cube to appreciate the size of the contact source in relation to size of the sample; followed by the waveform recorded directly on the source (we pointed the laser on the contact surface of the PZT); followed by the amplitude spectrum of these measurements directly on the PZT.

The recordings on PZT alone not only tell us about the sent waveform source, that is considerably different from one source to another, but also on the time where the wave is actually generated. The best illustration is on the recording of the V102 - 1 MHz source (Table IV.3 Waveform PZT alone), where the wave is not generated at time of origin t_0 = 0 µs but has a delay of about 6 µs. This is due to all the electronic paths between the trigger and the actual wave generation. Each PZT source has a different time delay. To find it, we make a measurement with the receiver laser directly on the ceramic of the PZT and generate a wave. The recorded time of the first break of wave arrival corresponds to the time delay of the source (see Table IV.3 "Waveform PZT alone" for signals on the used PZT).

Table IV.3: Used piezoelectric sources, waveform recorded directly on the source and amplitude spectrum. Normalized amplitudes.

<table>
<tr><th colspan="3">Piezoelectric transmitter source</th></tr>
<tr><td>V1011 - 100 kHz
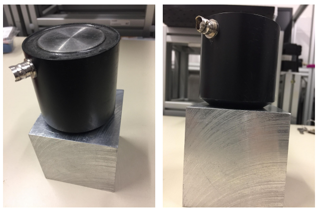</td><td>V150 - 250kHz
</td><td>V151 - 500 kHz
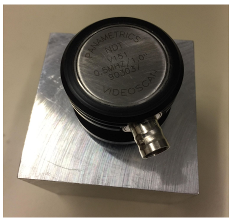</td></tr>
<tr><th colspan="3">Waveform PZT alone</th></tr>
<tr><td>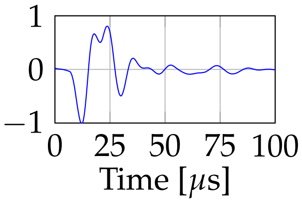
</td><td>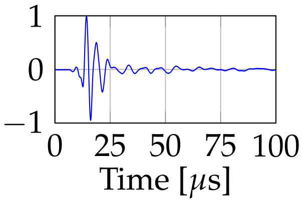
</td><td>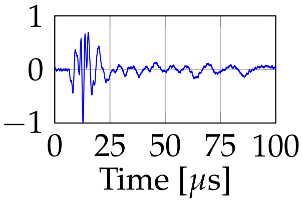
</td></tr>
<tr><th colspan="3">Amplitude spectrum</th></tr>
<tr><td>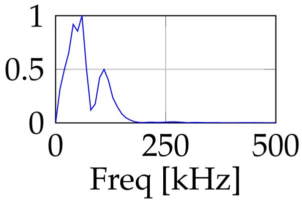
</td><td>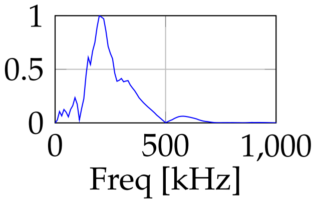
</td><td>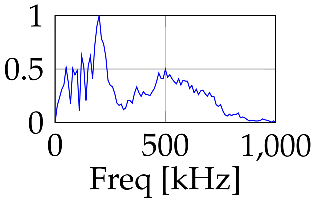
</td></tr>
</table>

<table>
<tr><th colspan="3">Piezoelectric transmitter source</th></tr>
<tr><td>V102 - 1 MHz
</td><td>A197S - 2.25 MHz
</td><td>V1091 - 5 MHz
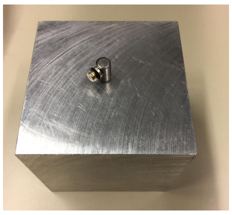</td></tr>
<tr><th colspan="3">Waveform PZT alone</th></tr>
<tr><td>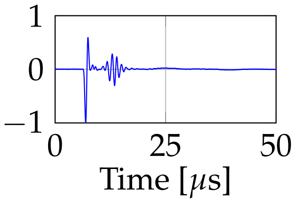
</td><td>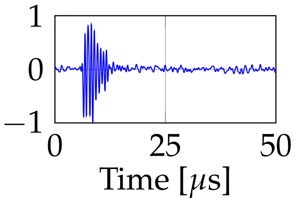
</td><td>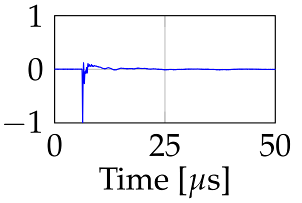
</td></tr>
<tr><th colspan="3">Amplitude spectrum</th></tr>
<tr><td>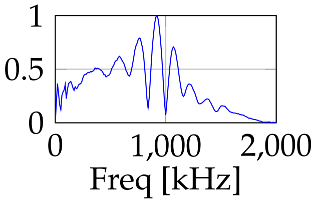
</td><td>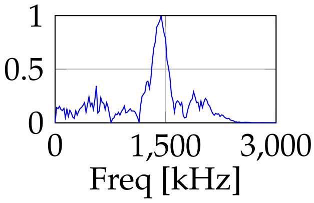
</td><td>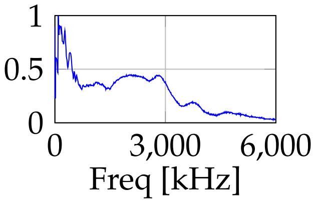
</td></tr>
</table>

1.3 Calibration

In this part, we test and compare different acquisition set-ups. The goal here is to find the best configuration that will save us time while having a sufficient signal-to-noise ratio. In the following, we made our tests by propagating seismic waves through the aluminum cube with the piezoelectric transmitter source V1091 - 5 MHz that displays a bad signal-to-noise ratio between the noise and the first wave arrival amplitudes. By doing so, we place ourselves in the "worst conditions" in terms of signal-to-noise ratio, and we try to improve the signal as much as possible.

The two main levers that can be used to improve the signal-to-noise ratio is the number of stack, and the presence of a reflective tape, that presents advantages and inconveniences.

Concerning the presence or not of reflective tape, we have to be very careful as we are willing to work on attenuation. As the presence of reflective tape will help focus the laser and increase the signal-to-noise ratio, it might actually modify slightly the boundary condition and roughness - inducing scattering at this point. If we look at Figure IV.2 comparing the signal with and without reflective tape at the measurement point with a stack of 5000, we notice that the signal-to-noise ratio is considerably increased with the reflective tape, and is a real added value to the signal. We decide to always record the signal with a small piece of reflective tape at the point of acquisition.

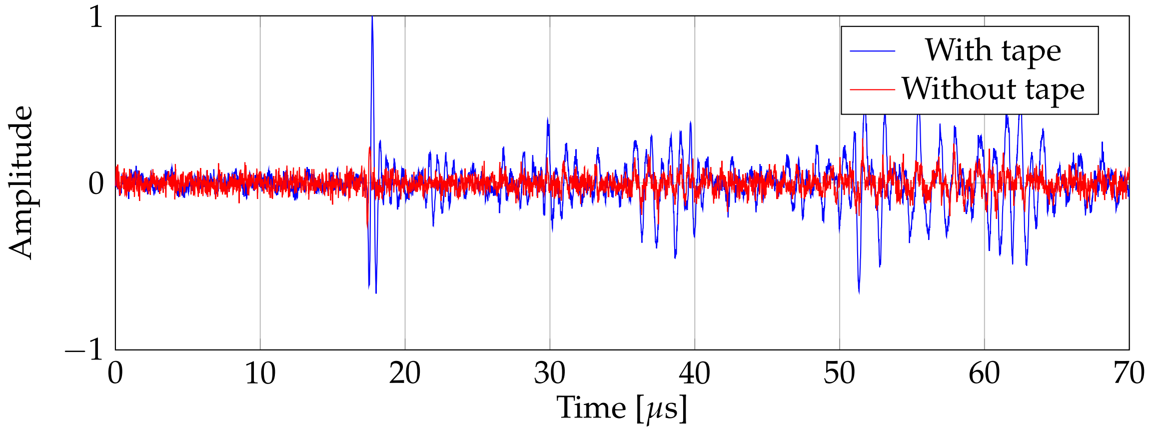

Figure IV.2: Comparison of a recording through a 7 cm x 7 cm x 7 cm aluminum cube with and without reflective tape at the measurement point. Zoom on the first arrivals and amplitudes normalized on the signal with tape.

The number of stack is the number of traces generated, transmitted, recorded and averaged for one single acquisition point. As we can guess that the more stack the better, it can actually take a significant amount of time to record one single point. Indeed, in the case of low attenuating medium, we need to verify that the signal vanishes and there is no longer reflections in the sample before emitting a new wave in the sample. This means that for aluminum, we are going to generate one wave every 100 ms. If we wish to record a stack of 1000, one point will take 1 minute and 40 second to be recorded. For a stack of 3000, we are going to need at least 5 minutes per point, and so on... It is important to save recording time in order to make as much experiments as possible. We can see on Figure IV.3 the decrease of noise level as we increase the number of stack. Nevertheless, the noise seems to reach a constant level after a stack of 4000, and we do not see a huge interest of waiting for more than a stack of 4000 to enhance the signal-to-noise ratio for our further recordings. This is the stack number we choose for the further experiments.

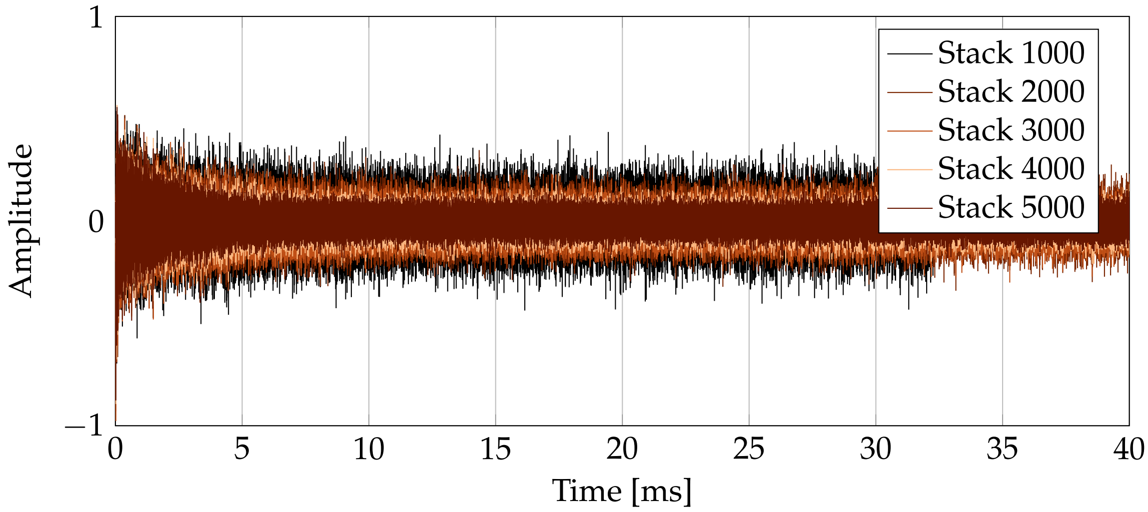

Figure IV.3: Comparison between recordings of different stack numbers.

2 Presentation of the measured media

In order to have a broad characterization of geophysical rock properties in terms of elastic modulus and attenuation values, experimental measurements were made in different rock formations: sedimentary, magmatic and metamorphic. We also make measurements in aluminum, because it is a homogeneous and isotropic medium. In this section we present the measured samples and we characterize the elastic properties of these rocks. In the next Section 3, we use the elastic properties of the rocks combined with attenuation measurements to calculate the viscosity (in the context of viscoelasticity) of the media.

2.1 Measured media

Pictures of the measured samples can be seen in Table IV.4. We make a short description of the different media below.

Aluminum: we measure two samples of aluminum 5083C of two different shapes, a cube of 7 cm x 7 cm x 7 cm, and a rectangular cuboid block of 7 cm x 10 cm x 12 cm. It is an alloy composed of a majority of aluminum with 4.5% of magnesium, 0.7% of manganese and other trace elements. The technical sheet can be found at `https://www.deville-rectif.com/pdf/5083C_AlMg4.5Mn0.7_FR.pdf`.

Fontainebleau sandstone is an eolian sandstone from Oligocene cemented by silica precipitation due to groundwater flowing [Thiry and Marechal, 2001]. This sample of Fontainebleau sandstone is well-cemented and composed of nearly 100% of quartz, and was used by [Pimienta et al., 2015a] for their petrophysical studies. (9 cm high and 5 cm diameter cylinder.)

Carrara marble is of importance in rock physics community because of its randomly oriented calcite grains composition [Delle Piane et al., 2015] making it isotropic. It is

Table IV.4: Pictures of the measured samples.

<table>
<tr><th colspan="2">Non rock samples</th></tr>
<tr><td>Aluminum cube
(7 cm x 7 cm x 7 cm)</td><td>Aluminum block
(7 cm x 10 cm x 12 cm)</td></tr>
<tr><td>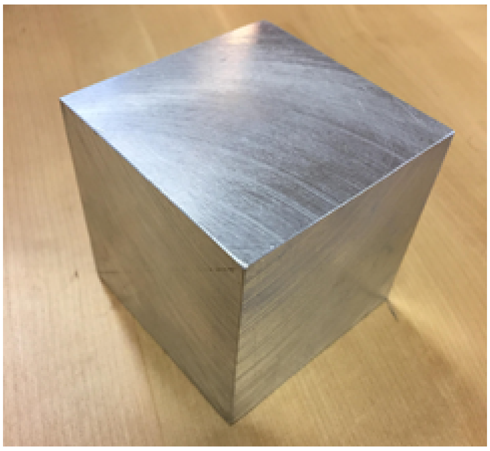</td><td>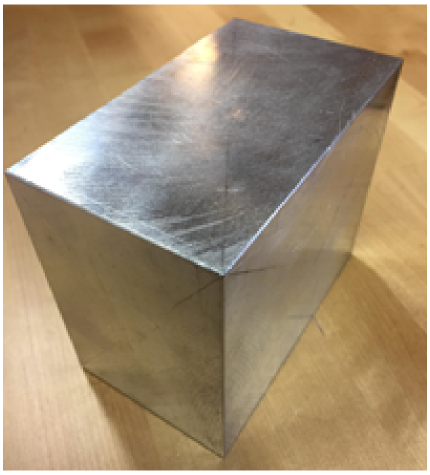</td></tr>
<tr><th colspan="2">Rock samples (dry)</th></tr>
<tr><td>Fontainebleau sandstone
(h = 9 cm ; Ø= 5 cm)</td><td>Carrara marble
(h = 11 cm ; Ø= 5.3 cm)</td></tr>
<tr><td></td><td></td></tr>
<tr><td>Diorite not heated
(h = 11 cm ; Ø= 5.4 cm)</td><td>Diorite 600°C
(h = 11 cm ; Ø= 5.5 cm)</td></tr>
<tr><td>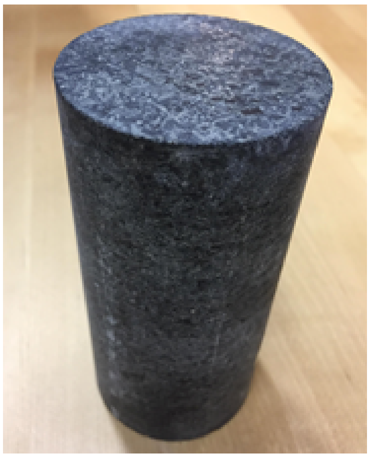</td><td></td></tr>
</table>

mainly used as an artwork material - for instance Michelangelo's artworks - because of its calcite purity and good quality [Coli and Criscuolo, 2021]. The protolith was a limestone rock formed during Trias / Lias and was metamorphosed into marble between Oligocene and Miocene [Molli et al., 2000]. (11 cm high and 5.3 cm diameter cylinder.)

Diorite is a magmatic rock. We do not know the provenance of the samples of diorites. One sample has been heated at 600°C in order to create microcracks inside the sample inducing attenuation [Pimienta et al., 2019], the other sample is the "reference" sample and has not been heated. (Not heated: 11 cm high and 5.4 cm diameter cylinder; 600°C: 11 cm high and 5.5 cm diameter cylinder.)

2.2 Waves propagation analysis

Here, in a first part, we aim to analyze deeply the wavefield in experimental conditions in aluminum cube, chosen to be isotropic and homogeneous. By doing so, we are able to point out and understand the wave propagation, reflection and conversion process into the sample. In a second part, we characterize the elastic properties of the media with the first wave arrivals.

2.2.1 First arrivals on aluminum cube

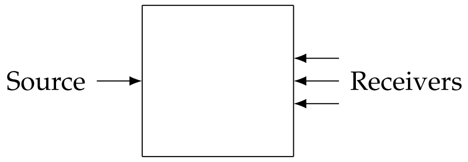

Figure IV.4: Illustration of the experimental set-up for the waves' measurement in transmission throughout the 7x7x7 cm aluminum cube. The source is a piezoelectric transmitter, and the data is recorded via an interferometer laser (receivers).

The following measurements in the aluminum cube are made in transmission (Figure IV.4) on a horizontal receivers line facing the source. The sample corresponds to the numerical simulations (Chapter III) in terms of wave propagation velocities $V_P = 6320\,\mathrm{m\,s^{-1}}$, $V_S = 3100\,\mathrm{m\,s^{-1}}$ and density $\rho = 2650\,\mathrm{kg\,m^{-3}}$. The source is a piezoelectric transmitter 5 MHz Videoscan V1091 located at the center of one facet. We chose this PZT for its size. Indeed, we are going to make measurements along a line facing the source. The direct waves arrivals can be detected by their hyperbolic shape on the seismogram, on which we are able to make interpretation in terms of body and surface waves velocities as in Figure III.21. For this matter, we need a source contact surface as small as possible [Shen et al., 2022].

We choose to make an analysis of first wave arrivals on aluminum in order to have solid tools for the physical characterization of the other media. Indeed, with aluminum we expect to have an isotropic wave propagation in a perfectly homogeneous sample. It means that we will be able to follow smoothly the different waves propagating, reflecting and converting into the sample, and to localize these events.

The first wave arrivals along the line of receivers can be seen in Figure IV.5 where we can clearly identify the first wave fronts as they come to the surface. The marked wave trains (as in Shen [2020]) are P-wave, S-wave, Rayleigh (surface) wave, PP-wave

(P-wave reflected as a second P-wave) and PS-wave (P-wave converted as a S-wave). We note that the first recorded Rayleigh wave comes from the P-wave who met a diffraction corner of the cube before being converted into high-amplitude Rayleigh and S-wave.

We can compare this measured seismogram (Figure IV.5) with the calculated seismogram (Figure III.21, receivers 1051 to 1751) of numerical simulations with conditions similar to the experimental measurement. Although the wavelength is larger in the numerical simulation (2.5 cm for P-wave at 250 kHz compared to 6.3 mm at 1 MHz of actual peak frequency in laboratory measurements), we are still able to follow the first waves arrival and compare them with the experimental data. The experimental and numerical seismograms are very similar in terms of first waves arrival time and it proves that we can actually rely on numerical simulations to investigate methods used in experimental measurements.

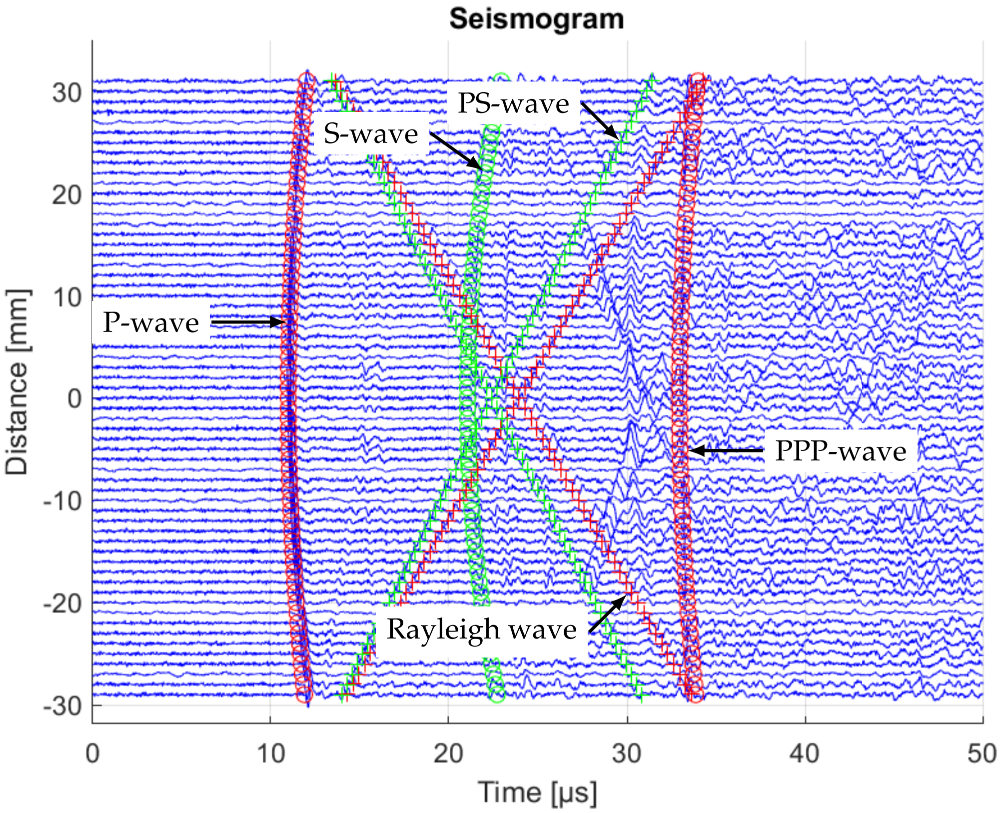

Figure IV.5: Recording in 7 cm x 7 cm x 7 cm aluminum cube in transmission along a line facing the source (PZT V1091 - 5 MHz), and highlight of some first wave arrivals. The y- axis represents the distance to the center of the face. The set-up corresponds to the Figure IV.4.

2.2.2 Measured elastic properties of the samples

The characterization of elastic properties is made with the recovery of P- and S- waves velocities V_P and V_S in the first arrivals of the recorded seismic signal. For this matter, we choose to work with the source PZT V102 - 1 MHz peak frequency because of its good signal-to-noise ratio combined with a relatively short wavelength (Table IV.3).

The measurements are made in transmission, the receiver being on the opposite face from the source. That means that the wave propagation in the cylinders is done in the length, the source and the receivers located at the center of the disks. Concerning the aluminum block, the source and receivers are located at the center of the 7 cm x 10 cm facets, meaning that the direct waves propagates on 12 cm length.

The first waves arrivals in transmission for the measured media are displayed in Figure IV.6. The P-wave direct arrival is clear and allow us an accurate determination of P-wave velocity value. Concerning the determination of S-wave velocity value, we see in Figure IV.5 that many waves arrive at the same time of the direct S-wave in transmission (measured at the center of the face). Thus, after the direct P-wave, we do not know if the second wave is the actual S-wave, or the converted Rayleigh wave generated from the P-wave at a corner, or again a reflection. For this reason, and to not take any risk of misinterpretation, the S-wave velocity of the different media will be taken from literature.

The Diorite 600°C makes an interesting seismic trace (Figure IV.6e). The first information to get is the noise level, way higher than in the other media. Then, if we look at the first arrival at 50 µs, we notice that the wavelength is wide and the first break is not as steep as the other media. These observations can lead to a first interpretation concerning the frequency-dependent attenuation. We can indeed infer that the attenuation is high, and that the high frequency content has been completely filtered by the medium, only remains the low frequency content. Thus, we can imagine an increasing attenuation as a function of frequency. We will analyze deeper the frequency-dependent attenuation in the next Section 3.

Rock samples were lent by Lucas Pimienta. It is therefore natural for us to look for S-waves velocities in his scientific articles, whose measured velocities at ultrasonic frequencies are concatenated in Table IV.5, in which we added our V_P measurements for comparison. Our V_P measurements are close to the ones made in the literature, besides for the diorite not heated that show a difference of 500 m s^{-1} that might be because the diorite sample we measured is not from the same core as Pimienta et al. [2019].

Table IV.5: Wave propagation velocities V_P and V_S of our rock samples found in the literature. "ss" stands for "sandstone". V_P* are the recovered velocities from the first wave's arrival (Figure IV.6). For comparison, we measured V_P = 6320 m s^{-1} and V_S = 3100 m s^{-1} in aluminum.

Sample	Reference article	V_P [m s^{-1}]	V_S [m s^{-1}]	V_P* [m s^{-1}]
Fontainebleau ss	Pimienta et al. [2018]	5300	3400	5415
Diorite not heated	Pimienta et al. [2019]	6280	3460	6760
Diorite 600°C	Pimienta et al. [2019]	2510	1380	2420
Carrara marble	Pimienta et al. [2018]	6200	3300	6190

Finally, we calculate the elastic Lamé parameters λ and μ from the equations (II.22) and (II.23) with V_P from our measurements, V_S from the literature in Table IV.5, and with the density ρ measured by weighting the samples and knowing their dimensions. The density ρ and Lamé parameters λ and μ are displayed in Table IV.6.

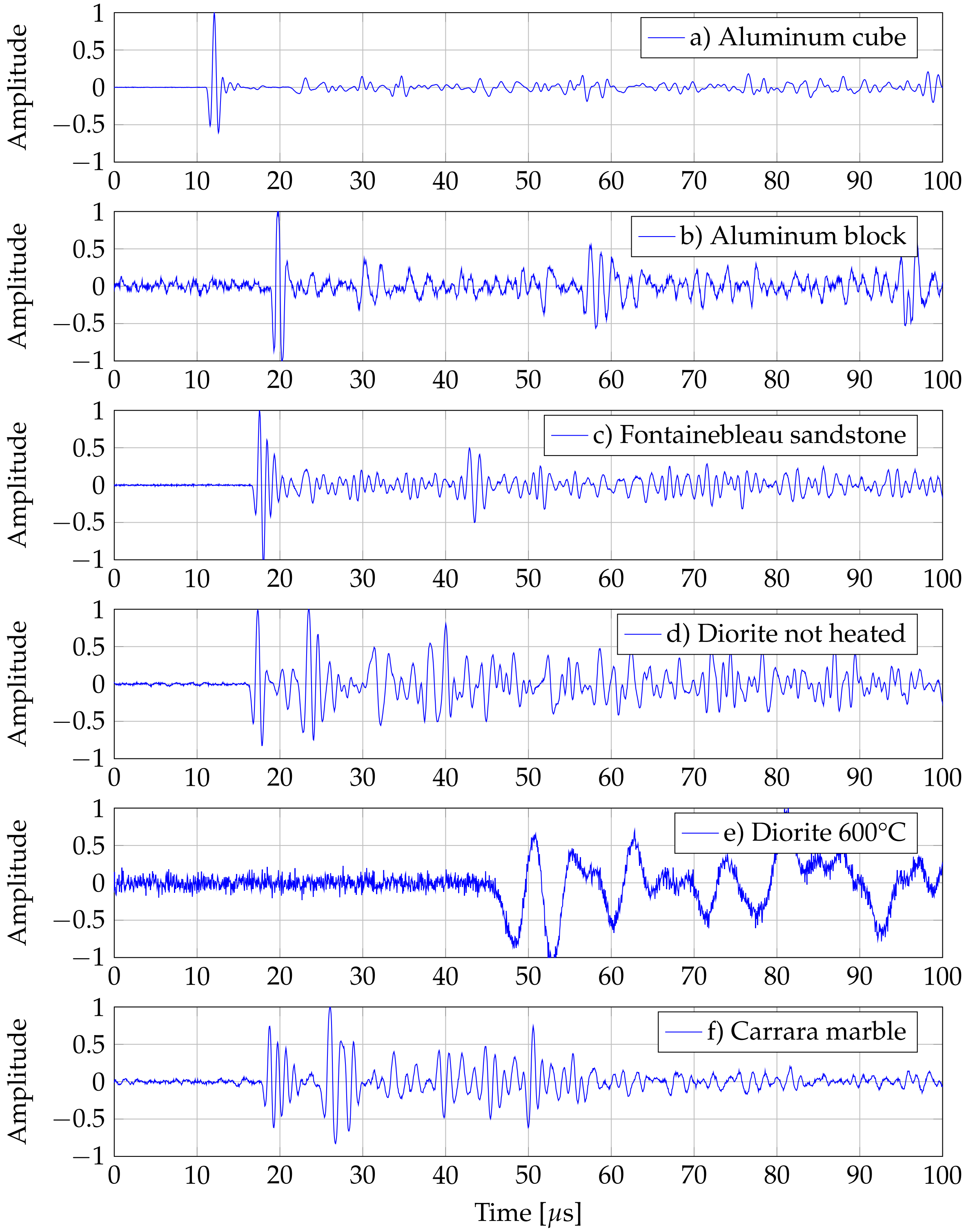

Figure IV.6: Seismic traces of first arrivals in measured samples in transmission with source PZT V102 - 1 MHz. The time delay is already corrected in these figures.

Table IV.6: Density ρ and Lamé parameters λ and μ of the measured media.

Medium	Density ρ [kg m^{-3}]	λ [GPa]	μ [GPa]
Aluminum	2650	54.94	25.47
Fontainebleau sandstone	2500	15.51	28.90
Diorite not heated	2985	64.94	35.74
Diorite 600°C	2862	5.86	5.45
Carrara marble	2700	44.65	29.40

3 Attenuation measurements on low attenuation media

In this section we use the method developed thanks to numerical simulations in Chapter III (Figure III.22) to recover the attenuation of actual samples. For this matter, we saw that we need (1) to ensure that we work with free-surface boundary conditions, (2) to record sufficient propagation time in order to reach an equilibrium of energy in the sample stating that the wavefield is governed by the S-waves, (3) to recover the frequency-dependent S-waves attenuation and (4) find the closest viscoelastic model that fits the attenuation recovery.

3.1 Examination of the samples

First of all, we need to calculate the time where the signal reaches the state of equipartition for every sample with Equation (III.13). That means the recorded signal has to reach and go beyond this value so we can recover the attenuation of the envelope where the wave's energy is at a state of equilibrium.

Table IV.7: Maximum equipartition time τ_{PS} for the measured samples.

Sample	τ_{PS}
Aluminum cube	100 µs
Aluminum block	170 µs
Fontainebleau sandstone	75 µs
Diorite not heated	130 µs
Diorite 600°C	267 µs
Carrara marble	110 µs

The next step is to examine the signal propagated in each sample with different sources (Figures IV.7 to IV.12). This analysis will allow us to select the samples with either sufficient wave propagation time to be able to reach equipartition state, and a good signal-to-noise ratio with respect to frequency bandwidth. Also, while it is useful to confront two attenuation measurements for two different sources at the same frequency, we have to keep in mind that a too high noise level can disturb the attenuation recovery (remember Chapter III Subsection 3.3) and it is important to be able to discard problematical recordings.

For instance, if we look at Figure IV.7 showing the wave propagation in the aluminum cube with six different piezoelectric sources, we can notice that the signal-to-noise ratio is relatively strong for the low-frequency bandwidth sources (from 100 kHz to 1 MHz), and the signal-to-noise ratio is relatively weak for the high-frequency bandwidth sources (2.25 MHz and 5 MHz). Moreover, if we look more precisely at the amplitude spectrum of the signal generated with the 5 MHz source, we notice that there is no signal for the frequencies higher than 1 MHz (or we cannot separate the signal from the noise). Thus, we can question the usefulness of this recording compared to the 2.25 MHz source offering a broader bandwidth. The same analysis can be done for the aluminum block (Figure IV.8), the Fontainebleau sandstone cylinder (Figure IV.9) and the diorite cylinder not heated (Figure IV.10).

Diorite cylinder heated at 600°C (Figure IV.11) shows interesting signals compared to the diorite not heated (Figure IV.10). First of all, as the heat induces microcracks in the sample, we expect a more attenuated wave in the diorite heated at 600°C. It is indeed what we observe when we compare the signal for the 250 kHz source. For the not heated diorite, the signal vanishes at about 3 ms; for the diorite heated at 600°C, we have signal only until 1 ms, while the signal-to-noise ratio is equivalent. Also, concerning the diorite not heated (Figure IV.10), we still notice a decreasing envelope of amplitudes until 1 ms with the sources of 1 MHz, 2.25 MHz and 5 MHz. With the diorite 600°C (Figure IV.11), as we still guess a decrease of amplitudes with the source of 1 MHz, no signal seems to be usable with the source of 2.25 MHz. Moreover, the amplitude spectra of the signals generated by the sources 500 kHz to 2.25 MHz in the Diorite 600°C seems unusable for our attenuation measurements: we need to have a strong signal in frequency as we are going to select small bandwidths for attenuation recovery (Figure III.22). These two last analyses are the reasons why we did not make recordings with the source of 5 MHz of central frequency that would have been unusable.

Equipartition time of 110 µs is not reached in the Carrarra marble for the sources of 500 kHz and 1 MHz (Figure IV.12). For that, we are not able to recover the attenuation using this data. We did not use the PZT 100 kHz because the contact diameter of the source is larger than the diameter of the sample. Concerning the source of 250 kHz, it seems that there is workable signal until 300 µs to recover the attenuation. This hypothesis has to be confirmed in a next Subsection 3.3 when we will select small bandwidth of frequencies in order to have frequency-dependent attenuation measurements.

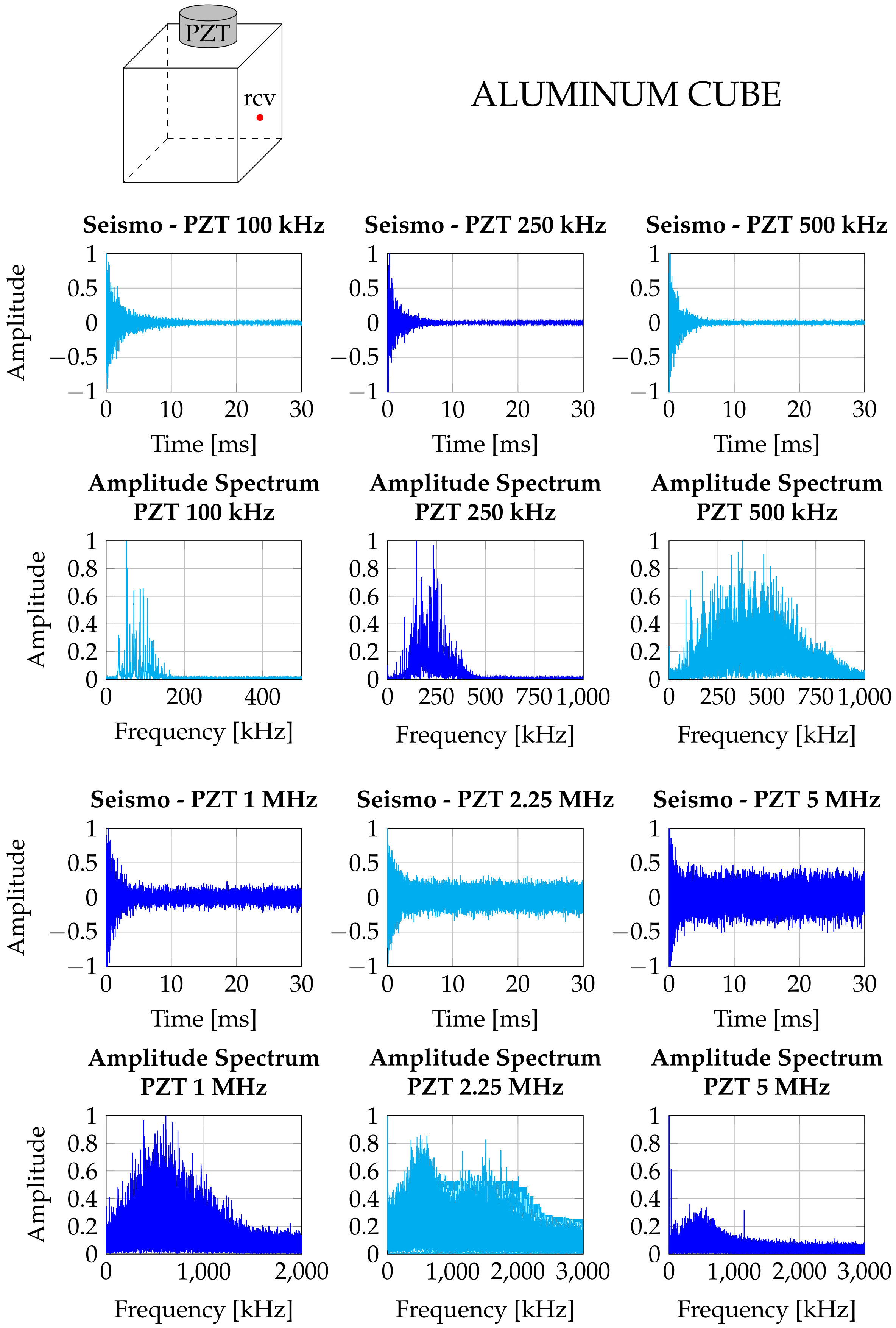

Figure IV.7: Source-receiver configuration and recordings (seismograms and amplitude spectrum) in aluminum cube with several sources of different central frequencies.

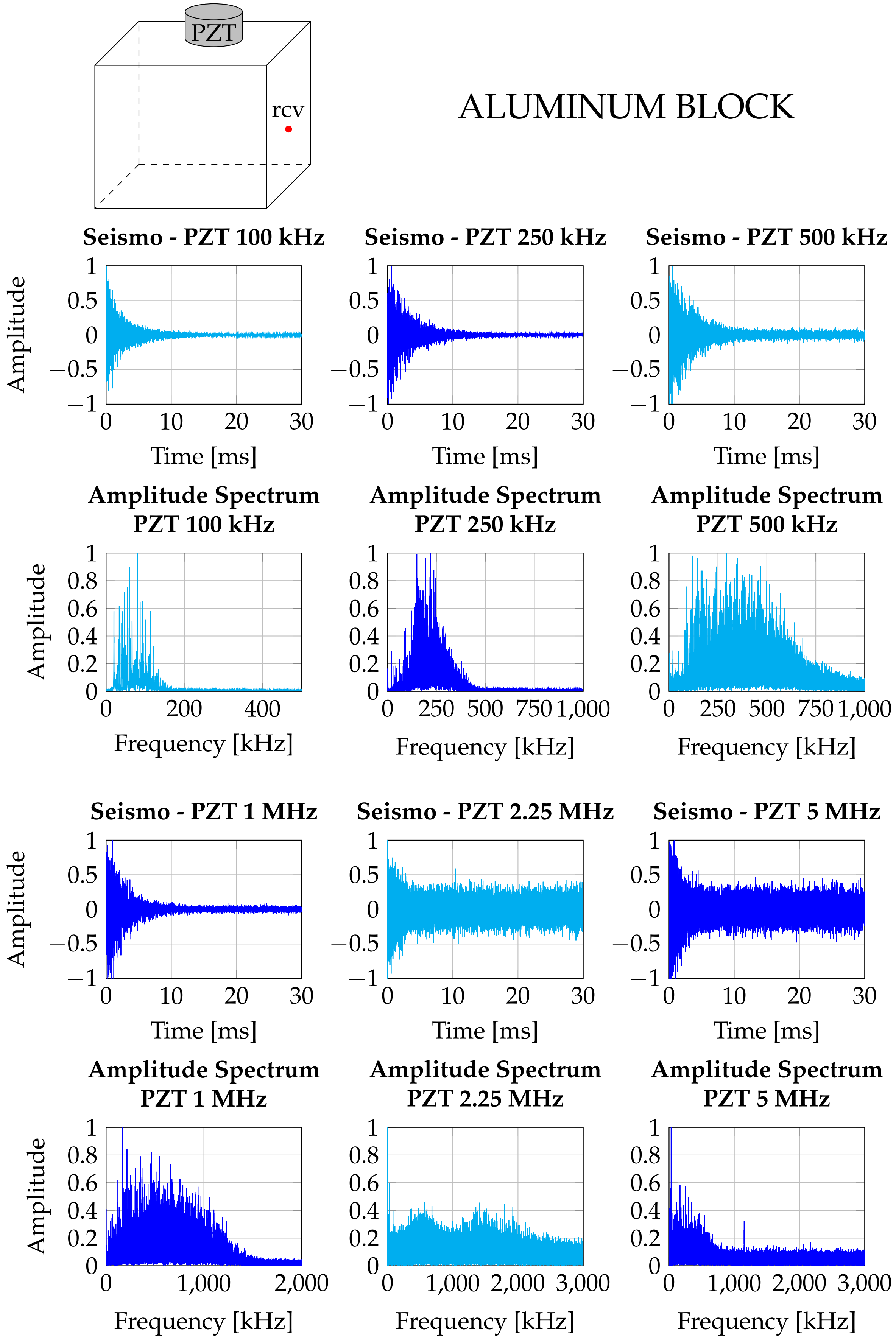

Figure IV.8: Source-receiver configuration and recordings (seismograms and amplitude spectrum) in aluminum parrallelepipedic block with several sources of different central frequencies.

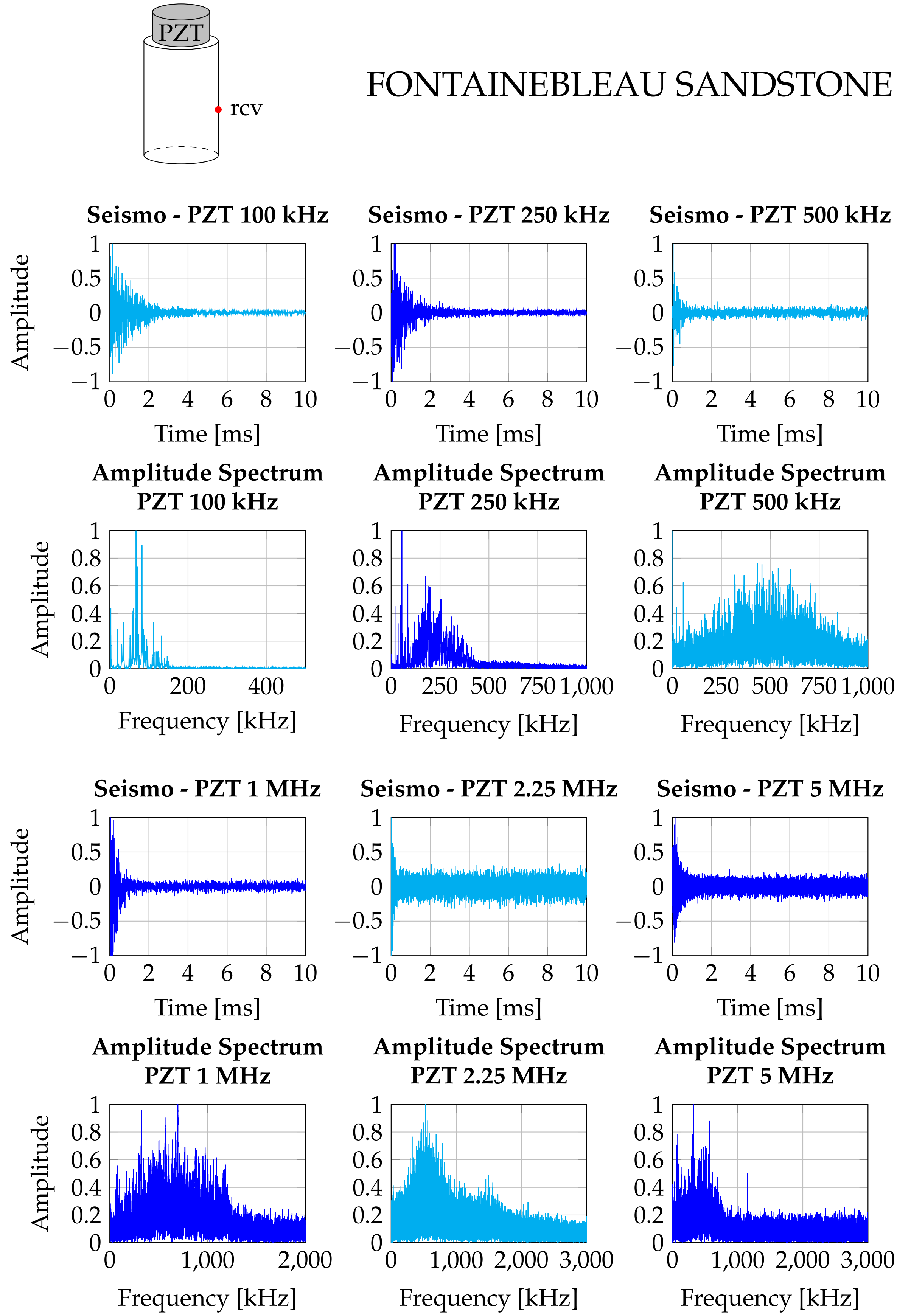

Figure IV.9: Source-receiver configuration and recordings (seismograms and amplitude spectrum) in Fontainebleau sandstone cylinder with several sources of different central frequencies.

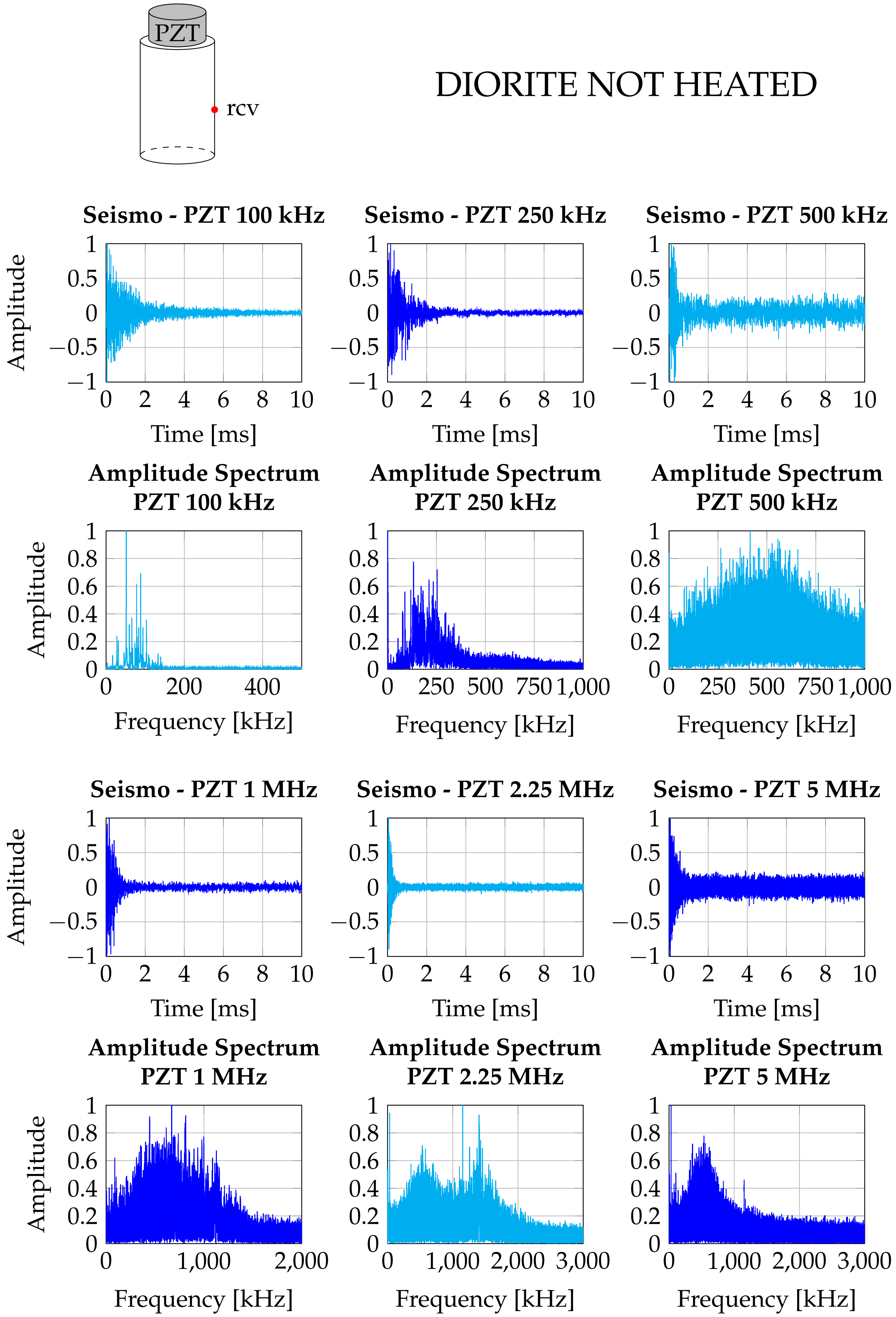

Figure IV.10: Source-receiver configuration and recordings (seismograms and amplitude spectrum) in diorite cylinder not heated, with several sources of different central frequencies.

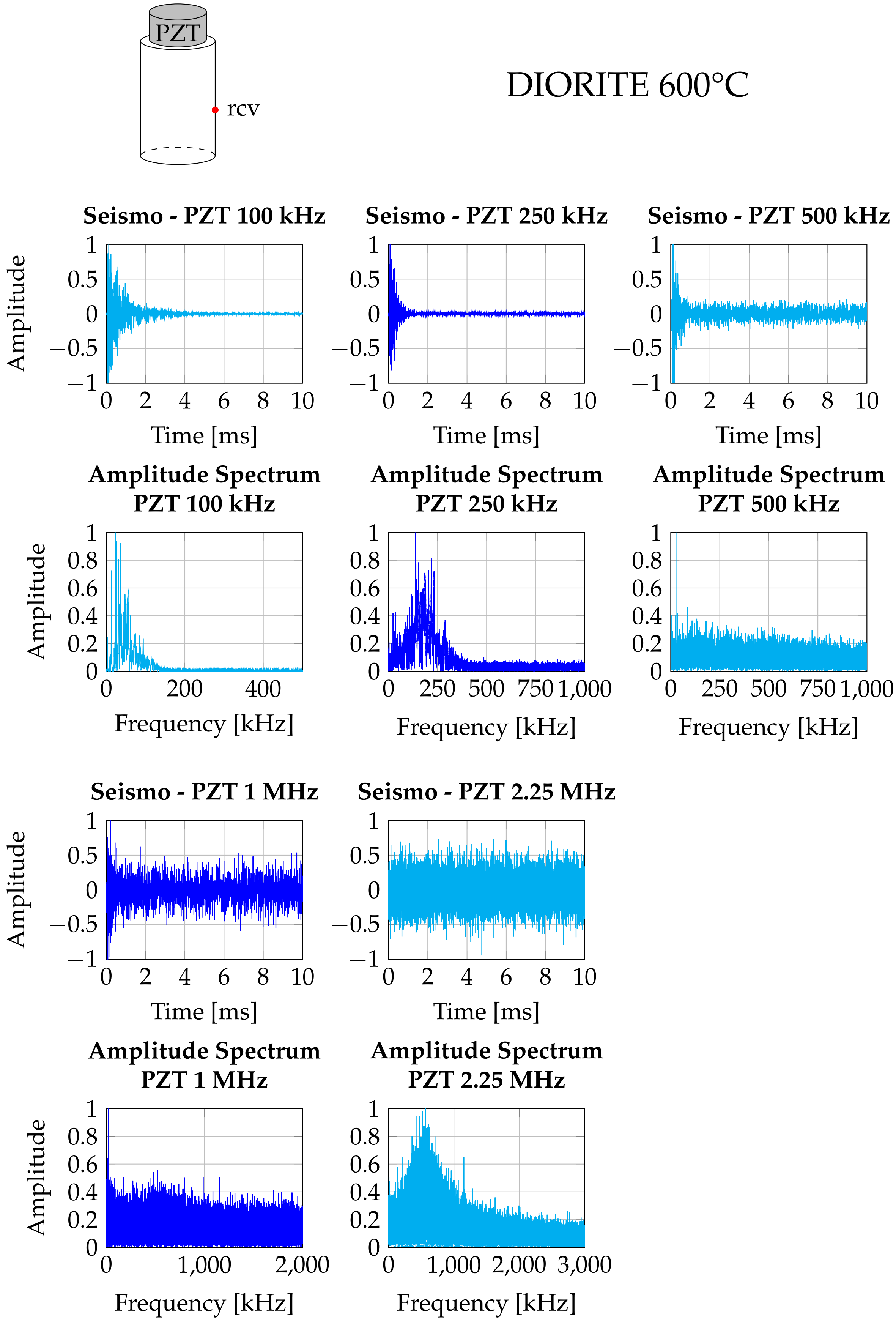

Figure IV.11: Source-receiver configuration and recordings (seismograms and amplitude spectrum) in diorite cylinder heated at 600°C, with several sources of different central frequencies.

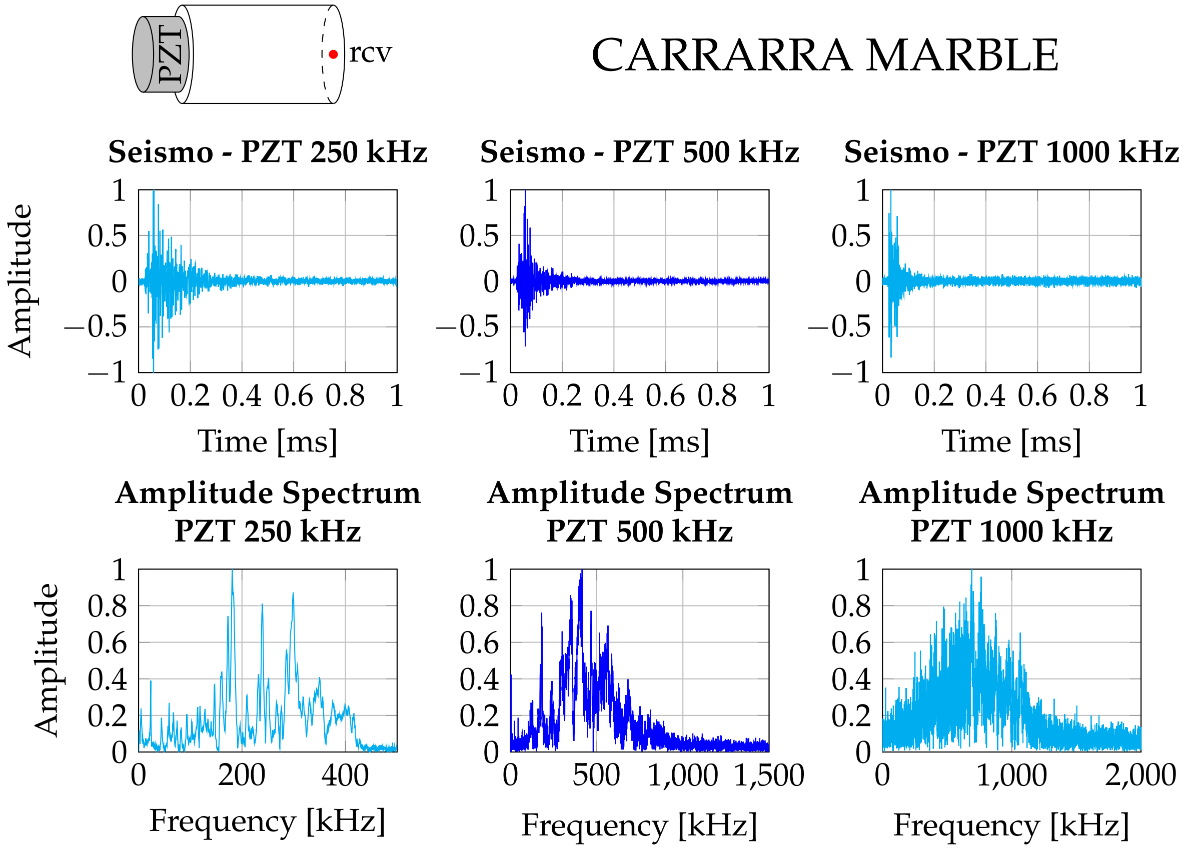

Figure IV.12: Source-receiver configuration and recordings (seismograms and amplitude spectrum) in Carrarra marble cylinder with several sources of different central frequencies.

3.2 Aluminum: a case study on acquisition biases

We saw with the numerical approach study that attenuation parameters of a sample is correctly recovered with free-surface boundary conditions. However, in actual experimental conditions, the source is in contact with the sample, changing the boundary conditions at this location. In this part we analyze the effect of the contact surface source-sample in order to be aware of potential biases while interpreting the results.

3.2.1 Presentation of the experiment

Table IV.8: Pictures of the two measured aluminum samples, a 7 cm x 7 cm x 7 cm cube and a 7 cm x 10 cm x 12 cm block with two PZT sources of 1 MHz central frequency, the V152 (2.54 cm of diameter) referred as "2 inches PZT" and the V153 (1.275 cm of diameter) referred as "1 inch PZT".

<table>
<tr><th colspan="2">ALUMINUM CUBE</th></tr>
<tr><td>2 inches PZT
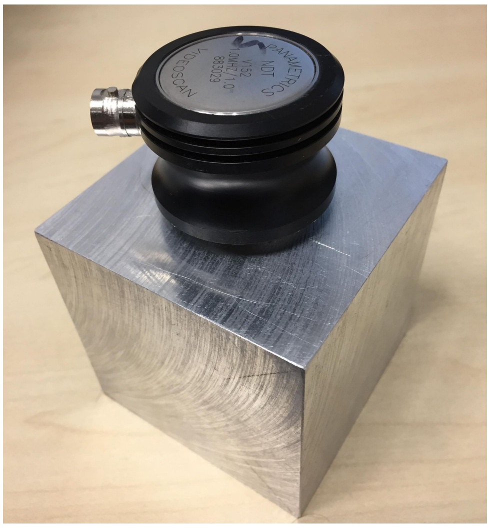</td><td>1 inch PZT
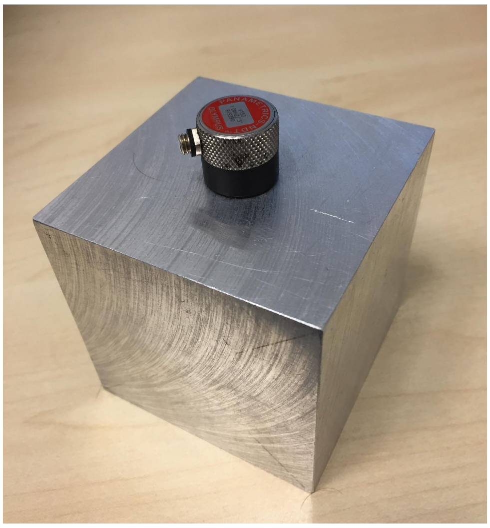</td></tr>
<tr><th colspan="2">ALUMINUM BLOCK</th></tr>
<tr><td>2 inches PZT
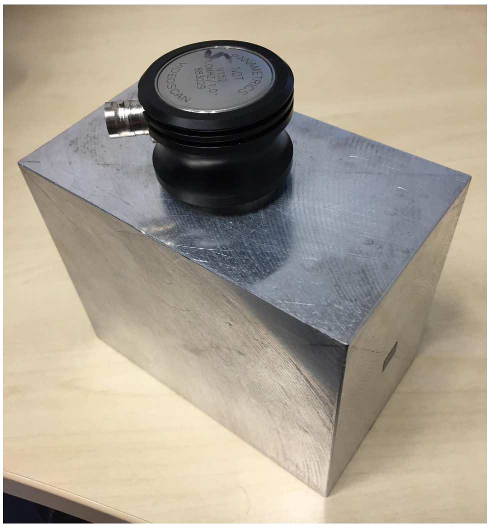</td><td>1 inch PZT
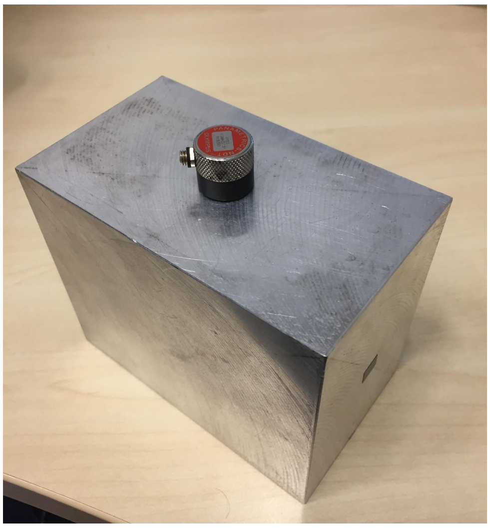</td></tr>
</table>

We use in this experiment the same aluminum 5083C for two samples of different size and geometries: a 7 cm x 7 cm x 7 cm cube and a 7 cm x 10 cm x 12 cm rectangular cuboid block. In terms of seismic source, we use two PZT of 1 MHz central frequency and two different contact diameter: V152 - 1 MHz - 2.54 cm of diameter (referred as "2 inches PZT") and V153 - 1 MHz - 1.275 cm of diameter (referred as "1 inch PZT"). Pictures of samples and used PZT can be found in Table IV.8. We only use the 1 inch PZT in this part, to make a qualitative study on the impact of the PZT size.

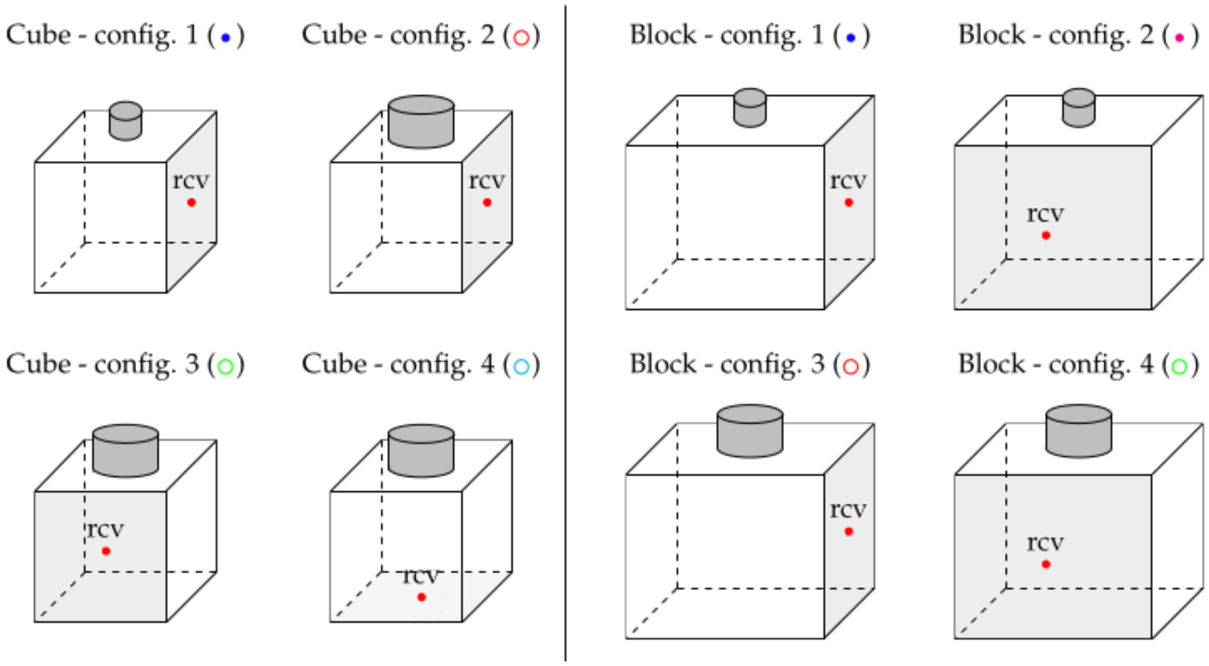

Figure IV.13: Shemes of the configurations made for attenuation recovery in aluminum cube (left) and block (right). "config." stands for "configuration". Cube - config. 1: 1 inch PZT source and signal recorded on the lateral face 1. Cube - config. 2: 2 inches PZT source and signal recorded on the lateral face 1. Cube - config. 3: 2 inches PZT source and signal recorded on the lateral face 2. Cube - config. 4: 2 inches PZT source and signal recorded on the opposite face. Block - config. 1: 1 inch PZT source and signal recorded on the lateral face 1 (7 cm x 10 cm). Block - config. 2: 1 inch PZT source and signal recorded on the lateral face 2 (10 cm x 12 cm). Block - config. 3: 2 inches PZT source and signal recorded on the lateral face 1. Block - config. 4: 2 inches PZT source and signal recorded on the lateral face 2. Symbols under the brackets () links to the results in Figure IV.16.

A total of four records are made for each sample (Figure IV.13). For each record, we used the method described in Figure III.22 to recover the frequency-dependent attenuation. We used a window of ± 30 kHz around the frequency of interest to display a decrease in amplitude of the envelope as a function of time (Figures IV.14 and IV.15).

We need to know when the signal reaches the noise level in the seismograms in order to automatize the process of attenuation recovery for each frequency of interest, from 200 kHz to 1200 kHz. For that, we display the amplitude envelope of the signal for some frequencies of interest covering a large bandwidth. If we look at the signal recorded through the cube with the 1 inch PZT (Figure IV.14), we see that the noise level is reached at about 6 ms for the 200 kHz frequency of interest, and is reached later at about 15 ms for the 1000 kHz frequency of interest, while the signal-to-noise ratio varies across the frequencies. In that case we choose to use the first 5 ms of the decreasing signal for attenuation recovery in the cube with the 1 inch PZT (Cube - config. 1 of Figure IV.13). The signal with the 2 inches PZT (Cube - config. 2 of Figure IV.13) shows a different behavior (Figure IV.15). The noise level is reached at a maximum of 5 ms regardless of the displayed frequency of interest, and the signal-to-noise ratio is weaker than with the 1 inch PZT. We choose to use the first 3 ms in this configuration to recover the frequency-dependent attenuation.

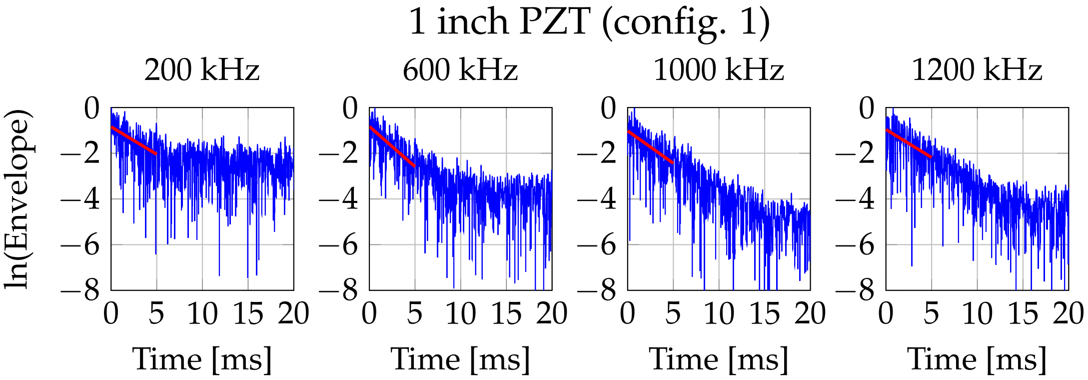

Figure IV.14: Envelopes of amplitudes for several frequencies of interest of the signal recorded through the cube on the lateral face 1 (Cube - config. 1 of Figure IV.13) the wave being generated with the 1 inch PZT. [——] envelope of amplitudes for a given central frequency ± 30 kHz; [——] attenuation recovery β in Np s^{-1} for this central frequency.

The envelopes of signal in the two other configurations in the cube (Cube - config. 3 and 4 of Figure IV.13) displays similar behavior than the ones in Figure IV.15. We decide not to show them in figures - as well as the envelopes of signals through the block - for the sake of conciseness. Nevertheless, we made the same analysis for each configuration to choose the best time for attenuation recovery.

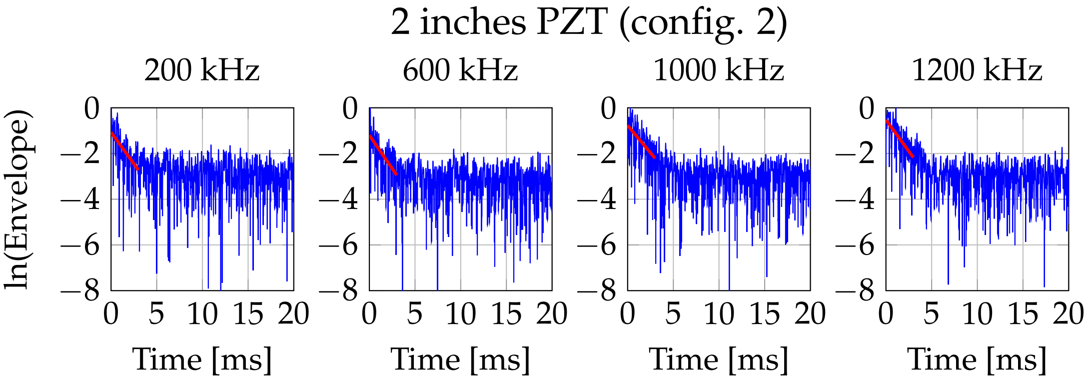

Figure IV.15: Envelopes of amplitudes for several frequencies of interest of the signal recorded through the cube on the lateral face 1 (Cube - config. 2 of Figure IV.13) the wave being generated with the 2 inches PZT. [——] envelope of amplitudes for a given central frequency ± 30 kHz; [——] attenuation recovery β in Np s^{-1} for this central frequency.

3.2.2 Results

The frequency-dependent attenuation recovery for each configuration of Figure IV.13 between 200 kHz and 1200 kHz can be found in Figure IV.16. At this stage, we do not interpret quantitatively the attenuation in terms of rheological model and viscosity, but we rather offer a qualitative analysis on the size of the PZT source with respect to the size of the sample.

Globally, we notice that the different attenuation results overlap when they are made with the same PZT (cube - config. 2 with the 2 inches PZT = cube - config. 3 with the 2 inches PZT and so on...), that confirms about the reproducibility of the results for

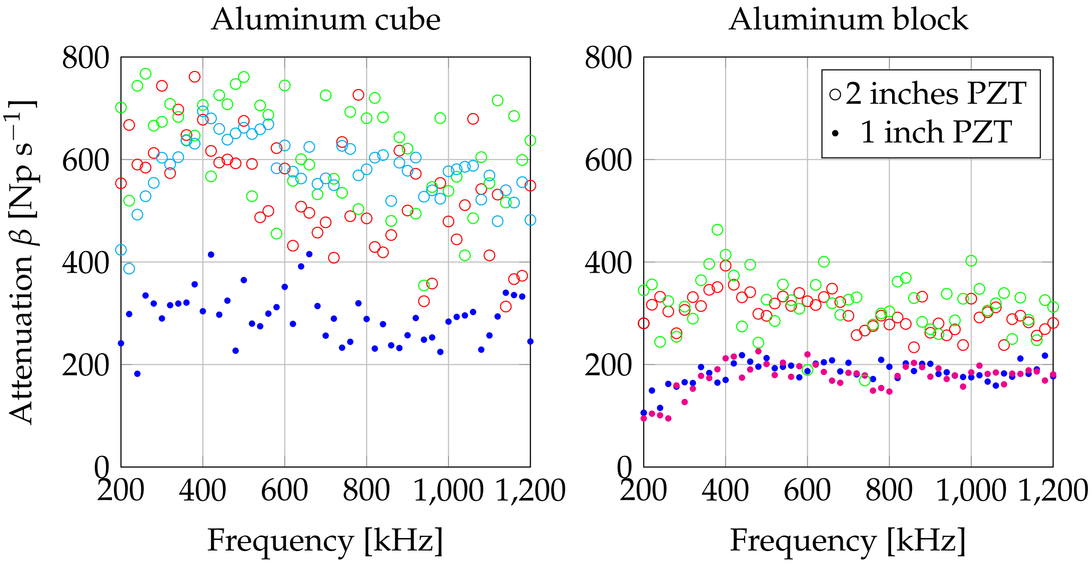

Figure IV.16: Recovered frequency-dependent attenuation in aluminum 7 cm x 7 cm x 7 cm cube (left) and 7 cm x 10 cm x 12 cm block (right) with two different sizes of PZT source. The symbols refer to the configurations shown in Figure IV.13.

one sample's size with one PZT size. In addition, we see that the attenuation recovered in the cube seems higher than the attenuation recovered in the aluminum although it is the exact same medium. In addition to that, the attenuation recovered with the 2 inches PZT seems higher than the attenuation recovered with the 1 inch PZT.

At first, one could believe that the results are different between the 2 inches PZT and the 1 inch PZT because of the difference of signal-to-noise ratio, we saw in Chapter III Subsection 3.3 that a higher noise level leads to a lower recovered attenuation value. In our case, the 2 inches PZT displays a high noise level as well as a high attenuation value. Thus, we can discard the impact of the noise in the explanation of the difference of recovered attenuation values. It can be due to the surface of contact between the PZT and the sample that might change the boundary conditions at this location: the larger the surface of the source in relation to the surface of the sample, the greater is its impact on apparent attenuation. Also, we assume that the contact of the sample with the table has a negligible effect on the boundary conditions: because there is no coupling gel between the sample and the table, the rugosity at small scale and the air layer leads to a few contact between the table and the sample. These suggestions would need to be verified numerically in the future to investigate further the discrepancies.

3.3 Attenuation recovery on rock samples

In this part we aim to recover the frequency-dependent S-waves attenuation in aluminum and rock samples covering a large bandwidth of frequencies following the method given in Figure III.22. Since we saw in the previous subsection that the contact of the PZT source on the sample may induce a bias, we choose to work with PZT sources of similar diameters. For this matter, we use the PZTs V150 - 250 kHz, V151 - 500 kHz, V102 - 1 MHz and A197S - 2.25 MHz (see Tables IV.2 and IV.3).

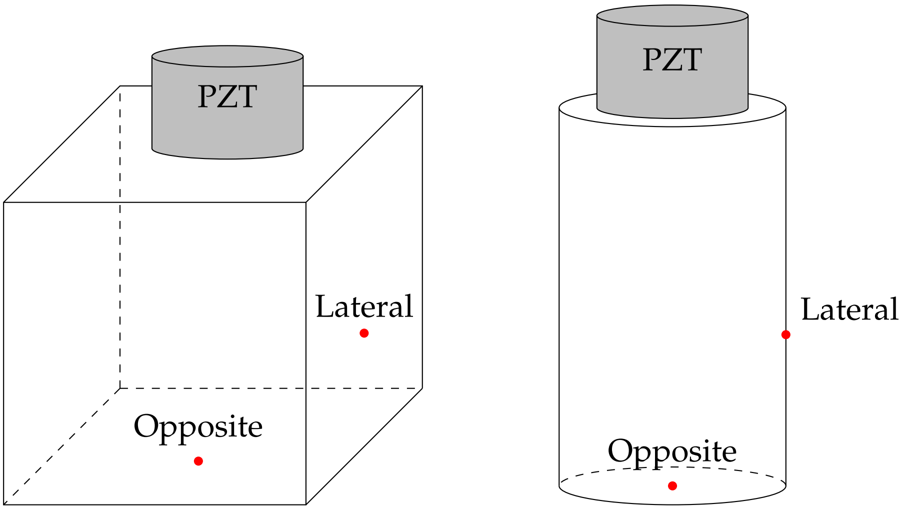

(a) **Aluminum cube** (b) **Rock cylinder**

Figure IV.17: Schematic representation (not at scale) of the experimental set-up with the location of the PZT source and the two recording points on the lateral and the opposite face with respect to the source. (a) Aluminum cube and (b) rock cylinder.

3.3.1 Configuration

Attenuation recovery is made on two distinct measurement points (on the lateral and the opposite face with respect to the PZT source as in Figure IV.17) in order to verify the reproducibility and robustness of the results. Indeed, as we saw on Chapter III Section 3, at a given frequency, we expect to recover the same attenuation value on different measurement points. A second way to verify our results is to use the frequency bandwidth of each PZT as large as possible in order to have an overlap in data between different sources.

For this matter, we use six different recordings to recover the attenuation in samples. Four recordings on the lateral face using the four PZT sources, and two recordings on the opposite face using the 250 kHz and the 1 MHz central frequency PZT sources for the aluminum cube, the Fontainebleau sandstone and the diorite not heated.

The high attenuation in high frequencies for the diorite 600°C and the Carrara marble only allow us to work with the 250 kHz PZT source for attenuation recovery.

3.3.2 Viscosity recovery on aluminum (Maxwell viscoelastic model)

We show in Figure IV.18 the results of attenuation quantification from the experiments performed in the aluminum cube. The attenuation β has a constant value around a mean of 530 $\mathrm{Np\,s^{-1}}$ throughout all the scanned frequencies, from 60 to 2000 kHz. the consequence (see (II.72)) is that the Q-factor linearly increases from 300 to 12000. In order to understand and interpret the increase in Q-factor vs. frequencies, we remind that the definition of the Q-factor is roughly the inverse of attenuation per wavelength or per cycle of a traveling seismic wave [Aki and Richards, 2002]. The consequence is that for the same decrease in amplitude of a seismic wave as a function of time (β) for various frequencies, the Q-factor will increase since the wavelength decreases with respect to frequency.

Following the results shown in Figure IV.18 (constant β and increasing Q-factor), we

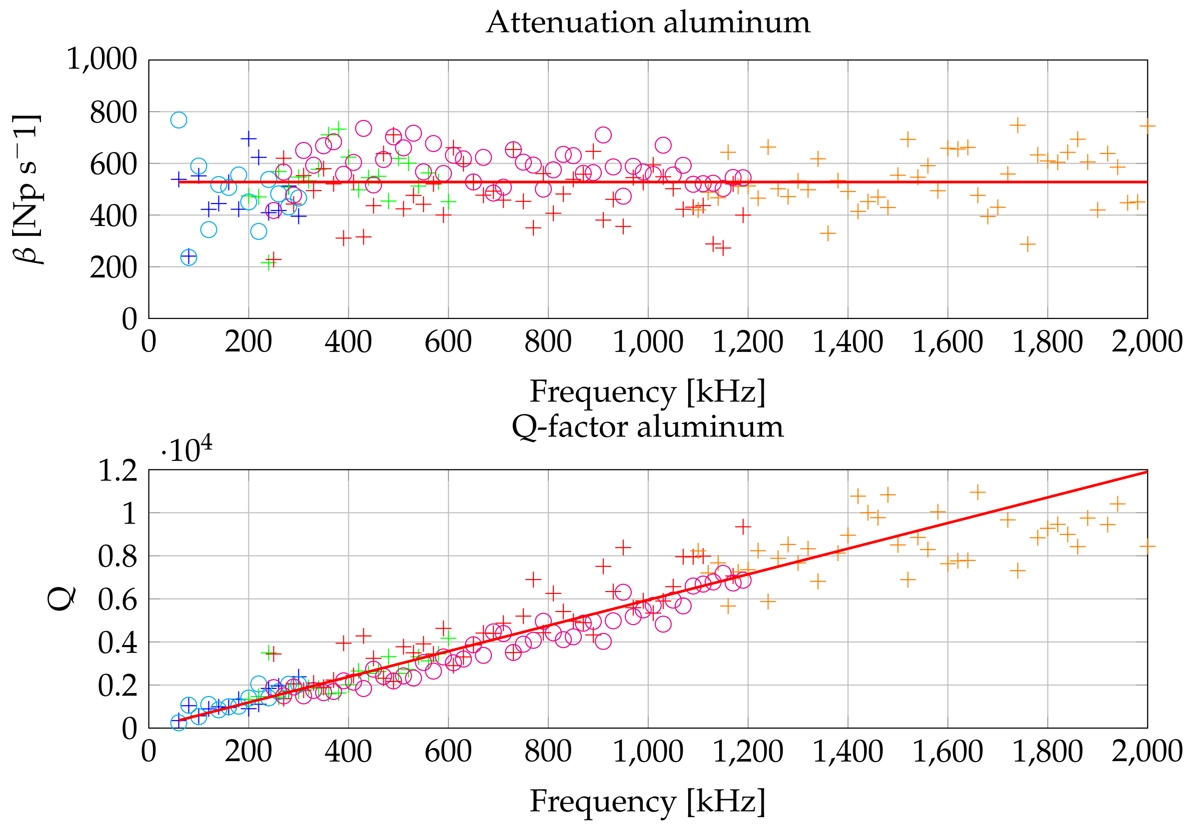

Figure IV.18: Attenuation β and Q-factor recovery on the aluminum cube from ultrasonic measurements: [+] on the lateral face for the 250 kHz PZT source, [+] on the lateral face for the 500 kHz PZT source, [+] on the lateral face for the 1 MHz PZT source, [+] on the lateral face for the 2.25 MHz PZT source, [○] on the opposite face for the 250 kHz PZT source, [○] on the opposite face for the 1 MHz PZT source. [——] corresponds to the best fit of a Maxwell model corresponding to parameters μ = 25.5 GPa and η_μ = 21.1 MPa s.

deduce that the attenuation law of the aluminum cube follows a Maxwell viscoelastic model. Using the constitutive law of the Maxwell model (II.54), we can express the complex-valued bulk modulus associated to the Maxwell attenuation model, μ_{Max}, in terms of the elastic parameter μ and the viscous parameter η_μ, such that,

$$\mu_{\text{Max}} = \frac{\mu\eta_\mu^2\omega^2 + \mathrm{i}\omega\mu^2\eta_\mu}{\eta_\mu^2\omega^2 + \mu^2}. \tag{IV.1}$$

The frequency-dependent Q-factor for the S-waves is given from equation (II.48) and writes as:

$$Q_{s_{\text{Max}}} = \frac{\mathrm{Re}\left(\mu_{\text{Max}}\right)}{\mathrm{Im}\left(\mu_{\text{Max}}\right)} = \omega\,\frac{\eta_\mu}{\mu}. \tag{IV.2}$$

Therefore, the S-wave quality factor for the Maxwell model increases linearly with frequency. Since the elastic parameter μ can be recovered from the S-waves velocity (equation (II.23)), the remaining unknown in equation (IV.2) is η_μ, which is calculated by computing the linear function fitting the measured value of Q as a function of frequency (Figure IV.18).

Deducing the elastic parameter μ = 25.5 GPa from Table IV.6, we compute the viscous parameter η_μ = 24.1 MPa s for aluminum 5083C within the frequency bandwidth 60 kHz to 2 MHz using (IV.2). However we have to keep in mind the impact of the contact of the PZT source with the sample.

As far as we are aware of, no other literature reports on attenuation measurements in aluminum 5083C at this large bandwidth in frequencies. Nonetheless, McCann and Sothcott [1992] measured $Q_s > 700$ for 850 kHz frequency in an aluminum sample using the reflection method under a pressure of 60 MPa, and Hurley [1999] found the Rayleigh-waves attenuation at 10 MHz to be 1852 $\mathrm{Np\,s^{-1}}$ in an 6061-T651 aluminum alloy sample. In conclusion, the obtained attenuation values in the current study are in the same range to those measured in both previous studies, knowing that the alloys are not the same.

3.3.3 Viscosity recovery on rocks (Zener viscoelastic model)

We show in Figure IV.19 the attenuation recovery on rocks, that are Fontainebleau sandstone, diorite and Carrara marble. We show that the frequency-dependent attenuation behavior is different than in aluminum. Indeed, both S-waves β and Q-factor increase across frequencies, we choose to model the rock samples as Zener viscoelastic media (Figure III.25). In this figure we notice that there is large dispersion in the measurements and we can only follow a trend on which we try to fit a Zener model.

The complex parameter associated to the Zener model, μ_{Zener} is obtained from (II.56) such that,

$$\mu_{\text{Zener}} = \mu \frac{1 + i\omega\tau_{\epsilon_s}}{1 + i\omega\tau_{\sigma_s}}, \tag{IV.3}$$

with $\mu = \dfrac{\mu_1\mu_2}{\mu_1 + \mu_2}$, $\tau_{\epsilon_s} = \dfrac{\eta_\mu}{\mu_2}$ and $\tau_{\sigma_s} = \dfrac{\eta_\mu}{\mu_1 + \mu_2}$.

We rewrite the Q-factor for the S-waves from equation (II.48) for the Zener viscoelastic model to obtain:

$$Q_{s_{\text{Zener}}} = \frac{1 + \omega^2\tau_{\epsilon_s}\tau_{\sigma_s}}{\omega(\tau_{\epsilon_s} - \tau_{\sigma_s})} = \frac{1}{\omega(\tau_{\epsilon_s} - \tau_{\sigma_s})} + \frac{\omega\tau_{\epsilon_s}\tau_{\sigma_s}}{\tau_{\epsilon_s} - \tau_{\sigma_s}} = \frac{a}{\omega} + b\omega, \tag{IV.4}$$

with $a = \dfrac{1}{\tau_{\epsilon_s} - \tau_{\sigma_s}}$ and $b = \dfrac{\tau_{\epsilon_s}\tau_{\sigma_s}}{\tau_{\epsilon_s}}$.

We can compute the values a and b by fitting the function $Q_{s_{Zener}}(\omega) = \dfrac{a}{\omega} + b\omega$ to the measured Q values as a function of frequency (Figure IV.19). Once the values of a and b are retrieved, we can recover the parameters τ_{ϵ_s} and τ_{σ_s} by developing the system

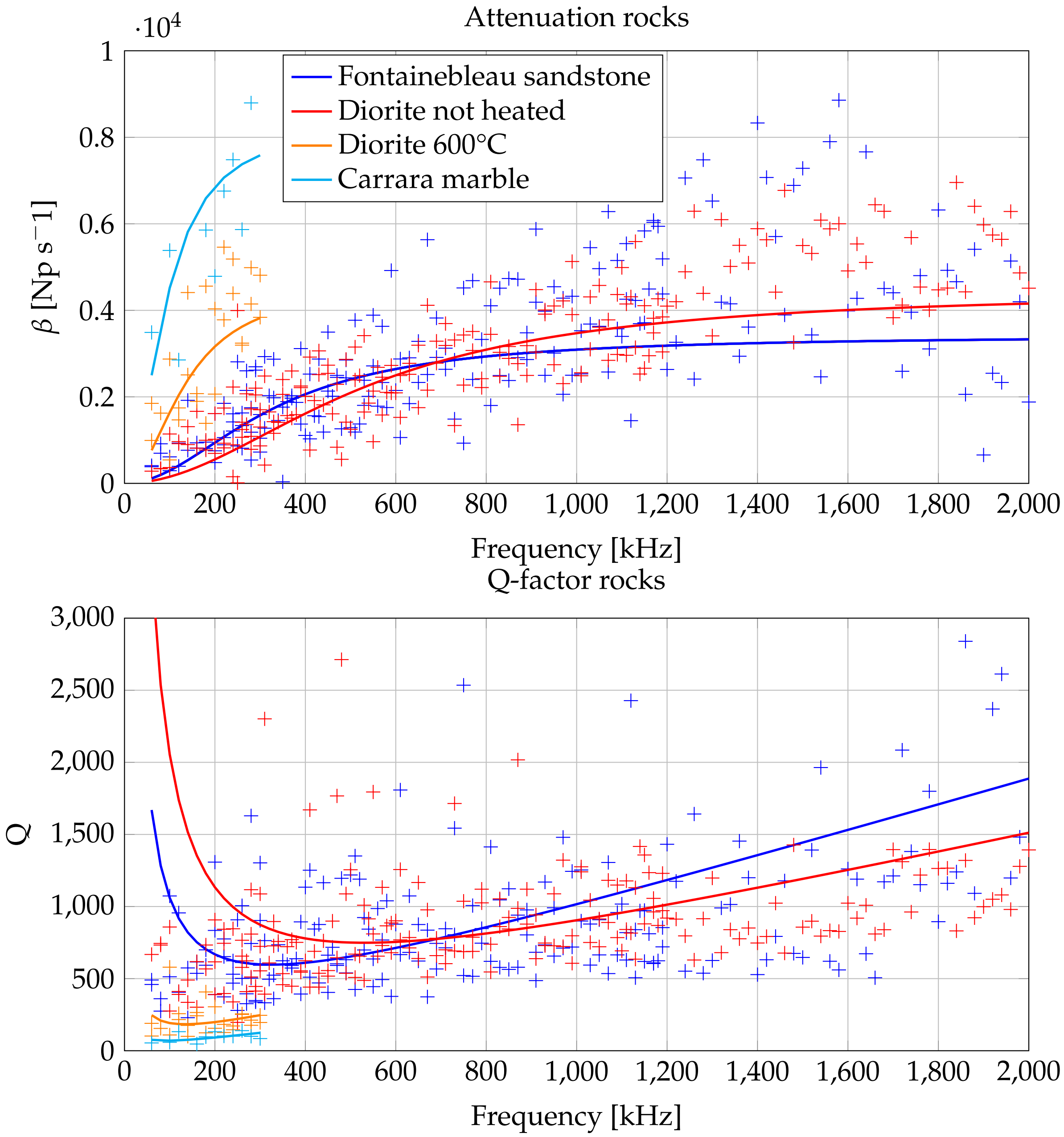

Figure IV.19: Attenuation β and Q-factor recovery on rock samples from ultrasonic measurements. Crosses [+] are the recovered attenuation for a given central frequency and the plain lines [——] are the best fit of a Zener model for each sample with the parameter in Table IV.9.

of equations:

$$
\begin{aligned}
&\begin{cases} a = \dfrac{1}{\tau_{\epsilon_s} - \tau_{\sigma_s}} \\ b = \dfrac{\tau_{\epsilon_s}\tau_{\sigma_s}}{\tau_{\epsilon_s} - \tau_{\sigma_s}} \end{cases} \\
\Leftrightarrow &\begin{cases} \tau_{\epsilon_s} = \dfrac{1}{a} + \tau_{\sigma_s} \\ b = \dfrac{\tau_{\epsilon_s}\tau_{\sigma_s}}{\tau_{\epsilon_s} - \tau_{\sigma_s}} \end{cases} \qquad \text{(IV.5)} \\
\Leftrightarrow &\begin{cases} \tau_{\epsilon_s} = \dfrac{1}{a} + \tau_{\sigma_s} \\ b = \tau_{\sigma_s} + a\tau_{\sigma_s}^2. \end{cases}
\end{aligned}
$$

We solve the second-order equation such that,

$$a\tau_{\sigma_s}^2 + \tau_{\sigma_s} - b = 0. \tag{IV.6}$$

Using that τ_{ϵ_s} and τ_{σ_s} are ≥ 0 [Carcione, 2007] and following the same development as equation (IV.5) for τ_{ϵ_s}, we have

$$\begin{aligned} \tau_{\epsilon_s} &= \frac{1+\sqrt{1+4ab}}{2a}, \\ \tau_{\sigma_s} &= \frac{-1+\sqrt{1+4ab}}{2a}. \end{aligned} \tag{IV.7}$$

We compute the subsequent viscoelastic relaxation times for each rock in Table IV.9.

Table IV.9: Recovered parameters corresponding to the best fit of a Zener model in data in Figure IV.19.

Sample	τ_{ϵ_s}	τ_{σ_s}
Fontainebleau sandstone	491 ns	490 ns
Diorite not heated	301 ns	300 ns
Diorite 600°C	1.19 µs	1.18 µs
Carrara marble	1.77 µs	1.72 µs

We obtain a good approximation of the evolution of attenuation with ultrasonic frequencies for the rock samples with the Zener model. Although it would be possible to employ multiple viscoelastic systems in parallel, such as generalized attenuation models [Carcione, 2007], or we could have even used poroelastic models, this was not within the scope of our study. Here we wish to approach a representative attenuation of the sample in order to use it as a starting model for inversion and imaging purposes.

Also, since we remember the impact of the source in contact with the sample for attenuation recovery, we still can make relative comparisons between the samples as we used the same PZT diameters thorough the experiment. We notice from Figure IV.19 that the Fontainebleau sandstone and the not heated diorite are of the same order of attenuation (here a weak attenuation). It can be explained by the matrix of these samples. The Fontainebleau sandstone is composed of pure well-cemented quartz grains and the wave can propagate freely in the sample without being attenuated much. Bourbie and Zinszner [1985] measured in the same type of sandstone $Q = 100$ at a frequency of 9.5 kHz with a resonant bar method, while Pimienta et al. [2015a], with a forced oscillation method, measured a bulk Q-factor > 50. Once more, the values of attenuation that we obtain for Fontainebleau sandstone are consistent with those obtained in other studies.

Concerning the diorite composed of heterogeneous minerals, as it is a magmatic rocks, every minerals are well cemented together resulting in a smooth seismic wave propagation within the sample. However, the heat to 600°C leads to a formation of microfracturation inside the diorite inducing more attenuation [Pimienta et al., 2019; Liu et al., 1993]. This is due to the minerals expansion during the heat then contraction during the cooling process back to room temperature. We can see in Figure IV.19 that the attenuation in heated diorite is three times higher than its reference. Another factor to consider is the possible change in mineralogy due to the heat. As we can notice in

Table IV.4, there is a change in color between the two diorites. It would not be surprising to find out that the heated diorite has been metamorphosed. Thus, we cannot precisely conclude on the attenuation factor, due to either microfracturation and/or change in mineralogy.

Carrara marble is even more attenuating, and is often used as a reference medium for seismic wave attenuation [Sarout et al., 2017]. Frequency-dependent Q-factor research by Lu and Jackson [1996] showed an increasing Q-factor in Carrara marble between 0.01 Hz and 1 Hz and under a confining pressure of 50 MPa. The closest configuration to our research is the work of Peacock et al. [1994] that found a S-waves attenuation of 100 $\mathrm{dB\,m^{-1}}$ (or 36300 $\mathrm{Np\,s^{-1}}$) of a water saturated Carrara marble at 400 kHz under a pressure of 15 MPa via reflection buffer method. They also show an increasing attenuation *vs.* frequency. Once again this value does not share the same frequency content as our measurements, but if we take β results of Figure IV.19, we can actually extrapolate to higher frequencies and link to the results of Peacock et al. [1994].

4 Summary of experimental measurements

After having developed a method in Chapter III that recovers the frequency-dependent characteristic attenuation of a laboratory-scale sample, the goal in this Chapter IV was to use this same method for actual samples.

The first part was dedicated to a presentation of the experimental set-up, followed by a characterization of elastic parameters of aluminum, Fontainebleau sandstone, Carrara marble and diorite via ultrasonic measurements in transmission with a 1 MHz piezoelectric transmitter (PZT) source.

Measurements on aluminum allowed us to test the impact of the size of the source on attenuation results. Indeed, since the method works well with strict free-surface boundary conditions, we showed that using a piezoelectric transmitter in contact with the sample disturbs the attenuation recovery. A perspective for future experimental attenuation measurements would be to use a non-contact source such as a pulsed laser for instance [Shen et al., 2022] to ensure free-surface boundary conditions in each facet of the samples.

Knowing this effect, we chose to work with PZT sources of same diameter size. It allowed us to recover the attenuation of 5 different media (aluminum, Fontainebleau sandstone, Carrara marble, diorite not heated and diorite heated at 600°C) between 60 kHz and 2 MHz, and to fit a Maxwell viscoelastic model on aluminum and Zener viscoelastic models on rocks. As the Maxwell viscoelastic model seems to be accurate enough to model aluminum, we might need to use other models than Zener to approach the frequency-dependent attenuation behavior on rocks, but this is limited by (1) the contact of the source bias and (2) the large scattering (standard deviation) of the attenuation results. This second point might be improved by having a more powerful source, or a stronger signal-to-noise ratio. Indeed, if the wave travels for a longer period of time before reaching the noise level, the decrease in amplitude recovery would be more accurate.

Nonetheless, if our goal is to image the attenuation variations inside a sample, the approximation we made with our fitted viscoelastic models can be sufficient enough to create a starting model for the inversion. In the next Chapter V we lay the foundations for the use of Full-Waveform Inversion for imaging elastic velocity or/and viscous attenuation anomalies inside a sample starting with viscoelastic homogeneous models as we would do with the method we developed.

Chapter V

Towards full-waveform inversion (FWI)

1 Introduction

In the previous chapters, we consider direct problems and perform numerical simulations, that is, we simulate a wave propagation knowing the physical parameters of a medium using the wave equation. In the following, with the wave recorded at receivers, we try to identify the physical parameters of a medium. This is the inverse problem.

One difficulty in inversion in seismic is that we have measurements only at the surface of the medium. Thus, we do not know about the wavefield inside the measured body. We need to interpret from the limited data at the receivers. Consequently, inversion may be non-unique [Tarantola and Valette, 1982], that is, it may be that two sets of different parameters generate similar wavefield response at the receivers.

One approach to solve the inverse problem is to consider a minimization problem where we try to fit the measured wavefield with simulated ones. This is the principle of full waveform inversion (FWI), that considers this minimization problem and performs iterative update of the physical parameters. We refer to Bamberger et al. [1979], Tarantola [1984] and Pratt [1999] for the first studies on FWI problems in time and frequency domains, and to Virieux and Operto [2009] for an overview on FWI.

2 Methodology

2.1 The Newton's iterative method

We start by reviewing the Newton's method which serves to find a minimum of a function J, and whose principles are followed by FWI. Here, the misfit function $J(\boldsymbol{m})$ measures the difference between the simulated and the measured wavefields as a function of physical parameters included in $\boldsymbol{m}$. The parameter $\boldsymbol{m}$ can represent the elastic parameters λ, μ, the density ρ, or even the viscous parameters η_λ and η_μ. We aim to find the $\boldsymbol{m}$ such that $J(\boldsymbol{m})$ is at a minimum. A minimum of the function J corresponds to a value of $\boldsymbol{m}$ where the derivative $J'(\boldsymbol{m}) = 0$.

The Taylor's series tells us that we can approximate a function using its derivative such that

$$J(\boldsymbol{m} + \delta) = J(\boldsymbol{m}) + \delta J'(\boldsymbol{m}) + ..., \tag{V.1}$$

where δ is a small variation that can be seen as a step between the point $\boldsymbol{m}$ and another point $\boldsymbol{m}_{+1}$ on the function.

Starting from a position $\boldsymbol{m}_0$ that is assumed to be closed to the minimum, we can expect that the perturbation δ leads us to the minimum, such that,

$$J'(\boldsymbol{m}_0 + \delta) = 0. \tag{V.2}$$

Taking into account Taylor's series, we develop $J'(\boldsymbol{m}_0 + \delta) \approx J'(\boldsymbol{m}_0) + \delta J''(\boldsymbol{m}_0) = 0$, or

$$\delta = -\frac{J'(\boldsymbol{m}_0)}{J''(\boldsymbol{m}_0)}. \tag{V.3}$$

In practice, because the point $\boldsymbol{m}_0$ is far from the minimum, the Newton method follows an iterative approach: the next iteration starts at $\boldsymbol{m}_1 = \boldsymbol{m}_0 + \delta$, and the process is repeated.

One issue with this method is the cost of calculation of $J''(m)$ in large-scale seismic applications [Métivier et al., 2013]. For FWI, we rather use the truncated Newton's method based on a defined iteration step ζ such that

$$\boldsymbol{m}_1 = \boldsymbol{m}_0 + \delta = \boldsymbol{m}_0 - \zeta \cdot s(\boldsymbol{m}_0), \tag{V.4}$$

with $s(\boldsymbol{m}_0)$ the search direction. In our experiments, the search direction only depends on the gradient of the misfit function at the point $\boldsymbol{m}_0$. Also, the search direction is normalized so that the step value ζ directly relates to the amplitude of the inverted parameter. In the context of multiparameter inversion (*e.g.* inverting simultaneously λ and μ), each of the parameter can have a different step (that we denote with ζ_λ and ζ_μ for instance).

2.2 FWI workflow

We synthesize the principles of FWI in Figure V.1. We first compare the wavefield generated from an initial model that we refer to as $\boldsymbol{m}_0$ with the wavefield measured by the receivers (also called "true model"). Then, we calculate the differences between these two wavefields for each source and all receivers via a misfit function such as the L2 norm of the difference given in equation (V.5). If the difference is "big", we iterate following the equation (V.4) and the initial model $\boldsymbol{m}_0$ is changed to a new model $\boldsymbol{m}_i$, i being the number of iteration.

$$J_{L2} = \frac{1}{2} \sum_{src} \left(\sum_{rcv} (simulation(src, rcv) - data(src, rcv))^2 \right), \tag{V.5}$$

where J_{L2} represents the least square cost function (also called L2 norm of the difference), *simulation* represents the forward simulation and associated wavefield calculated at the receivers for the initial or updated models, and *data* represents the wavefield recorded at the receivers.

While we aim to find the best parameters $\boldsymbol{m}$ that create simulations that resemble the data, it is possible (and unfortunate) that the solution is non unique, *i.e.* a wrong inverted model gives sufficiently low minimum, and/or that we reach a local minimum where the Newton method stagnates. One important step to avoid these issues is to be very careful about the initial model and the choice of frequencies so that the differences between the true and the updated model is less that one wavelength [Pratt, 1999]. Furthermore, Bretaudeau et al. [2013] pointed out that in experimental conditions, the free-surface boundary conditions and the surface waves can cause difficulties in designing a very accurate initial model.

In this thesis, we have used the software *Hawen* [Faucher, 2021] to perform the inversion. The inversion parameters are set by the user, and we can choose between elastic parameters λ and μ, velocities V_P and V_S, or also viscous parameters η_λ and η_μ. We also consider the step value ζ (equation (V.4)), that is given as an input to define a framework to the update, and is reevaluated by the software by a backtracking linesearch method (not discussed in this manuscript but we refer to Nocedal and Wright [2006] for further information). Along with the consideration of parameters and their values, we need to define when to stop the calculations. For that, we compare the evolution of the misfit functions between successive iterations: when the improvement is small, in which case it indicates that the minimization stagnates, we can stop the iterative process. Otherwise, we can fix the maximal number of iterations. The inverted model is then denoted by $\boldsymbol{m}_{end}$.

Two other important parametrizations to consider for FWI are the choice of the misfit function and the choice of the parameter function, that are discussed later in this chapter in Section 4.

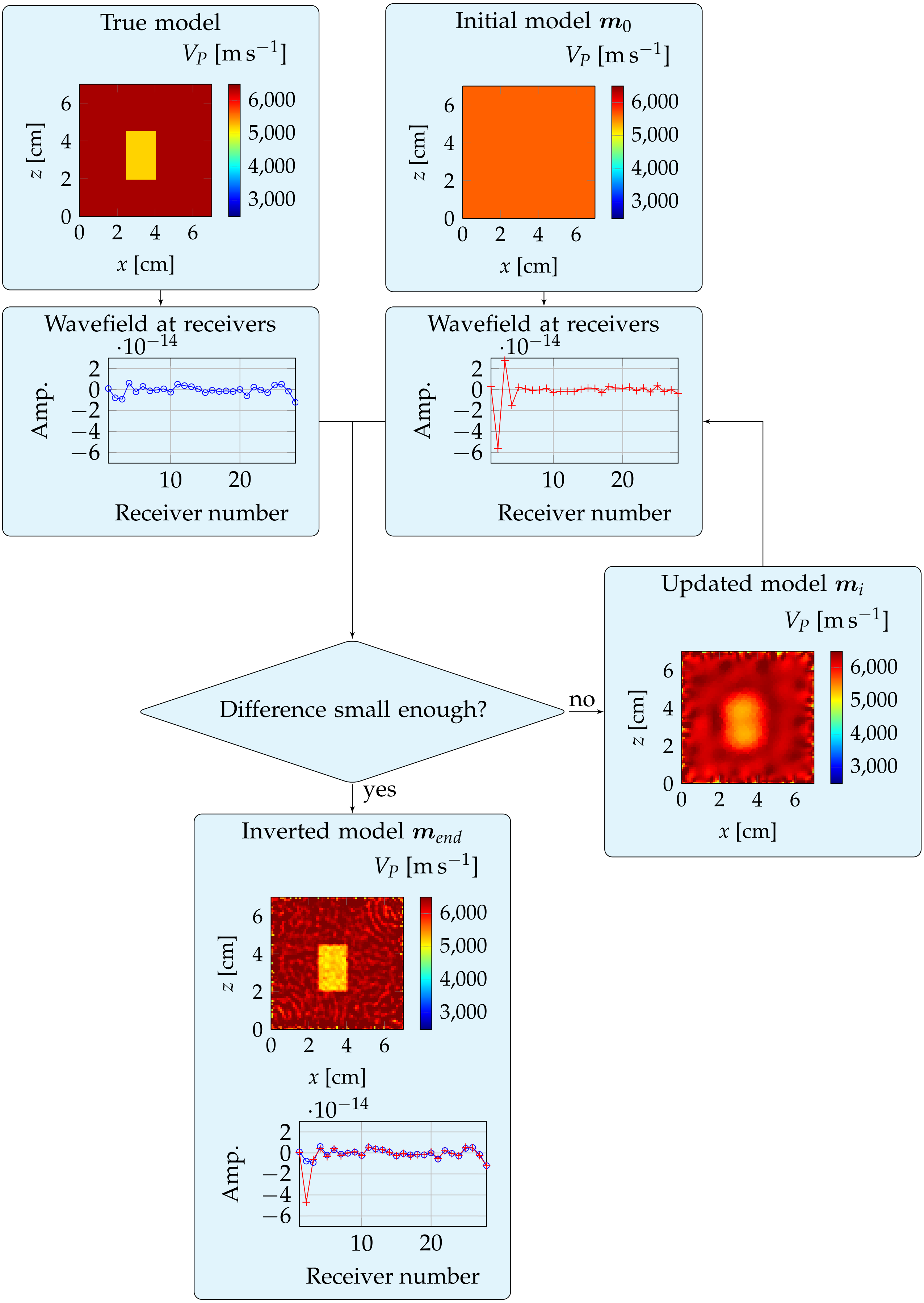

Figure V.1: FWI synthesized workflow. [−○−] Wavefield at receivers for the true model. [−+−] Wavefield at receivers for the inverted models. The acquisition details are described in Section 3

3 Reconstruction of a velocity anomaly

As preliminary analysis, we consider the 2D numerical experiments in order to highlight the difficulties of inverting the physical elastic parameters in laboratory context (free-surface boundary conditions and receivers at the surface of the sample), and how to overcome these. We use the software *Hawen* Faucher [2021] to perform FWI in frequency domain, that present the advantages to allow us to invert on a few frequency values instead of the whole data content and to implement attenuation without adding computational cost [Brossier et al., 2009; Prieux et al., 2013a,b].

We consider a two-dimensional synthetic experiment of size 7 cm x 7 cm with an anomaly in velocity (Figure V.2) that we aim to invert. Next, we perform forward numerical simulations in frequency domain with synthetic sources and receivers as in Chapter III. Here, in order to be close to the experimental conditions, we choose to place 12 sources and 28 receivers all around the sample (Figure V.2) that record the wavefield in frequency domain. Each source works independently and generate a wave in the horizontal u_x and vertical u_z components, and the receivers record the wavefield in the u_x and u_z components.

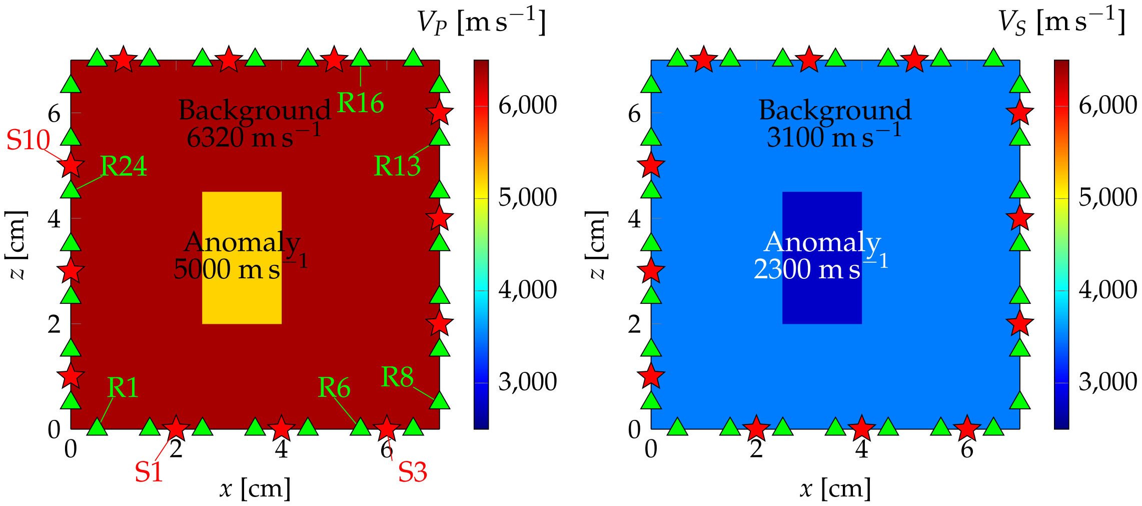

Figure V.2: True model of velocity and location of sources and receivers.

The receivers and sources are numbered from R1 to R28 and from S1 to S12 following the trigonometric direction (see Figure V.2). The source and receivers coordinates can be found in Table V.1.

In this example, the P-wave velocity in the background of the sample is taken to be 6320 m s^{-1} with a P-wave anomaly of 5000 m s^{-1}. The S-wave velocity in the background is 3100 m s^{-1} with S-wave anomaly of 2300 m s^{-1}. The density is constant and of ρ = 2700 kg m^{-3}. We add attenuation with a Kelvin-Voigt viscoelastic model of constant viscosity (no anomaly in attenuation here) η_λ = 250 Pa s and η_μ = 500 Pa s.

Table V.1: Sources and receivers coordinates (in cm).

Source	Coord. (x,z)	Receiver	Coord. (x,z)	Receiver	Coord. (x,z)
S1	(2.0 , 0.0)	R1	(0.5 , 0.0)	R15	(6.5 , 7.0)
S2	(4.0 , 0.0)	R2	(1.5 , 0.0)	R16	(5.5 , 7.0)
S3	(6.0 , 0.0)	R3	(2.5 , 0.0)	R17	(4.5 , 7.0)
S4	(7.0 , 2.0)	R4	(3.5 , 0.0)	R18	(3.5 , 7.0)
S5	(7.0 , 4.0)	R5	(4.5 , 0.0)	R19	(2.5 , 7.0)
S6	(7.0 , 6.0)	R6	(5.5 , 0.0)	R20	(1.5 , 7.0)
S7	(5.0 , 7.0)	R7	(6.5 , 0.0)	R21	(0.5 , 7.0)
S8	(3.0 , 7.0)	R8	(7.0 , 0.5)	R22	(0.0 , 6.5)
S9	(1.0 , 7.0)	R9	(7.0 , 1.5)	R23	(0.0 , 5.5)
S10	(0.0 , 5.0)	R10	(7.0 , 2.5)	R24	(0.0 , 4.5)
S11	(0.0 , 3.0)	R11	(7.0 , 3.5)	R25	(0.0 , 3.5)
S12	(0.0 , 1.0)	R12	(7.0 , 4.5)	R26	(0.0 , 2.5)
		R13	(7.0 , 5.5)	R27	(0.0 , 1.5)
		R14	(7.0 , 6.5)	R28	(0.0 , 0.5)

3.1 Absorbing boundary conditions

We first consider a synthetic experiment where we impose absorbing boundary conditions in order to avoid issues due to reflections at boundaries [Bretaudeau et al., 2013]. The wavefields in frequency domain propagating through the sample from the source S1 for the u_z component at the frequency 100 kHz and 900 kHz are given in Figure V.3 and the associated recordings at receivers in Figure V.4.

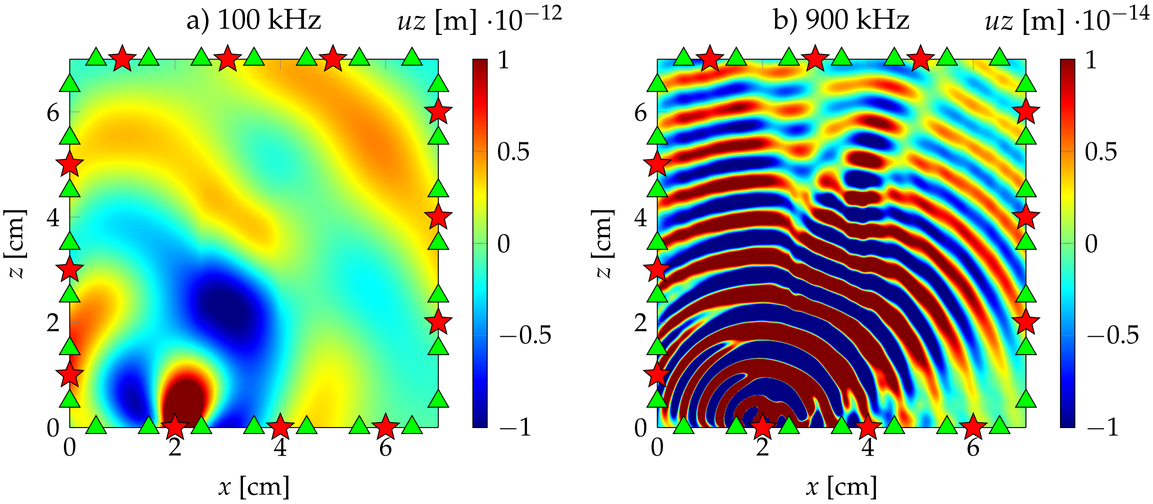

Figure V.3: Wavefield in frequency domain (real part) of a wave generated from the source S1 propagating through the true model at a frequency of a) 100 kHz and b) 900 kHz for the vertical component u_z.

In the following examples, we consider an homogeneous initial model of value between the background and the anomaly Figure V.5. Indeed, if we make experimental measurements in transmission from two opposite sides of the sample, the wave would go through the background, the anomaly and again the background before reaching the receiver, and the apparent measured velocity measured with the first arrivals would be

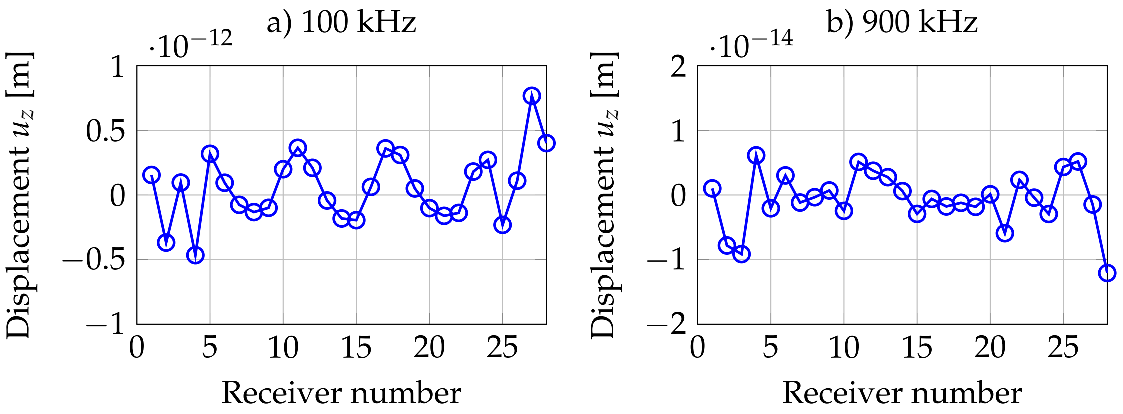

Figure V.4: Wavefield recorded at receivers in frequency domain (real part) of a wave propagating through the true model from the source S1 at a) 100 kHz frequency and b) 900 kHz frequency.

in between the velocity of the background and the velocity of the anomaly. Consequently we consider constant initial model of $V_P = 5500\ \mathrm{m\,s^{-1}}$ and $V_S = 2700\ \mathrm{m\,s^{-1}}$.

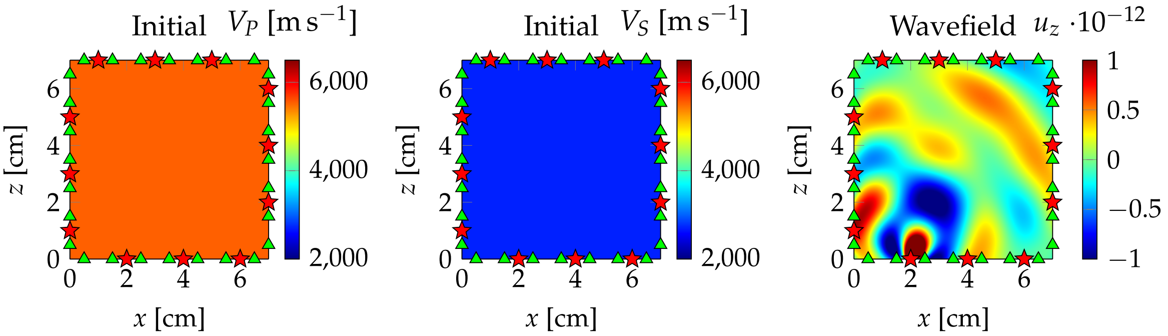

Figure V.5: Initial velocity model V_P = 5500 $\mathrm{m\,s^{-1}}$ [left] and V_S = 2700 $\mathrm{m\,s^{-1}}$ [center]. Associated wavefield at 100 kHz [right].

We perform the inversion with frequency step of 100 kHz from 100 kHz to 900 kHz. We update the initial model by inverting the elastic parameters ($\boldsymbol{m} = (\lambda, \mu)$, related to V_P and V_S) minimizing the L2-norm misfit function (equation (V.5)). Also, the parameter function is of importance and a parametrization study is given by Faucher [2017] in chapter 5. For this example, we choose to invert on $1/\lambda$ and $1/\mu$ simultaneously with a step of 2×10^{-12} for and 1×10^{-11} respectively. These values were chosen after trial and errors, where we noticed that we have better results where the step size ζ is around 5%-10% the parameter itself (equation (V.4)). Note that this step could be automatically refined with more advanced linesearch method [Nocedal and Wright, 2006] but that would be more costly. For this inversion, we assumed the sources are known as well as known attenuation model (Kelvin-Voigt) of viscosity $\eta_\lambda = 250$ Pa s and $\eta_\mu = 500$ Pa s.

It can be seen in Figure V.6 how the V_P model is updated from the initial model to the 15th and 30th iterations for the 100 kHz frequency. The wavefield at receivers for the initial model and the wavefield at receivers for the measured (true) model do not fit well, but are close in terms of amplitude (because we assumed a known source) and in terms of variations (oscillations) with respect to receiver number, meaning that the initial velocity model is close to the real one. After 15 iterations, we notice that the anomaly in velocity starts to appear, and the velocity of the background is updated to a higher value than the initial model. Also, the wavefield at receivers are getting closer to

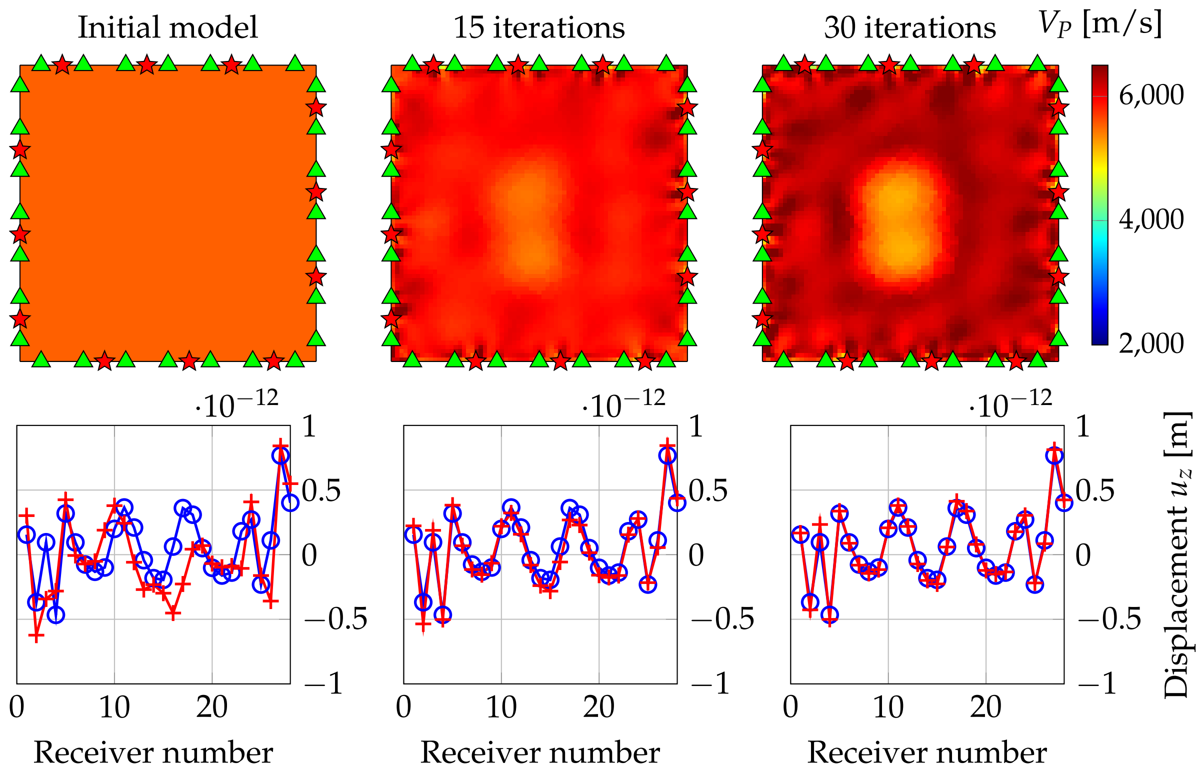

Figure V.6: On the top part are the V_P initial model [left], inverted model after 15 iterations [center] and inverted model after 30 iterations [right] at 100 kHz. On the bottom part are the wavefield recorded at each receivers at 100 kHz (real part) generated by the source S1 comparing the wavefield through the true model [−○−] with the wavefield through the initial or inverted model [−+−]

the measured wavefield. When we continue until 30 iterations, there is almost no more differences between the two measured and simulated wavefields, and we have a good insight of the background V_P value and the location, shape and size of the V_P anomaly. At this stage it would be useless to perform more update iterations at 100 kHz because the misfit function J stagnates (Figure V.8). We then go on to the next frequency (200 kHz) by using the result of inversion at 100 kHz as an initial model, and we continue the iterations in order to have a better definition of the shape and values of the anomaly, and so on until 900 kHz (Figure V.7). At the end of inversion, we see that the V_P and V_S values are correctly inverted, from the value of the background to the location, shape and value of the anomaly.

We show the value of the misfit function after all the iterations in Figure V.8. On this example, we perform the inversion on 30 iterations for each frequency. We see that as we update the inverted model for each frequency, the error value drops quickly for the first iterations, and is slowly stabilized. Also, we notice that the misfit can take a higher value when we change frequency. This can be due to the inversion over a new frequency that can have a different amplitude of source (depending on its frequency spectrum), and also inversion over new wavefields that does not necessarily fit as well as for the previous frequency.

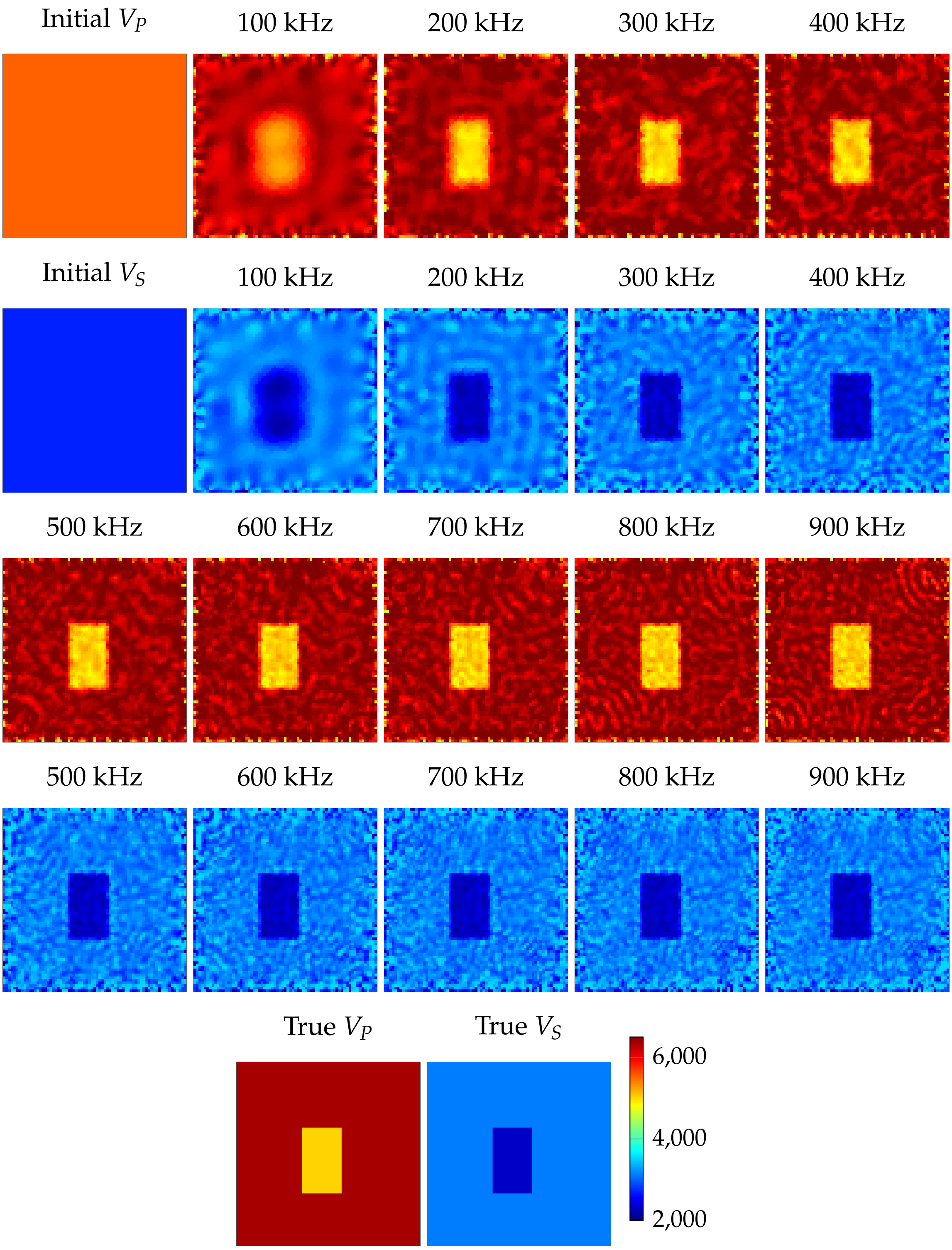

Figure V.7: V_P **and** V_S **inversion results for the frequencies 100 kHz to 900 kHz with a step of 100 kHz, with 30 iterations per frequency (270 in total).**

a) Misfit value

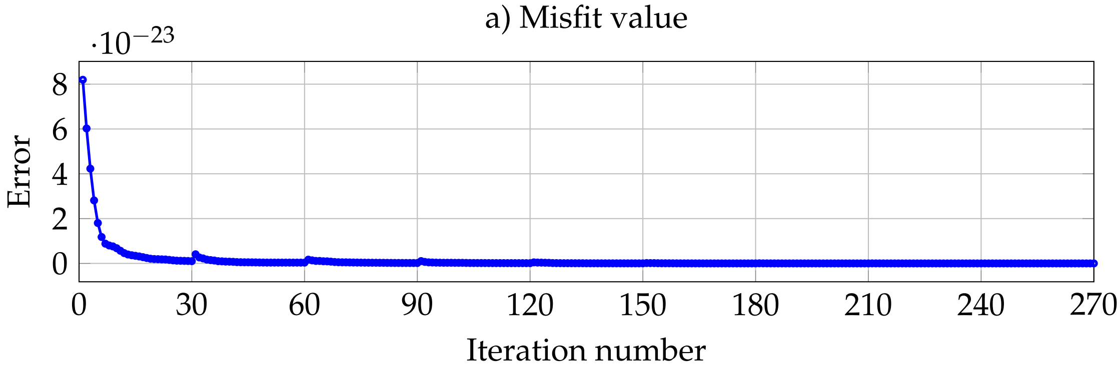

b) Misfit value (log scale)

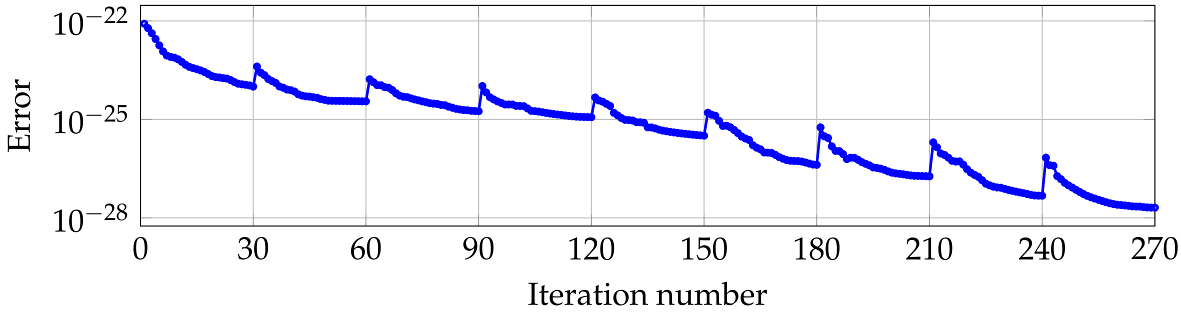

Figure V.8: Evolution of the misfit function (V.5) with the number of iterations for the reconstruction results of Figure V.7. The inversion is performed from 100 kHz to 900 kHz and we move on to the next frequency after 30 iterations.

3.2 Free-surface boundary conditions

We now consider a more realistic experiment, replacing the absorbing boundary conditions by free-surface boundary conditions to see the effect of reflections in the wavefield and their impact for FWI.

3.2.1 Velocity inversion

We invert elastic parameters λ and μ (with the same parametrization as the previous subsection) from different initial models to see the impact of free-surface boundary conditions and picture the reconstruction of V_P in Figure V.9, where in one case the initial velocities are a value between the background and the anomaly as in the example presented before ($V_P = 5500\ \mathrm{m\,s^{-1}}$ and $V_S = 2700\ \mathrm{m\,s^{-1}}$), in a second case the initial velocities are equal to the background values ($V_P = 6320\ \mathrm{m\,s^{-1}}$ and $V_S = 3100\ \mathrm{m\,s^{-1}}$), and in a third case the initial velocities are equal to the anomaly values ($V_P = 5000\ \mathrm{m\,s^{-1}}$ and $V_S = 2300\ \mathrm{m\,s^{-1}}$). We notice that in this example, when we consider an initial model equal to the background value, we manage to correctly recover the velocity anomaly. Nevertheless, when we consider an initial model of velocity in between the background and the anomaly (as we would have in experimental conditions and as we had in the previous subsection with absorbing boundary conditions), the inversion fails. The result is even worse when we consider the initial model being of the anomaly value.

We picture the evolution of the misfit in Figure V.10 where we notice an overall decrease in value as a function of iteration numbers for the three different initial models. However, the final results are not satisfactory. Other observations that can be made on the misfit are the absolute values with respect to initial models. The yellow misfit

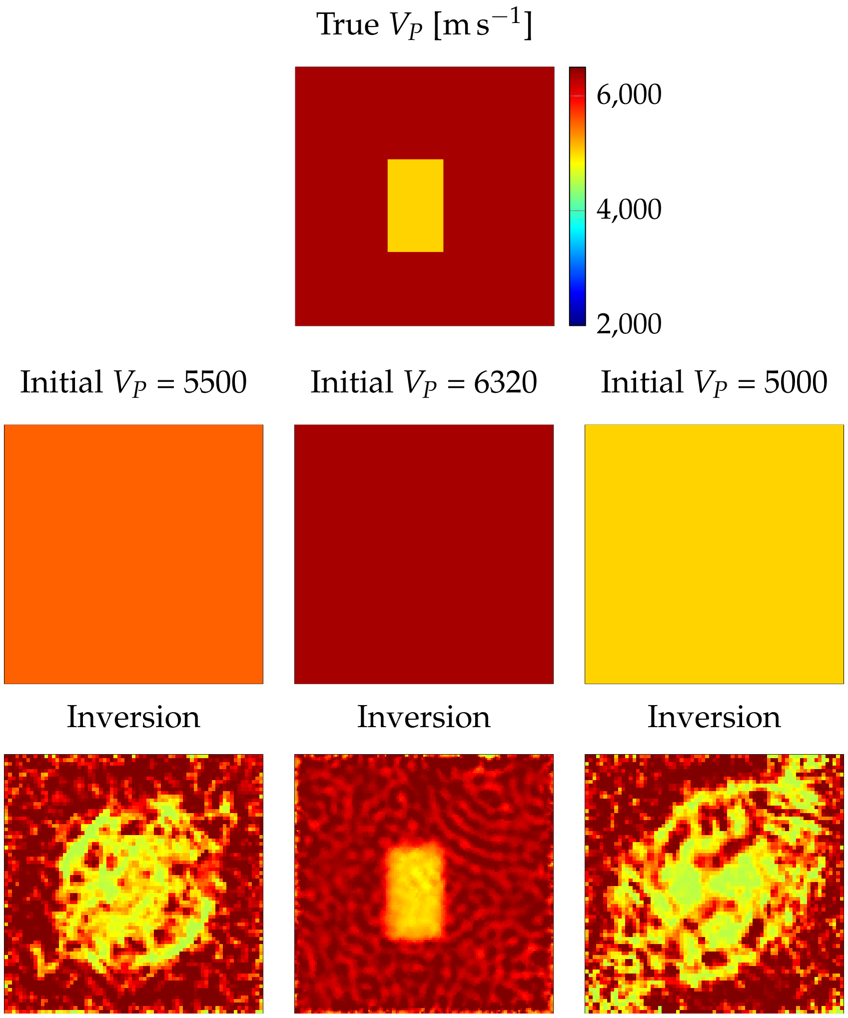

Figure V.9: V_P final inversion result for the frequencies 100 kHz to 900 kHz with a step of 100 kHz with three different initial models: [left] V_P = 5500 m s^{-1} and V_S = 2700 m s^{-1}; [center] V_P = 6320 m s^{-1} and V_S = 3100 m s^{-1}; [right] V_P = 5000 m s^{-1} and V_S = 2300 m s^{-1}.

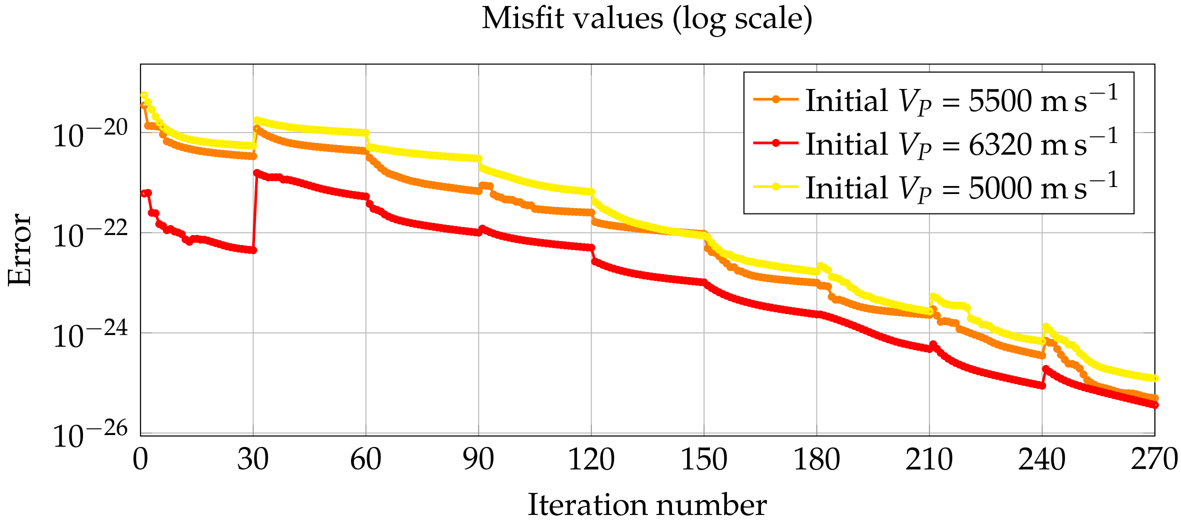

Figure V.10: Misfit value corresponding to the inversion of Figure V.9 for three different initial models. Inversion from 100 kHz to 900 kHz with a step of 100 kHz, 30 iterations for each frequency.

(initial $V_P = 5000\,\mathrm{m\,s^{-1}}$) is the worst of all three as it starts and ends with the highest error values. This case is an illustration of the inversion process that stagnates in a local minimum over iterations. The red misfit (initial $V_P = 6320\,\mathrm{m\,s^{-1}}$) for the successful inversion has an error value already lower than the two others from the very first iteration, and stays low during the whole iteration process. The orange misfit function (initial $V_P = 5500\,\mathrm{m\,s^{-1}}$) shows an interesting pattern. It starts with a higher error value, and reach an error value close to the successful inversion (red) at the end of the 270 iterations, even though the reconstruction is not accurate. This case is a good illustration of the non unicity of the problem, where drastically different simulated models give similar minimum values in the misfit.

We now take a closer look at the wavefields to better understand the situation. In Figure V.11 we see the impact of the presence of reflections due to free-surface boundary conditions for the first inverted frequency (100 kHz). The first visible effect is the amplitude of the wavefield with respect to the velocities of the medium. Indeed, the numerous reflections leads to destructive or constructive interference depending on the wavelengths (at 100 kHz, the P- and S- wavelength are of 5.5 cm and 2.7 cm for $V_P = 5500\,\mathrm{m\,s^{-1}}$ and $V_S = 2700\,\mathrm{m\,s^{-1}}$, 6.32 cm and 3.1 cm for $V_P = 6320\,\mathrm{m\,s^{-1}}$ and $V_S = 3100\,\mathrm{m\,s^{-1}}$ and 5 cm and 2.3 cm for $V_P = 5000\,\mathrm{m\,s^{-1}}$ and $V_S = 2300\,\mathrm{m\,s^{-1}}$). Another effect, visible if we compare the wavefield with free-surface boundary conditions and absorbing boundary conditions (Figures V.3 and V.11), is that the wavefields do not have a circular pattern and thus we cannot follow the wavefronts starting from the source with free-surface boundary conditions.

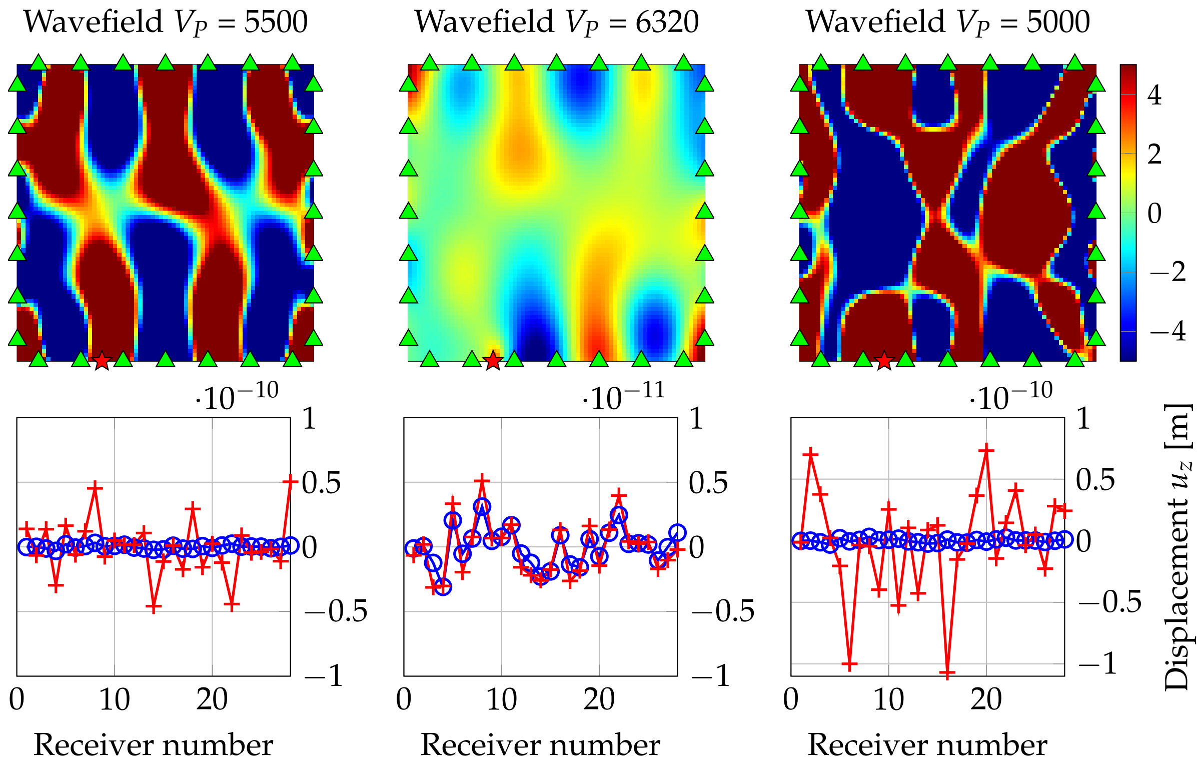

Figure V.11: Wavefields (real part) of a wave generated from the source S1 [top] and recorded at receivers [bottom] at a frequency of 100 kHz for the vertical component u_z (colorbar = displacement in [m] *1e-12). [−⊖−] wavefield at receivers for the true model, [−+−] wavefield at receivers for the initial models. [left] $V_P = 5500\,\mathrm{m\,s^{-1}}$ and $V_S = 2700\,\mathrm{m\,s^{-1}}$; [center] $V_P = 6320\,\mathrm{m\,s^{-1}}$ and $V_S = 3100\,\mathrm{m\,s^{-1}}$; [right] $V_P = 5000\,\mathrm{m\,s^{-1}}$ and $V_S = 2300\,\mathrm{m\,s^{-1}}$.

The free-surface boundary conditions and reflections are an inherent part of the data in experimental conditions. These reflections hinder the reconstruction and it is necessary to treat them while keeping the same data, physical properties and boundary conditions. This can be achieved with complex frequencies that we present in the next part.

3.2.2 Complex frequencies

Complex frequencies in seismics can be used to generate an artificial damping coefficient in the data that not only allows to create a smooth initial model when the imaginary part is used alone [Shin and Cha, 2008] (also called inversion in the Laplace domain), but also enhances the inversion when used jointly with the usual real frequencies [Shin and Cha, 2009; Shin et al., 2010]. It is indeed shown to enlarge the convergence radius of FWI, *i.e.* to relax the need of accurate initial guess [Faucher et al., 2020]. In our study, we use them to artificially attenuate the signal so that it is less impacted by the reflections at the boundaries.

We remind the time-harmonic formulation of the motion of wave from equation (II.58):

$$\hat{u}(\boldsymbol{x},\omega) = u_0 \cdot \exp(-\mathrm{i}k\boldsymbol{x}), \tag{V.6}$$

with k the wavenumber in $[\mathrm{m}^{-1}]$. Taking complex wavenumber with viscosity (implying complex velocity) and complex frequency, we have:

$$k_c = \frac{\omega_c}{V_c} = \frac{\omega_{real} - \mathrm{i}\omega_{imag}}{V_{real} + \mathrm{i}V_{imag}} = \frac{\omega_{real} - \mathrm{i}f_L}{V_{real} + \mathrm{i}V_{imag}}, \tag{V.7}$$

with f_L the Laplace frequency in [Hz], that is the imaginary part of the frequency.

We can develop and rewrite the equation (V.6) to separate the real and imaginary parts such that,

$$\hat{u}(\boldsymbol{x},\omega) = u_0 \cdot \exp(-\alpha\boldsymbol{x}) \cdot \exp(-\mathrm{i}k_{real}\boldsymbol{x}), \tag{V.8}$$

with $\alpha = \dfrac{\omega_{real}V_{imag} + f_L V_{real}}{V_{real}^2 - V_{imag}^2}$ and $k_{real} = \dfrac{\omega_{real}V_{real} - f_L V_{imag}}{V_{real}^2 - V_{imag}^2}$.

When there is viscosity and we work with real frequency, or $f_L = 0$, then

$$\alpha = \frac{\omega_{real}V_{imag}}{V_{real}^2 - V_{imag}^2} \quad \text{and} \quad k_{real} = \frac{\omega_{real}V_{real}}{V_{real}^2 - V_{imag}^2}, \tag{V.9}$$

as in equation (II.60). We notice that k_{real} is impacted by the complex velocity.

When we work with pure elasticity and complex frequency, or $V_{imag} = 0$, we have

$$\alpha = \frac{f_L}{V_{real}} \quad \text{and} \quad k_{real} = \frac{\omega_{real}}{V_{real}}, \tag{V.10}$$

where we remind $\beta = \alpha V_{real}$ such that in this case f_L is also the amplitude decay β in $[\mathrm{Np\,s}^{-1}]$. We see that using the complex velocity can also change the wavelength of the signal by modifying k_{real}, while Laplace frequency only generates attenuation of the amplitude.

We illustrate the effect of using Laplace frequencies in Figure V.12, that is the representation of the wavefield through the true model of the previous parts, using complex frequencies. Adding an imaginary part to the frequency allows to add artificial attenuation (i.e., not from the physical properties of the medium) so that the wave propagates from the source to a boundary with too little amplitude to be reflected, thus we obtain a clearer wavefront.

The actual attenuation values with respect to complex frequencies corresponding to the wavefields of Figure V.12 are presented in Figure V.13. We first notice the frequency-dependent attenuation behavior due to Kelvin-Voigt viscoelastic model. Secondly, we see that the addition of Laplace frequency only adds a constant value to the amplitude decay. During the inversion process, we need to be careful about the choice of the f_L value so that the artificial attenuation is not too high nor too low so the inversion is still efficient [Faucher et al., 2020].

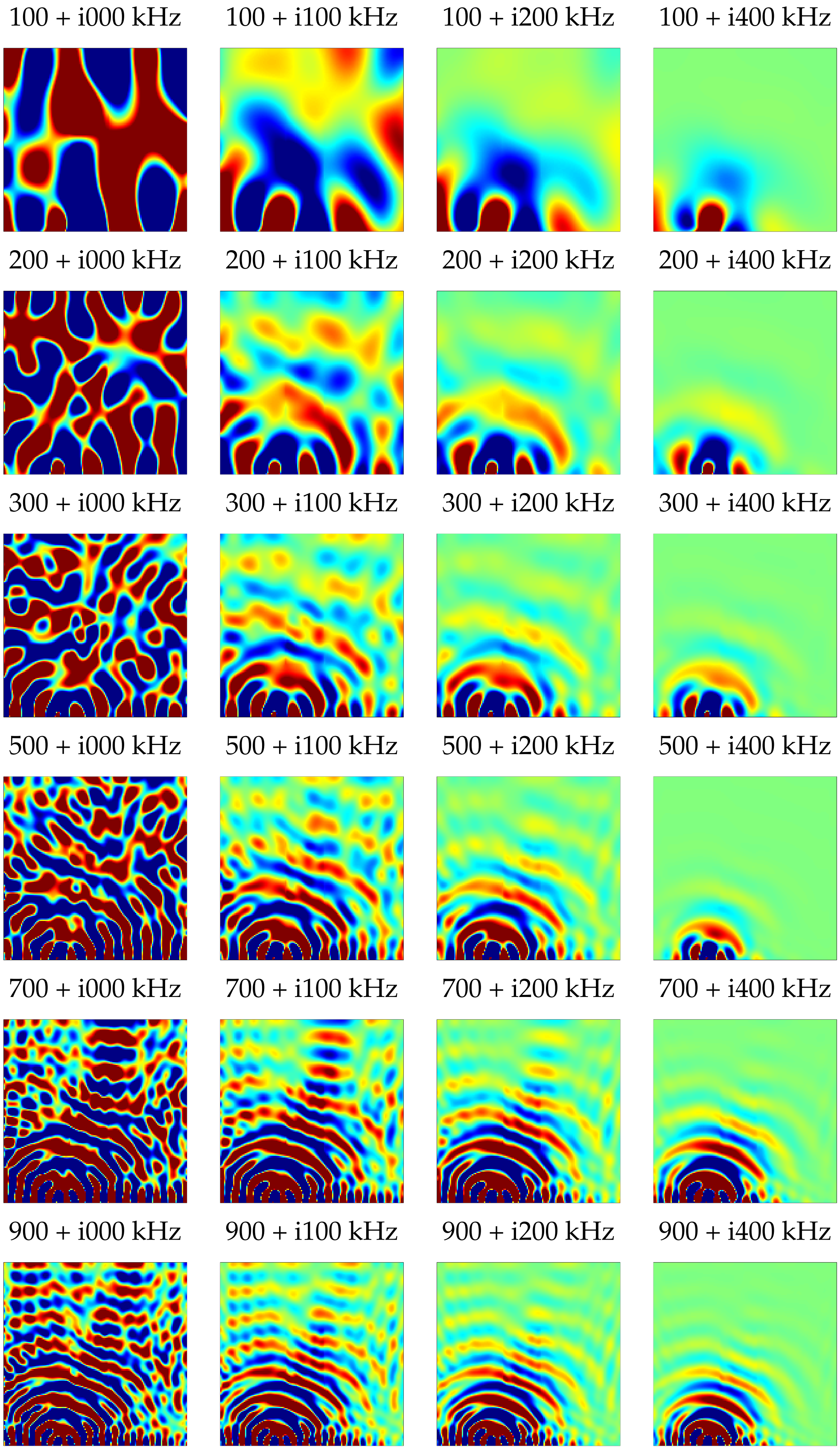

100 + i000 kHz 100 + i100 kHz 100 + i200 kHz 100 + i400 kHz

200 + i000 kHz 200 + i100 kHz 200 + i200 kHz 200 + i400 kHz

300 + i000 kHz 300 + i100 kHz 300 + i200 kHz 300 + i400 kHz

500 + i000 kHz 500 + i100 kHz 500 + i200 kHz 500 + i400 kHz

700 + i000 kHz 700 + i100 kHz 700 + i200 kHz 700 + i400 kHz

900 + i000 kHz 900 + i100 kHz 900 + i200 kHz 900 + i400 kHz

Figure V.12: Real part of the wavefield (u_z component) generated from the source S1 propagating through the true model at real frequencies of [100:100:900] kHz combined with Laplace frequencies of [0;100;200;400] kHz. The used constant viscoelastic model is Kelvin-Voigt of viscosity η_λ = 250 and η_μ = 500 Pa s and the boundary conditions are free-surface.

Laplace frequency in FWI are used in our case with the method given by Faucher et al. [2020], that is, we start the inversion from the lowest real frequency (here 100 kHz) and highest Laplace frequency (here 400 kHz), and we remove attenuation sequentially by lowering the Laplace frequency value (here 200 kHz then 100 kHz then no Laplace frequency). This is similar to first illuminating the medium close to the source and then deeper and deeper as the Laplace frequency decreases. For instance, in our inversions, we started to invert with 100 kHz + i400 kHz, then 100 kHz + i200 kHz, then 100 kHz + i100 kHz, then 100 kHz (+i0kHz), then we move on to the next real frequency and invert on 200 kHz + i400 kHz, then 200kHz + i200 kHz, and so on until we inverted each frequency.

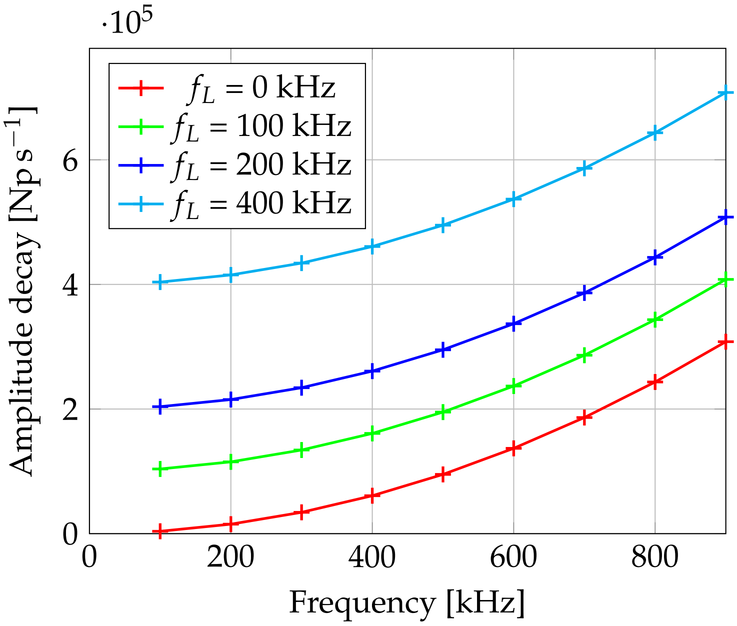

Figure V.13: Attenuation value of a S-wave propagating through a Kelvin-Voigt viscoelastic medium of V_S = 3100 m s^{-1} (μ = 25.95 GPa) and η_μ = 500 Pa s with and without addition of Laplace frequency (f_L).

We present the Figure V.14 to emphasize the use of complex frequencies with respect to viscosity to numerically add attenuation in the domain. As we already saw in Figure V.9, having free-surface boundary conditions when the medium does not contain any attenuation can cause problems for FWI (see also Figure V.14b). We would like to be able to follow smooth wavefronts as with absorbing boundary conditions (Figure V.14a). When we add attenuation while keeping free-surface boundary conditions, we see in Figure V.14 c and d that we reduce reflections and thus we are able to follow the wavefronts.

To conclude with the interest of complex frequencies, we show the inversion of velocity results where we are in laboratory conditions, with free-surface boundary conditions and an initial model values being in between the background and the anomaly in Figure V.15 in presence of intrinsic attenuation due to Kelvin-Voigt viscoelastic model, and in Figure V.16 where there is no intrinsic attenuation. We notice from these two figures that when we perform FWI on only real parts of frequencies (without Laplace frequency), the shape of anomaly is not accurately defined. Nevertheless, when we invert progressively from high Laplace frequency to low Laplace frequency, the inversion is way better, even though the recovery of V_S could certainly be improved with a

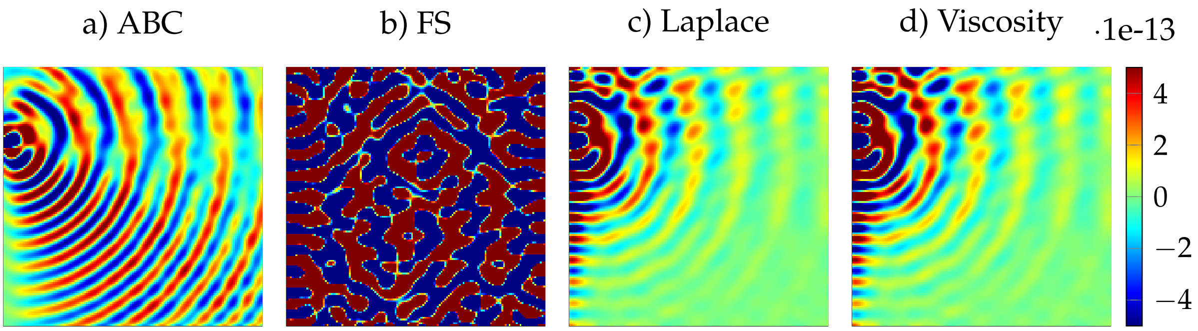

Figure V.14: Real part of the 500 kHz wavefield (u_x component) generated from the source S10 propagating through a model of constant velocities V_P = 6320 $\mathrm{m\,s^{-1}}$ and V_S = 3100 $\mathrm{m\,s^{-1}}$. a) No attenuation, absorbing boundary conditions. b) No attenuation, free-surface boundary conditions. c) Attenuation due to Laplace frequency f_L = 200 kHz. d) Attenuation due to viscosity η_λ = 2267.6 Pa s and η_μ = 1051.6 Pa s.

more careful study of parametrization. Here we would suggest to define another misfit function, or maybe a bigger step ζ for μ parameter. This was not done in this thesis in order to be able to give more focus on attenuation anomaly inversion, presented in the next section.

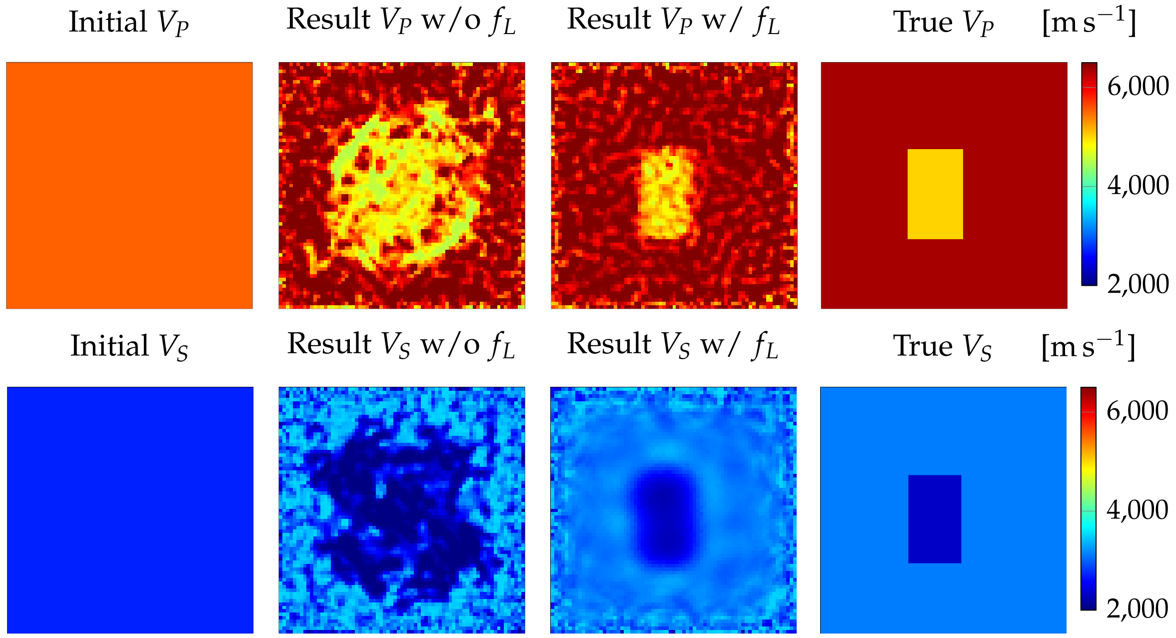

Figure V.15: Inversion on viscoelastic medium with and without the use of complex (Laplace) frequencies. V_P and V_S final inversion results for the frequencies 100 kHz to 900 kHz with a step of 100 kHz with the initial model V_P = 5500 $\mathrm{m\,s^{-1}}$ and V_S = 3100 $\mathrm{m\,s^{-1}}$. Results without (w/o) and with (w/) the use of Laplace frequencies f_L = [400;200;100;0] kHz. The true model follows a Kelvin-Voigt viscoelastic law of viscosity η_λ = 250 Pa s and η_μ = 500 Pa s.

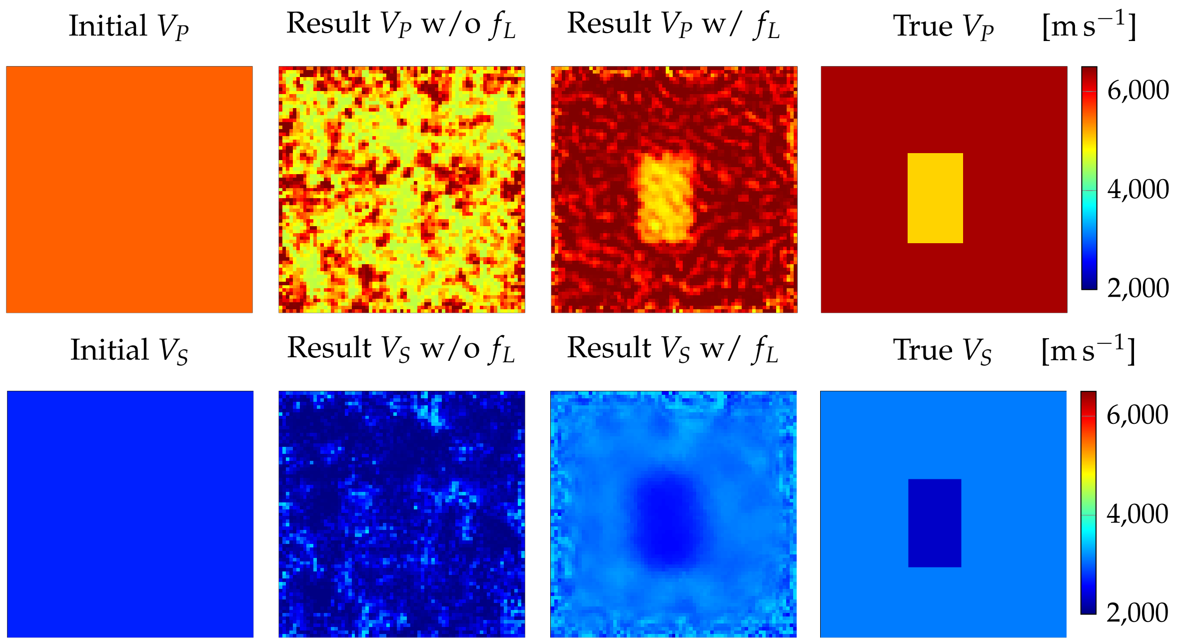

Figure V.16: Inversion on elastic medium (no viscosity) with and without the use of complex (Laplace) frequencies. V_P and V_S final inversion results for the frequencies 100 kHz to 900 kHz with a step of 100 kHz with the initial model V_P = 5500 $\mathrm{m\,s^{-1}}$ and V_S = 3100 $\mathrm{m\,s^{-1}}$. Results without (w/o) and with (w/) the use of Laplace frequencies f_L = [400;200;100] kHz. There is no viscous attenuation in the true model.

4 Reconstruction of a viscosity anomaly

4.1 Introduction

In this section we aim to recover the change in viscosity inside a 7 cm x 7 cm 2D synthetic experiment following a Kelvin-Voigt viscoelastic model with constant velocities V_P = 6320 $\mathrm{m\,s^{-1}}$ and V_S = 3100 $\mathrm{m\,s^{-1}}$ and viscosities containing an anomaly (η_λ = 250 Pa s with an anomaly of 500 Pa s and η_μ = 500 Pa s with an anomaly of 1000 Pa s) as in Figure V.17.

In viscoelastic FWI, studies have focused on reconstructing the quality factor [Malinowski et al., 2011; Prieux et al., 2013a; Fabien-Ouellet et al., 2017; Pan and Wang, 2020; Yong et al., 2021; Masmoudi et al., 2023]. This is mainly because there is no need to know the viscoelastic model which governs the medium. In our case, we are able to find the viscoelastic models from frequency-varying measurements as seen in Chapter III. Thus, we will focus on inverting the viscosity coefficients.

Another motivation lies on the quality factor definitions, for instance for the use of Kelvin-Voigt model, we remind

$$\omega M_\eta Q_{KV}(\omega) = M_e, \tag{V.11}$$

with Q_{KV} the quality factor following a Kelvin-Voigt viscoelastic law, M_η the viscous modulus and M_e the elastic modulus. It means that in viscoelasticity, quality factor is linked to elastic parameters as well as viscous parameters. Inverting with respect to parameters that characterize the attenuation models allows to work with independant quantities instead. Therefore, we expect to reduce the cross-talk between the inverted parameters.

In the following parts we test different misfit functions and different parameter functions in order to find the best parametrization for viscous FWI. We assume known velocities being the true velocities and the initial viscosity models are constant and equal to the background (η_λ = 250 Pa s and η_μ = 500 Pa s). Also, we consider absorbing boundary conditions.

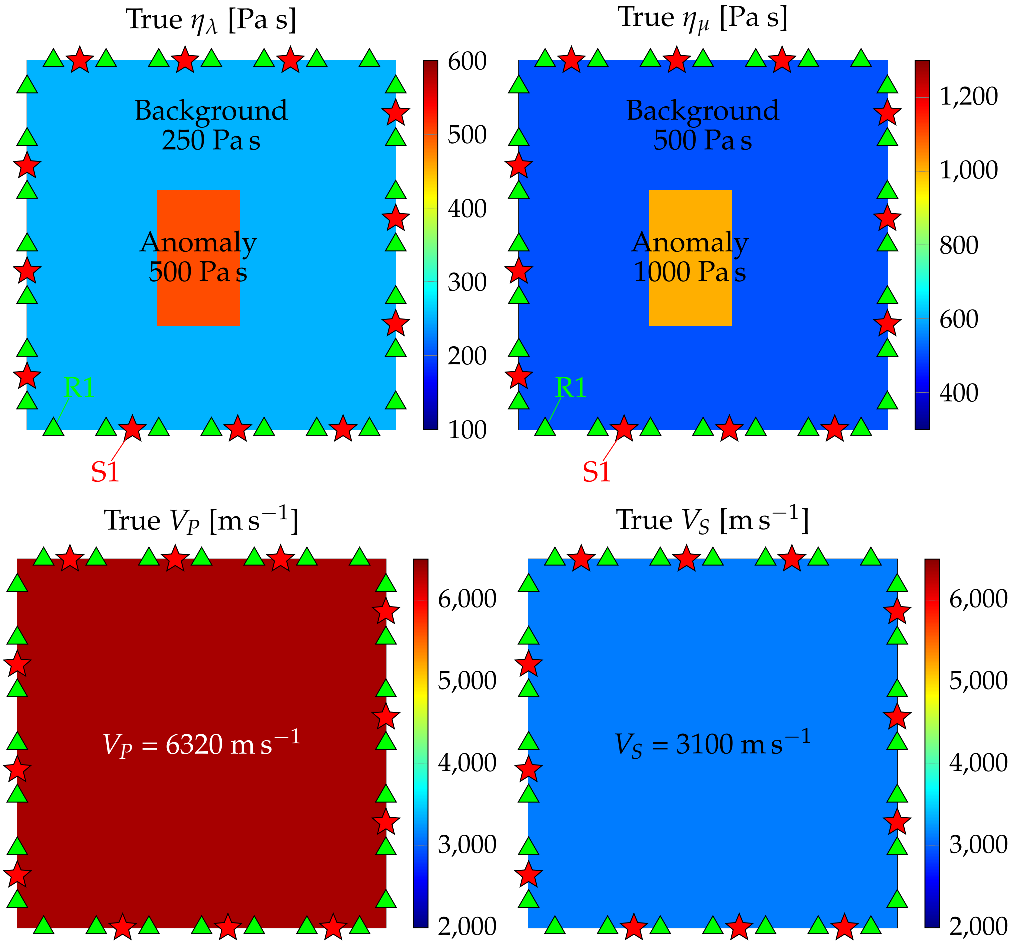

Figure V.17: True model of velocity and viscosity and location of sources and receivers.

4.2 Test of different misfit functions

The inversion process has different sensibilities under the chosen misfit function (see for instance Pan and Wang [2020]). In the following we invert the viscous parameters η_λ and η_μ. We remind that we need to choose step values for FWI model update (equation (V.4)), that are for each inverted parameter ζ_{η_λ} = 10 and ζ_{η_μ} = 20. We perform FWI over different misfit functions in order to select the best one to invert viscosity. We invert over the low real frequencies 100 kHz, 200 kHz and 300 kHz in order to save computational resources and time, and present the inversion results in Figure V.18.

The misfit functions proposed by *Hawen* [Faucher, 2021] that we test are defined as follows. We define the misfit function J_0 as the difference between the simulation and the data:

$$J_0 = \frac{1}{2}\sum_{src}\left(\sum_{rcv}(simulation - data)^2\right). \tag{V.12}$$

We can define variations using only the real of imaginary part of the signals

$$J_{0R} = \frac{1}{2}\sum_{src}\left(\sum_{rcv}\left(\mathrm{Real}(simulation) - \mathrm{Real}(data)\right)^2\right). \tag{V.13}$$

$$J_{0I} = \frac{1}{2}\sum_{src}\left(\sum_{rcv}\left(\mathrm{Imag}(simulation) - \mathrm{Imag}(data)\right)^2\right). \tag{V.14}$$

We define the misfit function J_{log} as the L2 difference between the natural logarithm of the signals:

$$J_{log} = \frac{1}{2}\sum_{src}\left(\sum_{rcv}\left(\ln(simulation) - \ln(data)\right)^2\right). \tag{V.15}$$

We define J_{mod} as the L2 difference between the modulus of the signals:

$$J_{mod} = \frac{1}{2}\sum_{src}\left(\sum_{rcv}\left(\,|simulation| - |data|\,\right)^2\right). \tag{V.16}$$

A variant is to use the L2 difference between the natural logarithm of the modulus of the wavefields:

$$J_{log-mod} = \frac{1}{2}\sum_{src}\left(\sum_{rcv}\left(\ln(|simulation|) - (\ln(|data|))\right)^2\right). \tag{V.17}$$

We can also use the L2 difference between the phase of the signals:

$$J_{\phi} = \frac{1}{2}\sum_{src}\left(\sum_{rcv}\left(\mathrm{Phase}(simulation) - \mathrm{Phase}(data)\right)^2\right). \tag{V.18}$$

The final reconstructions using the different misfit functions are shown in Figure V.18, and the difference values with respect to the chosen misfits are presented in Figure V.19. Final results in Figure V.18 clearly show different results for η_λ and η_μ. The goal here is to find the most efficient misfit functions to invert viscosity before manipulating the parameter functions and find the best couple (misfit - parameter functions) for viscosity recovery. The parameter η_μ is approximately well recovered (at least concerning the shape of the anomaly) for almost every chosen misfit functions, besides J_{log} and J_ϕ. When we look at the misfit values for these two functions in Figure V.19, we see that the difference value decreases slowly for each inverted frequency (or even increases brutally in the misfit J_{log} at the end of inversion). This is not expected as we want to see a decrease as iterations progress. Hence we discard these two misfit functions for viscosity inversion.

Concerning η_λ recovery, none of the misfits seems satisfactory. It might be that the inversion is stuck in a local minimum or that the data (wavefield) are not sensitive enough to variation of η_λ. We could try to improve results with another parameter function and/or with more iterations (by inverting on higher frequencies). The already discarded misfit functions J_ϕ and J_{log} show the worst recovery of the shape of anomaly as well for η_λ. We can also discard the misfit functions J_0 and its variants J_{0R} and J_{0I} because they seem to invert a very strong artifact in the upper part of the medium. Also,

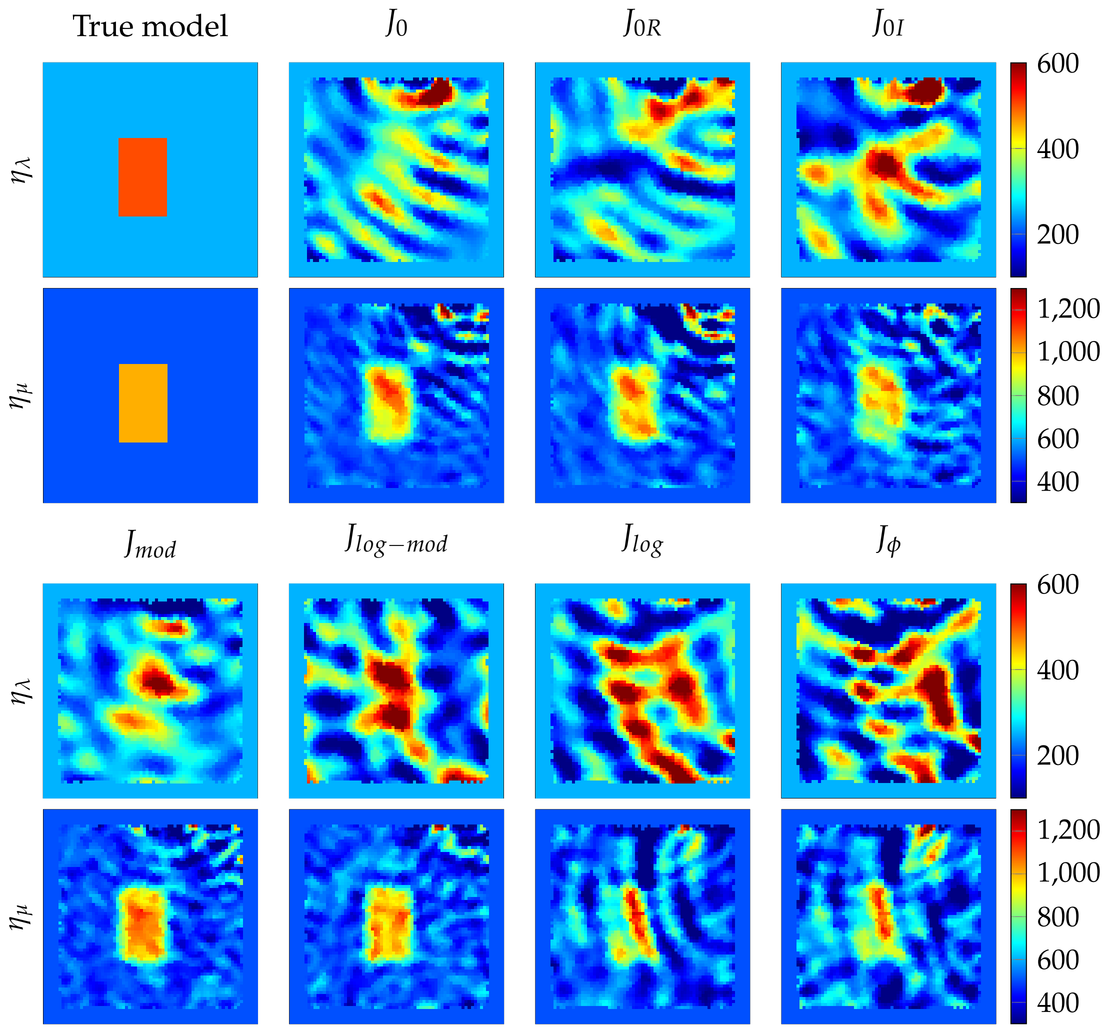

Figure V.18: Comparison of different misfit functions on η_λ and η_μ inversion results in [Pa s] on the frequencies 100, 200, 300 kHz (only the result in 300 kHz is displayed) with constant initial models of $\eta_\lambda = 250$ Pa s and $\eta_\mu = 500$ Pa s. Absorbing boundary conditions.

η_μ parameter is not very well inverted for misfit J_{0I} compared to the two remaining misfit functions J_{mod} and $J_{log-mod}$.

It is not surprising to have the best results when we use the modulus of the wavefields, because viscosity is directly linked to attenuation and amplitude of the signal. Therefore, we expect the misfit function based upon the modulus of the signals to give us the best results.

According to this analysis of inversion results for different misfit functions in Figure V.18, we keep the two misfits functions J_{mod} and $J_{log-mod}$ for the following experiments. We now want to investigate if we can correctly invert the viscous parameter η_λ with different parameter functions, that we develop in the next subsection, and with more iterations thanks to the addition of higher frequencies.

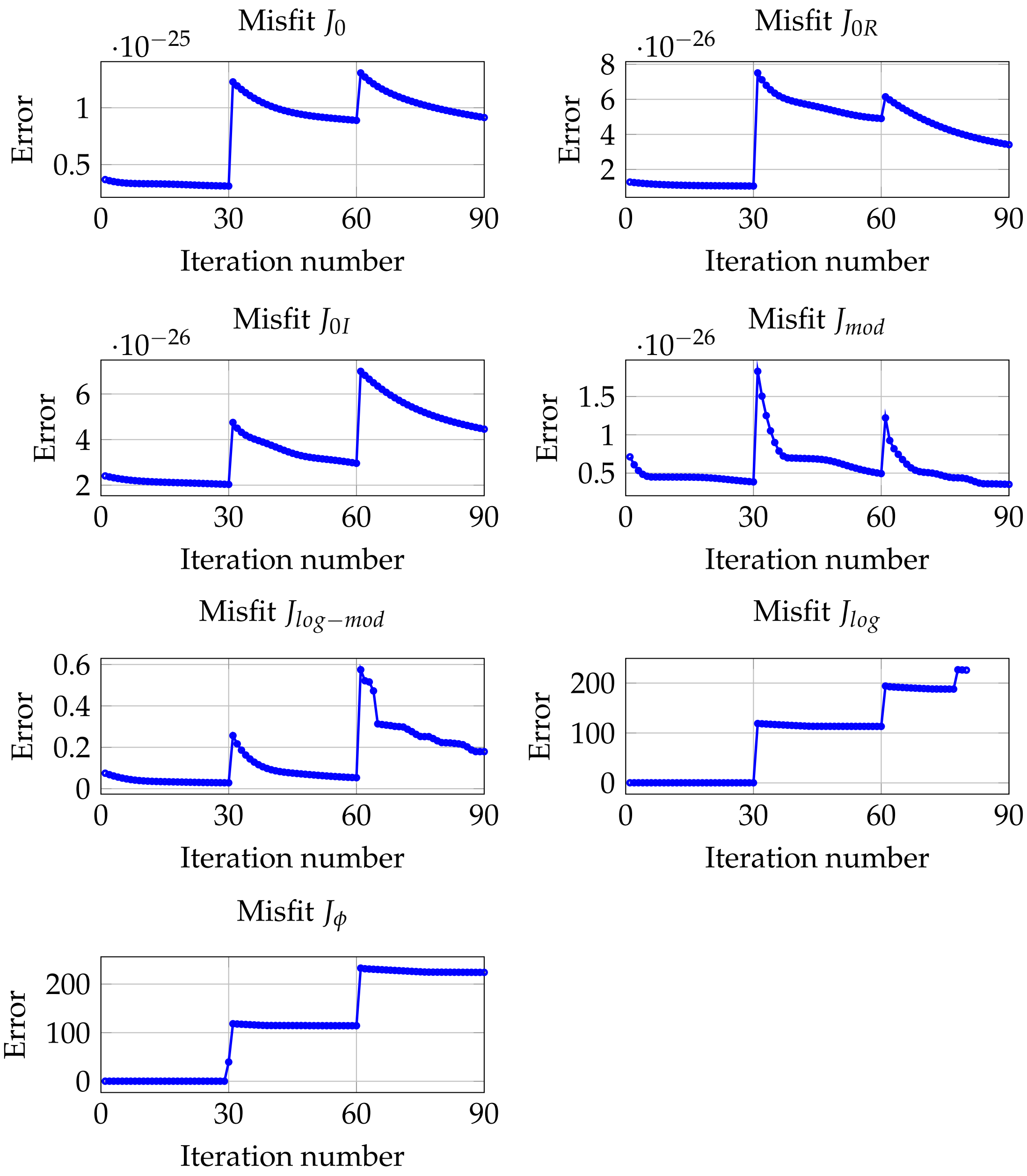

Figure V.19: Misfit values corresponding to the inversion of Figure V.18 for different misfit functions (equations (V.12)–(V.18)) between 100 and 300 kHz for a maximum of 30 iterations per frequency).

4.3 Test of different parameter functions

Along with sensitivity to misfit functions as seen in the previous subsections, inversion results can differ depending on the chosen parameter function that plays an important role, as shown by Faucher [2017] in chapter 5. We define the parameter p, that is in our case η_λ or η_μ. The tested parameter functions available in *Hawen* [Faucher, 2021] as well as their used step values ζ_{η_λ} for η_λ and ζ_{η_μ} for η_μ are listed below:

- $[p]$ for inversion of the parameter itself (as the previous subsection), of steps $\zeta_{\eta_\lambda} = 10$ and $\zeta_{\eta_\mu} = 20$.
- $[p^2]$ for inversion of the parameter squared, of steps $\zeta_{\eta_\lambda} = 5000$ $\zeta_{\eta_\mu} = 20000$.
- $[1/p]$ for inversion of the inverse of the parameter, of steps $\zeta_{\eta_\lambda} = 0.1$ and $\zeta_{\eta_\mu} =$

0.05 for the misfit funtion J_{mod} ; and of steps $\zeta_{\eta_\lambda} = 0.2$ and $\zeta_{\eta_\mu} = 0.1$ for the misfit function $J_{log-mod}$.

- $[\sqrt{p}]$ for inversion of the square root of the parameter, of steps $\zeta_{\eta_\lambda} = 4$ and $\zeta_{\eta_\mu} = 5$.
- $[1/\sqrt{p}]$ for inversion of the inverse square root of the parameter, of steps $\zeta_{\eta_\lambda} = 0.25$ and $\zeta_{\eta_\mu} = 0.2$.
- $[\ln(p)]$ for inversion of the natural logarithm of the parameter, of steps $\zeta_{\eta_\lambda} = 1$ and $\zeta_{\eta_\mu} = 1.5$.

These step values were defined after numerous trial and errors, that are not developed here.

Inversion results with respect to different parameter functions and using the two misfit functions J_{mod} and $J_{log-mod}$ (equations (V.16) and (V.17)) are displayed in Figure V.20. We performed the inversion over the real frequencies 100 kHz, 200 kHz and 300 kHz. The goal here is to find the best couple [misfit function - parameter funtion] to invert attenuation, before going to the higher frequencies and save computational resources.

Once again, the η_μ parameter is the best recovered, apart from a few exceptions (misfit J_{mod} with parameter function $[1/\sqrt{p}]$) and misfit $J_{log-mod}$ with parameter function $[1/p]$). Concerning the η_λ inversion, the best results are without hesitation when we use the parameter functions $[p]$ and $[p^2]$. In conclusion we select these two parameter functions to carry on the inversion using the higher frequencies, from 400 kHz to 900 kHz every 100 kHz.

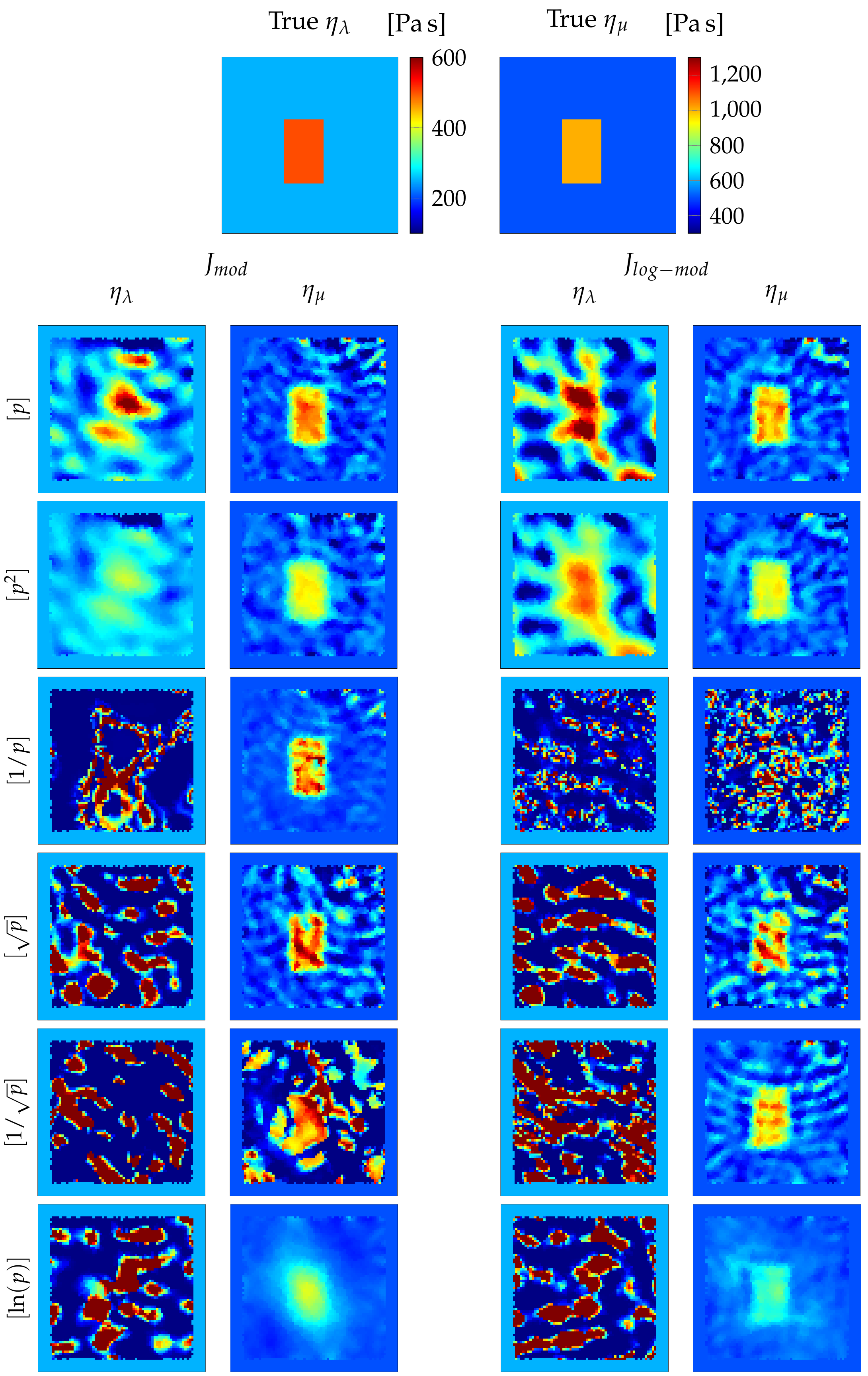

Figure V.20: Comparison of different parameter functions on η_λ and η_μ with the misfit functions J_{mod} and $J_{log-mod}$. Inversion results on the frequencies 100, 200, 300 kHz (only the result in 300 kHz is displayed) with constant initial models of η_λ = 250 Pa s and η_μ = 500 Pa s. Absorbing boundary conditions.

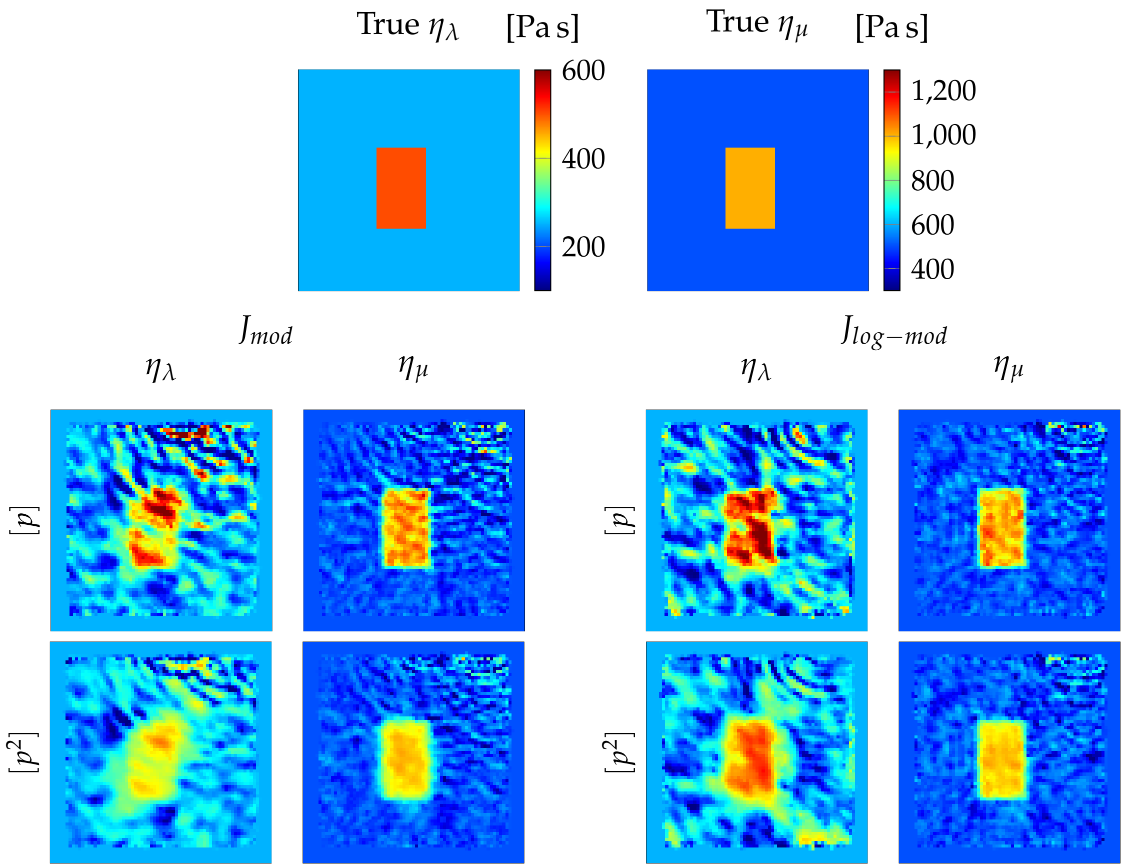

Figure V.21: Viscosity inversion result at 900 kHz with misfit functions J_{mod} and $J_{log-mod}$ and parameter functions $[p]$ and $[1/p]$, using constant initial modeld of η_λ = 250 Pa s and η_μ = 500 Pa s and absorbing boundary conditions.

Final inversion result is shown in Figure V.21, where we see that the shape and values are well recovered for η_μ for the couples misfit - parameter function (J_{mod} - $[p]$), ($J_{log-mod}$ - $[p]$) and ($J_{log-mod}$ - $[p^2]$). As for η_λ, it is subject to discussion, but we find that the best recovery is when we use the misfit function $J_{log-mod}$. Also, when we compare the two used parameter functions, we see that the use of $[p]$ causes large variation of η_λ values within the background and the anomaly, while the use of $[p^2]$ allows a smoother (and more accurate) result.

After having tested different couples misfit functions - parameter functions for attenuation inversion, we select the couple ($J_{log-mod}$ - $[p^2]$) for attenuation recovery in the next section, when we have a velocity anomaly as well as an attenuation anomaly to recover. Note that the tests have been carried out under one specific configuration (data all around, one positive anomaly, with Kelvin-Voigt viscoelastic model). Such a study should be performed in other contexts to see if the (misfit - parameter function) selection is universal. We could also envision to update the misfit function at some point in inversion to get the best results.

5 Velocity and viscosity anomaly

We consider in this section a 7 cm x 7 cm medium containing an anomaly in velocity and in viscosity located at the same place, and absorbing boundary conditions. Similarly to the two previous sections, the V_P values are of 6320 m s^{-1} in the background with an anomaly of 5000 m s^{-1}, the V_S values are of 3100 m s^{-1} in the background with an anomaly of 2300 m s^{-1} (Figure V.22), the medium follows a Kelvin-Voigt viscoelastic model of η_λ is of 250 Pa s in the background with an anomaly of 500 Pa s, and η_μ is of 500 Pa s in the background with an anomaly of 1000 Pa s (Figure V.23).

The method here is to first invert the velocity (it means that the attenuation parameters remain at the initial values and are not updated). Then, we use the velocity inversion results as a known input parameter for viscosity inversion in a second time (as in Pan and Wang [2020]).

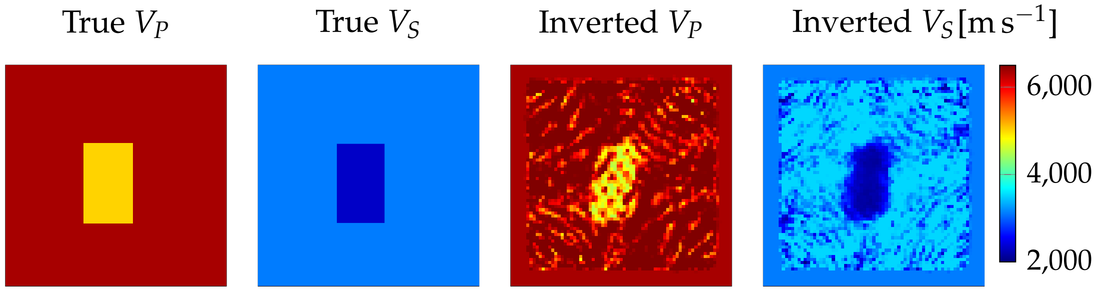

Figure V.22: Velocity inversion results with absorbing boundary conditions at 900 kHz with constant initial models V_P = 6320 m s^{-1}, V_S = 3100 m s^{-1} and input constant viscosity η_λ = 375 Pa s and η_μ = 750 Pa s.

Velocity inversion is shown in Figure V.22, where we invert over the real frequencies from every 100 kHz from 100 kHz to 900 kHz, with a constant initial velocity model of V_P = 6320 m s^{-1} and V_S = 3100 m s^{-1}. The input attenuation was assumed constant (even if it not) and of values η_λ = 375 Pa s and η_μ = 750 Pa s. Here, we use the misfit function J_0 and invert over the inverse of elastic parameters $[1/p]$ λ and μ with steps ζ_λ = 5×10^{-12} for λ and ζ_μ = 2×10^{-11} for μ. We see in this figure that inversion did not work as well as in Figure V.7 where viscosity is constant, but we still recover the good location of the anomaly. Concerning the recovered values, we see that V_P is too high in the background and V_S is too low in the background. It may be due to the wrong input viscosity that adds errors in the simulated wavefield. This highlights the importance of knowing accurately the attenuation values, even for velocity inversion [Groos et al., 2014].

We propose two examples of viscosity inversion. One with the true velocities as an input parameter (Figure V.23), and one with inverted velocities as an input parameter (Figure V.24). In both cases, the initial viscosity values are η_λ = 500 Pa s and η_μ = 1000 Pa s, and we invert the parameters squared $[p^2]$ over the misfit function $J_{log-mod}$. When we assume we know the true velocity (Figure V.23), the viscous parameters are fairly recovered, as in Figure V.21. the parameter η_μ is more accurately recovered than η_λ which, at least, shows an anomaly at the appropriate location.

When we use the inverted velocity to invert the viscous parameters (Figure V.24), as we would do in practice, we do not accurately recover the models. In our example, anomaly in η_μ is not captured, and η_λ has not the expected shape. It could be the effect of cross-talk between parameters [Operto et al., 2013; Pan and Wang, 2020], where the first inversion in velocity tries to compensate the wrong input viscosity.

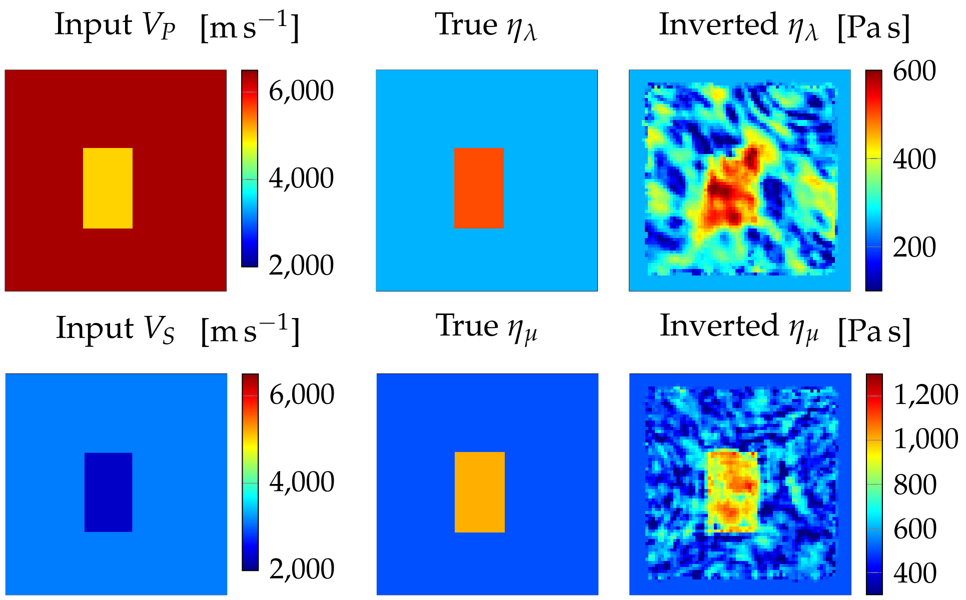

Figure V.23: Viscosity inversion results with absorbing boundary conditions at 900 kHz with constant initial models η_λ = 500 Pa s, η_μ = 1000 Pa s and input velocities being the true velocities.

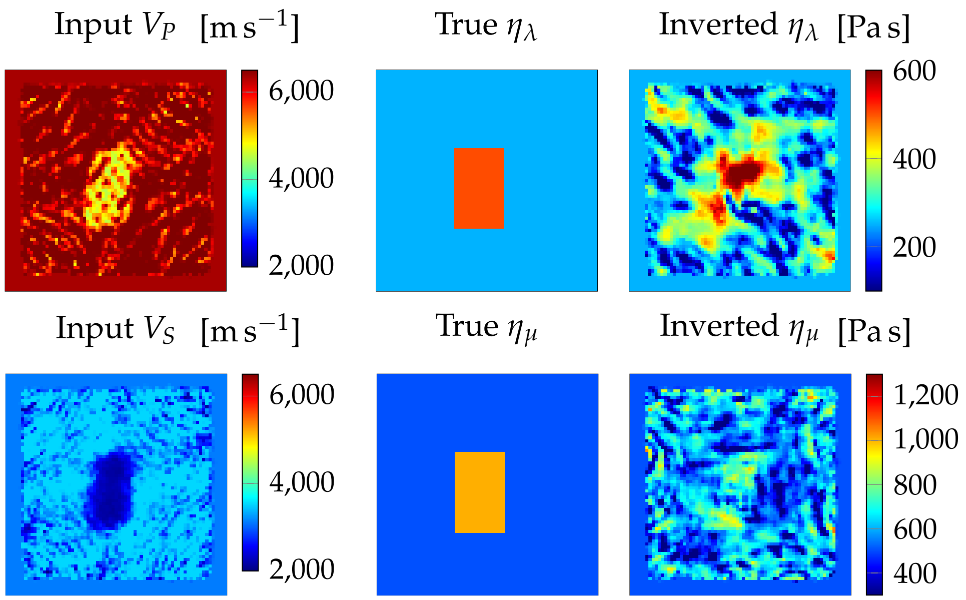

Figure V.24: Viscosity inversion results at 900 kHz with constant initial models η_λ = 500 Pa s, η_μ = 1000 Pa s and input velocities being the inverted velocities. Absorbing boundary conditions.

6 Conclusions and perspectives on FWI chapter

We first invert an anomaly in elastic parameters in a 2D domain of 7 cm x 7 cm, considering absorbing boundary conditions. Then, we consider free-surface boundary conditions to highlight the difficulties in performing FWI in laboratory context for inversion of elastic parameters due to the reflections. We showed that the difficulty can be overcome by using the complex frequency, the imaginary part - Laplace frequency f_L - playing the role of a damper.

We have investigated the reconstruction of the viscosity - attenuation - by testing several couples (misfit function - parameter function) and choose the best one for attenuation recovery. We showed that in the tested conditions (absorbing boundary conditions, constant model of velocity, positive viscosity anomaly, Kelvin-Voigt viscoelastic model), the misfit functions that present the best results are the ones using the modulus of the wavefield J_{mod} (equation (V.16)) and $J_{log-mod}$ (equation (V.16)). After, we test different parameter functions over these two misfit functions and showed that we best recover η_λ and η_μ by inverting the parameter itself $[p]$ or the parameter squared $[p^2]$. The perspective of this work would be to test other configurations (free-surface boundary condition, other viscoelastic model, negative anomaly) to see if and how it may change the results.

Finally, we investigated the recovery of both the velocity and viscosity with difficulties. We need to be careful to understand where does the cross-talk between velocity and viscosity comes from. A first test could be to invert the viscosity on the experiment of Figure V.7 and check if it remains constant, that is, we want to see how FWI captures incorrect variation of viscosity to decrease the misfit, and up to which extent it hampers the reconstructions. A similar test with inverting velocity in the experiment of Figure V.17 can be done as well.

Furthermore, we have only considered absorbing boundary conditions when reconstructing both the velocities and viscosities. In order to take laboratory conditions into account, the next step would be to successfully invert an anomaly in velocity and viscosity with free-surface boundary conditions. Only then, we can perform 3-D FWI in order to try to overcome and understand every difficulty with synthetic experiments before trying to perform FWI with real data.

Chapter VI

Conclusions and perspectives

In this thesis, we investigated the reconstruction of the attenuation properties of natural samples from the measurements of seismic waves. Attenuation is an intrinsic component of the medium that results in the loss of energy of waves. Attenuation also relates with the change in porosity of the material or can indicate the presence of fluids [Dasgupta and Clark, 1998; Pang et al., 2019]. Therefore, it is a key component for fully understanding the composition and behaviour of materials. In our work, we first provide a comprehensive review of the equations describing the propagation of waves with attenuation. Attenuation is a frequency-dependent phenomenon, and we have carried out numerical simulations in the frequency domain to illustrate the effect of attenuation depending on various parameters such as the geometry of the sample, the assumptions regarding the boundary conditions, and the level of attenuation. It served us to design a method to reconstruct the representative attenuation coefficient of a sample from the measurements of the global wavefield, and where we are also able to reconstruct the attenuation model characterizing the medium. The method is subsequently applied to experimental data, and we identify the representative attenuation parameters of two samples of different natures with aluminum and Fontainebleau sandstone. Then, to uncover the finer heterogeneities within a medium, we provided some preliminary studies using the full waveform inversion method.

In the theoretical chapter, we set up the mathematical framework by detailing the equations for wave propagation. As its name indicates, viscoelasticity is composed of a viscous and an elastic component, which can be assembled in different ways. Here, we focused on three attenuation models with the Maxwell, Kelvin–Voigt, and Zener models. Each model has its specificity and proposes a different behaviour of attenuation of waves with frequency, for instance attenuating more or less the low-frequency waves. One difficulty in the characterization of media is that the attenuation model is typically unknown a priori. Working in the frequency domain is particularly convenient as all of the different models can be unified in the same equation, working with complex-valued parameters. In this chapter, we further introduced the representative parameters that quantify the level of attenuation of a medium, with the quality factor Q and attenuation coefficient β.

In the numerical chapter 3, we perform numerical simulations in order to investigate the wave propagation with attenuation, starting by considering a homogeneous isotropic medium. We first use absorbing boundary conditions surrounding the sample, that is, assuming waves can freely escape. This allows us to study direct waves, avoiding reflection and conversion. We separate the P- and S-waves by applying a divergence or a curl operator to the global wavefield, and we recover the viscoelastic parameters associated with each type of waves. We progressively consider the configuration of laboratory experiments by incorporating free-surface boundary conditions, that is, with waves being reflected on the boundary of the sample. We then analyze the first wave arrivals from a source at the surface of the sample to receivers located all around the sample. The signal is drastically affected by the reflections and conversions at the boundaries, leading to complicated signals where events are superposed.

To recover the attenuation properties of a medium from waves measured at the boundary, we develop a method that works with consecutive windows of frequency. For each window, we identify the decay of the wavefield amplitude, which gives us the representative frequency-dependent attenuation parameters of the medium and, with all of the frequency windows, we reconstruct the attenuation model as well. The method takes advantage of the multiple reflections inside the domain from the free-surface boundary conditions, such that the loss of energy of the wave measured at the receivers is only due to the medium's attenuation properties. The method further uses the equilibration of energy (equipartition) between the P- and S- waves: after several reflections (reached after a given propagation time referred to as the equipartition time), the S-waves overwhelm the wavefield and the measured decrease in amplitude of the global wavefield corresponds to the S-wave attenuation. Therefore, the method needs a relatively long propagation time and recording in order to be as accurate as possible in attenuation recovery. While the method is unable to capture the P-wave attenuation (because of equipartition that consequently lead to measured data that are relatively insensitive the P-wave attenuation), we have shown that it is efficient regardless of the geometry of the sample, of the positions of the measurement and of the wave directions / components measured.

In the experimental chapter, we built an experimental set-up allowing to record wave propagation with a piezoelectric source and a non-contact interferometer laser receiver. We measured the wavefield in aluminum blocks and natural rock samples cylinders (Fontainebleau sandstone, Carrara marble, and diorite). We recovered the elastic properties of the samples, first using the first-arrivals in the measurements to identify the P- and S-velocities of the seismic waves. Then, we studied the impact of the PZT source in contact with the samples, that seems to result in a local modification of the boundary conditions. Eventually, we use the method developed in Chapter 3 and validated with the numerical simulations to recover the representative S-waves frequency-dependent viscoelastic law, as well as the elastic and viscous parameters of the media. We recover a Maxwell viscoelastic law in aluminum and a Zener viscoelastic law in the Fontainebleau sandstone, Carrara marble, and diorite rock samples. These viscoelastic models and parameters may serve as initial models for FWI for the purpose of recovering finer heterogeneities.

In Chapter 5, we review the principles of Full Waveform Inversion, which can quantitatively reconstruct the heterogeneities within a medium from the measurements of seismic waves, and that is based upon an iterative minimization algorithm. As preliminary synthetic experiments, we investigated the reconstruction in 2D media containing an anomaly in velocity and/or viscosity.

For the reconstruction of anomaly in velocity, we encounter difficulties when we follow the configuration of a laboratory experiment, that is, when we impose free-surface boundary conditions around the samples, leading to multiple reflections. To overcome this issue, we have proposed to work with complex frequencies. Indeed, the imaginary part of the frequency plays the role of an artificial damper in the wavefield and the reflections are thus reduced without modifying the data.

When considering an anomaly in viscosity, we carried out preliminary experiments with absorbing boundary conditions to evaluate the most efficient parametrization for FWI. We investigate several couples (misfit function - parameter function) that allow the most accurate inversion.

We see that there exist difficulties in inverting accurately the viscous parameter η_λ that is associated with the Lamé parameter λ. This can be due to the imprint of the parameters μ and λ in the wavefield, as both the P- and S- waves are functions of μ while only the P-waves depend on λ. Following this idea, the measured data (mixing P-and S-waves) would be more sensitive to variation of μ than to variation of λ.

Eventually, we considered a medium containing both velocity and viscosity anomalies at the same location, but the results of the inversion show the possible trade-off between parameters, despite the use of a two-step approach where we first reconstruct the velocity (fixing the attenuation) and the attenuation (keeping fixed the velocities reconstructed at the first step).

To summarize, we have investigated the reconstruction of attenuation by first proposing a method to recover the representative attenuation of a medium from surface measurements. Then the recovered representative parameters would serve as initial guesses for FWI to recover heterogeneities. Some limitations remain and we highlight the three following. One first limitation is that the attenuation of the P-waves is not obtained because of the equipartition. Another limitation is the impact of the surface contact of the PZT source on the sample that can lead to local artifacts. In addition, the reconstruction of the viscoelastic heterogeneities in a laboratory context with FWI requires efficiently treating the trade-off between the parameters.

We recover the representative attenuation law and values of a medium with equipartition theory, indicating that the recovered attenuation values are close to the S-waves ones. The limitation is that we do not know about the P-waves attenuation values, or if the P-wave attenuation is higher or lower than the S-waves attenuation. Further analyses need to be done, for instance with working with the direct wave arrivals in order to be able to work before the first wave conversion. The difficulty here lies on the *low* attenuation definition. In that case, the difference in amplitude between one point measured close to the source and another point measured further is going to be low (after beam spreading correction). In order to make parallel numerical/experimental analysis, a sufficiently small wavelength as well as accurate amplitude measurements would be needed.

In this work, we considered models of isotropic viscoelasticity to represent the media and to understand the phenomena of wave attenuation. One next step to accurate modeling is to enrich our formulations, for instance considering anisotropy. On the one hand, anisotropy would not change the formulation of the wave equations (yet working with a full elasticity tensor), it however introduces additional physical parameters [Carcione, 2007], hence increasing the number of unknowns to identify. Future step would also be the consideration of poroelasticity, which would be more challenging because it implies changing the equations of stress-strain relationships and thus wave propagation equations [Carcione, 2007], increasing the computational complexity in addition to the number of unknowns.

Concerning the experimental part, we pointed out that the surface of contact between the PZT source and the sample may have an impact in the data because the boundary conditions are locally modified. It would be interesting to quantify this impact with numerical experiments or laboratory measurements with aluminum samples of different sizes.

Reconstructing heterogeneity using FWI represents a longer-term perspectives that we initiated to recover a heterogeneous attenuation inside a sample measured in the laboratory. We have interesting first results with the comparison of different misfit functions and parameter functions, that pave the way towards preliminary applications. However, an extensive parametric study would be needed in order to understand how to reduce the trade-off between velocity and viscosity, and to enhance the η_λ viscous parameter recovery. Eventually, inversions would need to be performed in 3D with free-surface boundary conditions. Here, we expect that the use of complex frequencies would be as effective as in our 2D experiments. Nonetheless, the computational cost of 3D FWI remains challenging and we expect that having selected the appropriate misfit functions and parametrization would help control the required number of iterations.

Chapter VII

Résumé en français

Ce chapitre rédigé en français décrit les résultats principaux de la thèse. Il a pour but de donner un aperçu des théories et développements majeurs exposés en anglais dans les chapitres précédents.

1 Introduction

En sismique, l'atténuation des ondes est un bon indicateur de changement de porosité, fracturation, ou encore de présence de fluides dans la roche [Dasgupta and Clark, 1998; Pang et al., 2019]. L'atténuation varie avec la fréquence [Müller et al., 2010; Carcione, 2007; Gurevich and Pevzner, 2015] et est souvent associée au terme "facteur qualité" Q qui décrit la capacité d'une roche à propager une onde.

Le choix s'est porté sur la viscoélasticité pour prendre en compte l'atténuation des ondes sismiques, défini par α la décroissance en amplitude en fonction de la distance de propagation $[\mathrm{Np\,m^{-1}}]$. Dans un sismogramme, l'atténuation sera plutôt définie par le terme β en $[\mathrm{Np\,s^{-1}}]$, obtenu en multipliant α par la vitesse de propagation de l'onde. Le facteur qualité est relié à la décroissance en amplitude selon l'équation ci-dessous:

$$Q = \frac{\omega}{2\alpha V} = \frac{\omega}{2\beta}, \tag{VII.1}$$

avec V la vitesse de propagation de l'onde en $[\mathrm{m\,s^{-1}}]$ et la pulsation $\omega = 2\pi f$, f étant la fréquence en [Hz].

La théorie viscoélastique consiste en un assemblage de ressorts élastiques et de pistons visqueux, où les ressorts vont aider à propager l'onde, et les pistons vont atténuer la propagation. Une illustration des modèles viscoelastiques de Maxwell, Kelvin-Voigt et Zener est donnée en Figure VII.1 où, selon Carcione [2007], M_e représente le module élastique, M_η représente le module visqueux, σ est la contrainte générée dans le système ressort-piston et ϵ est le déplacement associé. Par exemple, dans le cas du modèle de Maxwell, il faut imaginer une contrainte σ qui va être transmise par le ressort, puis atténuée par le piston pour générer un déplacement ϵ qui sera moindre par rapport au déplacement du ressort seul.

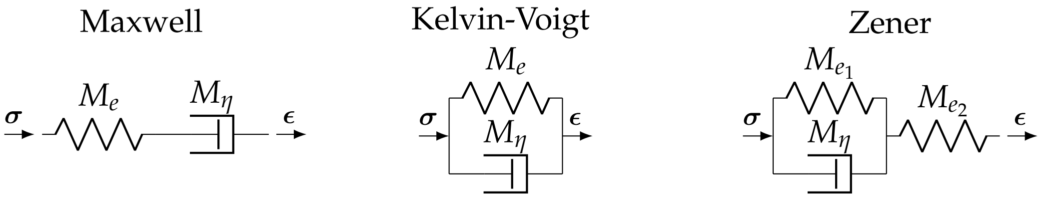

Figure VII.1: Représentation schématique des modèles viscoélastiques de Maxwell, Kelvin-Voigt et Zener.

Ces systèmes viscoélastiques, montés en série et/ou en parallèle, permettent de créer différents comportements en fonction de la fréquence, comme par exemple en Figure VII.2 où le facteur qualité décroît avec la fréquence pour le modèle de Kelvin-Voigt et croît avec la fréquence pour le modèle de Maxwell. Le modèle de Zener, quant à lui, se comporte comme un Kelvin-Voigt pour les basses fréquences et comme un modèle de Maxwell pour les hautes fréquences.

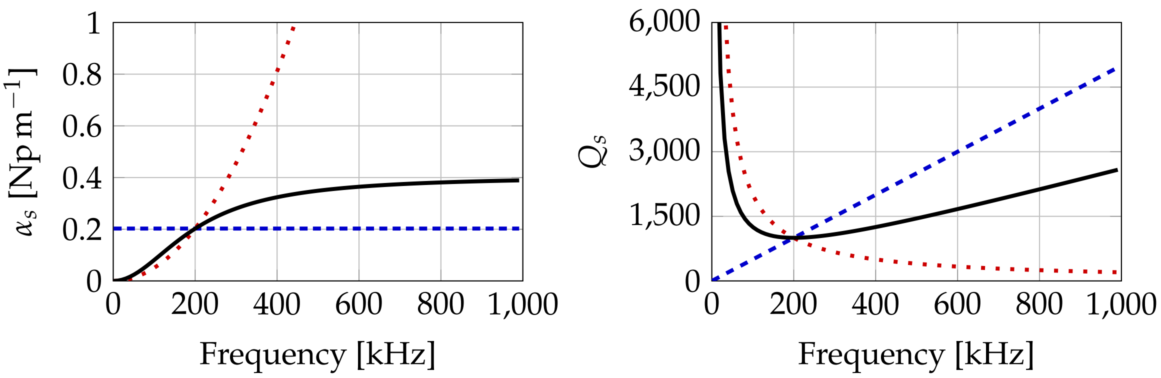

Figure VII.2: (gauche) Atténuation et (droite) facteur qualité des ondes S en fonction de la fréquence pour respectivement un modèle viscoélastique de [- - - -] Maxwell avec η_μ = 20.65 MPa s, [· · · ·] Kelvin-Voigt avec η_μ = 20.65 Pa s et [——] Zener avec τ_ϵ = 796.57 ns et τ_σ = 794.98 ns. Ici, le paramètre élastique μ est de 25.95 GPa.

2 Résultats principaux

2.1 Étude numérique

Pour l'étude de l'atténuation des ondes sismiques en contexte de laboratoire, il faut prendre en compte les conditions aux limites de surfaces-libres. Dans ce cas, en plus de la présence d'ondes de surface, les ondes de volumes (P et S) sont réfléchies et converties aux bords. Une étude numérique a permis de mettre en place une methode permettant de prendre parti de ces nombreuses réflexions et de retrouver l'atténuation des ondes S dans un milieu peu atténuant. En effet, à partir d'un certain nombre de réflexions et conversions définis par un temps minimum de propagation donné par l'équation (VII.2) [Snieder, 2002], le signal sismique atteint un point d'équilibre d'énergie entre les ondes P et S qui est dominé par les ondes S. Il s'agit du phénomène d'équi-répartition de l'énergie [Ryzhik et al., 1996; Margerin et al., 2009] et, dans ce contexte, il n'y a plus besoin de prendre en compte le phénomène de divergence géométrique lorsque l'onde se propage puisque l'énergie reste capturée à l'intérieur du domaine. Le temps de propagation pour atteindre l'état d'équilibre d'énergie est donné par [Snieder, 2002] :

$$\tau_{PS} = \frac{a(V_S^3 + 2V_P^3)}{2V_P V_S^3}, \tag{VII.2}$$

avec τ_{PS} le temps de propagation des ondes avant d'atteindre le point d'équi-répartition, V_S la vitesse des ondes S, V_P la vitesse des ondes P, et a la taille de l'échantillon.

La méthode pour déterminer les valeurs d'atténuation en fonction de la fréquence se définit comme suit (Figure VII.3) : à l'aide d'un filtre gaussien en fréquence, il faut sélectionner une petite fenêtre (de ± 10 kHz autour de la fréquence d'intérêt dans notre cas). Ensuite, revenir en temps avec une transformée de Fourier inverse. La décroissance en amplitude visible sur le sismogramme est uniquement due à l'atténuation à cause du phénomène d'équi-répartition décrit plus haut. Pour récupérer cette valeur d'atténuation, il faut lisser le signal en prenant l'envelope de la transformée de Hilbert, l'élever au logarithme néperien, et effectuer une régression linéaire dans le signal. La valeur de la pente de la fonction affine définit ainsi l'atténuation des ondes S pour la bande de fréquence sélectionnée. Répéter ces étapes sur toute la bande passante du

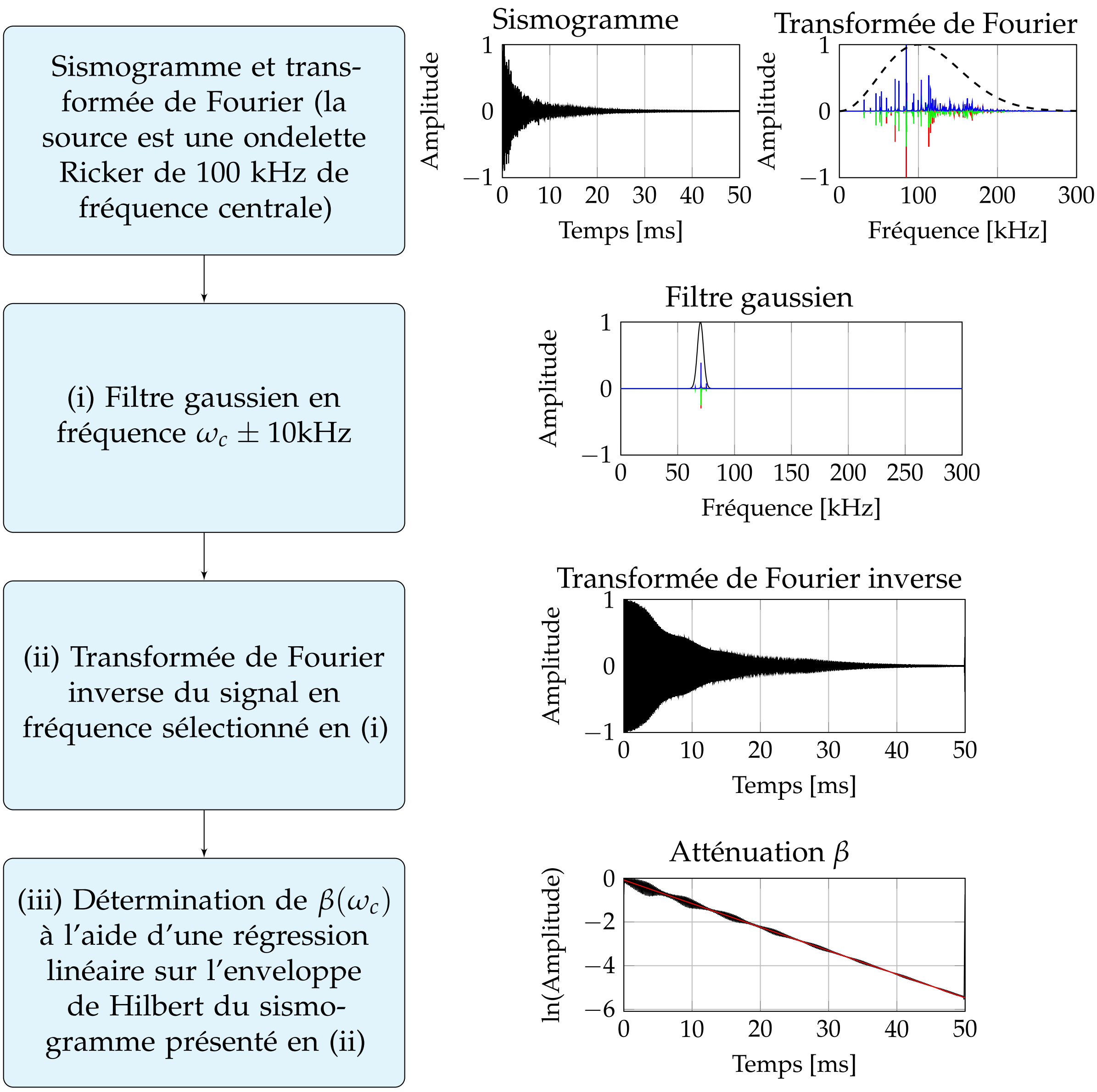

Figure VII.3: Schéma fonctionnel de la méthode de traitement du signal permettant de retrouver l'atténuation β d'une petite bande de fréquence.

signal permet de retrouver l'atténuation sur plusieurs fréquences et ainsi de retrouver des lois d'atténuation.

Cette méthode a été validée par des simulations numériques de propagation d'ondes à travers un cube de 7 cm de côté et un cylindre de 9 cm de haut pour 5 cm de diamètre présentés à la Figure VII.4. La source émet une onde dans les 3 composantes u_x, u_y et u_z, et les récepteurs enregistrent dans les 3 composantes également. La source est placée sur la base supérieure de chaque échantillon, le récepteur R1 se situe à l'intérieur de l'échantillon, le R2 se situe sur une face latérale et le R3 sur la face opposée à la source. Ainsi, il est possible de repérer un effet potentiel des ondes de surface sur l'enregistrement sismique.

Plusieurs simulations numériques ont été réalisées en changeant le modèle viscoélastique qui régit le milieu (Maxwell ou Kelvin-Voigt), et en ayant l'atténuation des ondes S supérieure à celle des ondes P, ou inversement. Les résultats montrent en

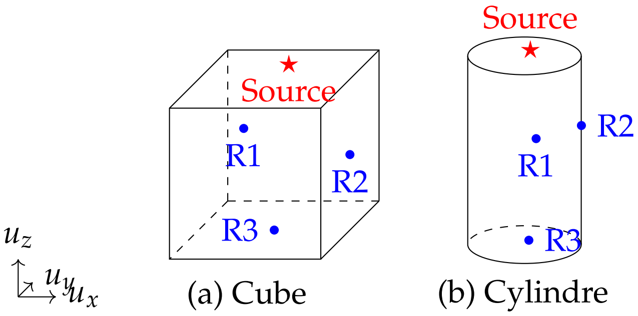

(a) Cube (b) Cylindre

Figure VII.4: Mise en place numérique. a) Cube de 7 cm de côté. b) Cylindre de 9 cm de haut pour 5 cm de large. La source est située sur la face supérieure de chaque échantillon et émet une onde dans les 3 composante. Les récepteurs enregistrent le signal dans les 3 composantes, et sont situés comme suit : le R1 est à l'intérieur des échantillons, le R2 est sur une face latérale, et le R3 est sur la face opposée par rapport à la source.

Figure VII.5 que la détermination de l'atténuation suit toujours les ondes S (comme attendu à cause du phénomène d'équi-répartition), indépendamment de la géométrie de l'échantillon, de la loi viscoélastique, de la différence $\beta_s < \beta_p$ ou $\beta_s > \beta_p$, de la localisation du récepteur (à l'intérieur ou à la surface du domaine) et de la composante d'enregistrement de celui-ci.

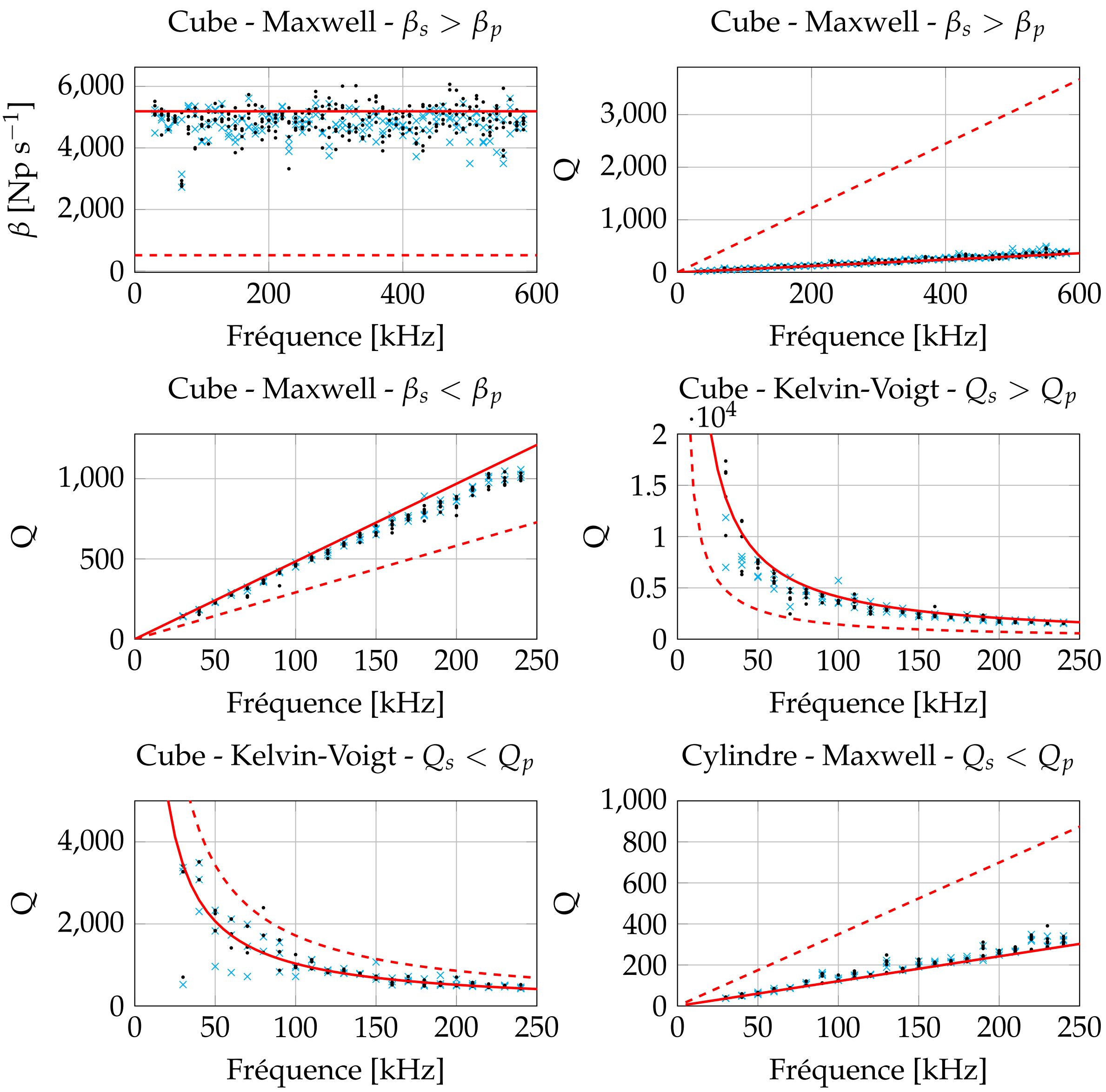
Cube - Maxwell - $\beta_s > \beta_p$

Cube - Maxwell - $\beta_s > \beta_p$

Cube - Maxwell - $\beta_s < \beta_p$

Cube - Kelvin-Voigt - $Q_s > Q_p$

Cube - Kelvin-Voigt - $Q_s < Q_p$

Cylindre - Maxwell - $Q_s < Q_p$

Figure VII.5: Détermination de l'atténuation β et du facteur qualité Q en fonction de la fréquence sur des simulations numériquesà travers un cube de 7 cm de côté ou un cylindre de 9 cm de haut pour 5 cm de diamètre qui suivent des lois viscoélastiques de Maxwell ou de Kelvin-Voigt. [- - -] β_p ou Q_p analytique. [——] β_s ou Q_s analytique. [·] Récepteurs R2 et R3 situés à la surface et enregistrant dans les 3 composantes u_x, u_y et u_z. [×] Récepteur R1 situé à l'intérieur et enregistrant dans les 3 composantes u_x, u_y et u_z.

2.2 Étude expérimentale en laboratoire

Il est donc possible d'affirmer après cette étude numérique que le signal enregistré sur un échantillon au laboratoire présentera les caractéristiques d'atténuation proches de celles des ondes S, à partir du moment où il a atteint le point d'équi-répartition. Une étude similaire a donc été menée au laboratoire à travers un cube d'aluminium de 7 cm de côté (Figure VII.6) et des carottes cylindriques de différentes roches (Figure VII.7) d'environ 5 cm de diamètre pour tous les échantillons de roche, et de 9 cm de hauteur pour le grès de Fontainebleau, et 11 cm de hauteur pour le marbre de Carrare et les deux diorites.

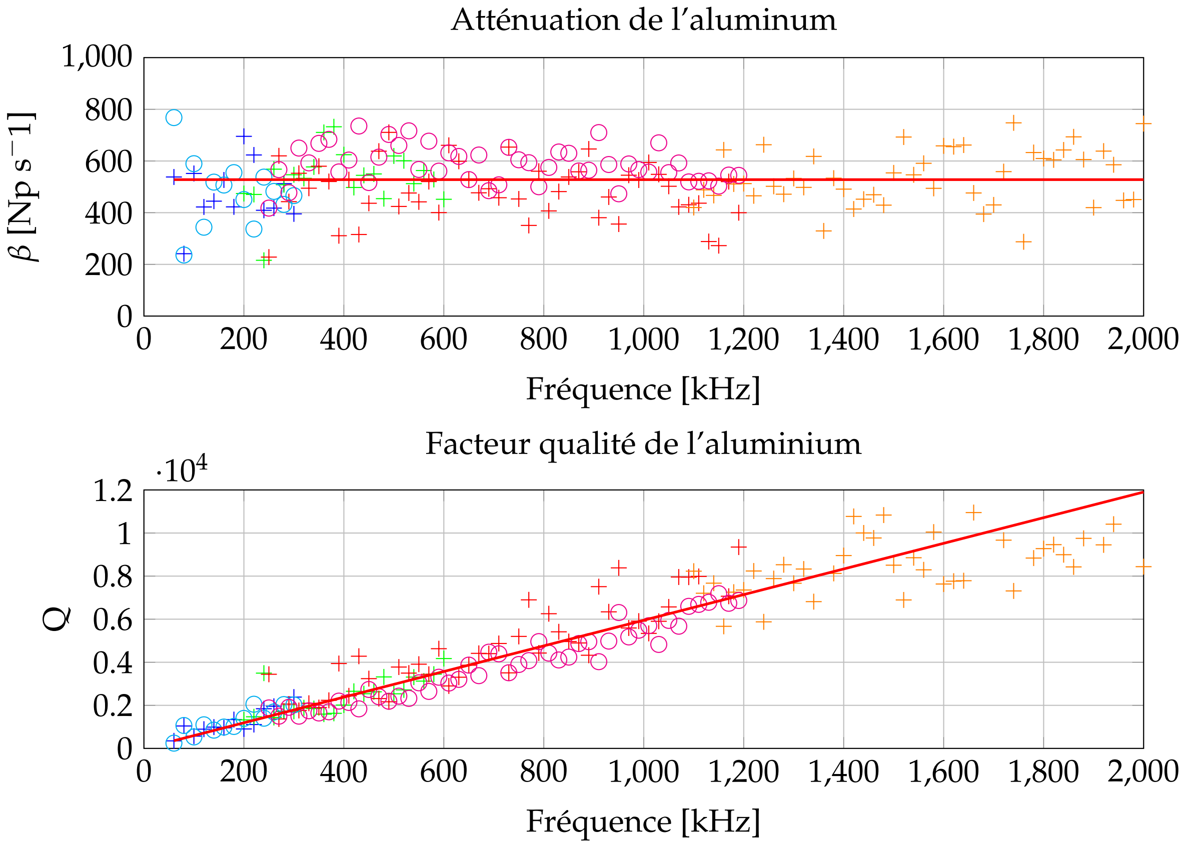

Figure VII.6: Détermination de l'atténuation β et du facteur qualité Q à travers des mesures ultrasoniques sur de l'aluminium : [+] sur la face latérale avec la source PZT de 250 kHz, [+] sur la face latérale avec la source PZT de 500 kHz, [+] sur la face latérale avec la source PZT de 1 MHz, [+] sur la face latérale avec la source PZT de 2.25 MHz, [○] sur la face opposée avec la source PZT de 250 kHz, [○] sur la face opposée avec la source PZT de 1 MHz. [——] correspond à la régression linéaire permettant de faire passer une loi viscoélastique de Macxell de paramètres μ = 25.5 GPa et η_μ = 21.1 MPa s.

Avec l'aide de plusieurs sources piézoélectriques, il a été possible d'atteindre une large bande passante et de retrouver des valeurs d'atténuation entre 60 kHz et 2 MHz. La Figure VII.6 montre que l'aluminium suit un modèle viscoélastique de Maxwell et la Figure VII.7 montrent que les roches mesurées suivent des modèles viscoélastiques de Zener. Cependant, le modèle de Zener concorde mal avec les résultats du grès de Fontainebleau et de la diorite non chauffée pour les plus basses fréquences. Cela est probablement dû à la largeur de la bande passante et aux seuls deux ressorts et un piston pour le modèle de Zener, qui ne permettent pas une grande liberté d'ajustement sur les données. Il aurait été préférable de choisir un modèle viscoélastique comportant plus de modules en série et en parallèle, comme par exemple un modèle généralisé, mais ce n'était pas l'objet de cette thèse étant donné que le but est de trouver un modèle global sur lequel se baser pour ensuite entrer dans plus de détails avec l'inversion de formes d'ondes complètes (de l'anglais Full-Waveform Inversion - FWI).

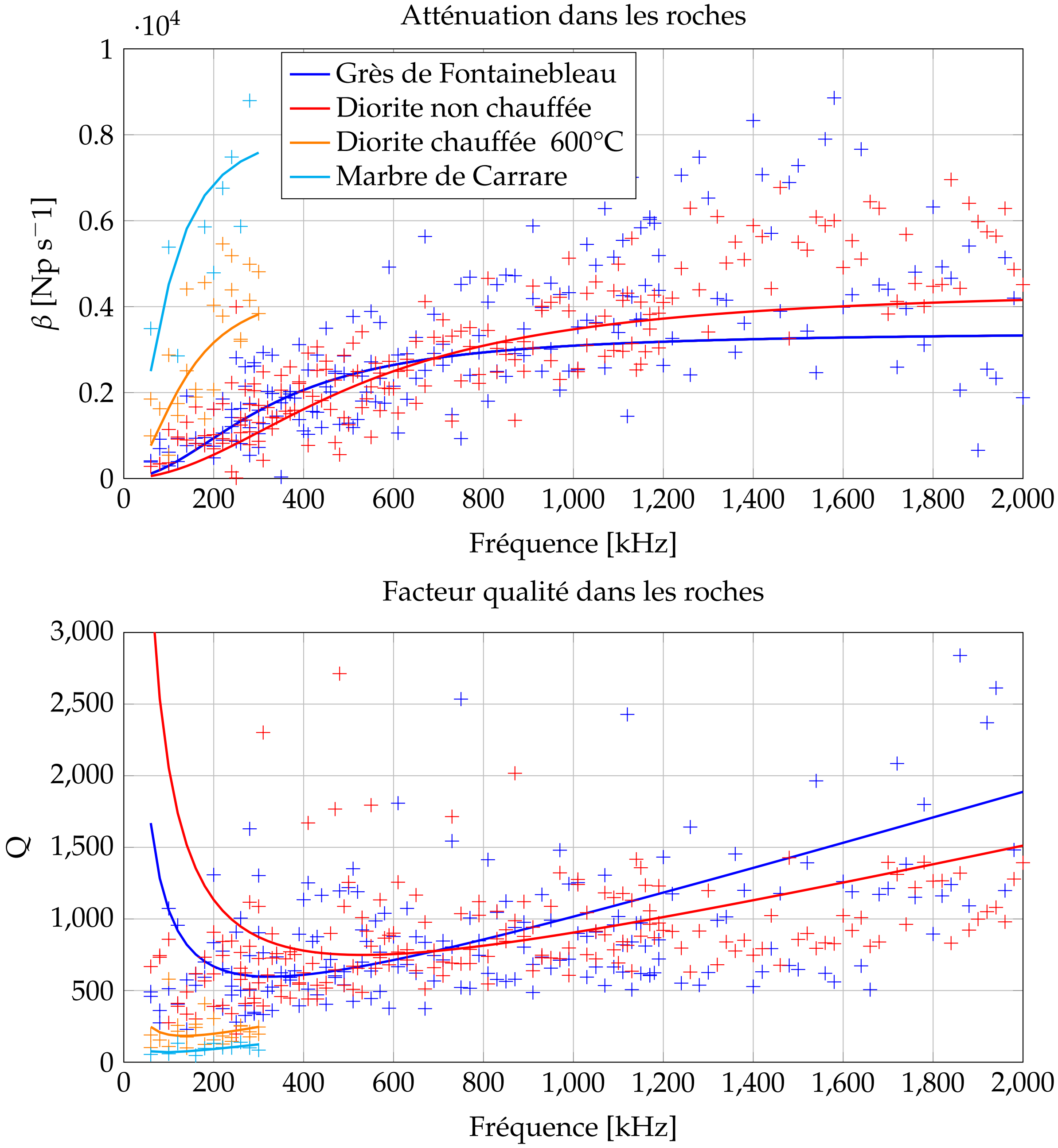

Figure VII.7: Détermination de l'atténuation et du facteur qualité Q sur des roches. [+] atténuation pour une fréquence centrale donnée. [——] Modèle viscoélastique de Zener pour des paramètres donnés en Table IV.9.

2.3 Inversion de formes d'ondes complètes (FWI)

La FWI est utilisée pour déterminer des hétérogénéités dans un milieu donné, à l'aide d'une fonction coût qui calcule la différence entre un champ d'onde enregistré avec des récepteurs et un champ d'onde simulé. Le modèle est ainsi affiné après plusieurs itérations jusqu'à ce que la différence entre les deux champs d'ondes atteigne un minimum. Une étude a été réalisée sur des synthétiques en 2D, comprenant une anomalie en vitesse et / ou en atténuation (viscosité).

Les conditions de laboratoire présentent des difficultés pour la FWI à cause des conditions aux limites de surfaces libres Ribodetti et al. [2004]. L'utilisation de la fréquence complexe sert à simuler de l'atténuation dans un milieu non atténuant sans en modifier les données. Cela va servir à faire en sorte que l'onde soit presque complètement atténuée lorsqu'elle atteint un bord de l'échantillon, et ainsi limiter les effets des réflexions dans le champ d'onde.

Il est prouvé que le choix des paramètres de FWI est primordial pour avoir des bons résultats d'inversion, notamment en choisissant correctement la fonction coût et les fonctions des paramètres inversés [Faucher, 2017; Pan and Wang, 2020]. Dans le cas de la présence d'une anomalie en atténuation, il a été vu dans ce manuscrit que dans le cas d'une anomalie en viscosité négative, suivant un modèle viscoélastique de Kelvin-Voigt, une vitesse constante dans tout le domaine et des conditions aux limites absorbantes, le couple (fonction coût - fonction des paramètres) le plus performant est lorsque l'inversion est faite sur le carré des paramètres avec la fonction coût prenant le logarithme néperien du module des champs d'ondes enregistrés et simulés.

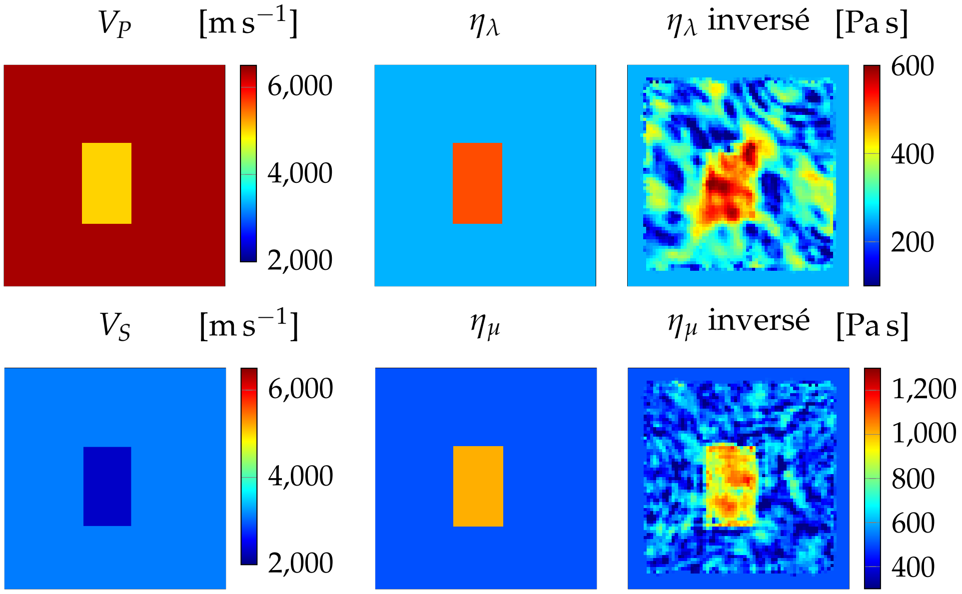

Figure VII.8: Inversion de la viscosité avec des conditions aux limites absorbantes pour un modèle de Kelvin-Voigt. Les vitesses sont supposées connues.

La Figure VII.8 présente les résultats d'inversion de viscosité dans un milieu contenant une anomalie en vitesse et en viscosité, et qui suit un modèle viscoélastique de Kelvin-Voigt. Dans cette inversion, la vitesse est considérée comme connue. Le paramètre η_μ a correctement été inversé, mais les résultats ne sont pas suffisamment satisfaisants pour le paramètre η_λ. En revanche, les études réalisées dans cette thèse posent les bases qui peuvent permettre d'aller plus loin dans l'inversion d'anomalies en viscosité en 3D, puis en contexte de laboratoire.

3 Conclusion

Ce manuscrit s'est focalisé sur la caractérisation de l'atténuation des ondes sismiques en laboratoire. La principale difficulté de l'étude sur des échantillons de taille décimétrique est la condition aux limites de surfaces libres, qui permet à la fois des réflexions dans le domaine, et aussi la présence d'ondes de surface.

Une étude numérique a été réalisée et a permis de développer et tester une méthode qui tire profit des réflexions / conversions pour déterminer une atténuation proche de celle des ondes S sur une large bande de fréquences. Des études en laboratoire ont ainsi pu être réalisées, où le modèle viscoélastique et les paramètres viscoélastiques ont été retrouvés à travers des mesures sur de l'aluminium, du grès de Fontainebleau, du marbre de Carrare, et de la diorite. Enfin, une étude synthétique a été réalisée pour caractériser une anomalie en vitesse et en atténuation avec la FWI.

Bibliography

Adam, L., Batzle, M., Lewallen, K. T., and van Wijk, K. (2009). Seismic wave attenuation in carbonates. *Journal of Geophysical Research: Solid Earth*, 114.

Aki, K. and Richards, P. G. (2002). *Quantitative seismology*. University Science Books.

Amestoy, P. R., de la Kethulle de Ryhove, S., L'Excellent, J.-Y., Moreau, G., and Shantsev, D. V. (2019). Efficient use of sparsity by direct solvers applied to 3d controlled-source em problems. *Computational Geosciences*, 23(6):1237–1258.

Bamberger, A., Chavent, G., and Lailly, P. (1979). About the stability of the inverse problem in 1-d wave equations—application to the interpretation of seismic profiles. *Applied Mathematics and Optimization*, 5:1–47.

Bardet, J. P. (1992). A Viscoelastic Model for the Dynamic Behavior of Saturated Poroelastic Soils. *Journal of Applied Mechanics*, 59(1):128–135.

Berenger, J.-P. (1994). A perfectly matched layer for the absorption of electromagnetic waves. *Journal of computational physics*, 114(2):185–200.

Biot, M. A. (1954). Theory of stress-strain relations in anisotropic viscoelasticity and relaxation phenomena. *Journal of Applied Physics*, 25(11):1385–1391.

Biot, M. A. (1956a). Theory of propagation of elastic waves in a fluid-saturated porous solid. i. low-frequency range. *The Journal of the Acoustical Society of America*, 28(2):168–178.

Biot, M. A. (1956b). Theory of propagation of elastic waves in a fluid-saturated porous solid. ii. higher frequency range. *The Journal of the Acoustical Society of America*, 28(2):179–191.

Blanc, E., Komatitsch, D., Chaljub, E., Lombard, B., and Xie, Z. (2016). Highly accurate stability-preserving optimization of the zener viscoelastic model, with application to wave propagation in the presence of strong attenuation. *Geophysical Supplements to the Monthly Notices of the Royal Astronomical Society*, 205(1):427–439.

Bonnasse-Gahot, M., Calandra, H., Diaz, J., and Lanteri, S. (2018). Hybridizable discontinuous galerkin method for the 2-d frequency-domain elastic wave equations. *Geophysical Journal International*, 213(1):637–659.

Bourbie, T. and Zinszner, B. (1985). Hydraulic and acoustic properties as a function of porosity in fontainebleau sandstone. *Journal of Geophysical Research: Solid Earth*, 90(B13):11524–11532.

Bourbié, T. and Nur, A. (1984). Effects of attenuation on reflections: Experimental test. *Journal of Geophysical Research: Solid Earth*, 89(B7):6197–6202.

Bretaudeau, F., Brossier, R., Leparoux, D., Abraham, O., and Virieux, J. (2013). 2d elastic full-waveform imaging of the near-surface: application to synthetic and physical modelling data sets. *Near Surface Geophysics*, 11(3):307–316.

Brossier, R., Operto, S., and Virieux, J. (2009). Seismic imaging of complex onshore structures by 2d elastic frequency-domain full-waveform inversion. *Geophysics*, 74(6):WCC105–WCC118.

Capps, R. N. (1983). Dynamic young's moduli of some commercially available polyurethanes. *The Journal of the Acoustical Society of America*, 73(6):2000–2005.

Carcione, J. M. (2007). *Wave fields in real media: Wave propagation in anisotropic, anelastic, porous and electromagnetic media*. Elsevier.

Chopra, S. and Marfurt, K. J. (2005). Seismic attributes—a historical perspective. *Geophysics*, 70(5):3SO–28SO.

Clayton, R. and Engquist, B. (1977). Absorbing boundary conditions for acoustic and elastic wave equations. *Bulletin of the seismological society of America*, 67(6):1529–1540.

Coli, M. and Criscuolo, A. (2021). The carrara marble: geology, geomechanics and quarrying. In *IOP Conference Series: Earth and Environmental Science*, volume 833, page 012120. IOP Publishing.

Colton, D. L. and Kress, R. (1998). *Inverse acoustic and electromagnetic scattering theory*, volume 93. Springer.

Dasgupta, R. and Clark, R. A. (1998). Estimation of q from surface seismic reflection data. *Geophysics*, 63(6):2120–2128.

Dash, B. P. and Obaidullah, K. A. (1970). Determination of signal and noise statistics using correlation theory. *Geophysics*, 35(1):24–32.

Delle Piane, C., Arena, A., Sarout, J., Esteban, L., and Cazes, E. (2015). Micro-crack enhanced permeability in tight rocks: An experimental and microstructural study. *Tectonophysics*, 665:149–156.

Donnelle, D. and Rust, B. (2005). The fast fourier transform for experimentalists. part i. concepts. *Computing in Science & Engineering*, 7(2):80–88.

Emmerich, H. and Korn, M. (1987). Incorporation of attenuation into time-domain computations of seismic wave fields. *Geophysics*, 52(9):1252–1264.

Fabien-Ouellet, G., Gloaguen, E., and Giroux, B. (2017). Time domain viscoelastic full waveform inversion. *Geophysical Journal International*, 209(3):1718–1734.

Faucher, F. (2017). *Contributions to seismic full waveform inversion for time harmonic wave equations: Stability estimates, convergence analysis, numerical experiments involving large scale optimization algorithms*. PhD thesis, Université de Pau et des Pays de l'Adour.

Faucher, F. (2021). hawen: time-harmonic wave modeling and inversion using hybridizable discontinuous galerkin discretization. *Journal of Open Source Software*, 6(57):2699.

Faucher, F., Chavent, G., Barucq, H., and Calandra, H. (2020). A priori estimates of attraction basins for velocity model reconstruction by time-harmonic full-waveform inversion and data-space reflectivity formulation. *Geophysics*, 85(3):R223–R241.

Faucher, F. and Scherzer, O. (2023). Quantitative inverse problem in visco-acoustic media under attenuation model uncertainty. *Journal of Computational Physics*, 472:111685.

Geertsma, J. and Smit, D. (1961). Some aspects of elastic wave propagation in fluid-saturated porous solids. *Geophysics*, 26(2):169–181.

Givoli, D. and Keller, J. B. (1990). Non-reflecting boundary conditions for elastic waves. *Wave Motion*, 12(3):261–279.

Golden, J. M. and Graham, G. A. (1988). *Boundary value problems in linear viscoelasticity*. Springer Science & Business Media.

Grandjean, G. and Leparoux, D. (2004). The potential of seismic methods for detecting cavities and buried objects: experimentation at a test site. *Journal of Applied Geophysics*, 56(2):93–106.

Groos, L., Schäfer, M., Forbriger, T., and Bohlen, T. (2014). The role of attenuation in 2d full-waveform inversion of shallow-seismic body and rayleigh waves. *Geophysics*, 79(6):R247–R261.

Guillot, F. M. and Trivett, D. H. (2011). Complete elastic characterization of viscoelastic materials by dynamic measurements of the complex bulk and young’s moduli as a function of temperature and hydrostatic pressure. *Journal of Sound and Vibration*, 330(14):3334–3351.

Gurevich, B. and Pevzner, R. (2015). How frequency dependency of q affects spectral ratio estimatespitfalls in q estimation. *Geophysics*, 80(2):A39–A44.

Hennino, R., Trégourès, N., Shapiro, N. M., Margerin, L., Campillo, M., van Tiggelen, B. A., and Weaver, R. L. (2001). Observation of equipartition of seismic waves. *Phys. Rev. Lett.*, 86:3447–3450.

Hurley, D. C. (1999). Nonlinear propagation of narrow-band rayleigh waves excited by a comb transducer. *The Journal of the Acoustical Society of America*, 106(4):1782–1788.

Imperiale, A., Leymarie, N., and Demaldent, E. (2020). Numerical modeling of wave propagation in anisotropic viscoelastic laminated materials in transient regime: Application to modeling ultrasonic testing of composite structures. *International Journal for Numerical Methods in Engineering*, 121(15):3300–3338.

Johnston, D. H., Toksöz, M. N., and Timur, A. (1979). Attenuation of seismic waves in dry and saturated rocks: Ii. mechanisms. *Geophysics*, 44(4):691–711.

Knopoff, L. and MacDonald, G. J. (1958). Attenuation of small amplitude stress waves in solids. *Reviews of Modern Physics*, 30(4):1178.

Kosloff, R. and Kosloff, D. (1986). Absorbing boundaries for wave propagation problems. *Journal of Computational Physics*, 63(2):363–376.

Kupradze, V., Gegelia, T., Basheleishvili, M. O., Burchuladze, T. V., and Sternberg, E. (1976). *Three-dimensional problems of the mathematical theory of elasticity and thermoelasticity*. North-Holland Publishing Company.

Leong, E.-C., Yeo, S.-H., and Rahardjo, H. (2004). Measurement of wave velocities and attenuation using an ultrasonic test system. *Canadian geotechnical journal*, 41(5):844–860.

Liu, E., Crampin, S., Queen, J., and Rizer, W. (1993). Velocity and attenuation anisotropy caused by microcracks and macrofractures in a multiazimuth reverse vsp. *Canadian Journal of Exploration Geophysics*, 29(1):177–188.

Liu, H.-P., Anderson, D. L., and Kanamori, H. (1976). Velocity dispersion due to anelasticity; implications for seismology and mantle composition. *Geophysical Journal International*, 47(1):41–58.

Lu, C. and Jackson, I. (1996). Seismic-frequency laboratory measurements of shear mode viscoelasticity in crustal rocks i: competition between cracking and plastic flow in thermally cycled carrara marble. *Physics of the Earth and Planetary Interiors*, 94(1):105–119.

Madigosky, W. M. and Lee, G. F. (1983). Improved resonance technique for materials characterization. *The Journal of the Acoustical Society of America*, 73(4):1374–1377.

Malehmir, A., Durrheim, R., Bellefleur, G., Urosevic, M., Juhlin, C., White, D. J., Milkereit, B., and Campbell, G. (2012). Seismic methods in mineral exploration and mine planning: A general overview of past and present case histories and a look into the future. *Geophysics*, 77(5):WC173–WC190.

Malinowski, M., Operto, S., and Ribodetti, A. (2011). High-resolution seismic attenuation imaging from wide-aperture onshore data by visco-acoustic frequency-domain full-waveform inversion. *Geophysical Journal International*, 186(3):1179–1204.

Manthei, G., Eisenblatter, J., and Spies, T. (2006). Determination of wave attenuation in rock salt in the frequency range 1-100 khz using located acoustic emission events. *Progress in Acoustic Emission*, 13:129.

Margerin, L., Campillo, M., and van Tiggelen, B. (2000). Monte Carlo simulation of multiple scattering of elastic waves. *Journal of Geophysical Research : Solid Earth*, 105:7873–7892.

Margerin, L., Campillo, M., Van Tiggelen, B., and Hennino, R. (2009). Energy partition of seismic coda waves in layered media: theory and application to pinyon flats observatory. *Geophysical Journal International*, 177(2):571–585.

Masmoudi, N., Stone, W., and Ratcliffe, A. (2023). Visco-elastic full-waveform inversion and imaging using ocean-bottom node data. In *84th EAGE Annual Conference & Exhibition*, volume 2023, pages 1–5. European Association of Geoscientists & Engineers.

McCann, C. and Sothcott, J. (1992). Laboratory measurements of the seismic properties of sedimentary rocks. *Geological Society, London, Special Publications*, 65(1):285–297.

Métivier, L., Brossier, R., Virieux, J., and Operto, S. (2013). Full waveform inversion and the truncated newton method. *SIAM Journal on Scientific Computing*, 35(2):B401–B437.

Moczo, P. and Kristek, J. (2005). On the rheological models used for time-domain methods of seismic wave propagation. *Geophysical Research Letters*, 32(1).

Molero, M., Segura, I., Aparicio, S., Hernández, M. G., and Izquierdo, M. (2010). On the measurement of frequency-dependent ultrasonic attenuation in strongly heterogeneous materials. *Ultrasonics*, 50(8):824–828.

Molli, G., Conti, P., Giorgetti, G., Meccheri, M., and Oesterling, N. (2000). Microfabric study on the deformational and thermal history of the alpi apuane marbles (carrara marbles), italy. *Journal of Structural Geology*, 22(11-12):1809–1825.

Molyneux, J. B. and Schmitt, D. R. (2000). Compressional-wave velocities in attenuating media: A laboratory physical model study. *Geophysics*, 65(4):1162–1167.

Morochnik, V. and Bardet, J. (1996). Viscoelastic approximation of poroelastic media for wave scattering problems. *Soil Dynamics and Earthquake Engineering*, 15(5):337–346.

Müller, T. M., Gurevich, B., and Lebedev, M. (2010). Seismic wave attenuation and dispersion resulting from wave-induced flow in porous rocks — a review. *Geophysics*, 75(5):75A147–75A164.

Nocedal, J. and Wright, S. J. (2006). *Numerical optimization, Springer series in operations research*. Siam J Optimization.

Norris, D. M. and Young, W.-C. (1970). Complex-modulus measurement by longitudinal vibration testing. *Experimental Mechanics*, 10(2):93–96.

O'connell, R. and Budiansky, B. (1978). Measures of dissipation in viscoelastic media. *Geophysical Research Letters*, 5(1):5–8.

Operto, S., Gholami, Y., Prieux, V., Ribodetti, A., Brossier, R., Metivier, L., and Virieux, J. (2013). A guided tour of multiparameter full-waveform inversion with multicomponent data: From theory to practice. *The leading edge*, 32(9):1040–1054.

Pan, W. and Wang, Y. (2020). On the influence of different misfit functions for attenuation estimation in viscoelastic full-waveform inversion: synthetic study. *Geophysical Journal International*, 221(2):1292–1319.

Pandit, B. and King, M. (1979). The variation of elastic wave velocities and quality factor q of a sandstone with moisture content. *Canadian Journal of Earth Sciences*, 16(12):2187–2195.

Pang, M., Ba, J., Carcione, J. M., Picotti, S., Zhou, J., and Jiang, R. (2019). Estimation of porosity and fluid saturation in carbonates from rock-physics templates based on seismic q. *Geophysics*, 84(6):M25–M36.

Papadakis, E. P., Fowler, K. A., and Lynnworth, L. C. (1973). Ultrasonic attenuation by spectrum analysis of pulses in buffer rods: Method and diffraction corrections. *The Journal of the Acoustical Society of America*, 53(5):1336–1343.

Peacock, S., McCann, C., Sothcott, J., and Astin, T. R. (1994). Experimental measurements of seismic attenuation in microfractured sedimentary rock. *GEOPHYSICS*, 59(9):1342–1351.

Pimienta, L., Borgomano, J. V. M., Fortin, J., and Guéguen, Y. (2017). Elastic dispersion and attenuation in fully saturated sandstones: Role of mineral content, porosity, and pressures. *Journal of Geophysical Research: Solid Earth*, 122(12):9950–9965.

Pimienta, L., Fortin, J., and Guéguen, Y. (2015a). Bulk modulus dispersion and attenuation in sandstones. *Geophysics*, 80(2):D111–D127.

Pimienta, L., Fortin, J., and Guéguen, Y. (2015b). Experimental study of young's modulus dispersion and attenuation in fully saturated sandstones. *Geophysics*, 80(5):L57–L72.

Pimienta, L., Orellana, L. F., and Violay, M. (2019). Variations in elastic and electrical properties of crustal rocks with varying degree of microfracturation. *Journal of Geophysical Research: Solid Earth*, 124(7):6376–6396.

Pimienta, L., Schubnel, A., Violay, M., Fortin, J., Guéguen, Y., and Lyon-Caen, H. (2018). Anomalous vp/vs ratios at seismic frequencies might evidence highly damaged rocks in subduction zones. *Geophysical Research Letters*, 45(22):12,210–12,217.

Pratt, R. G. (1999). Seismic waveform inversion in the frequency domain, part 1: Theory and verification in a physical scale model. *Geophysics*, 64(3):888–901.

Prieux, V., Brossier, R., Operto, S., and Virieux, J. (2013a). Multiparameter full waveform inversion of multicomponent ocean-bottom-cable data from the valhall field. part 1: Imaging compressional wave speed, density and attenuation. *Geophysical Journal International*, 194(3):1640–1664.

Prieux, V., Brossier, R., Operto, S., and Virieux, J. (2013b). Multiparameter full waveform inversion of multicomponent ocean-bottom-cable data from the valhall field. part 2: Imaging compressive-wave and shear-wave velocities. *Geophysical Journal International*, 194(3):1665–1681.

Rao, M., Sarma, L., and Lakshmi, K. (2002). Ultrasonic pulse-broadening and attenuation in volcanic rock-a case study. *IJPAP*.

Ribodetti, A., Gaffet, S., Operto, S., Virieux, J., and Saracco, G. (2004). Asymptotic waveform inversion for unbiased velocity and attenuation measurements: numerical tests and application for Vesuvius lava sample analysis. *Geophysical Journal International*, 158(1):353–371.

Rietsch, E. (1980). Estimation of the signal-to-noise ratio of seismic data with application to stacking. *Geophysical Prospecting*, 28(4):531–550.

Ritchie, I. (1973). Improved resonant bar techniques for the measurement of dynamic elastic moduli and a test of the timoshenko beam theory. *Journal of Sound and Vibration*, 31(4):453–468.

Robertsson, J. O. and Curtis, A. (2002). Wavefield separation using densely deployed three-component single-sensor groups in land surface-seismic recordings. *Geophysics*, 67(5):1624–1633.

Roderick, R. L. and Truell, R. (1952). The measurement of ultrasonic attenuation in solids by the pulse technique and some results in steel. *Journal of Applied Physics*, 23(2):267–279.

Ryan, H. (1994). Ricker, ormsby; klander, bntterwo-a choice of wavelets. *CSEG Recorder*, 19(07).

Ryzhik, L., Papanicolaou, G., and Keller, J. B. (1996). Transport equations for elastic and other waves in random media. *Wave Motion*, 24(4):327–370.

Sachse, W. and Pao, Y. (1978). On the determination of phase and group velocities of dispersive waves in solids. *Journal of Applied Physics*, 49(8):4320–4327.

Sarout, J., Cazes, E., Delle Piane, C., Arena, A., and Esteban, L. (2017). Stress-dependent permeability and wave dispersion in tight cracked rocks: Experimental validation of simple effective medium models. *Journal of Geophysical Research: Solid Earth*, 122(8):6180–6201.

Schön, J. H. (2015). *Physical properties of rocks: Fundamentals and principles of petrophysics*. Elsevier.

Sena-Lozoya, E. B., González-Escobar, M., Gómez-Arias, E., González-Fernández, A., and Gómez-Ávila, M. (2020). Seismic exploration survey northeast of the tres virgenes geothermal field, baja california sur, mexico: a new geothermal prospect. *Geothermics*, 84:101743.

Shapiro, N. M., Campillo, M., Margerin, L., Singh, S. K., Kostoglodov, V., and Pacheco, J. (2000). The Energy Partitioning and the Diffusive Character of the Seismic Coda. *Bulletin of the Seismological Society of America*, 90(3):655–665.

Shen, C. (2020). *Études expérimentales et numériques de la propagation d'ondes sismiques dans les roches carbonatées en laboratoire*. PhD thesis, Pau.

Shen, C., Brito, D., Diaz, J., Sanjuan, F., Bordes, C., and Garambois, S. (2022). Pulsed-laser source characterization in laboratory seismic experiments. *Geomechanics and Geophysics for Geo-Energy and Geo-Resources*, 8:1–26.

Shen, Y., Ren, Y., Gao, H., and Savage, B. (2012). An Improved Method to Extract Very-Broadband Empirical Green's Functions from Ambient Seismic Noise. *Bulletin of the Seismological Society of America*, 102(4):1872–1877.

Shin, C. and Cha, Y. H. (2008). Waveform inversion in the laplace domain. *Geophysical Journal International*, 173(3):922–931.

Shin, C. and Cha, Y. H. (2009). Waveform inversion in the laplace—fourier domain. *Geophysical Journal International*, 177(3):1067–1079.

Shin, C., Koo, N.-H., Cha, Y. H., and Park, K.-P. (2010). Sequentially ordered single-frequency 2-d acoustic waveform inversion in the laplace–fourier domain. *Geophysical Journal International*, 181(2):935–950.

Snieder, R. (2002). Coda wave interferometry and the equilibration of energy in elastic media. *Phys. Rev. E*, 66:046615.

Spencer Jr., J. W. (1981). Stress relaxations at low frequencies in fluid-saturated rocks: Attenuation and modulus dispersion. *Journal of Geophysical Research: Solid Earth*, 86(B3):1803–1812.

Subramaniyan, S., Quintal, B., Tisato, N., Saenger, E. H., and Madonna, C. (2014). An overview of laboratory apparatuses to measure seismic attenuation in reservoir rocks. *Geophysical Prospecting*, 62(6):1211–1223.

Sun, R., McMechan, G. A., and Chuang, H.-H. (2011). Amplitude balancing in separating p-and s-waves in 2d and 3d elastic seismic data. *Geophysics*, 76(3):S103–S113.

Sánchez-Sesma, F. J., Pérez-Ruiz, J. A., Luzón, F., Campillo, M., and Rodríguez-Castellanos, A. (2008). Diffuse fields in dynamic elasticity. *Wave Motion*, 45(5):641–654. Special Issue on Selected Papers Presented at the International Symposium on Mechanical Waves in Solids - Volume 2.

Sánchez-Sesma, F. J., Victoria-Tobon, E., Carbajal-Romero, M., Rodríguez-Sánchez, J. E., and Rodríguez-Castellanos, A. (2018). Energy equipartition in theoretical and recovered seismograms. *Journal of Applied Geophysics*, 150:153–159.

Taner, M. T., Koehler, F., and Sheriff, R. (1979). Complex seismic trace analysis. *Geophysics*, 44(6):1041–1063.

Tarantola, A. (1984). Inversion of seismic reflection data in the acoustic approximation. *Geophysics*, 49(8):1259–1266.

Tarantola, A. and Valette, B. (1982). Generalized nonlinear inverse problems solved using the least squares criterion. *Reviews of Geophysics*, 20(2):219–232.

Tatham, R. H. and McCormack, M. D. (1991). *Multicomponent seismology in petroleum exploration*. Society of Exploration Geophysicists.

Thiry, M. and Marechal, B. (2001). Development of tightly cemented sandstone lenses in uncemented sand: example of the fontainebleau sand (oligocene) in the paris basin. *Journal of Sedimentary Research*, 71(3):473–483.

Tisato, N. and Madonna, C. (2012). Attenuation at low seismic frequencies in partially saturated rocks: Measurements and description of a new apparatus. *Journal of Applied Geophysics*, 86:44–53.

Tisato, N. and Quintal, B. (2014). Laboratory measurements of seismic attenuation in sandstone: Strain versus fluid saturation effects. *Geophysics*, 79(5):WB9–WB14.

Tisato, N., Quintal, B., Chapman, S., Madonna, C., Subramaniyan, S., Frehner, M., Saenger, E. H., and Grasselli, G. (2014). Seismic attenuation in partially saturated rocks: Recent advances and future directions. *The Leading Edge*, 33(6):640–646.

Toksöz, M. N., Johnston, D. H., and Timur, A. (1979). Attenuation of seismic waves in dry and saturated rocks: I. laboratory measurements. *Geophysics*, 44(4):681–690.

Turkel, E. and Yefet, A. (1998). Absorbing pml boundary layers for wave-like equations. *Applied Numerical Mathematics*, 27(4):533–557.

Vinh, P. C. and Malischewsky, P. G. (2007). An approach for obtaining approximate formulas for the rayleigh wave velocity. *Wave Motion*, 44(7-8):549–562.

Virieux, J. and Operto, S. (2009). An overview of full-waveform inversion in exploration geophysics. *Geophysics*, 74(6):WCC1–WCC26.

Wang, S., de Hoop, M. V., and Xia, J. (2011). On 3d modeling of seismic wave propagation via a structured parallel multifrontal direct helmholtz solver. *Geophysical Prospecting*, 59(Modelling Methods for Geophysical Imaging: Trends and Perspectives):857–873.

Winkler, K. W. and Nur, A. (1979). Pore fluids and seismic attenuation in rocks. *Geophysical Research Letters*, 6(1):1–4.

Winkler, K. W. and Nur, A. (1982). Seismic attenuation: Effects of pore fluids and frictional-sliding. *Geophysics*, 47(1):1–15.

Winkler, K. W. and Plona, T. J. (1982). Technique for measuring ultrasonic velocity and attenuation spectra in rocks under pressure. *Journal of Geophysical Research: Solid Earth*, 87(B13):10776–10780.

Yim, H. J., Kim, J. H., and Kwak, H.-G. (2010). Ultrasonic wave attenuation measurement for nondestructive evaluation of concrete. In Shull, P. J., Diaz, A. A., and Wu, H. F., editors, *Nondestructive Characterization for Composite Materials, Aerospace Engineering, Civil Infrastructure, and Homeland Security 2010*, volume 7649, pages 446 – 454. International Society for Optics and Photonics, SPIE.

Yong, P., Brossier, R., Métivier, L., and Virieux, J. (2021). Q estimation by full-waveform inversion: Analysis and misfit functions comparison. In *First International Meeting for Applied Geoscience & Energy*, pages 827–831. Society of Exploration Geophysicists.

Zhao, Y., Liu, Y., Li, X., and Jiang, N. (2014). Time–frequency domain snr estimation and its application in seismic data processing. *Journal of Applied Geophysics*, 107:25–35.

Zhu, S., Kang, J., Wang, Y., and Zhou, F. (2022). Effect of co2 on coal p-wave velocity under triaxial stress. *International Journal of Mining Science and Technology*, 32(1):17–26.

ECOLE DOCTORALE :
Sciences Exactes et leurs Applications (ED 211 SEA)

LABORATOIRES :
LFCR – INRIA Bordeaux University, équipe MAKUTU